4-12-2019 10:30 AM

Synthesis of Chemically Stable VO2 Particles Using Green Solvents and their Application as Smart Coatings

Dicho Zomaya
The University of Western Ontario

Supervisor
Charpentier, Paul
The University of Western Ontario

Graduate Program in Chemical and Biochemical Engineering
A thesis submitted in partial fulfillment of the requirements for the degree in Doctor of Philosophy

Abstract

Heating and cooling buildings consumes a tremendous amount of energy worldwide, often >50% for Northern climates such as Canada. A major part of this energy is lost through windows. The use of thermochromic windows provides a new intriguing option, in which the window automatically regulates the amount of solar transmission in response to environmental temperature changes. Of the potential thermochromic materials, vanadium dioxide (VO_2) is known to display a fully reversible semiconductor-metal transition (SMT). VO_2 responds thermochromically to environmental temperature changes by changing its crystal structure as a function of temperature. VO_2 is transparent to infrared radiation (IR) when its temperature is below a so-called phase transition temperature (T_c), but is IR light reflective above T_c, while retaining visible light transmittance. Such an intrinsic property makes VO_2 an attractive material for designing a new generation of "smart" thermochromic coatings to efficiently utilize solar energy. The main goal of this dissertation focuses on developing innovative VO_2 based particles and their integration into polymeric smart coatings using an economical and green chemistry approach, while examining the assemblies optical and thermal properties for potential application in smart windows.

Water as a “green” solvent was examined in Ch. 2 using ammonium metavanadate as a low toxicity VO_2 source, which was reduced by aspartic acid, for the novel synthesis of monoclinic vanadium dioxide [VO_2(M)]. In this chapter, various experimental parameters including annealing temperature, annealing time, anti-oxidation time, reagent concentration and W(tungsten) doping concentration were examined. This study examined finding the optimum conditions for synthesising an oxidation stable, W-doped, monoclinic vanadium oxide exhibiting a low Tc with small hysteresis. Meanwhile, the luminous transmittance and solar modulation ability of VO_2

based films was found to be enhanced simultaneously, an excellent result for potential commercial usage. The molar ratio of ammonium metavanadate and aspartic acid was varied systematically as well as the annealing temperature and reaction time. An aspartic acid/NH_4VO_3 molar ratio of "0.7/1" and "0.6/1", calcined at 800 °C for 2 h was found to deliver the purest VO_2(M) phase. Optimized VO_2(M) was then doped with tungsten (W) with nominal concentrations up to 4 at. %, with the annealing conditions optimized. The lowest transition temperature of 53.6 °C was found for the 3% W-nominal doping concentration using an 800 °C annealing temperature for 2 h. This material was shown to be stable against oxidation and showed an integrated luminous transparency (T_{lum}) of 68% at 22 °C and a solar modulation efficiency (ΔT_{sol}) of 20.7% between 22 °C and 80 °C in a polyvinylpyrrolidone (PVP) coating. Additionally, a pure VO_2(M) phase was achieved at lower annealing temperatures (i.e. 450 °C) and shorter times with the addition of W or PVP, which was not possible with the undoped sample. In general, these coatings showed better optical properties compared to most films reported in the literature, although their VO_2 transition temperature was still relatively high, not near room temperature. Window coatings for thermochromic glass at higher switching temperatures are also of industrial interest for solar thermal applications, making these results useful for the scientific community.

To make small particles with low T_c, a hydrothermal method was applied. Ch. 3 investigated reducing ammonium metavanadate (NH_4VO_3) with hydrazine in water using a hydrothermal method, followed by a relatively brief time heat treatment (calcination). A high yield of VO_2(M) crystals was obtained using this synthesis methodology. The reaction parameters (concentration, temperature and time) were examined to optimize the synthesis conditions of VO_2 (M) using a

parametric approach. Then, the influences of the calcination parameters including temperature and ramping rate were examined on the size, morphology, phase purity and phase transition temperature of Mo and W-doped VO_2 (M). Various nominal Mo and W contents from 0 to 4 at. % were investigated. The results showed that flower-like and stick-shaped morphologies of W-doped VO_2 and Mo-doped VO_2 particles were obtained, respectively. It was found that tungsten doping was more effective for reducing the phase transition temperature of VO_2 (68 °C) to an ambient temperature (23 °C) compared to molybdenum doping (54.4 °C). Furthermore, a high transition reduction efficiency of 23 K/at. % was obtained for the W-doped VO_2 crystals. The thermochromic properties of VO_2/PVP coatings on glass were investigated with the un-doped coatings exhibited high infrared modulation (up to 35% at 2000 nm), and simultaneously high visible light transmittance (> 62%). For the 1at. % W-doped coatings, high infrared modulation was obtained (up to 28% at 1500 nm) with high visible transmittance (> 75%). This could open an economical route to large-scale VO_2 (M) particles synthesis to produce low cost smart windows.

To further improve the chemical stability and thermochromic performance of VO_2, Ch. 4 examines a novel approach for the rapid synthesis of VO_2/SiO_2 composite structure. In this study, ammonium metavanadate was reduced with maleic acid using water as the green solvent, with VO_2/SiO_2 obtained at various (Si/V) molar ratios. The effect of SiO_2 addition on the size, dispersion, chemical stability and thermochromic performance of VO_2 was investigated. This study reveals that the SiO_2 significantly improved the anti-oxidation stability of VO_2 in air at room temperature for testing times up to seven months. Further, the infrared (IR) contrast transmittance displayed a VO_2/SiO_2 composite film which demonstrated an excellent IR switching quality (20%) that was 4X greater than the plain VO_2 film (5%), while maintaining high visible transmittance (70%) at the wavelength of 680 nm. Moreover, using a reflux approach at low temperature

reaction, the phase transition temperature (T_c) of 2 at. % W-doped VO_2 was reduced considerably to 23 °C, when tungstic acid (as the W-doping source) was pre-dissolved in hydrogen peroxide (H_2O_2) prior to use.

To examine a low temperature approach to making VO_2(M), Ch. 5 examines a novel synthetic approach at room temperature (RT) using hydrolysis for preparation of tungsten W-doped VO_2 particles. The hydrolysis of vanadyl acetylacetonate [$VO(acac)_2$] was achieved at RT by adding HCl as a catalyst, converting the green aqueous solution into a blue one, indicating the formation of VO_2(M). In addition to examining different drying methods, various experimental parameters including concentration, reaction time, annealing time and W doping concentration were investigated. The W-doping system is different from the high temperature hydrothermal process usually reported in the literature. The W-doped VO_2 NPs were found to exhibit a low semiconductor-metal phase transition temperature (SMT). It was discovered that small NPs of vanadium (V) oxide, present in the formed product, could enhance the dispersion of VO_2(M) (IV) particles in a polyvinylpyrrolidone (PVP) matrix. By implementing this dispersion strategy, a VO_2(M)/PVP coated glass with an excellent infrared (IR) switching efficiency (40%) and good visible transmittance (35%) was accomplished. In addition to PVP, hydrophobic poly(methyl methacrylate) (PMMA) and hydrophilic poly(4-vinylpyridine) (P4VP) were inspected as matrix polymers to achieve weather resistant films and films with good dispersion of VO_2 particles, respectively. Additionally, the effect of variable film thickness with controlled ratios of VO_2/PMMA and VO_2(M)/P4VP on the optical performance of the films was investigated. VO_2(M)/P4VP based-film demonstrated an excellent IR switching ability (47%) with great visible transmittance (41%) compared to (30%) and (29%) of VO_2/PMMA, respectively. The better performance is ascribed to the uniform dispersion of particles in P4VP. Importantly, the synthetic

method is a green chemistry approach and scalable, which can potentially enable a large scale production of VO_2.

KEYWORDS: Vanadium dioxide, VO_2, phase transition temperature, T_c, thermochromic, green, anti-oxidation, T_{lum}, ΔT_{sol}, W-doped VO_2, Mo-doped VO_2, VO_2/PVP coatings, VO_2/SiO_2 composite, energy consumption, SMT, IR, PVP, PMMA, P4VP

Dedication

This work is dedicated to my loving and supportive family, wife (Achtar Gabrial) and children (Julie, Elona and Zomaya), who have given me the strength and confidence with an amazing patience to pursue my dreams.

Acknowledgements

I would like to sincerely thank my supervisor Prof. Paul Charpentier, and to acknowledge the valuable leadership, excellent guidance, support and encouragement that he provided to me during this work. His affection and great trust in me was very courteous and inspired me to approach my PhD study topics with much passion.

I am also very grateful to Dr. Silvia Mittler, a professor from Physics & Astronomy, and Dr. Bernd Grohe, a senior research scientist with the Department of Chemical & Biochemical Engineering and the Schulich School of Medicine and Dentistry, at the University of Western Ontario in London, for their careful review of my manuscripts, and for suggestions and comments that proceeded.

I also thank Dr. William Xu, from Chemical & Biochemical Engineering at the University of Western Ontario in London, for all his scientific support and discussions.

Finally, Special thanks to all the amazing students that I had the opportunity to work alongside.

Table of Contents

List of Tables

List of Figures

Abbreviations

at.%	Atomic percent
ΔT_{sol}	Solar modulation efficiency
DSC	Differential Scanning Calorimetry
EDX	Energy Dispersive X-ray
FTIR	Fourier Transform Infrared Spectroscopy
IR	Infrared
Mo	Molybdenum
NH_4VO_3	Ammonium metavanadate
NMR	Nuclear Magnetic Resonance
PMMA	Poly (methyl methacrylate)
P4VP	Poly(4-vinylpyridine)
PVP	Poly(vinylpyrrolidone)
RT	Room temperature (°C)
SEM	Scanning Electron Microscopy
SMT	Semiconductor-metal phase transition
T_c	Phase transition temperature (°C)
T_{lum}	Luminous transmittance
VO_2(M)	Monoclinic vanadium dioxide
W	Tungsten
XPS	X-ray Photoelectron Spectroscopy
XRD	X-ray diffractometer

Chapter 1

Introduction

1.1 OVERVIEW

A substantial component of primary energy (~40%) is used globally in the form of heating, cooling, ventilation and lighting in buildings to obtain desired indoor conditions for human comfort [1, 2]. Of this energy, greater than 50% is wasted through window losses [3]. For example, in Canada, windows can account for up to 31% of a building's total energy loss [4, 5]. This not only leads to high energy costs, but also leads to a high carbon footprint through increased CO_2 emissions [6]. To save energy, low emissivity windows (Low-E window) are used extensively in buildings to achieve a high infrared light reflection. However, it is not possible to change their optical performance in response to environmental changes [7-9]. Energy-saving smart materials (chromogenic materials) such as electrochromic, thermochromic, gasochromic and photochromic can sense and respond to an external stimulus involving an electric voltage, heat, gas or ultraviolet irradiation, respectively, and then intelligently block the passing solar energy [10-15]. Among chromogenic technologies, thermochromic vanadium dioxide (VO_2) has many advantages which includes having a simple structure, self-activating solar/heat control, and the potential for scalable mass production [10]. Vanadium dioxide (VO_2) can initiate a reversible semiconductor-metal phase transition (SMT) at ~68 °C, changing from a monoclinic structure ($P2_1/c$, M1 phase) below Tc to a tetragonal structure ($P4_2/mnm$, R phase) above Tc. This change in crystal structure causes an abrupt modification in the optical properties from infrared (IR) transmitting to a highly IR

reflecting material [16-19]. This distinctive property makes VO_2(M) a promising material for application in smart windows [20].

Vapor-based deposition methods are often used to achieve VO_2 coatings on transparent substrates for smart windows, but these techniques are expensive and complex due to the high cost of equipment and the challenge to control the variable valences of the vanadium ions [7]. Currently, solution-based methods are of increase interest for preparing VO_2(M) coating on substrates due to their economical, scalability and flexibility for substrate selection [7, 11]. However, to date, the major practical challenges that still restrict the use of VO_2 (M/R) systems for smart windows, and addressed in this dissertation are how to fabricate high performance polymer based VO_2 smart films with simultaneous high luminous transmittance (T_{lum}) and high solar modulation efficiency (ΔT_{sol}), while reducing energy costs in the fabrication process. Several applications to be explored in this thesis include low temperature reflux doping for the synthesis of W-doped VO_2 with high chemical stability, delivering PVP-coatings with high luminous transparency (T_{lum}) and solar modulation efficiency (ΔT_{sol}), hydrothermal synthesis of W- and Mo-doped VO_2(M) with low phase transition temperature (T_c) for the fabrication of VO_2/PVP with excellent infrared (IR) transmission modulation, synthesis of chemically stable VO_2/SiO_2 composite with high IR switching capability coating and room temperature synthesis of VO_2(M) and W-doped VO_2(M) for high IR switching efficiency coatings with excellent NPs dispersion using P4VP and hydrophobic PMMA polymer.

1.2 LITERATURE REVIEW

1.2.1 Magneli phases of the vanadium oxides

Vanadium is known to form switchable valence states from V^{2+} to V^{5+} that form vanadium-oxygen complexes with multivalent oxides including VO, V_2O_3, VO_2 and V_2O_5 [21, 22]. Non-stoichiometric vanadium oxides displaying a phase transition response are comprised of two types: one type exists between V_2O_5 and VO_2, with a general formula of V_nO_{2n+1} and the second one is a so-called Magnéli type with a general formula of V_nO_{2n-1} [23, 24]. Compared to the Magnéli family, V_nO_{2n+1} has less constituents which include V_3O_7 with phase transition temperatures (T_c) at 5.2 K and V_6O_{13} with an antiferromagnetic Neel temperature (T_N) at 155 K [25, 26]. Nonetheless, the Magnéli family contains structures V_nO_{2n-1} ($3 \leq n \leq 10$, based on the rutile VO_2(R) structure) with different T_c values as shown in Figure 1.1 [24, 27]. Examples include V_8O_{15} (70 K), V_5O_9(135 K), V_6O_{11} (170 K), V_4O_7 (250 K) and metallic V_7O_{13} [27].

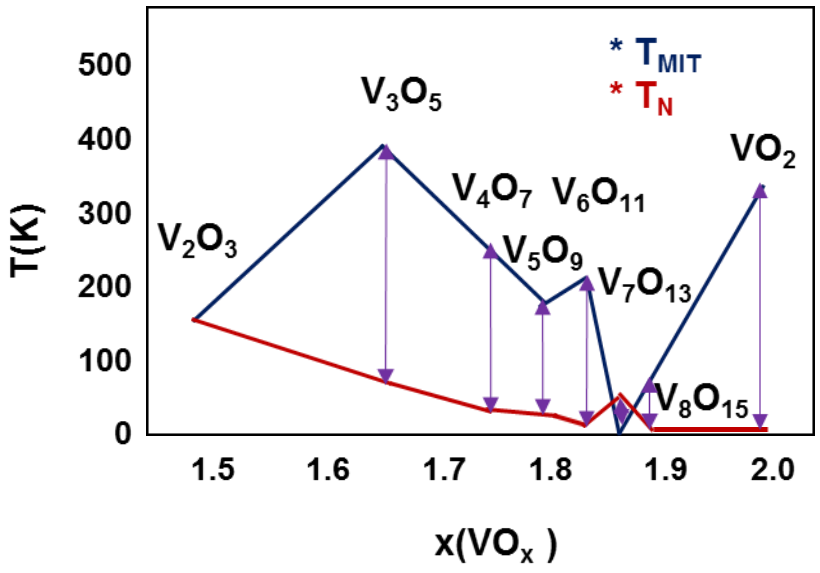

Figure 1.1 Néel temperatures or magnetic ordering temperatures (T_N) and metal–insulator transition (T_{MIT}) temperatures in the Magneli families [24].

1.2.2 Vanadium dioxide VO_2(M)

Vanadium dioxide (VO_2) has a number of polymorphs with more than ten types of crystalline phases. These include monoclinic distorted rutile structure VO_2 (M) (P21/c), tetragonal rutile-type VO_2 (R) (P4/mmm), and at least five metastable phases such as low temperature-tetragonal phase VO_2(A) (P4/ncc), high temperature tetragonal phase VO_2 (A) (I4/m), monoclinic VO_2 (B) (C2/m), layer-structured VO_2 (C) and the recently reported VO_2 (D) [28-30]. The crystallographic structures of these polymorphs are established on an oxygen *bcc* lattice, where the oxygen octahedra are more or less regular and the vanadium (V) ions lie in the octahedral sites [30]. Amongst these metal oxides, only VO_2(M/R) exhibits a fully first-order reversible semiconductor-metal phase transition (SMT) 68 °C due to the structural and electronic structure changes [31]. Each vanadium ion (V^{4+}) is centered in an octahedron formed by six oxygen ions (O^{2-}) at the vertices [32]. Nevertheless, this phase transition depends on the crystallinity, divergence and size of the VO_2.

Monoclinic vanadium dioxide VO_2(M) has been investigated since its reversible semiconductor-metal transition (SMT) was first reported by Morin in 1959 [17]. VO_2(M) has been studied as a model material for elucidating the electron–electron correlations and it belongs to V_nO_{2n-1} family when $n = \infty$ [33]. When the temperature of VO_2(M/R) is increased beyond 68 °C, the semiconductor-monoclinic phase (VO_2(M)) ($P2_1/c$, M1 phase, the most stable phase at RT) undergoes a structural transition to the metallic-tetragonal phase (VO_2(R)) ($P4_2/mnm$, R phase). This phenomena is known as thermochromism [34, 35] which results in a striking change of optical properties of VO_2(M/R) from infrared (IR) and ultraviolet transmittance below SMT to IR and ultraviolet reflectance above SMT. These optical changes are coupled with a change in resistivity

of ~4–5 orders of magnitude, while retaining the visible transparency [36, 37]. During the semiconductor-metal transition (SMT), the infinite linear chains of VO_2(R) is twisted into zigzag chains of VO_2(M) as shown in Figure 1.2 [38, 39]. The strengths of electron–electron correlation for the cation–cation (V^{3+}–V^{3+} and V^{4+}–V^{4+} ions) interactions determine whether the outer 3d electrons of vanadium oxide are restricted or not. As revealed by Goodenough, the judgmental separation value ($R_c \approx 2.93$) for the 3d electron coupling interaction for vanadium ions can be concluded from semi empirical expressions [40]. Accordingly, when the separation value (R) is smaller than the critical separation value (R_c), the 3d electrons are migrant, otherwise the electrons are localized when R is larger than R_c. For instance, the zigzag chains in VO_2(M), with V–V distance of 0.316 nm (>R_c) and 0.262 nm (<R_c) along the c_R-axis establish dimers of vanadium atoms which result in semiconductor/insulator performance and a resistance on the order of 0.1 Ω m (Figure 1.2) [41]. While the infinite chains of VO_2(R), with a V–V distance of 0.288 nm (<R_c) along the c_R-axis cause the d electrons to be shared by all vanadium ions in the same direction and obtain a low resistivity of about 10^{-6} Ω m [42, 43].

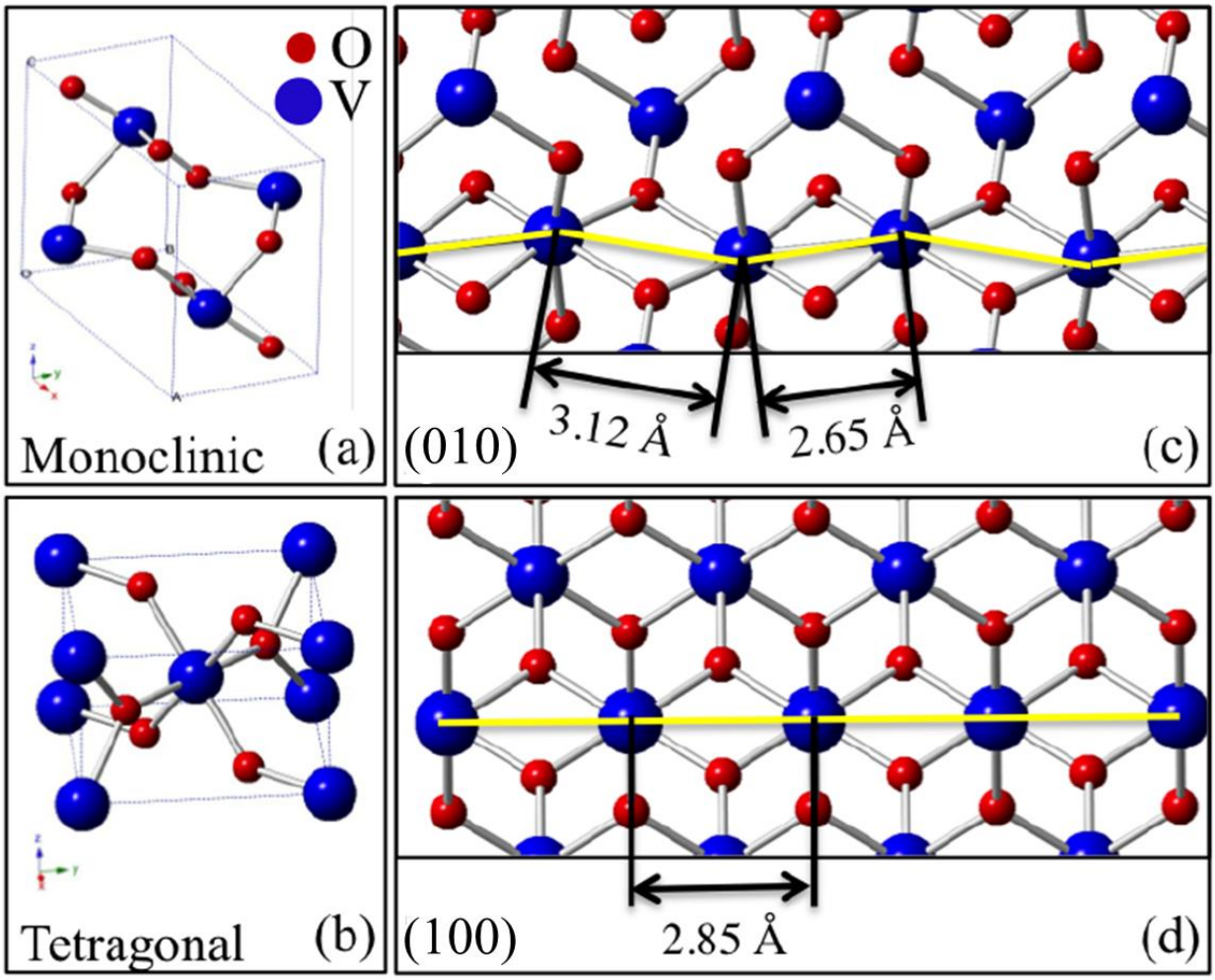

Figure 1.2 Crystal models of (a) VO_2(M) and (b) VO_2(R). Views along the c_R-axis of monoclinic (twisted V) (c) and tetragonal (d) structure, respectively [38].

Furthermore, the phase transition (SMT) can also accomplished by other phenomena such as physical stress, an electric field or an electromagnetic wave [44]. Accordingly, VO_2 (M) has attracted the attention of researchers for its prospective applications in energy-efficient thermochromic smart windows, sensors, thermal camouflage, switches, energy storage devices, four-dimensional imaging, field effect transitions, and so forth [19]. There are many factors that influence the metal-insulator transition of VO_2 (M) including the size effect, interfacial strain, external strain, defects, stoichiometry and doping.

It is usually very difficult to obtain a pure phase of VO_2(M) in one step which is normally synthesized by converting VO_2(B) and VO_2(A) at high temperatures (550 °C or more) into VO_2(M/R) [45-49]. Both VO_2 (B) and VO_2 (A) can be used as precursors to be reverted to a stable VO_2 (R) phase using thermal treatment and this is an irreversible transformation, because VO_2 (R) transforms into stable VO_2 (M) phase upon cooling [32]. Using a hydrothermal process with changes in pressure, temperature and time, VO_2 (B) can be transformed into VO_2 (A), which is often reported as the intermediate phase during transition from the metastable VO_2 (B) to the more stable VO_2(R) phase [50, 51].

A pure phase of VO_2 (M) in good quantities was synthesised by Cao et al. [52] and Liang et al. [31] using a one-step hydrothermal technique. However, agglomeration of particles with favorable orientation growth along the [110] direction was subject to grow in one-dimension nanostructures such as nanorods and nanowires, hence limiting the particles' dispersion, transparency and application for smart windows [52-54]. The size, shape and crystallographic phases of VO_2 particles are known to be difficult to be controlled simultaneously [55]. Quasi-spherical nanoparticles with high crystallinity and invariable sizes of VO_2 are ideal for good-quality production, in order to prepare stable dispersions needed to obtain good infrared light regulation and high visible transparency [30]. It is still a major challenge to synthesize spherical VO_2 nanoparticles which requires a depression of energetically inimical high-index faces or the promoted development of low-energy surfaces [30]. Chen et al. [56], Rajeswaran et al. [57], Zou et al. [58] and Ji at al. [59] successfully synthesized a pure phase of VO_2(M) by a solvent-thermal reduction, novel reduction, simple carbothermal reduction and hydrothermal method, respectively, however, the particles were large, non-spherical with wide size distribution and a wide variety of nanostructures.

The driving force for the SMT has been in debate for a long time. The Mott model explains that the powerful electron-electron interaction is behind the restriction of the electrons, hence forming a Mott–Hubbard insulator. However, based on Peierls model, the formation of an insulating phase is due to lattice instability or structural distortions induced by electron–phonon interactions [60, 61].

1.2.3 Phase transition mechanisms of VO_2

There is currently a controversy about the mechanisms of metal-insulator transition (MIT) in VO_2, and understanding the nature of this phenomenon is a current scientific challenge [60-62]. It is believed that the interaction between spin, charge, orbital dynamics and atomic structure is accountable for the MIT perceived in VO_2. Generally, the transition is due to either a Mott transition (intense electron-electron interaction), Peierls transition (electron-phonon interaction) or a combination of both mechanisms [39, 63-65]. Warwick et al. [66] and Wentzcovitch et al. [60] have shown that the electron-electron(e-e) interactions play a significant part in the insulator phase due to a strong Coulombic repulsion between the electrons. As shown in Figure 1.3, the d-levels of the vanadium ions in the metal phase are divided into higher energy e_g states(empty) and lower energy t_{2g} states [67]. Based on Goodenough [68], in the tetragonal structure, the t_{2g} multiplet splits into an e^{π}_g (π^*) doublet and an $a_{1g}(d_{II})$ state, and the (d_{II}) orbitals form strong bonding of the V-V pair along the c direction (see Figure 1.4) [69]. In the insulating phase, the tilting and dimerization of the V-V pairs cause the d_{II} band to split into an antibonding state (higher energy) and a bonding state (lower energy). This leaves the bonding d_{II} with half-filled and the antibonding π^* states are pushed into higher energy (above the Fermi level) to overlap more with O states resulting in a (Peierls- transition) band gap (see Figure 1.4) [69]. In order to study the aspect of the structural transformation during phase transition, Xie et al. [70] have tested X-ray absorption to direct electronic and atomic kinetics, and they have found that the modification in the electronic

structure is due to a change in the closest vanadium atoms. While Zhu et al. [71] have applied band theory to explain the electronic, structural and magnetic essence during phase transition. Bai et al. [72], Booth et al. [73] and Tselev et al. [74] have found that the MIT is driven by a structural transition. However, Lu et al. [75], Kim et al. [76] and Qazilbash et al. [62] presented strong evidence in favour of an electronic transition alone. Recently, Gao et al. [77] have applied density functional theory (DFT)-based first-principle calculations by relating band gap change with orbital occupancy and structure change, concluding that the structure-driven Peierls transition and staged electron-correlation-driven Mott transition are both involved in the MIT of VO_2 (M).

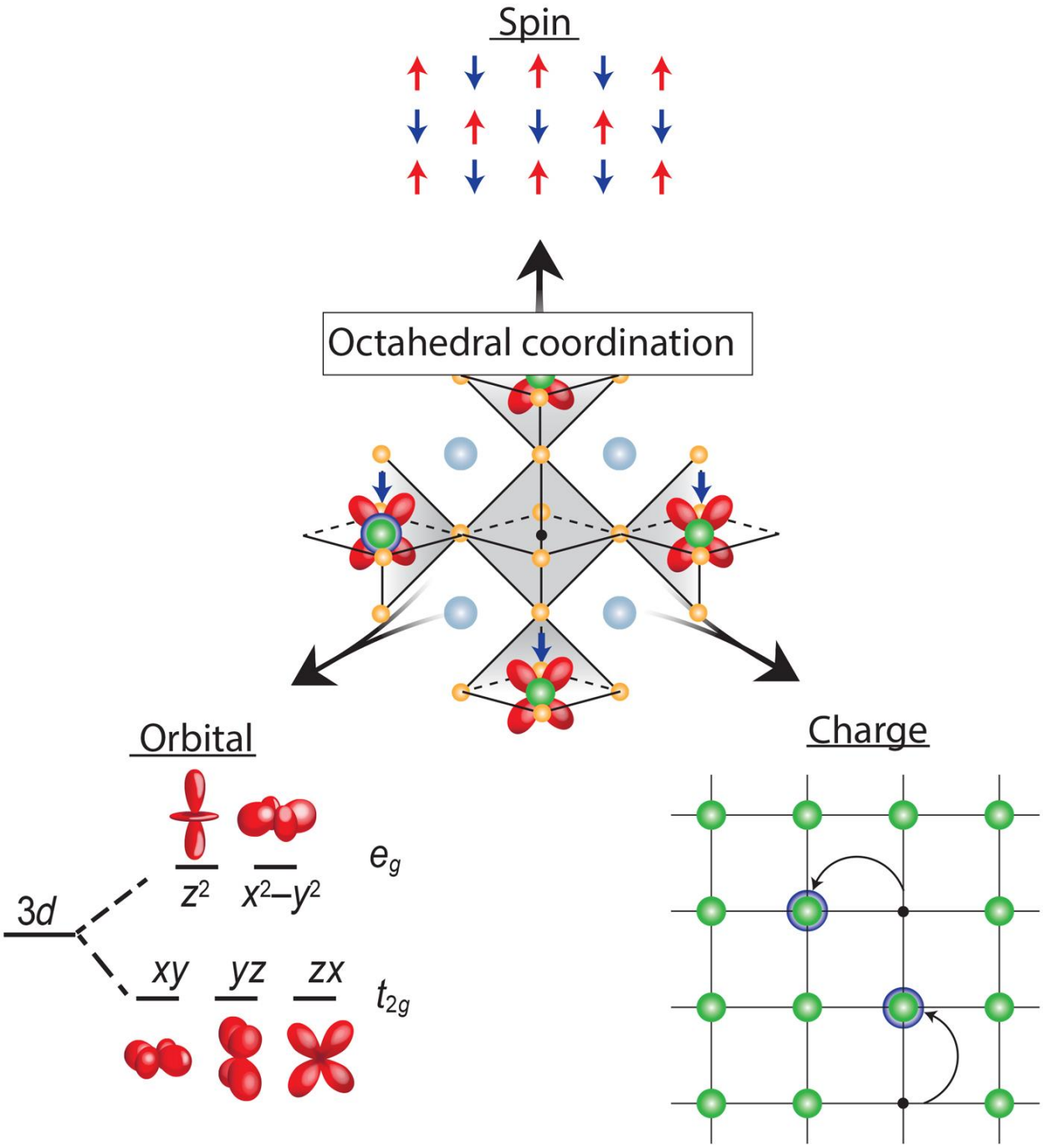

Figure 1.3 Octahedral organization of the V cation in all V_xO_y phases, and the effect of coupling between the competing spin, charge, and orbital degrees of freedom on the optical and electronic properties in vanadium oxides [67].

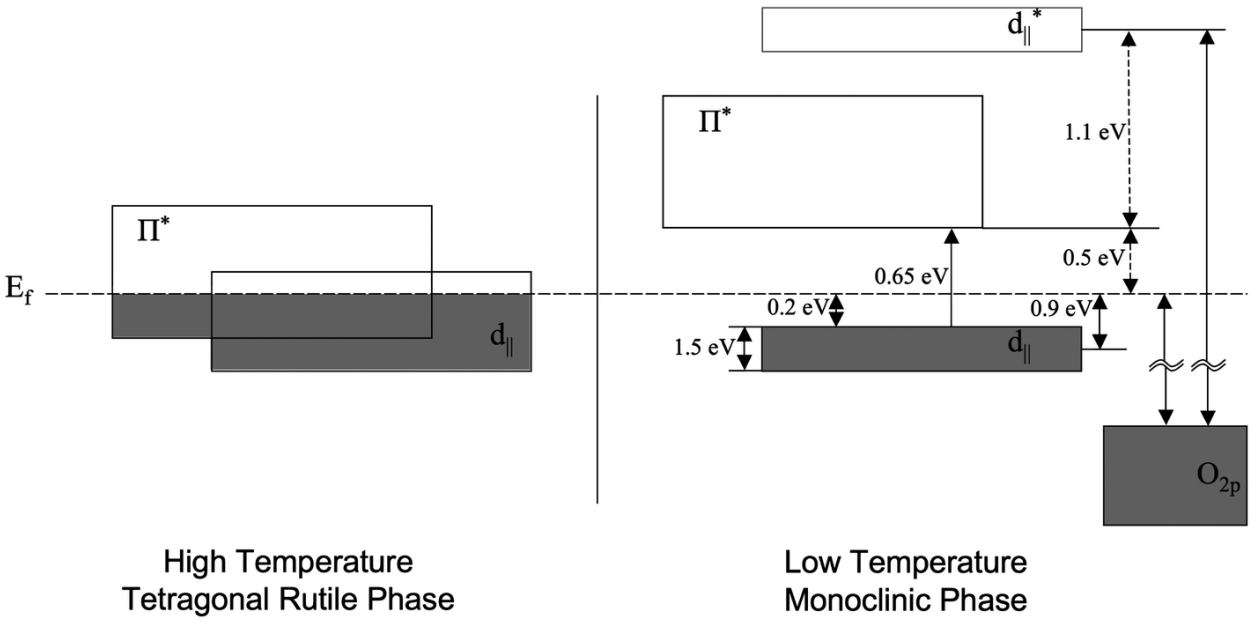

Figure 1.4 Schematic energy bands structure digram of VO_2 [69].

1.2.4 Phase transition temperature and hystersis loop calculations

To determine the phase transition temperature of the film, the optical transmittance is recorded at 2000 nm during a cooling and heating process. Then, a plot of d(Tr)/d(T) &T is aquired for each hysteresis loop, giving two peaks with a proper designated maximum [78]. T and Tr represent the temperature and transmittance, respectivily. The two maxima correspond to the phase transition temperature of heating(T_h) and cooling (T_c). Accordingly, the final phase transition temperature (T_t) of the VO_2 film can be attained by: $T_t=(T_h+T_c)/2$ [79]. Meanwhile, the difference between T_c and T_h , measued at full width at half maximum (FWHM), represent the hysteresis loop width (ΔT_t) of the film. A smaller ΔT_t value is requied for a sharper transition [20].

1.2.5 Elemental doping effect on the T_c and optical properties of VO_2 (M)

In order for VO_2 to be used for various applications such as optical memory devices, sensors and intelligent window coatings; the optical properties, SMT and related electronic transitions of VO_2 need to be controlled through stress, defects, grain size or dopants [16, 80-83]. Amongst these strategies, the elemental doping strategy is considered to be an effective process to control optical properties and reduce T_c of VO_2 [84]. For practical applications in smart windows, the phase transition (T_c=68°C) of VO_2 should be decreased to ambient temperature(~25°C), and this can be achieved by elemental doping [85, 86]. Transition temperatures of VO_2 can be reduced by doping with high-valent cations such as $Nb^{5+,}$ $Mo^{6+,}$ $Ta^{5+}$and W^{6+} or increased by doping with low-valent cations at high concentration such as Al^{3+}, Cr^{3+}, Ti^{+4}, Ga^{3+} and Fe^{3+} [36, 87, 88]. However, doping with low-valent cations at low concentration levels helps shift Tc lower [11]. Mai et al. [89] were able to lower the SMT of VO_2 from 64 to 42 °C due to semiconductor phase destabilization and loss of V^{4+}–V^{4+} pairs caused by Mo doping. Zhang et al. [90] used a silicon-doped VO_2 film to achieve a T_c of 52.7°C. Zhang et al. [91] have demonstrated a T_c of 18 °C using N-doped samples such as $VO_{1.87}N_{0.13}$ and $VO_{1.9}N_{0.1}$. Gentle et al. [92] and Chen et al. [93] showed that the T_c of Al-doped VO_2 sample can be lowered to 323 K and 313 K, respectively. Wan et al. [94] effectively decreased the T_c from 80.0 to 62.9 °C using N-doped VO_2(M). Gagaoudakis et al. [95] have used Mg (0.3 at. %)–doped VO_2 to achieve a characteristic low SMT at 49.2 °C. Chen et al. [96] obtained a T_c of ~ 51 °C for Ti(4%)-doped VO_2. Mlyuka et at. [97] and Zhou et al. [98] were able to reduce T_c from 64.5 °C to 45 °C and from 68 °C to 54 °C for the Mg(7%)-doped VO_2, respectively. Wan et al. [99] used density functional theory calculations and found that the band gap of Eg2 for C-doped VO_2 was the least (~0.434 eV) compared to B, N, Mg, Al-doped VO_2 samples, indicating that the T_c can be reduced more effectively by doping with carbon. However,

among all dopants, tungsten (W) has been found experimentally as the most practical element to decrease the SMT of VO_2-based films to ambient temperature. Accordingly, Mo, F and W are used to lower T_c by 15 K, 20 K and 28 K at. %, respectively, and Tc can be lowered by 15 °C, 19 °C and 23 °C per 1 at. % for Mo, F and W doping, respectively [99-104].

In explanation for W decreasing the SMT of VO_2, high-valent cation dopants such as W^{6+} perform as electron donors into the V 3d valent band, and the loss of a homopolar V^{4+}–V^{4+} pair causes destabilization in the semiconducting structure of VO_2. These electron donation effects result in the decreasing of T_c [105]. However, the mechanism for reducing SMT in VO_2(M) due to W doping is still a subject of debate. To elucidate the connection between tungsten doping and SMT, Wu et al. [106] investigated the electronic and geometrical structures surrounding vanadium and tungsten atoms in W-doped VO_2 samples using X-ray absorption fine structure (XAFS) spectroscopy. They found that the internal stresses caused by W doping promotes the detwisting of accessible VO_2(M) lattice in view of the electronic band structures of W-doped VO_2. Additionally, the detwisting of the monoclinic VO_2 lattice induces a minor gap between the bonding and antibonding of $d_{\|}$ orbitals besides to downward shift of the π^* electron band, causing a decrease in the band gaps of W-doped VO_2. As a result, the potential energy barrier is decreased for the SMT of VO_2 leading to a T_c reduction. Additionally, He et al. [107] methodically examined the orbital structures of W-doped VO_2(M/R) based-films using a double beam ultraviolet-infrared spectroscopy joined with first principle calculations. They found that the $d_{\|}$ orbital was very significant in the phase transition process of VO_2 and that the T_c change comes from the orbital structure discrepancy. When the concentration of W doping increases, the overlap of $d_{\|}$ and π^* increases for the rutile VO_2 structure. Meanwhile, the optical band gap decreases for the monoclinic VO_2 as shown in Figure 1.5 (a-d). For the rutile structure, when doping content is increased, the strength

of covalent bonding V–V interactions reduces due to a decrease in the $d_{\parallel}$ orbital occupancy which results in the observed T_c reduction (see Figure 1.5(e)).

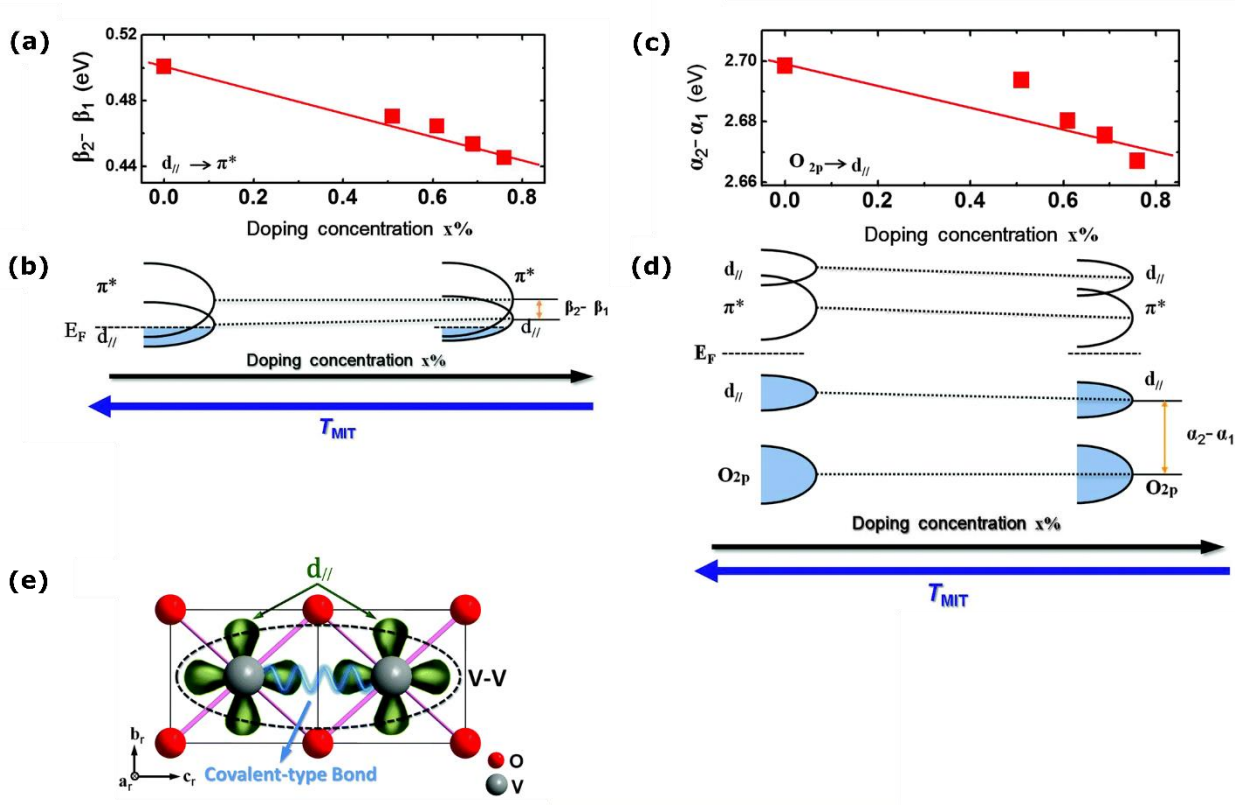

Figure 1.5 For rutile phase: (a) the relationship of tungsten doping concentration x% and β2–β1; (b) schematic of the orbital structure change due to increase in tungsten contents. For the monoclinic phase: (c) the relationship of tungsten doping concentration x% and α2–α1; (d) schematic of the orbital structure change due to increase in tungsten contents. Nearby vanadium atoms can form covalent bond due to the $d_{\parallel}$ orbital occupation [107].

Moreover, the optical and thermochromic properties of VO_2 are also affected by doping. For example, VO_2 based films show excellent switching when doped with Si using a magnetron sputtering technique [90]. Zhang et al. [108] also improved the thermochromic and optical characteristics of VO_2 through doping with Sn additives. The temperature dependent properties such as grain size, hysteresis width (the difference in T_c of heating and cooling phase transition) and transmittance are also affected by the addition of dopants. For example, Li et al. [109], besides

a visible transmittance improvement, were able to reduce the hysteresis width of VO_2 from 17.8 to 10.7°C. Gao, Yanfeng, et al. [30] were able to control the morphology, size and polymorphology of vanadium dioxide nanoparticles by antimony doping. Liu at al. [110] also demonstrated that the morphology, size and phase of $NaGdF_4$ nanocrystals can be tuned by lanthanide doping. However, doping VO_2 films are still far from being studied comprehensively.

1.2.6 Solution phase deposition of VO_2(M) based films

Synthetic methods to prepare VO_2 films consist of both gas and solution based processes. Gas based deposition processes include chemical vapor deposition (CVD) (such as electric-field assisted chemical vapor deposition (EACVD)) and physical vapor deposition (PVD) (such as radio-frequency inverted cylindrical magnetron (ICM) sputtering process and pulse laser deposition (PLD)) [111-113]. Usually these techniques are complicated and expensive, as the equipment is normally complex due to the difficulties in controlling the variable valences of vanadium ions, and expensive due to requiring high vacuum conditions and maintenance [114]. Solution-based processes for deposition of VO_2 based coatings on substrates are of interest to this dissertation because of their potential for scalability, low cost, flexibility and high yield [7]. Examples include sol–gel technique, polymer assisted deposition and hydrothermal method. Typically, a vanadium source is reduced from a V (V) to V (IV) oxidation state and the resultant solution is filtered or centrifuged, washed with water or alcohol, then dried in an oven and annealed under inert/reducing gas at different temperatures and times. Accordingly, the final VO_2(M) crystals, whether doped or not, core/shelled or composites, are then mixed with a transparent polymer or matrix. Further, the VO_2/polymers are either used directly as smart films or coated on transparent substrates (such as polyethylene terephthalate (PET) or glass) by dip or spin coating. Other ways to fabricate VO_2 based films using the solution method can be obtained by mixing

vanadium source and a reductant with a polymer in solution. Then, the polymer solution is dried and annealed after being coated on a substrate. In the following section, solution deposition approaches are reviewed in detail.

1.2.6.1 Sol–gel process

The sol-gel process is used to fabricate monoclinic VO_2 based films due to its simplicity for large area deposition, low cost and practicability for easily integrating metal doping [114]. Greenberg et al. [115] was first to demonstrate the sol–gel technique in 1983, depositing VO_2(M) based films with $VO(OC_3H_7)_3$, and since then it was found that VO_2 can be produced using an equivalent n-propoxide vanadium compound. The sol–gel process is solution based, and the basic concept is to form an oxide network (mainly metal oxide) via polymerization of chemical precursors dissolved in a liquid medium (sol) [6]. Later, the sol is transformed into an inorganic network consisting of a liquid phase (gel) through a polycondensation process. The growth of the oxide network is affected through the self-assembly among the precursor molecules, both by covalent bonding, hydrogen bonding and Van der Waals interconnections [116]. Commonly used chemical precursors that go through hydrolysis and polycondensation reactions to create a colloid are metal salts, metal chlorides and metal alkoxides. Examples of V alkoxides include tetravalent alkoxides such as vanadium tetrabutoxide ($C_{16}H_{36}O_4V$), vanadyl acetylacetonate ($VO(acac)_2$ or $V(acac)_4$) [3, 6, 117]. The fabrication of metal oxide is obtained by generating metal-hydroxo or metal-oxo polymers in solution by connecting the metal centers with hydroxo (M–OH–M) or with oxo (M–O–M) bridges, respectively [118]. Subsequently, these generated polymers are cast or deposited on substrates or used to make powders [119]. For example, by using spin coating the precursor of VO_2 can be coated on a substrate (glass) to form a VO_2-based film. After drying and forming a

porous material, a calcination process is usually carried out to improve the mechanical property and crystallization of VO_2. The sol–gel is a low-temperature process and widely used to synthesize niobium or tungsten-doped VO_2 with low transition temperature. This method can also be applied to synthesize doped VO_2 films on silicon, sapphire, aluminum, or glass substrates providing a high degree of homogeneity [120]. Factors that have an impact on the reaction of sol-gel process include temperature, additives, timing and composition of solution [119, 121]. Yin et al. [122] suppressed the molten V_2O_5 in distilled H_2O after heat treatment in air at 800–900°C. Then, VO_2 film was obtained, after the molten product was coated onto a substrate and heat treated at 500 °C in a low vacuum environment. However, the highly toxic vapor V_2O_5 was generated during this process which is a significant disadvantage. Partlow et al. [123] hydrolyzed $VO(OC_3H_7)_3$ in C_2H_5OH with little H_2O to formulate VO_2 sol. Thereafter, to prepare VO_2 film, the sol was coated on a substrate and calcined at 500 °C in a suitable reducing gas environment. However, the film was not contained of pure monoclinic VO_2, while the vanadium alkoxide was unstable and expensive. Similarly, Huang et at. [124] prepared VO_2 at low annealing temperatures by an inorganic sol–gel process, mixing H_2O with molten V_2O_5, and then coating onto a muscovite (011) substrate. However, the VO_2 films were thermally unstable at 300 °C due to oxidation of VO_2 to V_2O_5. Hence, preparing a stable VO_2 sol through a simple process and under good safety conditions remains a challenge. Recently, Li et al. [125] successfully prepared a stable VO_2 sol using inorganic $VOSO_4$–$NH_3{\cdot}H_2O$–H_2O_2 reactants. However, the optical properties were not analyzed. VO_2 film coating on sapphire substrates was obtained using vanadyl triisopropoxide ($VO(OC_3H_7)_3$) as a precursor [126, 127]. However, the annealing time was prolonged to seven hours causing the VO_2 particles to aggregate to a larger size.

1.2.6.2 Hydrothermal process

The hydrothermal technique using water is commonly used to synthesize monoclinic VO_2 nanoparticles due to its low cost, simple processing, and being an environmentally friendly low temperature process [31]. This technique is often used to synthesize VO_2 nano-structures with desired phases and morphologies due to its sensitivity to temperature, time, pressure, concentration, reducing agents and pH [117, 128]. Hydrothermal processing is based on the reduction of water-soluble vanadium (V) precursors under pressure and temperature in the presence of reductants [120]. Example of vanadium precursors (vanadium sources) include vanadium pentoxide (V_2O_5), ammonium metavanadate (NH_4VO_3) and vanadyl sulfate ($VOSO_4$). Meanwhile, the reductants can be an organic acid such as oxalic acid ($H_2C_2O_4$) or inorganic compounds such as hydrazine (N_2H_4). A usual process for the hydrothermal method consists of mixing the reactants by magnetic stirring to establish a homogenous solution or suspension. Then the resultant solution is added to an autoclave and heated hydrothermally for at least 12 hours at temperatures ranging from 120-260°C. The final product is then separated using centrifugation and dried in an oven after washing with water or an alcohol [120]. Normally, the hydrothermal process forms a product of metastable and non-thermochromic phases such as VO_2(A), VO_2(B), VO_2(P) or VO_2(D); or a mixture of VO_2 (M) and a metastable phase, rather than a pure VO_2(M) [129]. Therefore, the metastable phases are converted into a pure monoclinic VO_2 phase by a post heating treatment at different temperatures, pressures and times. For instance, VO_2(B) can be transformed into VO_2(M) by annealing at 500 °C or greater temperatures, while VO_2(M) is obtained by annealing VO_2(D) at 300 °C [130, 131]. Further, the structure of VO_2 was found to be changed from VO_2 (B) nanobelts to VO_2 (A) rod-like and VO_2 (R) snowflake- like particles when the process time was increased from 3 to 24 h together with increasing the temperature up to 270

°C [132]. Powel et al. [133] prepared VO_2(M) nanoparticles in a size range of 50 to 200 nm by a two-step synthesis route using Continuous Hydrothermal Flow Synthesis (CHFS) accompanied by a post heat treatment step. Additionally, Srirodpai et al. [134] hydrothermally synthesized monoclinic VO_2 and followed by calcination at 700 °C for 3 h to develop a VO_2/ethylene vinyl acetate (EVA) composite film. Similarly, Ma et al. [37] annealed the hydrothermal plate-like $(NH_4)_{0.6}V_2O_5$ product in vacuum and successfully synthesized flake-like VO_2 (M). Further, Banerjee et al. [135] prepared VO_2(R/M) nanowires using stepwise hydrothermal process. In this process, a mixture of VO_2(B) and VO_2(A) nanowires were synthesized hydrothermally and converted into VO_2(R) upon calcination, after subsequent reduction of $V_3O_7{\cdot}H_2O$. Moreover, Wang et al. [117] also synthesized VO_2(M) nanostructures with various morphologies by hydrothermal and post annealing. First, ammonium metavanadate (NH_4VO_3) was hydrothermally reduced by oxalic acid $C_2H_2O_4$ at 160–220°C, then the VO_2(D) product was further annealed at 250–600°C. However, the post heat treatment step is known to cause severe aggregation between the particles, hence deteriorating the thermochromic performance of VO_2. Additionally, these two steps may consume a lot of energy and time due to high temperature and being an additional unit operation. Therefore, much attempt has been placed by researchers on a one step hydrothermal reaction. Liang et al. [31] used one-step tartaric acid (TA)-assisted hydrothermal synthesis process to transform tungsten doped-VO_2 (A) nanobelts into VO_2(M) nanorods. However, the VO_2 composite films exhibited low luminous transmittance (T_{lum}) of less than 40% and the phase transition temperature of 37.3 °C remains too high. The RE (rare earth: Eu, Tb)/W-codoped VO_2 nanoparticles, with grain sizes of less than 100 nm were synthesized by Wang et al. [136] under one-step hydrothermal conditions. But the coated glass exhibited low solar efficiently with high phase transition temperature, ΔT_{sol} = 6.3% and T_c=40.8 °C, respectively. Additionally, Mutta et

al. [137], Alie et al. [138] and Chen et al. [28] prepared VO_2(M/R) and W-doped VO_2(M/R) in different shapes via a one-step hydrothermal process using different precursors and reaction conditions. Moreover, as shown in Figure 1.6, Chen et al. [139] synthesized relatively pure W-doped VO_2(M) nanorods with exclusive doping efficiency by using a one-step hydrothermal approach. Overall, it is evident that the high temperature and long reaction times are necessary for one-step hydrothermal reaction, which will result in increased energy consumption and induce the growth of larger undesirable particles. Hence, a general process for the one-step hydrothermal synthesis of VO nano-structures with high thermochromic potential is needed.

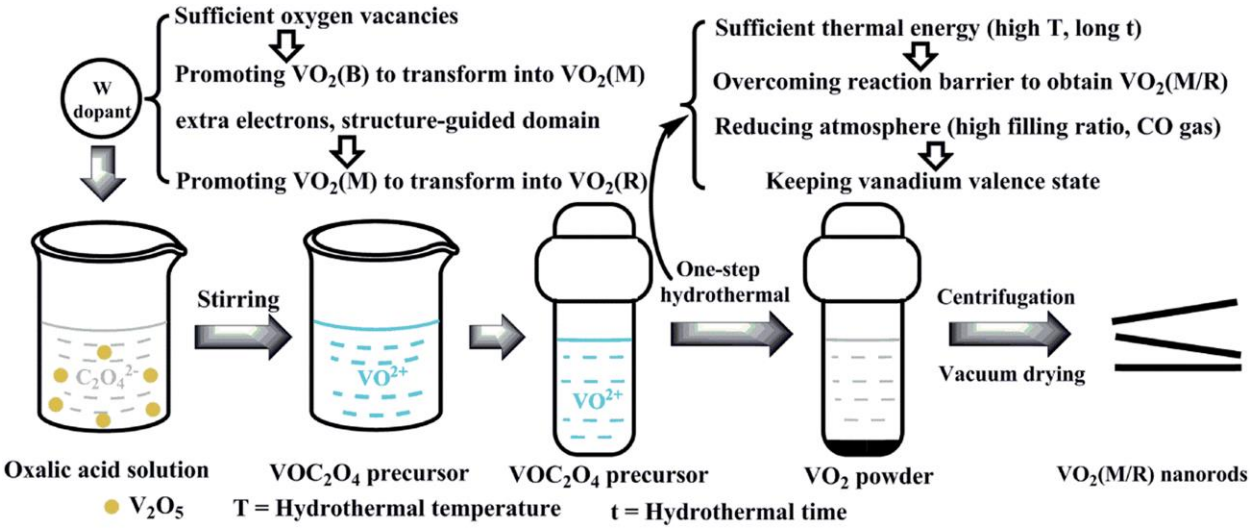

Figure 1.6 Illustration mechanism for hydrothermal synthesis of W-doped VO_2(M/R) nanorods [139].

1.2.6.3 Other solution-based processes

A polymer assisted deposition (PAD) as a solution process of VO_2 film have been prepared in which a soluble polymer and doped V were added into a previously treated aqueous transparent vanadium oxide solution. The precursor VO_2 film was then dried and annealed at 300–600 °C in nitrogen after being spun or dip coated to form crystalline film [80, 140]. Miao et al. [78] prepared

VO_2/SiO_2 composite films by mixing $VOC_2O_4.xH_2O$ with SiO_2 sol to form a blue and homogeneous solution. Then, the composite film was coated onto various substrates after adding a pore forming agent (Pluronic F-127). However, expensive and toxic reagents were used such as $VOCl_2$, in addition to using a high temperature, multistep process with films suffering from a wide hysteresis loop width. Breckenfeld et al. [141] synthesised a precursor of VO_2 PAD solution using propylene glycol instead of water solvent. This approach enabled the growth of VO_2 films with reproducible property and thickness, permitting a complicated shape printing through direct write techniques. Further, transport characteristic of the films were provided by establishing a multi-coating deposition and UV laser sintering method which gave a better film density and greater particle size, respectively. However, though the hysteresis width was improved, it remained too high to be commercially useful. Cezar et al. [142] used an electrochemical technique to prepare VO_2 films. This method contains several steps including deposition which were carried out by a cathodic potential from $OSO_4.xH_2O$ solution, storage and vacuum calcinations. However, the deposited xerogel needed to be stored for one and half months before calcination in vacuum, in addition to achieving only a very thin VO_2 layer. Gao et al. [143] prepared a flexible and stable VO_2/SiO_2/PU(polyurethane) based composite films using different solution based method. First, poly(vinylpyrrolidone) (PVP) was adsorbed into VO_2 by pre-treatment in the solution, then shelled with SiO_2 by modified Stober growth technique to form core(VO_2)/shell(SiO_2) particles. Accordingly, the composite was farther treated with an aqueous solution of silane coupler, for uniform dispersion in polyurethane (PU), before casting on a polyethylene terephthalate (PET) substrate. However, when solar modulation efficiency (ΔT_{sol}) is over 10%, the luminous

transmittance (T_{lum}) is less than 40% and vice versa. The trade-off between improving ΔT_{sol} and T_{lum} still exists today, hence limiting the commercialization of VO_2(M)-based smart windows.

1.2.7 Anti-oxidation properties

Oxidation of VO_2 over time limits the application of VO_2 in smart windows. Thermochromic properties of VO_2 become deteriorated because of its progressive oxidation into toxic V_2O_5 when misused at high temperature (above 300 °C) or revealed to air for a long time [144-146]. Therefore, enhancing the chemical stability of VO_2(M) by improving an oxidation resistance is crucially needed which can be achieved by surface modification of VO_2 nanoparticles. For example, silica (SiO_2), titania (TiO_2) and zirconia (ZrO_2) oxides have been deposited onto the surface of VO_2 nanoparticles to form core-shell or composites [147-149]. Among them, silica has various advantages including being chemically inert, optically transparent, polymer compatibility, in addition to improving the mechanical stability of various nanoparticles [149]. Zhao et al. [78] have demonstrated that the inclusion of inert silica dioxide (SiO_2) into the composite structure can dramatically preserve VO_2(M) from oxidation. As shown in Figure 1.7, all the XRD peaks are assigned to monoclinic VO_2 when VO_2/SiO_2 composite films were exposed to air for six months.. Li et al. [11] prepared VO_2/TiO_2 core/shell materials and confirmed that the TiO_2 shell provided an effective hindrance coating for the diffusion of oxygen into the VO_2 structure when calcined at (290-320°C) in air for fifteen minutes. Hence, the chemical stability was improved against oxidation. Similarly, Wang et al. [150] and Gao et al. [143] improved the optical and chemical stability of VO_2 by the formation of SiO_2/VO_2 core/shell structures. Additionally, the refractive index (RI) of VO_2 nanofiller can be changed by adjusting the core/shell structure, which can reduce the scattering generated by the refractive index mismatch across the polymer and VO_2 nanoparticles [151].

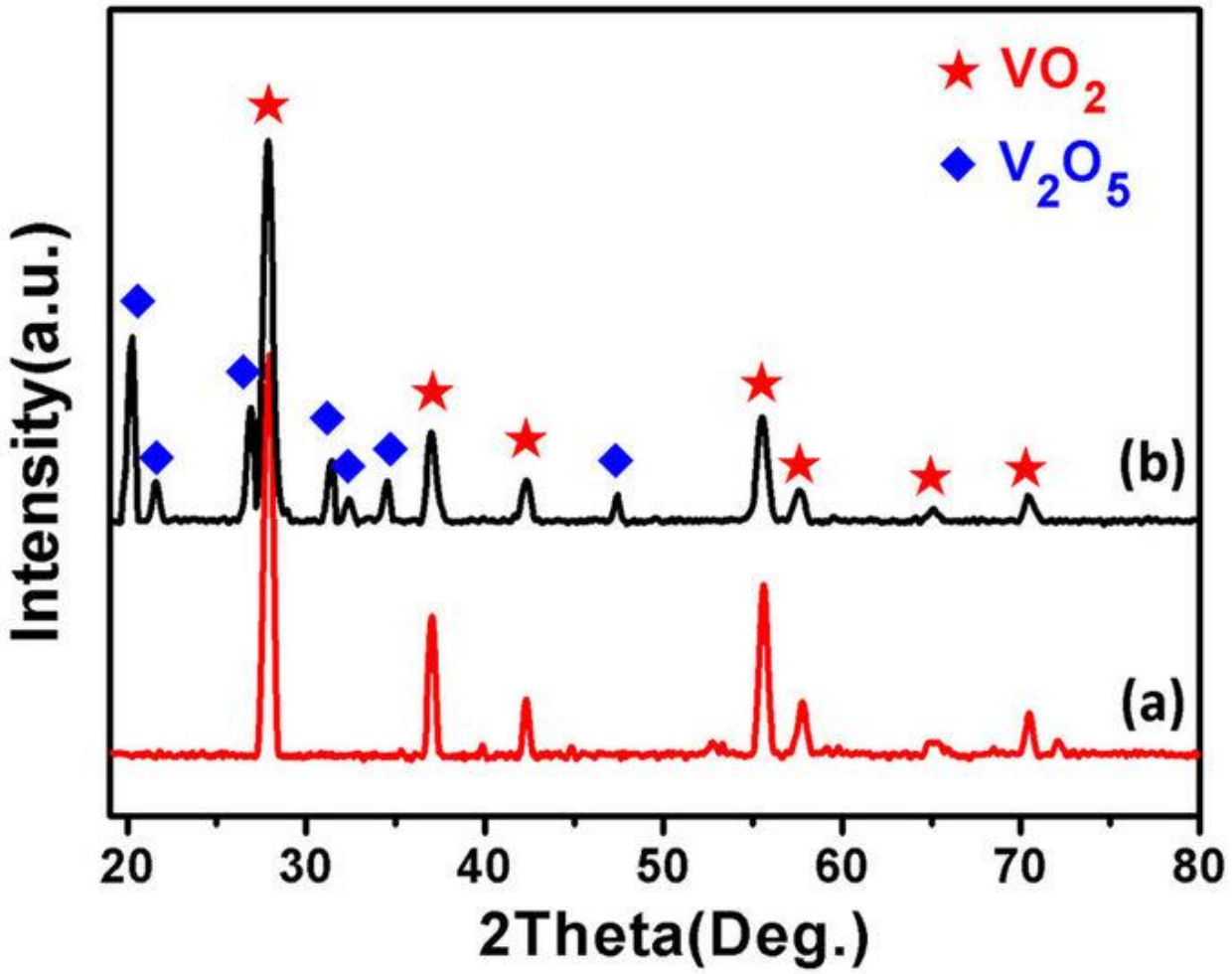

Figure 1.7 XRD of (a) VO_2 film and (b) VO_2/SiO_2 composite film [78].

1.2.8 Optical properties

A black body emits a maximum amount of energy and absorbs all incidental electromagnetic radiation (i.e., A (l) = 1) at each wavelength and in all directions [152]. The sun is a blackbody and its radiation reaches the earth with a bell-shaped spectrum due to partial absorption as shown in Figure 1.8a [153]. Since the solar energy is not overlapping with thermal radiation from materials at <100°C, many devices can be designed based on thermal or solar radiation. Solar energy is divided into 3 intervals: ultra-violet (UV) (wavelength (λ) <0.4 μm), luminous radiation (0.4 < λ

< 0.7 μm) and near infrared (NIR) (λ >0.7μm) which contribute to solar heat as shown in Figure 1.8b. An object can respond in three ways, it can reflect, transmit or absorb the electromagnetic energy [154]. These operations need to fulfill the energy conservation law at each wavelength, and the law of total radiation (W) is obtained by the following:

$$W = \alpha W + \tau W + \rho W \quad (1.1)$$

where:

$$\alpha + \tau + \rho = 1 \quad (1.2)$$

Here, α, τ and ρ are coefficients denoting the absorption, transmission and reflection, respectively [155]. Each coefficient may have a value between 0 and 1. For example, if τ = 0, ρ = 0 and α = 1, this means that 100% of the radiation is absorbed (a perfect blackbody). Part of the α energy will heat up the object and give rise to an emittance [155]. Kirchhoff's law states that:

$$\alpha(\lambda) = \varepsilon\,\mathrm{therm}(\lambda) \quad (1.3)$$

Where (ε) is emissivity of the body and (ε therm) is the thermal emittance.

In the case of opaque bodies (τ = 0), equation 1.2 can be simplified by:

$$\rho + \varepsilon = 1 \quad (1.4)$$

However, in the case of the black body ρ = 0:

$$\varepsilon = 1 \quad (1.5)$$

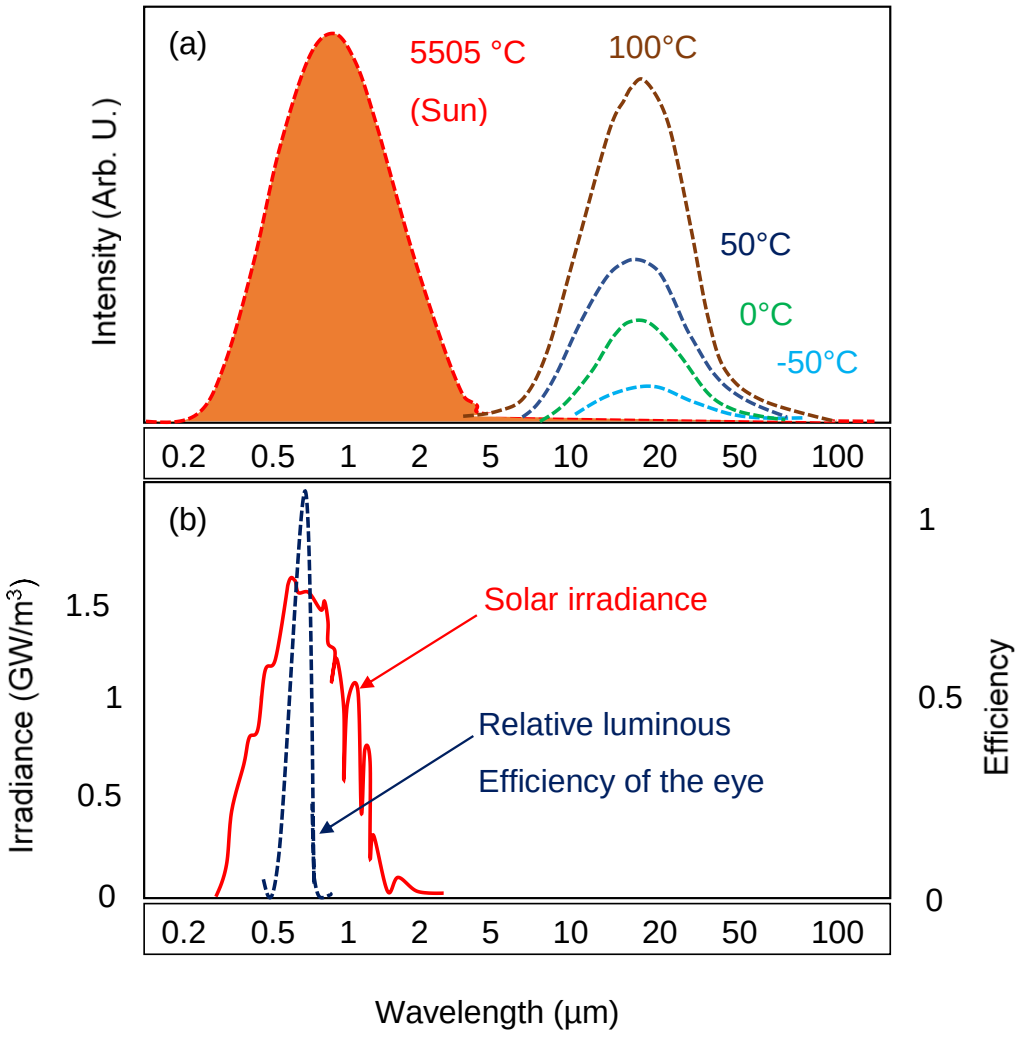

Figure 1.8 (a) Blackbody(Sun) radiation at various temperatures with surface temperature at 5505°C, (b) luminous efficiency of the human eye, and solar irradiance spectrum [156].

To evaluate the potential application of VO_2 based films, an integral luminous transmittance, T_{lum} (380–780 nm), infrared transmittance, T_{IR} (780–2500 nm) and solar transmittance T_{sol} (250–2500 nm) are calculated based on the measured spectra utilizing the following formula:

$$T_{lum/IR/sol} = \frac{\int \varphi_{lum/IR/sol}(\lambda)\, T(\lambda) d\lambda}{\int \varphi_{lum/IR/sol}(\lambda) d\lambda} \quad (1.6)$$

$T(\lambda)$ represents the transmittance at wavelength (λ), where φ_{lum} is the standard luminous efficiency function for the photopic vision of human eyes. φ_{ir} and φ_{sol} denote the IR/solar irradiance spectrum for the air mass 1.5 (correlative to the sun standing 37° over the horizon) [157]. The solar energy modulation (ΔT_{sol}) is defined as the difference of T_{sol} between semiconducting state (at low temperature) and metallic state (at high temperature), and is obtained by:

$$\Delta T_{lum/IR/sol} = T_{lum/IR/sol(s)} - T_{lum/IR/sol(m)} \quad (1.7)$$

However, VO_2(M) is not directly suitable for smart windows because the thermochromic reflectance modulation is weak in the solar radiation wavelength, while strong in the near-mid infrared [158, 159]. Accordingly, poor ΔT_{sol} (less than 10%) and low T_{lum} (less than 40%) remain two major challenges for the practical application of VO_2 based film for smart windows. These optical property challenges for VO_2 films are related to the microstructure, optical constants and film thickness. To address these challenges, suitable strategies include forming multilayers, doping, controlled nanostructures, composite films or depositing on various substrates [97, 160, 161]. For example, F or Mg-doping triggers a blue shift in the absorption edge of VO_2 based films which results in an increase of T_{lum} at the expense of ΔT_{sol} [104]. Additionally, optical calculations propose that VO_2(M) particles distributed in a dielectric matrix produce better ΔT_{sol} and T_{lum} values than pure VO_2(M) based films [159]. Previously reported

values of T_{lum} and ΔT_{sol} include (41.0%, 6.7%) for a single layer VO_2(M) film [162], (46.0%,7.0%) for a double layer VO_2/TiO_2 film [163], (35.9%, 8.4%) for VO_2/SiO_2 core/shell foils [11] and (44%, 12.1%) for a five layer $TiO_2/VO_2/TiO_2/VO_2/TiO_2$ film [164]. However, integrating dielectric layers with a definite thickness and refractive index into a complicated stack structures is technologically a challenge. The scattering effect of VO_2(M) particles diminish with a refractive index decrease or particle size reduction (below the wavelength of visible and infrared light). This means that the visible transmittance and IR transmittance change with SMT would logically increase [165-168]. The early reflectance of VO_2 particles can be reduced by adding SiO_2, which limits the aggregation and growth of these particles, thus enhancing the resulting optical properties [160]. Recently, Zhao et al. [78] fabricated VO_2/SiO_2 composite films and was able to improve the luminous transmittance by 18.9% (from 29.6% to 48.5%) as well as the solar modulation efficiency by 6.0% (from 9.7% to 15.7%) at a molar ratio of Si/V of 0.8.

Moreover, the optical properties can be optimized by controlling the thickness of the films through changing the rate of spin coating. As shown in Figure 1.9, when the thickness of the film is decreased, the IR switching is decreased as well, while the optical transmittance in both visible and NIR regions is increasing. Opposite results were obtained when the coating thickness was increased [29, 168].

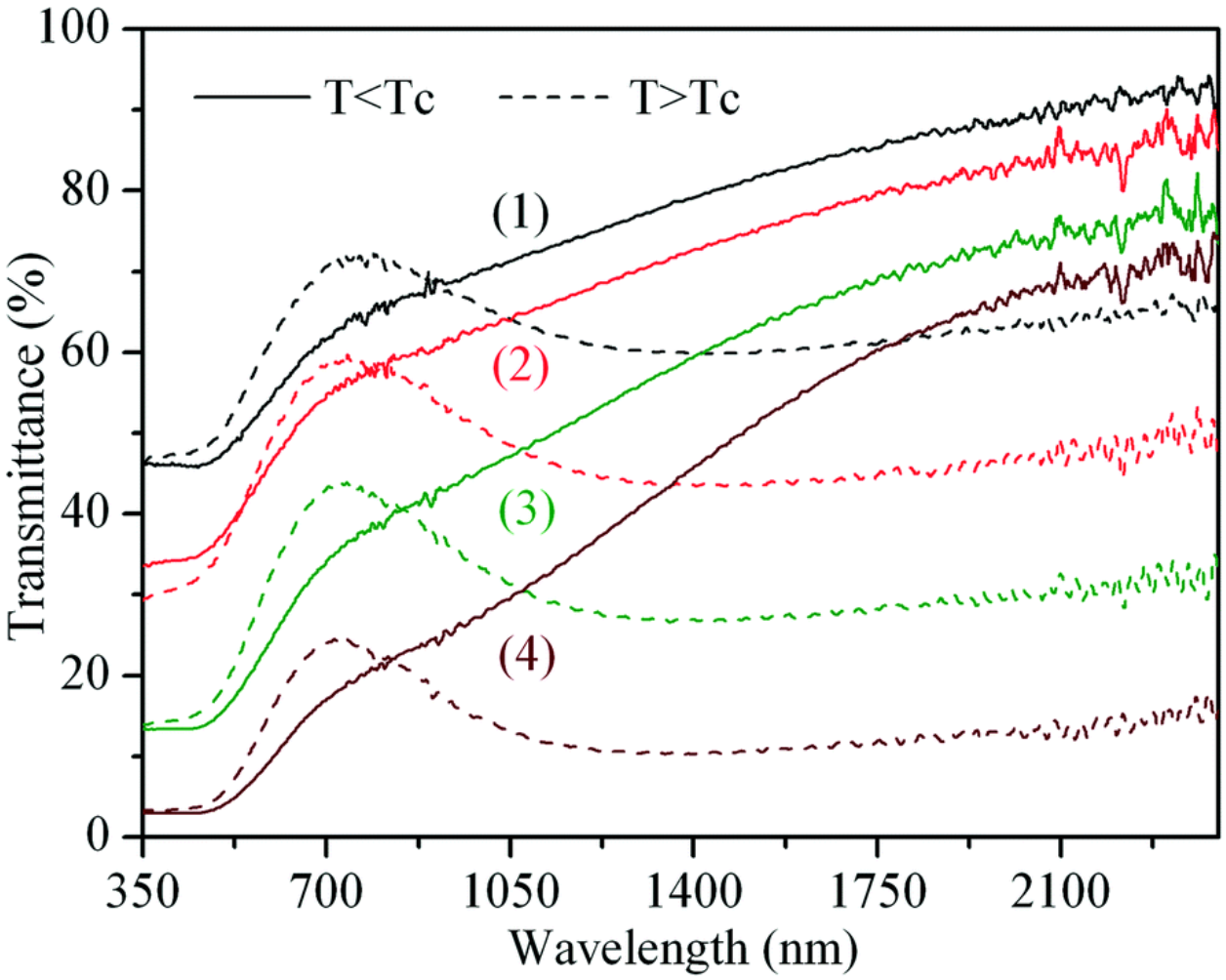

Figure 1.9 Optical transmittance of VO_2 based films coated on glass before (25 °C, $T < T_c$) and after (100 °C, $T > T_c$) phase transition with different thicknesses: (1) 250, (2) 325, (3) 480 and (4) 510 nm [29].

1.2.9 Mechanism of VO_2-PVP interaction

Agglomeration of VO_2 occurs during post heating due to the sintering effect (i.e., hydrothermal method) or during the gel formation stage (i.e., sol-gel method) [160, 169]. Therefore, it is important to modify the surface of VO_2 nanoparticles either with inert oxides such as TiO_2 and SiO_2 or with transparent polymers such as Pluronic F-127, poly vinyl alcohol (PVA), polyacrylamide (PAM) or Poly(vinylpyrrolidone) (PVP). To be more practical and

efficient, VO_2 nanoparticles should be imbedded into polymeric host matrices, and then coated onto glass or flexible substrate [6]. The nano-thermochromism of this composite system has been shown to improve the infrared (IR) modulation efficiency and luminous transmittance of films using theoretical calculation [159]. Mixing VO_2(M) nanoparticles with a transparent polymer in solution utilizes coordination between metal ions and polymers, enhancing the distribution of VO^{+2} ions in the polymer, providing films with excellent thermochromic properties. PVP is soluble in water and commonly synthesized from the thermally initiated free radical polymerization of N-vinylpyrrolidone [170]. There are many applications for PVP due to dispersion, solubility, hydrophilicity, biological and adhesion activity [171]. PVP is known to be an optimum matrix to prevent the deactivation and agglomeration of VO_2 [80], therefore is investigated for all film-based techniques in this thesis. Other advantages [80, 172] include:

- PVP facilitates the formation of M/R-phase. Coincidental degradation temperature of PVP with the crystallization temperature of VO_2 could induce VO_2(M) formation
- The interaction between aqua vanadium ions (V^{4+}) and PVP in solution can enhance the homogeneity of the precursor film by preventing the segregation of inorganic solute in the precursor solution, hence stabilizing it, leading to the formation of a relatively pure monoclinic phase of VO_2 nanoparticles.
- Good film-forming promoter and adhesive behavior on many solid substrates
- Exhibit good optical quality (high transmission in the visible range)
- Mechanical strength
- Amorphous structure of PVP also provide a low scattering loss
- Improve anti-oxidation of VO_2 film

PVP has two mesomeric forms (Figure 1.10a) and can be expected to form a strong interaction with VO_2 similar as shown by metal oxide interaction mechanisms, mainly by hydrogen bonding (Figure 1.10b) based on literatures [173, 174].

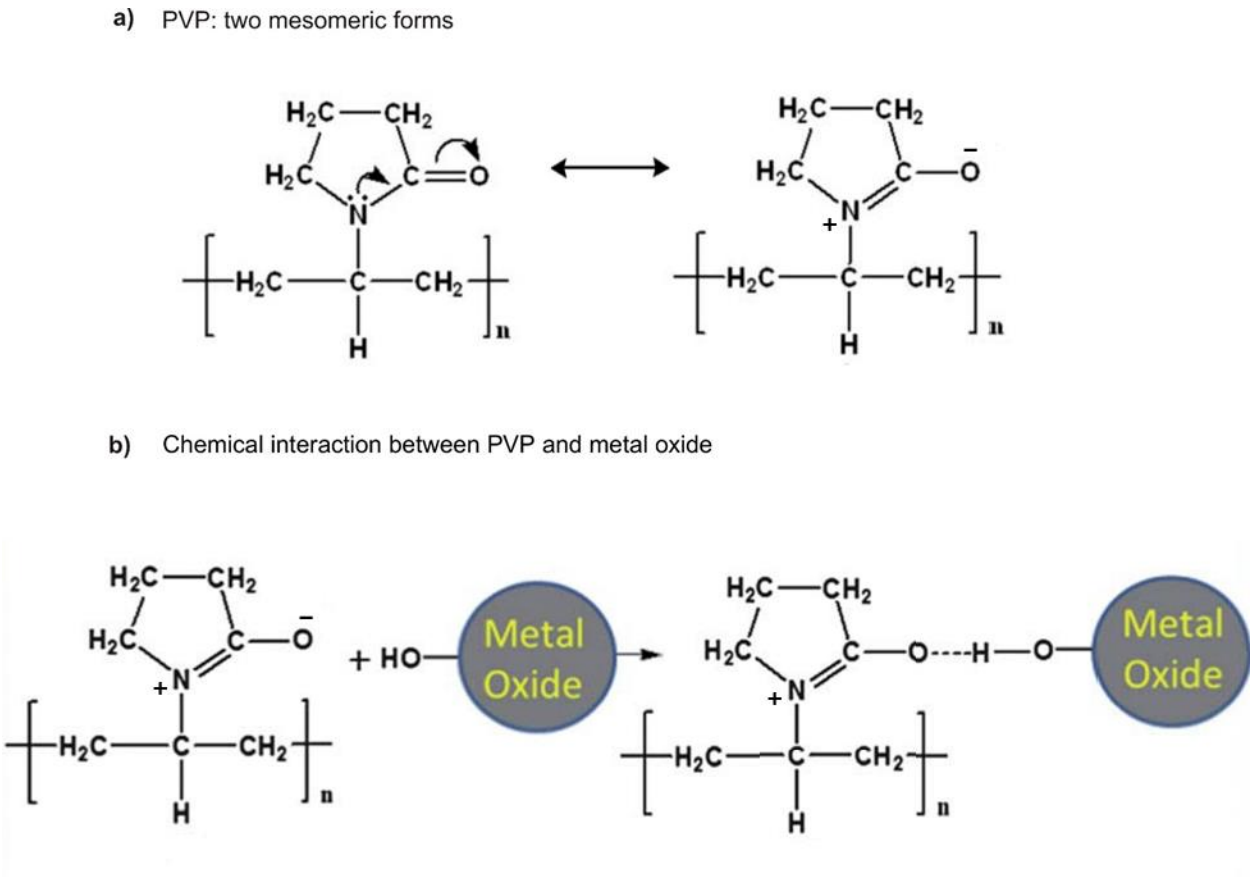

Figure 1.10 (a) two mesomeric forms [173] and (b) a schematic of the chemical interaction between metal oxide and PVP [174].

1.2.10 PMMA and P4VP polymers

Polymethylmethacrylate (PMMA) is an optically transparent polymer with refractive index of 1.49 [175]. Hydrophobic PMMA can outstand weather resistance and scratch resistance and it is generally used as a replacement for window glass due to its high impact strength, shatter-resistant properties, favorable processing and lightweight, low gas permeability, and good dimensional stability [176-178].

Films with high water-repellent surfaces are of interest for application in smart windows and PMMA has been shown to provide other useful properties [179, 180]. Accordingly, PMMA was selected for the study of VO_2/PMMA composite coatings in this thesis.

Poly(4-vinylpyridine) P4VP is produced by the thermally initiated free radical polymerization of 4-vinylpyridine [170]. Applications of P4VP coatings include corrosion inhibition and humidity sensors [181, 182]. P4VP is used as an environmentally, novel responsive molecule because it is soluble in water and protonated at pH < 4.7, while being insoluble, deprotonated and hydrophobic in water at pH values > 4.7 [183, 184]. Further, P4VP can coordinate with particles and stabilize them due to a good affinity for metals or metal oxide particles [185], hence being of interest for this thesis.

1.2.11 Effective medium theory and dielectric matrix

Calculations based on effective medium theory have shown that thermochromic VO_2 nanoparticles dispersed in a dielectric host have advantages over a thin solid film. This composite can be viewed as an "effective medium" with properties being an intermediate between matrix and nanoparticles, giving superior solar energy transmittance modulation and luminous transmittance [158, 159, 186, 187]. The optical properties of the "effective medium" are dominated by an effective dielectric function ε^{MG} according to:

$$\varepsilon^{MG} = \varepsilon_m \frac{1 + \frac{2}{3} f\alpha}{1 - \frac{1}{3} f\alpha} \tag{1.2}$$

Here, (f) is the filling factor, for example, the volume fraction inhabited by particles and (ε^m) is the dielectric permeability of the matrix (f=0.01 is used in the calculations below). Equation (1.8) involves the Maxwell-Garnett theory, which is suitable for a topology with nanoparticles imbedded in a continuous matrix [188, 189]. There are other effective medium formulas that are significant

to different nano-topologies. However, they correspond in the dilute limit, therefore, equation (1.8) can be applied without any deficit of universality.

(α) of equation (1.8) is obtained by:

$$\alpha = \frac{\varepsilon_p - \varepsilon_m}{\varepsilon_m - L\,(\varepsilon_p - \varepsilon_m)} \tag{1.9}$$

Where (L) is an appropriate depolarization factor and (ε_p) is the dielectric function of the particles. Spheres are characterized by L=1/3.

1.3 OBJECTIVES

One of the major challenges which has limited the application of a VO_2 (M/R) system for smart windows is to simultaneously and significantly improve both the solar modulation efficiency (ΔT_{sol}) and luminous transmittance (T_{lum}) through an economical process [78, 136]. When ΔT_{sol} is high, the T_{lum} is low or vice versa [190]. Though extensive efforts are presented, the problem is still unsolved, which is critical for the application of VO_2. VO_2-based films should meet the following criteria in order to be utilized in large scale on buildings : $T_{lum} \geq 40\%$ and $\Delta T_{sol} \geq 10\%$ [78, 158]. ΔT_{sol} is the key factor to evaluate the effectiveness of energy efficiency windows, which is the difference in solar transmittance between the transparent state at low temperature and opaque state at high temperature [191]. Luminous transmittance (T_{lum}) is also another important evaluation for visual contact between people who reside inside a building and an outside environment [192]. The performance can be further enhanced by improving the chemical stability of VO_2, and reducing the hysteresis width (i.e. the difference in phase transition (T_c) between the heating and cooling processes) for fast switching response to environmental temperature [193, 194].

Additionally, VO_2 is not immediately applicable to application in smart windows because it has a high T_c of 68 °C [195, 196]. This temperature is too high to sustain a comfortable temperature for people inside buildings. The ideal transition temperature(T_c) for comfort temperature zone should be near room temperature ~25 °C [78].

Moreover, high energy is consumed in the fabrication process for making the VO_2 films which would make their cost high. Usual doping process for VO_2 is done by a hydrothermal method which consumes significant energy for heating the water. For example, doped VO_2 was synthesized by Srirodpai et al. [134], Wang et al. [136], Liang et al. [31], Zhang et al. [197], Chen et al. [77] and Zhang et al. [198] at 180-280 °C for 24-72 h, besides to an additional annealing was required for post heat treatment. The expensive fabrication method limits the application of VO_2 smart windows and finding a method for doping with less usage of energy is a big challenge.

Further, non-green solvents are extensively identified to be of great environmental concern and replacing them with 'green' solvents in the synthesis of VO_2 without effecting the reaction outcome is an advantageous to minimize the environmental impacts [199].

To tackle the above problems, in this thesis, solution-based methods which include hydrothermal, reflux and room temperature methods, all using water as a green chemistry solvent, to improve the thermochromic and optical properties of VO_2 smart films. Low temperature reflux doping for the synthesis of large batch W-doped VO_2 delivering PVP-coatings with high luminous transparency (T_{lum}) and excellent solar modulation efficiency (ΔT_{sol}) sufficient for smart windows (Ch. 2). The hydrothermal synthesis of W- and Mo-doped VO_2 (M) particles were examined to reduce the T_c and fabricate VO_2/PVP coatings with excellent infrared transmission modulation (Ch. 3). The synthesis of chemically stable VO_2/SiO_2 composites with high IR modulation coating

were examined in Ch. 4. The room temperature synthesis of VO_2(M) and W-doped VO_2(M) were found to reduce energy consumption in the process for high IR switching efficiency coatings with excellent NPs dispersion using P4VP and hydrophobic PMMA polymers (Ch. 5).

REFERENSES

1. Dou, S., et al., *Facile preparation of double-sided VO 2 (M) films with micro-structure and enhanced thermochromic performances.* Solar Energy Materials and Solar Cells, 2017. **160**: p. 164-173.
2. Granqvist, C.-G., et al., *Progress in chromogenics: new results for electrochromic and thermochromic materials and devices.* Solar Energy Materials and Solar Cells, 2009. **93**(12): p. 2032-2039.
3. Gao, Y., et al., *Nanoceramic VO 2 thermochromic smart glass: a review on progress in solution processing.* Nano Energy, 2012. **1**(2): p. 221-246.
4. Bastien, D. and A.K. Athienitis, *Methodology for selecting fenestration systems in heating dominated climates.* Applied Energy, 2015. **154**: p. 1004-1019.
5. CMHC, *Energy audits of high-rise residential buildings.* Tech. rep. Canadian Mortgage and Housing Corporation, 1996.
6. Seyfouri, M.M. and R. Binions, *Sol-gel approaches to thermochromic vanadium dioxide coating for smart glazing application.* Solar Energy Materials and Solar Cells, 2017. **159**: p. 52-65.
7. Zhang, J., et al., *Hydrothermal growth of VO2 nanoplate thermochromic films on glass with high visible transmittance.* Scientific reports, 2016. **6**: p. 27898.
8. Chen, S., et al., *The visible transmittance and solar modulation ability of VO 2 flexible foils simultaneously improved by Ti doping: an optimization and first principle study.* Physical Chemistry Chemical Physics, 2013. **15**(40): p. 17537-17543.
9. Granqvist, C.G., *Transparent conductors as solar energy materials: A panoramic review.* Solar energy materials and solar cells, 2007. **91**(17): p. 1529-1598.
10. Sun, G., et al., *A novel multifunctional thermochromic structure with skin comfort design for smart window application.* Solar Energy Materials and Solar Cells, 2017. **159**: p. 553-559.
11. Li, Y., et al., *Core-shell VO2@ TiO2 nanorods that combine thermochromic and photocatalytic properties for application as energy-saving smart coatings.* Scientific reports, 2013. **3**.
12. Sun, G., et al., *Self-Assembled Multilayer Structure and Enhanced Thermochromic Performance of Spinodally Decomposed TiO2–VO2 Thin Film.* ACS applied materials & interfaces, 2016. **8**(11): p. 7054-7059.
13. Zheng, J., S. Bao, and P. Jin, *TiO 2 (R)/VO 2 (M)/TiO 2 (A) multilayer film as smart window: Combination of energy-saving, antifogging and self-cleaning functions.* Nano Energy, 2015. **11**: p. 136-145.
14. Kunyapat, T., Y. Xia, and Y. Zhu, *Recent progress in chromogenic research of tungsten oxides towards energy-related applications.* Progress in Materials Science, 2017.
15. Chen, Y., et al., *Free-standing SWNTs/VO 2/Mica hierarchical films for high-performance thermochromic devices.* Nano Energy, 2017. **31**: p. 144-151.
16. Pan, G., et al., *Synthesis and thermochromic property studies on W doped VO2 films fabricated by sol-gel method.* Scientific Reports, 2017. **7**.
17. Morin, F., *Oxides which show a metal-to-insulator transition at the Neel temperature.* Physical Review Letters, 1959. **3**(1): p. 34.

18. Yoon, H., et al., *Reversible phase modulation and hydrogen storage in multivalent VO2 epitaxial thin films.* Nature materials, 2016. **15**(10): p. 1113-1119.
19. Ke, Y., et al., *Controllable Fabrication of Two-Dimensional Patterned VO2 Nanoparticle, Nanodome, and Nanonet Arrays with Tunable Temperature-Dependent Localized Surface Plasmon Resonance.* ACS nano, 2017.
20. Yu, J.-H., et al., *Enhanced visible transmittance of thermochromic VO2 thin films by SiO2 passivation layer and their optical characterization.* Materials, 2016. **9**(7): p. 556.
21. Ureña-Begara, F., A. Crunteanu, and J.-P. Raskin, *Raman and XPS characterization of vanadium oxide thin films with temperature.* Applied Surface Science, 2017. **403**: p. 717-727.
22. Beke, S., *A review of the growth of V 2 O 5 films from 1885 to 2010.* Thin Solid Films, 2011. **519**(6): p. 1761-1771.
23. Greenwood, N. and A. Earnshaw, *Chemistry of the Elements 2nd Edition*. 1997: Butterworth-Heinemann.
24. Wu, C., F. Feng, and Y. Xie, *Design of vanadium oxide structures with controllable electrical properties for energy applications.* Chemical Society Reviews, 2013. **42**(12): p. 5157-5183.
25. Kosuge, K., T. Takada, and S. Kachi, *Phase Diagram and Magnetism of V2O3—V2O5 System.* Journal of the Physical Society of Japan, 1963. **18**(2): p. 318-319.
26. Heidemann, A., et al., *Hyperfine interaction in V3O7.* physica status solidi (a), 1977. **39**(1).
27. Schwingenschlögl, U. and V. Eyert, *The vanadium Magnéli phases VnO2n-1.* Annalen der physik, 2004. **13**(9): p. 475-510.
28. Chen, R., et al., *Shape-controlled synthesis and influence of W doping and oxygen nonstoichiometry on the phase transition of VO2.* Scientific reports, 2015. **5**: p. 14087.
29. Zhong, L., et al., *Star-shaped VO 2 (M) nanoparticle films with high thermochromic performance.* CrystEngComm, 2015. **17**(30): p. 5614-5619.
30. Gao, Y., et al., *Phase and shape controlled VO 2 nanostructures by antimony doping.* Energy & Environmental Science, 2012. **5**(9): p. 8708-8715.
31. Liang, S., et al., *One-Step Hydrothermal Synthesis of W-Doped VO2 (M) Nanorods with a Tunable Phase-Transition Temperature for Infrared Smart Windows.* ACS Omega, 2016. **1**(6): p. 1139-1148.
32. Rúa, A., et al., *Semiconductor-insulator transition in VO2 (B) thin films grown by pulsed laser deposition.* Journal of Applied Physics, 2015. **118**(12): p. 125308.
33. Hu, B., et al., *Self-heating and external strain coupling induced phase transition of VO2 nanobeam as single domain switch.* Advanced Materials, 2011. **23**(31): p. 3536-3541.
34. Blackburn, B., et al., *[{VOCl 2 (CH 2 (COOEt) 2)} 4] as a molecular precursor for thermochromic monoclinic VO 2 thin films and nanoparticles.* Journal of Materials Chemistry C, 2016. **4**(44): p. 10453-10463.
35. Chen, Y., et al., *Pressure–Temperature Phase Diagram of Vanadium Dioxide.* Nano Letters, 2017. **17**(4): p. 2512-2516.
36. Liang, Z., et al., *Tungsten-doped vanadium dioxide thin films as smart windows with self-cleaning and energy-saving functions.* Journal of Alloys and Compounds, 2017. **694**: p. 124-131.

37. Ma, Y., et al., *Synthesis of flake-like VO 2 (M) by annealing a novel (NH 4) 0.6 V 2 O 5 phase and its thermochromic characterization.* Ceramics International, 2016. **42**(14): p. 16382-16386.
38. Asayesh-Ardakani, H., et al., *Atomic origins of monoclinic-tetragonal (rutile) phase transition in doped VO2 nanowires.* Nano letters, 2015. **15**(11): p. 7179-7188.
39. Biermann, S., et al., *Dynamical Singlets and Correlation-Assisted Peierls Transition in V O 2.* Physical Review Letters, 2005. **94**(2): p. 026404.
40. Goodenough, J.B., *Anomalous properties of the vanadium oxides.* Annual Review of Materials Science, 1971. **1**(1): p. 101-138.
41. Everhart, C. and J. MacChesney, *Anisotropy in the electrical resistivity of vanadium dioxide single crystals.* Journal of Applied Physics, 1968. **39**(6): p. 2872-2874.
42. Liu, M., et al., *S. a. Wolf, FG Omenetto, X. Zhang, K. a. Nelson and RD Averitt.* Nature, 2012. **487**: p. 345-348.
43. Strelcov, E., Y. Lilach, and A. Kolmakov, *Gas Sensor based on metal− insulator transition in VO2 nanowire thermistor.* Nano letters, 2009. **9**(6): p. 2322-2326.
44. Hong, S.C., M. Lee, and D. Kim, *The Optical Behavior of VO2 Film Modulated by the Morphology and Preferred Growing Axis.* Bulletin of the Korean Chemical Society, 2017. **38**(1): p. 85-90.
45. Valmalette, J.-C. and J.-R. Gavarri, *High efficiency thermochromic VO 2 (R) resulting from the irreversible transformation of VO 2 (B).* Materials Science and Engineering: B, 1998. **54**(3): p. 168-173.
46. Zhang, H., et al., *A Facile Method to Control the Diameter of Monoclinic Vanadium Dioxide Rods.* Journal of Nanoscience and Nanotechnology, 2017. **17**(4): p. 2791-2795.
47. Dong, B., et al., *An intermediate phase (NH 4) 2 V 4 O 9 and its effects on the hydrothermal synthesis of VO 2 (M) nanoparticles.* CrystEngComm, 2016. **18**(4): p. 558-565.
48. Song, Z., et al., *Controllable synthesis of VO 2 (D) and their conversion to VO 2 (M) nanostructures with thermochromic phase transition properties.* Inorganic Chemistry Frontiers, 2016. **3**(8): p. 1035-1042.
49. Popuri, S.R., et al., *Rapid hydrothermal synthesis of VO2 (B) and its conversion to thermochromic VO2 (M1).* Inorganic chemistry, 2013. **52**(9): p. 4780-4785.
50. Zhang, Y., et al., *Hydrothermal treatment with VO2 (B) nanobelts for synthesis of VO2 (A) and W doped VO2 (M) nanobelts.* Materials Research Innovations, 2015. **19**(4): p. 295-302.
51. Srivastava, A., et al., *Selective growth of single phase VO2 (A, B, and M) polymorph thin films.* APL materials, 2015. **3**(2): p. 026101.
52. Cao, C., Y. Gao, and H. Luo, *Pure single-crystal rutile vanadium dioxide powders: synthesis, mechanism and phase-transformation property.* The Journal of Physical Chemistry C, 2008. **112**(48): p. 18810-18814.
53. Chou, J., et al., *Vanadium oxide nanowire phase and orientation analyzed by Raman spectroscopy.* Journal of Applied Physics, 2009. **105**(3): p. 034310.
54. Baik, J.M., et al., *Nanostructure-dependent metal− insulator transitions in vanadium-oxide nanowires.* The Journal of Physical Chemistry C, 2008. **112**(35): p. 13328-13331.
55. Son, J.-H., et al., *Hydrothermal synthesis of monoclinic VO2 micro-and nanocrystals in one step and their use in fabricating inverse opals.* Chemistry of Materials, 2010. **22**(10): p. 3043-3050.

56. Chen, K., et al., *Oxidative desulfurization of dibenzothiophene over monoclinic VO 2 phase-transition catalysts.* Applied Catalysis B: Environmental, 2017. **212**: p. 32-40.
57. Rajeswaran, B. and A. Umarji, *Phase evolution and infrared transmittance in monophasic VO 2 synthesized by a rapid non-equilibrium process.* Materials Chemistry and Physics, 2017. **190**: p. 219-229.
58. Zou, J., et al., *A simple method to prepare V 1-x W x O 2 (x= 0, 0.01, 0.02, 0.03, 0.04, and 0.05) controllable phase transition temperature powder.* Journal of Alloys and Compounds, 2017. **708**: p. 706-712.
59. Ji, H., et al., *Snowflake-Like Monoclinic VO2 Powders: Hydrothermal Synthesis, Characterization and In Situ Monitoring Phase-Transition Behavior.* Science of Advanced Materials, 2017. **9**(6): p. 861-867.
60. Wentzcovitch, R.M., W.W. Schulz, and P.B. Allen, *VO 2: Peierls or Mott-Hubbard? A view from band theory.* Physical review letters, 1994. **72**(21): p. 3389.
61. Rice, T., H. Launois, and J. Pouget, *Comment on" V O 2: Peierls or Mott-Hubbard? A View from Band Theory".* Physical review letters, 1994. **73**(22): p. 3042.
62. Qazilbash, M.M., et al., *Mott transition in VO2 revealed by infrared spectroscopy and nano-imaging.* Science, 2007. **318**(5857): p. 1750-1753.
63. Kim, M.-W., et al., *Substrate-mediated strain effect on the role of thermal heating and electric field on metal-insulator transition in vanadium dioxide nanobeams.* Scientific reports, 2015. **5**.
64. Pouget, J., et al., *Electron Localization Induced by Uniaxial Stress in Pure V O 2.* Physical Review Letters, 1975. **35**(13): p. 873.
65. Pouget, J., et al., *Dimerization of a linear Heisenberg chain in the insulating phases of V 1− x Cr x O 2.* Physical Review B, 1974. **10**(5): p. 1801.
66. Warwick, M.E. and R. Binions, *Advances in thermochromic vanadium dioxide films.* Journal of Materials Chemistry A, 2014. **2**(10): p. 3275-3292.
67. Brahlek, M., et al., *Opportunities in vanadium-based strongly correlated electron systems.* MRS Communications, 2017. **7**(1): p. 27-52.
68. Goodenough, J.B., *The two components of the crystallographic transition in VO2.* Journal of Solid State Chemistry, 1971. **3**(4): p. 490-500.
69. Shin, S., et al., *Vacuum-ultraviolet reflectance and photoemission study of the metal-insulator phase transitions in VO 2, V 6 O 13, and V 2 O 3.* Physical Review B, 1990. **41**(8): p. 4993.
70. Yao, T., et al., *Understanding the nature of the kinetic process in a VO 2 metal-insulator transition.* Physical review letters, 2010. **105**(22): p. 226405.
71. Zhu, Z. and U. Schwingenschlögl, *Comprehensive picture of VO 2 from band theory.* Physical Review B, 2012. **86**(7): p. 075149.
72. Bai, L., et al., *Pressure-induced phase transitions and metallization in VO 2.* Physical Review B, 2015. **91**(10): p. 104110.
73. Booth, J.M. and P.S. Casey, *Anisotropic structure deformation in the VO 2 metal-insulator transition.* Physical review letters, 2009. **103**(8): p. 086402.
74. Tselev, A., et al., *Symmetry relationship and strain-induced transitions between insulating M1 and M2 and metallic R phases of vanadium dioxide.* Nano letters, 2010. **10**(11): p. 4409-4416.
75. Kittiwatanakul, S., S.A. Wolf, and J. Lu, *Large epitaxial bi-axial strain induces a Mott-like phase transition in VO2.* Applied Physics Letters, 2014. **105**(7): p. 073112.

76. Hyun-Tak, K., et al. *Micro X-Ray Diffraction Study of VO2 Films--Separation between Metal-Insulator Transition and Structural Phase Transition*. in *APS Meeting Abstracts*. 2008.
77. Chen, S., et al., *Calculation Evidence of Staged Mott and Peierls Transitions in VO2 Revealed by Mapping Reduced-Dimension Potential Energy Surface.* The journal of physical chemistry letters, 2015. **6**(18): p. 3650-3656.
78. Zhao, L., et al., *Solution-processed VO2-SiO2 composite films with simultaneously enhanced luminous transmittance, solar modulation ability and anti-oxidation property.* Scientific reports, 2014. **4**.
79. Kumar, S., F. Maury, and N. Bahlawane, *Electrical Switching in Semiconductor-Metal Self-Assembled VO2 Disordered Metamaterial Coatings.* Scientific reports, 2016. **6**: p. 37699.
80. Kang, L., Y. Gao, and H. Luo, *A novel solution process for the synthesis of VO2 thin films with excellent thermochromic properties.* ACS applied materials & interfaces, 2009. **1**(10): p. 2211-2218.
81. Chen, L., et al., *Energetics, electronic and optical properties of X (X= Si, Ge, Sn, Pb) doped VO 2 (M) from first-principles calculations.* Journal of Alloys and Compounds, 2017. **693**: p. 211-220.
82. Chen, L., et al., *Tuning the work function of VO 2 (100) surface by Ag adsorption and incorporation: Insights from first-principles calculations.* Applied Surface Science, 2016. **367**: p. 507-517.
83. Jeong, J., et al., *Suppression of metal-insulator transition in VO2 by electric field–induced oxygen vacancy formation.* Science, 2013. **339**(6126): p. 1402-1405.
84. Sun, C., et al., *The modulation of metal–insulator transition temperature of vanadium dioxide: a density functional theory study.* Journal of Materials Chemistry C, 2014. **2**(43): p. 9283-9293.
85. Saeli, M., et al., *Energy modelling studies of thermochromic glazing.* Energy and Buildings, 2010. **42**(10): p. 1666-1673.
86. Beteille, F., et al., *Switching properties of V1− xTixO2 thin films deposited from alkoxides.* Materials research bulletin, 1997. **32**(8): p. 1109-1117.
87. Barron, S.C., J.M. Gorham, and M.L. Green, *Thermochromic Phase Transitions in VO2-Based Thin Films for Energy-Saving Applications.* ECS Transactions, 2014. **61**(2): p. 387-393.
88. Barron, S.C., et al., *High-Throughput Measurements of Thermochromic Behavior in V1–x Nb x O2 Combinatorial Thin Film Libraries.* ACS combinatorial science, 2014. **16**(10): p. 526-534.
89. Mai, L., et al., *Electrical Property of Mo-Doped VO2 Nanowire Array Film by Melting–Quenching Sol− Gel Method.* The Journal of Physical Chemistry B, 2006. **110**(39): p. 19083-19086.
90. Zhang, H., et al., *Metal–insulator transition properties of sputtered silicon-doped and un-doped vanadium dioxide films at terahertz range.* Applied Surface Science, 2015. **331**: p. 92-97.
91. Zhang, W., et al., *Hole Carriers Doping Effect on the Metal–Insulator Transition of N-Incorporated Vanadium Dioxide Thin Films.* The Journal of Physical Chemistry C, 2014. **118**(24): p. 12837-12844.

92. Gentle, A. and G. Smith, *Dual metal insulator and insulator insulator switching in nanoscale and Al doped VO2.* Journal of Physics D Applied Physics, 2008. **41**(1).
93. Chen, B., et al., *Al 3+-doped vanadium dioxide thin films deposited by PLD.* Solar Energy Materials and Solar Cells, 2009. **93**(9): p. 1550-1554.
94. Wan, M., et al., *Observation of reduced phase transition temperature in N-doped thermochromic film of monoclinic VO 2.* Applied Surface Science, 2017. **410**: p. 363-372.
95. Gagaoudakis, E., et al., *Study of low temperature rf-sputtered Mg-doped vanadium dioxide thermochromic films deposited on low-emissivity substrates.* Thin Solid Films, 2016. **601**: p. 99-105.
96. Chen, S., et al., *Unraveling mechanism on reducing thermal hysteresis width of VO2 by Ti doping: a joint experimental and theoretical study.* The Journal of Physical Chemistry C, 2014. **118**(33): p. 18938-18944.
97. Mlyuka, N., G.A. Niklasson, and C.-G. Granqvist, *Mg doping of thermochromic VO 2 films enhances the optical transmittance and decreases the metal-insulator transition temperature.* Applied physics letters, 2009. **95**(17): p. 171909.
98. Zhou, J., et al., *Mg-doped VO 2 nanoparticles: hydrothermal synthesis, enhanced visible transmittance and decreased metal–insulator transition temperature.* Physical Chemistry Chemical Physics, 2013. **15**(20): p. 7505-7511.
99. Wan, J., et al., *Density functional theory study of M-doped (M= B, C, N, Mg, Al) VO 2 nanoparticles for thermochromic energy-saving foils.* Journal of Alloys and Compounds, 2016. **662**: p. 621-627.
100. Abdellaoui, I., et al., *Electronic and optical properties of Mg-, F-doped and Mg \| F-codoped M 1-VO 2 via hybrid density functional calculations.* Journal of Alloys and Compounds, 2016. **658**: p. 569-575.
101. Huang, Z., et al., *Tungsten-doped vanadium dioxide thin films on borosilicate glass for smart window application.* Journal of Alloys and Compounds, 2013. **564**: p. 158-161.
102. Ningyi, Y., L. Jinhua, and L. Chenglu, *Valence reduction process from sol–gel V 2 O 5 to VO 2 thin films.* Applied surface science, 2002. **191**(1): p. 176-180.
103. Hanlon, T., J. Coath, and M. Richardson, *Molybdenum-doped vanadium dioxide coatings on glass produced by the aqueous sol–gel method.* Thin Solid Films, 2003. **436**(2): p. 269-272.
104. Burkhardt, W., et al., *Tungsten and fluorine co-doping of VO 2 films.* Thin Solid Films, 2002. **402**(1): p. 226-231.
105. Yang, T.C.-K., et al., *The novel preparation method of high-performance thermochromic vanadium dioxide thin films by thermal oxidation of vanadium-stainless steel co-sputtered films.* Vacuum, 2015. **121**: p. 310-316.
106. Wu, Y., et al., *Depressed transition temperature of W x V 1− x O 2: mechanistic insights from the X-ray absorption fine structure (XAFS) spectroscopy.* Physical Chemistry Chemical Physics, 2014. **16**(33): p. 17705-17714.
107. He, X., et al., *Orbital change manipulation metal–insulator transition temperature in W-doped VO 2.* Physical Chemistry Chemical Physics, 2015. **17**(17): p. 11638-11646.
108. Zhang, Y., et al., *The additives W, Mo, Sn and Fe for promoting the formation of VO 2 (M) and its optical switching properties.* Materials Letters, 2013. **92**: p. 61-64.
109. Li, W., et al., *Preparation and characterization of VO 2 (M)–SnO 2 thermochromic films for application as energy-saving smart coatings.* Journal of Colloid and Interface Science, 2015. **456**: p. 166-173.

110. Liu, C., et al., *Morphology-and phase-controlled synthesis of monodisperse lanthanide-doped NaGdF 4 nanocrystals with multicolor photoluminescence.* Journal of Materials Chemistry, 2009. **19**(4): p. 489-496.
111. Leroy, J., et al., *Structural, electrical and optical properties of thermochromic VO 2 thin films obtained by reactive electron beam evaporation.* Thin Solid Films, 2012. **520**(14): p. 4823-4825.
112. Evans, P., et al., *Multi-functional self-cleaning thermochromic films by atmospheric pressure chemical vapour deposition.* Journal of Photochemistry and Photobiology A: Chemistry, 2007. **189**(2): p. 387-397.
113. Fan, L., et al., *Oxygen pressure dependent VO 2 crystal film preparation and the interfacial epitaxial growth study.* Thin Solid Films, 2012. **520**(19): p. 6124-6129.
114. Wan, M., et al., *Optical properties and formation mechanism of M1-phase VO 2 thin films annealed in a closed NH 3 atmosphere.* Journal of Alloys and Compounds, 2017. **706**: p. 289-296.
115. Greenberg, C.B., *Undoped and doped VO2 films grown from VO (OC3H7) 3.* Thin solid films, 1983. **110**(1): p. 73-82.
116. Livage, J., M. Henry, and C. Sanchez, *Sol-gel chemistry of transition metal oxides.* Progress in solid state chemistry, 1988. **18**(4): p. 259-341.
117. Wang, S., et al., *Recent progress in VO 2 smart coatings: Strategies to improve the thermochromic properties.* Progress in Materials Science, 2016. **81**: p. 1-54.
118. Nag, J. and R. Haglund Jr, *Synthesis of vanadium dioxide thin films and nanoparticles.* Journal of Physics: Condensed Matter, 2008. **20**(26): p. 264016.
119. Ullattil, S.G. and P. Periyat, *Sol-Gel Synthesis of Titanium Dioxide*, in *Sol-Gel Materials for Energy, Environment and Electronic Applications*. 2017, Springer. p. 271-283.
120. Osmolovskaya, O., et al., *Synthesis of vanadium dioxide thin films and nanopowders: a brief review.* Rev. Adv. Mater. Sci, 2014. **36**: p. 70-74.
121. Chen, D., *Anti-reflection (AR) coatings made by sol–gel processes: a review.* Solar Energy Materials and Solar Cells, 2001. **68**(3): p. 313-336.
122. Yin, D., et al., *High quality vanadium dioxide films prepared by an inorganic sol-gel method.* Materials research bulletin, 1996. **31**(3): p. 335-340.
123. Partlow, D., et al., *Switchable vanadium oxide films by a sol-gel process.* Journal of Applied Physics, 1991. **70**(1): p. 443-452.
124. Li, D., et al., *Thermal stability of VO2 thin films deposited by sol–gel method.* Journal of Sol-Gel Science and Technology, 2015. **75**(1): p. 189-197.
125. Li, Y., et al., *A novel inorganic precipitation–peptization method for VO 2 sol and VO 2 nanoparticles preparation: Synthesis, characterization and mechanism.* Journal of colloid and interface science, 2016. **462**: p. 42-47.
126. Guo, Y., et al., *Facile preparation of vanadium oxide thin films on sapphire (0001) by sol–gel method.* Journal of sol-gel science and technology, 2014. **70**(1): p. 40-46.
127. Guo, Y., et al., *Evolution of structure and electrical properties with annealing time in solution-based VO 2 thin films.* Journal of Alloys and Compounds, 2015. **622**: p. 913-917.
128. Ban, C. and M.S. Whittingham, *Nanoscale single-crystal vanadium oxides with layered structure by electrospinning and hydrothermal methods.* Solid State Ionics, 2008. **179**(27): p. 1721-1724.

129. Soltane, L. and F. Sediri, *Rod-like nanocrystalline B-VO 2: Hydrothermal synthesis, characterization and electrochemical properties.* Materials Research Bulletin, 2014. **53**: p. 79-83.
130. Li, M., et al., *Defect-mediated phase transition temperature of VO 2 (M) nanoparticles with excellent thermochromic performance and low threshold voltage.* Journal of Materials Chemistry A, 2014. **2**(13): p. 4520-4523.
131. Zhang, Y., *VO2 (B) conversion to VO2 (A) and VO2 (M) and their oxidation resistance and optical switching properties.* Materials Science-Poland, 2016. **34**(1): p. 169-176.
132. Ji, S., F. Zhang, and P. Jin, *Selective formation of VO 2 (A) or VO 2 (R) polymorph by controlling the hydrothermal pressure.* Journal of Solid State Chemistry, 2011. **184**(8): p. 2285-2292.
133. Powell, M., et al., *Direct and continuous synthesis of VO 2 nanoparticles.* Nanoscale, 2015. **7**(44): p. 18686-18693.
134. Srirodpai, O., et al., *Preparation, Characterization and Thermo-Chromic Properties of EVA/VO2 Laminate Films for Smart Window Applications and Energy Efficiency in Building.* Materials, 2017. **10**(1): p. 53.
135. Horrocks, G.A., et al., *Scalable hydrothermal synthesis of free-standing VO2 nanowires in the M1 phase.* ACS applied materials & interfaces, 2014. **6**(18): p. 15726-15732.
136. Wang, N., et al., *One-step hydrothermal synthesis of rare earth/W-codoped VO 2 nanoparticles: Reduced phase transition temperature and improved thermochromic properties.* Journal of Alloys and Compounds, 2017. **711**: p. 222-228.
137. Mutta, G.R., et al., *Facile hydrothermal synthesis of economically viable VO 2 (M1) counter electrode for dye sensitized solar cells.* Materials Research Bulletin, 2016. **83**: p. 135-140.
138. Alie, D., et al., *Direct synthesis of thermochromic VO 2 through hydrothermal reaction.* Journal of Solid State Chemistry, 2014. **212**: p. 237-241.
139. Chen, R., et al., *One-step hydrothermal synthesis of V 1− x W x O 2 (M/R) nanorods with superior doping efficiency and thermochromic properties.* Journal of Materials Chemistry A, 2015. **3**(7): p. 3726-3738.
140. Kang, L., et al., *Effects of annealing parameters on optical properties of thermochromic VO2 films prepared in aqueous solution.* The Journal of Physical Chemistry C, 2010. **114**(4): p. 1901-1911.
141. Breckenfeld, E., et al., *Laser-processing of VO 2 thin films synthesized by polymer-assisted-deposition.* Applied Surface Science, 2017. **397**: p. 152-158.
142. Cezar, A., et al., *Highly oriented VO2 thin films prepared by electrodeposition.* Electrochemical and Solid-State Letters, 2011. **14**(3): p. D23-D25.
143. Gao, Y., et al., *Enhanced chemical stability of VO 2 nanoparticles by the formation of SiO 2/VO 2 core/shell structures and the application to transparent and flexible VO 2-based composite foils with excellent thermochromic properties for solar heat control.* Energy & Environmental Science, 2012. **5**(3): p. 6104-6110.
144. Liu, C., N. Wang, and Y. Long, *Multifunctional overcoats on vanadium dioxide thermochromic thin films with enhanced luminous transmission and solar modulation, hydrophobicity and anti-oxidation.* Applied Surface Science, 2013. **283**: p. 222-226.
145. Lindström, R., et al., *Thin films of vanadium oxide grown on vanadium metal: oxidation conditions to produce V2O5 films for Li-intercalation applications and characterisation by XPS, AFM, RBS/NRA.* Surface and interface analysis, 2006. **38**(1): p. 6-18.

146. Shen, N., et al., *Lowered phase transition temperature and excellent solar heat shielding properties of well-crystallized VO 2 by W doping.* Physical Chemistry Chemical Physics, 2016. **18**(40): p. 28010-28017.
147. Zhao, F., Y. Gao, and H. Luo, *Reactive formation of zircon inclusion pigments by deposition and subsequent annealing of a zirconia and silica double shell.* Langmuir, 2009. **25**(23): p. 13295-13297.
148. Park, O.K., Y.S. Kang, and B.G. Jo, *Synthesis of TiO 2 Nanoparticles Coated with SiO 2 for Suppression of Photocatalytic Activity and Increased Dispersion Stability.* Journal of Industrial and Engineering Chemistry, 2004. **10**(5): p. 733-738.
149. Velikov, K.P. and A. van Blaaderen, *Synthesis and characterization of monodisperse core− shell colloidal spheres of zinc sulfide and silica.* Langmuir, 2001. **17**(16): p. 4779-4786.
150. Wang, M., et al., *Novel synthesis of pure VO 2@ SiO 2 core@ shell nanoparticles to improve the optical and anti-oxidant properties of a VO 2 film.* RSC Advances, 2016. **6**(110): p. 108286-108289.
151. Li, Y.-Q., et al., *Facile synthesis of highly transparent polymer nanocomposites by introduction of core–shell structured nanoparticles.* Chemistry of Materials, 2008. **20**(8): p. 2637-2643.
152. Iqbal, M., *An introduction to solar radiation*. 2012: Elsevier.
153. Delahaigue, A., et al., *Atmospheric laser heterodyne detection.* Infrared physics & technology, 1996. **37**(1): p. 7-12.
154. Pérez, M.A., O. González, and J.R. Arias, *Optical fiber sensors for chemical and biological measurements*, in *Current Developments in Optical Fiber Technology*. 2013, InTech.
155. Bidinotto, J.H. and E.M. Belo, *Modal Shape Analysis Using Thermal Imaging.* Journal of Aerospace Technology and Management, 2015. **7**(2): p. 185-192.
156. Li, S., *VO2-based thermochromic and nanothermochromic materials for energy-efficient windows: Computational and experimental studies*. 2013, Acta Universitatis Upsaliensis.
157. Chen, Z., et al., *VO 2-based double-layered films for smart windows: optical design, all-solution preparation and improved properties.* Solar Energy Materials and Solar Cells, 2011. **95**(9): p. 2677-2684.
158. Li, S.-Y., G.A. Niklasson, and C.-G. Granqvist, *Thermochromic fenestration with VO 2-based materials: three challenges and how they can be met.* Thin Solid Films, 2012. **520**(10): p. 3823-3828.
159. Li, S.-Y., G.A. Niklasson, and C.-G. Granqvist, *Nanothermochromics: calculations for VO 2 nanoparticles in dielectric hosts show much improved luminous transmittance and solar energy transmittance modulation.* Journal of Applied Physics, 2010. **108**(6): p. 063525.
160. Chen, H.-K., et al., *The preparation and characterization of transparent nano-sized thermochromic VO 2–SiO 2 films from the sol–gel process.* Journal of non-crystalline solids, 2004. **347**(1): p. 138-143.
161. Jin, P., et al., *Design, formation and characterization of a novel multifunctional window with VO 2 and TiO 2 coatings.* Applied Physics A: Materials Science & Processing, 2003. **77**(3): p. 455-459.

162. Mlyuka, N., G.A. Niklasson, and C.-G. Granqvist, *Thermochromic multilayer films of VO2 and TiO2 with enhanced transmittance.* Solar Energy Materials and Solar Cells, 2009. **93**(9): p. 1685-1687.
163. Jin, P., et al., *A VO2-based multifunctional window with highly improved luminous transmittance.* Japanese journal of applied physics, 2002. **41**(3A): p. L278.
164. Mlyuka, N.R., G.A. Niklasson, and C.G. Granqvist, *Thermochromic VO2-based multilayer films with enhanced luminous transmittance and solar modulation.* physica status solidi (a), 2009. **206**(9): p. 2155-2160.
165. Lopez, R., L.C. Feldman, and R.F. Haglund Jr, *Size-Dependent Optical Properties of V O 2 Nanoparticle Arrays.* Physical review letters, 2004. **93**(17): p. 177403.
166. Sun, Y., et al., *New aspects of size-dependent metal-insulator transition in synthetic single-domain monoclinic vanadium dioxide nanocrystals.* Nanoscale, 2011. **3**(10): p. 4394-4401.
167. Du, J., et al., *Formation and metal-to-insulator transition properties of VO 2–ZrV 2 O 7 composite films by polymer-assisted deposition.* Solar Energy Materials and Solar Cells, 2011. **95**(7): p. 1604-1609.
168. Xu, G., et al., *Tailoring of luminous transmittance upon switching for thermochromic VO2 films by thickness control.* Japanese journal of applied physics, 2004. **43**(1R): p. 186.
169. Li, R., et al., *Synthesis and characterization of plate-like VO 2 (M)@ SiO 2 nanoparticles and their application to smart window.* Materials Letters, 2013. **110**: p. 241-244.
170. Janakiraman, S., et al., *Kinetic analysis of the initiated chemical vapor deposition of poly (vinylpyrrolidone) and poly (4-vinylpyridine).* Thin Solid Films, 2015. **595**: p. 244-250.
171. Haaf, F., A. Sanner, and F. Straub, *Polymers of N-vinylpyrrolidone: synthesis, characterization and uses.* Polymer Journal, 1985. **17**(1): p. 143.
172. Gao, Y., et al., *Nanoceramic VO2 thermochromic smart glass: A review on progress in solution processing.* Nano Energy, 2012. **1**(2): p. 221-246.
173. Anjusree, G., et al., *Fabricating fiber, rice and leaf-shaped TiO 2 by tuning the chemistry between TiO 2 and the polymer during electrospinning.* RSC Advances, 2013. **3**(37): p. 16720-16727.
174. Binitha, G., et al., *Electrospun α-Fe 2 O 3 nanostructures for supercapacitor applications.* Journal of Materials Chemistry A, 2013. **1**(38): p. 11698-11704.
175. Li, Y., et al., *Towards centimeter thick transparent wood through interface manipulation.* Journal of Materials Chemistry A, 2018. **6**(3): p. 1094-1101.
176. Ortiz, R., et al., *Poly (methyl methacrylate) surface modification for surfactant-free real-time toxicity assay on droplet microfluidic platform.* ACS applied materials & interfaces, 2017. **9**(15): p. 13801-13811.
177. Ali, U., K.J.B.A. Karim, and N.A. Buang, *A review of the properties and applications of poly (methyl methacrylate)(PMMA).* Polymer Reviews, 2015. **55**(4): p. 678-705.
178. Lu, Y., et al., *Functional transparent nanocomposite film with thermochromic and hydrophobic properties fabricated by electrospinning and hot-pressing approach.* Ceramics International, 2018. **44**(1): p. 1013-1018.
179. Li, B., et al., *Optical and mechanical anisotropies of aligned electrospun nanofibers reinforced transparent PMMA nanocomposites.* Composites Part A: Applied Science and Manufacturing, 2016. **90**: p. 380-389.

180. Liu, Z., et al., *Tunable surface morphology of electrospun PMMA fiber using binary solvent.* Applied Surface Science, 2016. **364**: p. 516-521.
181. Abed, Y., et al., *Poly (4-vinylpyridine) and poly (4-vinylpyridine poly-3-oxide ethylene) as corrosion inhibitors for Cu60-Zn40 in 0.5 M HNO3.* Anti-Corrosion Methods and Materials, 2001. **48**(5): p. 304-308.
182. Sakai, Y., Y. Sadaoka, and M. Matsuguchi, *A Humidity Sensor Using Cross-linked Quaternized Polyvinylpyridine.* Journal of the Electrochemical Society, 1989. **136**(1): p. 171-174.
183. Sidorov, S.N., et al., *Influence of Metalation on the Morphologies of Poly (ethylene oxide)-b lock-poly (4-vinylpyridine) Block Copolymer Micelles.* Langmuir, 2004. **20**(9): p. 3543-3550.
184. Zhan, X., et al., *Polymer-entanglement-driven coassembly of hybrid superparamagnetic nanoparticles: Tunable structures and flexible functionalization.* Journal of colloid and interface science, 2017. **508**: p. 263-273.
185. Zhang, Z., et al., *Gold nanoparticles stabilized by poly (4-vinylpyridine) grafted cellulose nanocrystals as efficient and recyclable catalysts.* Carbohydrate polymers, 2018. **182**: p. 61-68.
186. Li, S.-Y., G.A. Niklasson, and C.-G. Granqvist, *Nanothermochromics with VO2-based core-shell structures: Calculated luminous and solar optical properties.* Journal of Applied Physics, 2011. **109**(11): p. 113515.
187. Li, S.-Y., G.A. Niklasson, and C.-G. Granqvist, *A thermochromic low-emittance coating: Calculations for nanocomposites of In2O3: Sn and VO2.* Applied Physics Letters, 2011. **99**(13): p. 131907.
188. Garnett, J.M., *Colours in metal glasses, in metallic films, and in metallic solutions. II.* Philosophical Transactions of the Royal Society of London. Series A, Containing Papers of a Mathematical or Physical Character, 1906: p. 237-288.
189. Niklasson, G.A., C. Granqvist, and O. Hunderi, *Effective medium models for the optical properties of inhomogeneous materials.* Applied Optics, 1981. **20**(1): p. 26-30.
190. Kang, L., et al., *Nanoporous thermochromic VO2 films with low optical constants, enhanced luminous transmittance and thermochromic properties.* ACS applied materials & interfaces, 2011. **3**(2): p. 135-138.
191. Zhou, L., et al., *Enhanced luminous transmittance of thermochromic VO2 thin film patterned by SiO2 nanospheres.* Applied Physics Letters, 2017. **110**(19): p. 193901.
192. Zhang, J., et al., *Mesoporous SiO 2/VO 2 double-layer thermochromic coating with improved visible transmittance for smart window.* Solar Energy Materials and Solar Cells, 2017. **162**: p. 134-141.
193. Yoon, J., et al., *Controlling the Temperature and Speed of the Phase Transition of VO2 Microcrystals.* ACS applied materials & interfaces, 2016. **8**(3): p. 2280-2286.
194. Zhang, D., et al., *VO2 Thermochromic Films on Quartz Glass Substrate Grown by RF-Plasma-Assisted Oxide Molecular Beam Epitaxy.* Materials, 2017. **10**(3): p. 314.
195. Zhang, P., et al., *The electro-optic mechanism and infrared switching dynamic of the hybrid multilayer VO2/Al: ZnO heterojunctions.* Scientific Reports, 2017. **7**.
196. Lee, S., et al., *Epitaxial stabilization and phase instability of VO2 polymorphs.* Scientific reports, 2016. **6**: p. 19621.

197. Zhang, Y. and Y. Huang, *A facile hydrothermal synthesis of tungsten doped monoclinic vanadium dioxide with B phase for supercapacitor electrode with pseudocapacitance.* Materials Letters, 2016. **182**: p. 285-288.
198. Zhang, C., et al., *Simple and facile synthesis W-doped VO2 (M) powder based on hydrothermal Pathway.* Int. J. Electrochem, 2015. **10**: p. 6014-6019.
199. Welton, T. *Solvents and sustainable chemistry*. in *Proc. R. Soc. A*. 2015. The Royal Society.

Chapter 2

Aqueous Based Reflux for the Synthesis of W-doped VO_2 Delivering PVP-Coatings with High Luminous Transparency and Solar Modulation Efficiency

ABSTRACT

The preparation of VO_2-based polymer coatings with simultaneously high visible transmittance and high solar modulation ability has been elusive for smart window design. In this work, reflux synthesis uisng a green chemistry water-based approach is examined with ammonium metavanadate as a non-toxic precursor, being reduced by aspartic acid for the synthesis of monoclinic vanadium dioxide [VO_2(M)]. The optimum synthesis conditions were determined for synthesising an oxidation stable, W-doped, monoclinic vanadium oxide showing a low transition temperature (T_c) between its monoclinic and tetragonal phases with small hysteresis.

Systematically, the molar ratio of ammonium metavanadate and aspartic acid, the annealing temperature and annealing time on the resulting VO_2(M) crystal structure were varied. The results showed that an aspartic acid/NH_4VO_3 molar ratio of 0.6/1, calcined at 800 °C for 2 h gave VO_2(M) in high yields without containing V_2O_5, which is considered a toxic byproduct to be avoided. Optimized VO_2(M) was then doped with tungsten with nominal concentrations up to 4 at. % with the annealing conditions optimized. The lowest T_c of 53.6 °C was found at 3 at. % W-nominal doping concentration with an 800 °C annealing for 2 h. This material was shown stable against oxidation and exhibited a visible transparency

(T_{lum}) of 68.3% at 22 °C and a solar modulation efficiency (ΔT_{sol}) of 20.4% between 22 °C and 80 °C in a polyvinylpyrrolidone (PVP) coating. In addition, a pure VO_2(M) phase was achieved at lower annealing temperatures and shorter times with the addition of W or PVP, which was not possible for un-doped or the pristine sample.

KEYWORDS: vanadium dioxide (VO_2), semiconductor-metal transition (SMT), phase transition (T_c), luminous transmittance, (T_{lum}), solar modulation efficiency (ΔT_{sol}).

2.1 INTRODUCTION

Vanadium dioxide (VO_2) has many polymorphs including tetragonal rutile-type VO_2(R), and at least three metastable phases [1]. Of particular scientific and technical interest is the thermodynamically stable monoclinic phase, VO_2(M), because of its unique optical and electrical properties [2]. When VO_2(M) is heated, it undergoes a reversible, first order semiconductor-metal transition (SMT) at 67°C, also called the critical temperature (T_c) [3]. In this transition, its crystal structure changes from monoclinic VO_2(M) (at low temperature) to tetragonal VO_2(R) (R = rutile) (at high temperature) [4]. The low temperature semiconductor phase VO_2(M) is near-infrared (NIR) transparent, whereas the high temperature metallic VO_2(R) phase is highly NIR reflective with nearly maintained visible transmittance [5]. Exhibiting this unique low temperature SMT feature, VO_2 has many potential applications in optical and electrical switching devices, smart window coatings, as well as sensors and transducers [6, 7]. Smart coatings, which use the large optical property alterations of VO_2 with temperature change is of interest here. For instance, VO_2(M) coated "smart" windows can support the reduction of heating/cooling costs by transmitting available NIR sunlight to enter rooms through the windows on cold days while keeping rooms cool in the summer on sunny days by reflecting the undesired NIR [8].

Several methods can be used to prepare VO_2 coatings, e.g. vapor-based deposition techniques. But these methods are expensive and complex due to high cost equipment and in addition, difficulties in controlling the variable valance states of vanadium ions [9, 10]. Wet chemical approaches, on the other hand, show significant advantages in the fabrication of VO_2 coatings in comparison to traditional techniques including simple preparation approaches, low cost, short production times, scalability, and high flexibility in the selection of substrates [10]. A variety of

metals can be doped into VO_2 (M) using wet chemistry to tailor the T_c of VO_2 (M/R) [11, 12]. T_c can be decreased by using high-valent cations ($Nb^{5+,}$ Mo^{6+} and W^{6+}) or increased by doping VO_2 with low-valent cations (Al^{3+}, Cr^{3+}, Ti^{+4} and Fe^{3+}) [7]. Among many dopants, W is found to be most effective to reduce T_c of VO_2 [13]. However, to date, several barriers have not been overcome to permit the use of VO_2(M/R) in industrial applications. How to synthesize scalable VO_2 with high yield, achieve low-cost processing, and simultaneously enhance both the luminous light transmission (T_{lum}) and the solar modulation efficiency (ΔT_{sol}) of VO_2 containing the films has not been achieved. For example, Gao et al. prepared VO_2 nanocomposite foils based on SiO_2/VO_2 core/shell structures to obtain a T_{lum} of 55.3% [14, 15]. However, ΔT_{sol} exhibited only 7.5%, in addition to the very small batch size (0.125 g of V_2O_5) with complex steps such as heating in an autoclave at 220 °C for 24 h. There are several attempts [13, 15-27], still none have reached sufficient luminous light transmission and/or solar modulation efficiency (a brief overview can be found in Appendix A).

Various reactions of reductants and vanadium precursors have been investigated in literature. Nonetheless, in this work we examined the novel synthesis of VO_2(M) by using a low toxicity vanadium precursor, i.e. ammonium metavanadate (NH_4VO_3), which was reduced with the electron donor, L-aspartic acid ($C_4H_7NO_4$), using a water-based approach. Our objective was to produce VO_2 (M) particles with the ability to simultaneously improve ΔT_{sol} and T_{lum} of VO_2 containing polyvinylpyrrolidone (PVP) coatings. First, the optimal molar ratio of reagents for the synthesis of VO_2 were investigated at various annealing temperatures and times. Then, the effect of tungsten (W) on T_c, the monoclinic phase and the chemical stability of VO_2 was examined using the optimized conditions. The present work demonstrates a new, green synthetic route for achieving high yield (> 90%, yield is the ratio of actual yield (experimental) to theoretical yield

expressed in percentage) for W-doped monoclinic VO_2. It is shown that for nominally 3 at. % W-doped VO_2/PVP coatings, satisfactory optical properties with simultaneous improvement of both T_{lum} (68.3% at 22 °C) and ΔT_{sol} (20.4%) is achieved. The nominally 3 at. % W-doped VO_2/PVP coating displayed an acceptable transition temperature of 53.6 °C, which moves the material closer to an application in smart windows where a Tc closer to 30 °C is required.

2.2 EXPERIMENTAL SECTION

2.2.1 Materials

L-aspartic acid ($C_4H_7NO_4$, ≥ 99%, HPLC), ammonium metavanadate (NH_4VO_3, ≥ 99%, A.C.S. reagent), polyvinylpyrrolidone (PVP, average molecular weight 40 kDa) and tungstic acid (H_2WO_4, 99%) were purchased from Sigma-Aldrich, Canada. Anhydrous ethyl alcohol was purchased from Commercial Alcohols, Inc., Canada. Microscope glass slides were purchased from VWR International. All the chemicals were used as received without any further purification.

2.2.2 Synthesis of VO_2 and W-doped VO_2 particles

The synthesis of VO_2(M) and W-doped VO_2(M) was carried out by a simple solution-based approach which is easily scalable. In a typical synthesis, 3.0 g of ammonium metavanadate were reduced by 2.0 g of aspartic acid in 50 mL of distilled water under magnetic stirring. After refluxing at 100 °C for 2 h, a black solution was obtained which indicated a reduction of vanadium (V) into vanadium (IV). For the preparation of W-doped VO_2(M), different concentrations of H_2WO_2 (1 - 4 at. %) in the ammonium metavanadate were used. Precipitates, doped or un-doped, were isolated by centrifugation and dried overnight in an oven at 50°C. Then calcination under argon gas (Praxair, Ultra High Purity) in a tube

furnace (F21100, Barnstead Thermolyne Corporation) at various temperatures (450 – 800 °C) and times (0.5 - 2 h) followed.

The following reaction mechanism (Scheme 2.1) is proposed based on Sherigawa et al. [28] and Booth et al. [29].

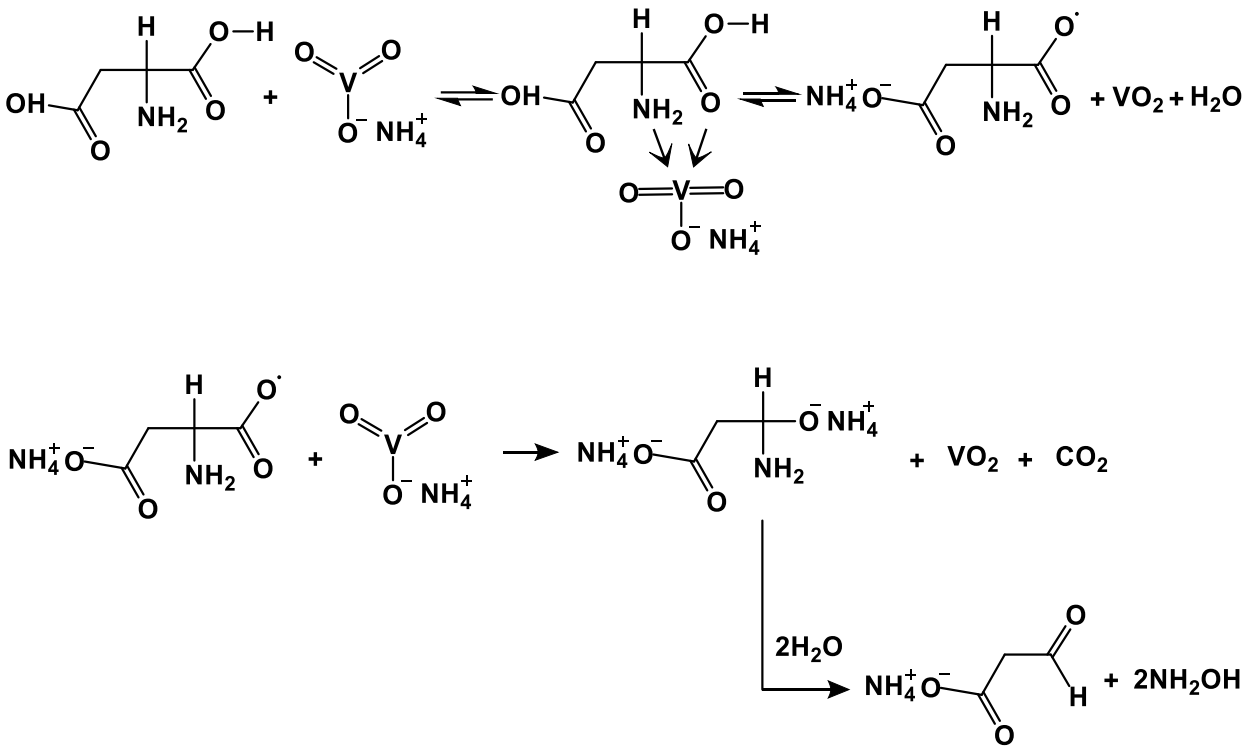

Scheme 2.1 Diagram of ammonium metavanadate reduction by aspartic acid.

2.2.3 Fabrication of VO_2-PVP Coatings on Glass

In a small vial, 0.12 g of PVP and 0.12 g of calcined VO_2 or W-doped VO_2(M) powders (800 °C-2 h) was mixed with 3 mL of ethanol and ultrasonicated (B2500A-MTH, VWR)) at 50 °C for 60 min. To prepare the coatings, 0.3 - 0.5 mL of the VO_2/PVP solution was spin-coated (WS-400B-6NPP-Lite, Laurell) on glass substrates at 1500 rpm for ca. 10 s.

Sucessively, the films were dryed in an oven (V0914C, Lindberg/Blue M^{TM}) at 80 °C for 30 min. The approximate thickness of the coatings were ~300 nm mesuared by AFM.

Similarly, in a small vial, 0.12 g of PVP and 0.12 g of the as synthesized VO_2 or W-doped VO_2(M) powders was mixed with 3 mL of ethanol and ultrasonicated (B2500A-MTH, VWR)) at 50 °C for 60 min. To prepare the coatings, 0.3 - 0.5 mL of the VO_2 (un-calcined)/PVP solution was spin-coated on glass substrates at 1500 rpm for ca. 10 s. Sucessively, the films were dryed in the oven at 80 °C for 30 min. Then, the VO_2/PVP coated glass was calcined under argon gas (Praxair, Ultra High Purity) in a tube furnace (F21100, Barnstead Thermolyne Corporation) at 500 °C for 30 min.

2.2.4 Characterization

The synthesized VO_2 was examined by X-ray diffraction (XRD; Bruker D2 phaser powder diffractometer, Billerica, MA, USA) using Cu Kα radiation ($\lambda_{K\alpha}$ = 1.54059 Å) with a scanning rate of 0.25°/second. The transition temperatures of VO_2 were determined by differential scanning calorimetry (DSC; SDT Q600, TA Instruments, USA) using a cooling-second heating-cycle between 10 °C and 100 °C. The data were analyzed via the instrument's software (Universal Analysis 2000, TA Instruments, USA). The optical transmittance was measured using a Shimadzu UV-3600 UV-vis-NIR spectrophotometer (Shimadzu, Kyoto, Japan) in the wavelength range of 250 – 2500 nm. The temperature was controlled using a Julabo F12-Refrigarated/Heating Circulator (Julabo GmbH, Seelbach, Germany). XPS analysis was carried out using a Kratos Axis Ultra spectrometer (Kratos, Manchester, UK) equipped with a monochromatic Al Kα source (15 mA, 14 kV). Prior to measurements, the instrument was calibrated using the $Au_{4f7/2}$ line (83.96 eV) of metallic gold. For calibration of the spectrometer's dispersion, the $Cu_{2p3/2}$ line (932.62 eV) of

metallic copper was used. The Kratos charge neutralizer system was used for all specimens. Survey scan analyses and high resolution analyses were carried out evaluating analysis areas of 300 x 700 μm with a pass energy of 160 eV and 20 eV, respectively. Spectra were then charge corrected to the main line of the carbon 1s spectrum (adventitious carbon) set to 284.8 eV and analyzed via the XPS software (CASA, version 2.3.14). V_{2p} and O_{1s} were curve-fitted following the procedure described by Biesinger et al. [30]. To characterize the VO_2 particles' sizes and their aggregation in the polymer coating on glass, a conventional optical microscope (Nicon, Eclipse TE 300, Inverted Microscope; objective: Nipon Plan Fluor 4x, Tokyo, Japan) was used and micrographs were analyzed via the imaging software ImageMaster (version 5, PTI incorporated USA). A Veeco diMultiMode V atomic force microscope (AFM, Veeco, Plainview, NY, USA) was used to meaure the thickness of the coatings via the Nanoscope V7.30 program software. EVA Software (Bruker D8 Advance) was used for VO_2 phase analysis by interpretation of XRD data. The particle sizes of VO_2 and its aggregates were measured using the Malvern Zeta-sizer Nano-ZS (Dynamic Light Scattering instrument (Malvern, UK).

2.3 RESULTS AND DISCUSSIONS

2.3.1 Optimization of Molar Ratios of Aspartic acid/ NH_4VO_3 and Calcination Parameters

Under refluxing water, various molar ratios of aspartic acid/NH_4VO_3 (1.3/1 - 0.2/1), calcination temperature (450 – 800 °C) and calcination times (1 - 4 h) were examined. The XRD spectra of VO_2 prepared with systematically varying molar ratios (aspartic acid/ NH_4VO_3: from 1.3/1 to 0.2/1), and calcined at 800 °C for 1 h, 2 h and 4 h are shown in Figure 2.1. The main products identified in the XRD spectra were VO_2 (M), V_2O_3 and V_2O_5, respectively with minor products being V_3O_7 and V_5O_9. The Bragg peaks of VO_2 (M) are indexed by stars (*), the ones from V_2O_3 by triangles (Δ), the peaks of V_2O_5 by rings (O), Θ indexes V_3O_7, and © indexes V_5O_9. The molar ratios and annealing times that exhibit diffraction peaks which can be assigned solemnly to the pure monoclinic VO_2(M) phase (*) (JCPDS card no. 43-1051) [20] for 2 h calcination time at 800 °C were at the molar ratios 0.7/1 and 0.6/1 (Figure 2.1b). When the concentration of aspartic acid was higher (i.e., aspartic acid/ NH_4VO_3: 0.8/1 to 1.3/1), V_2O_3 (Δ) (JCPDS no. 34-0187) [31] was obtained at all annealing times. At lower aspartic acid/ NH_4VO_3 ratios, i.e. 0.4/1 to 0.2/1, V_2O_5 (O) diffraction peaks appeared in the products for all annealing times.

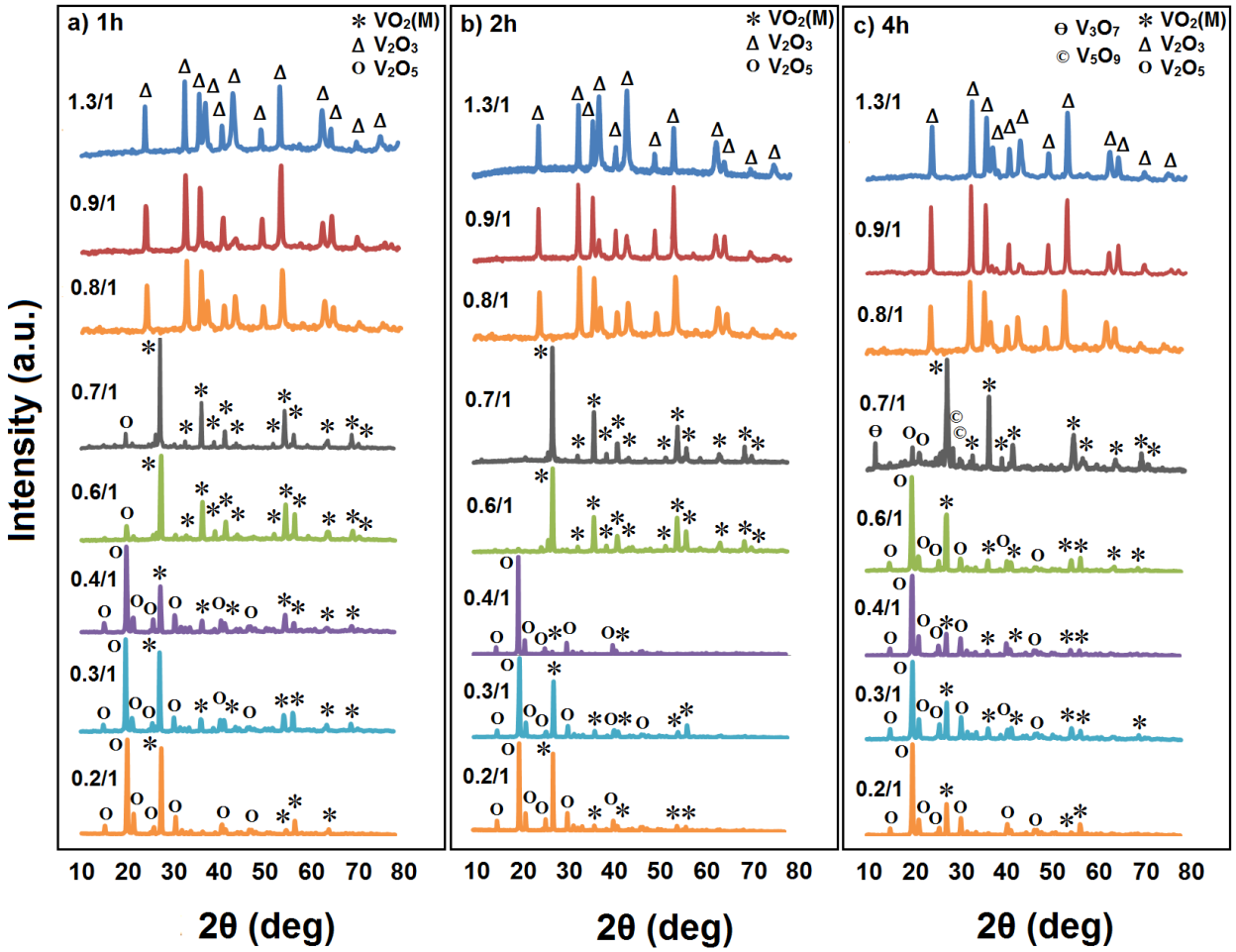

Figure 2.1 The XRD spectra of VO_2 prepared with various molar ratios (aspartic acid/ NH_4VO_3: 1.3/1 to 0.2/1) and annealed at 800 °C for (a) 1 h, (b) 2 h, and (c) 4 h. * indicate the Bragg peaks of VO_2(M), Δ of V_2O_3, O of V_2O_5, Θ of V_3O_7 and © of V_5O_9.

Powder diffraction software (EVA) was used for phase identification and quantitative phase analysis of the "0.7/1" and "0.6/1" samples (yielding the highest monoclinic VO_2(M) amounts) for all calcination times (Figure A1-A6). The results are summarized in Table 2.1a showing that the "0.7/1(2 h)" sample yielded the highest amount (91.6%) of the desired material, monoclinic VO_2(M). All "0.7/1" and "0.6/1" samples showed VO_2(M) and V_2O_5 phases, besides the "0.6/1(2 h)" sample which contained 29% of triclincVO_2(T). Since triclinic VO_2(T) is an intermediate

between the two monoclinic phases, VO_2(M1) and VO_2(M2) [2], the 0.6/1 molar ratio was chosen to be continued for more in-depth examination.

Figure 2.2 presents the XRD spectra of "0.6/1" samples before and after annealing examining the effects of calcination temperature between 450 °C and 800 °C for 1 and 2 h (VO_2(M) and V_2O_5 indexed identical to Figure 2.1; V_4O_9 and VO_2(B) indexed by (Δ) and (Θ), respectively). Pure VO_2(M) was obtained only when annealed at 800 °C for 2 h (Figure 2.2). The Bragg peaks of VO_2 became more dominant and narrower as calcination temperature increased to 800 °C for 2 h, indicating that larger crystals are formed at higher calcination temperature, which was described earlier as a thermally promoted crystallite growth [32]. Because the size of particles increased attributed to agglomeration at higher calcination temperature, the temperature effects above 800 °C were not examined.

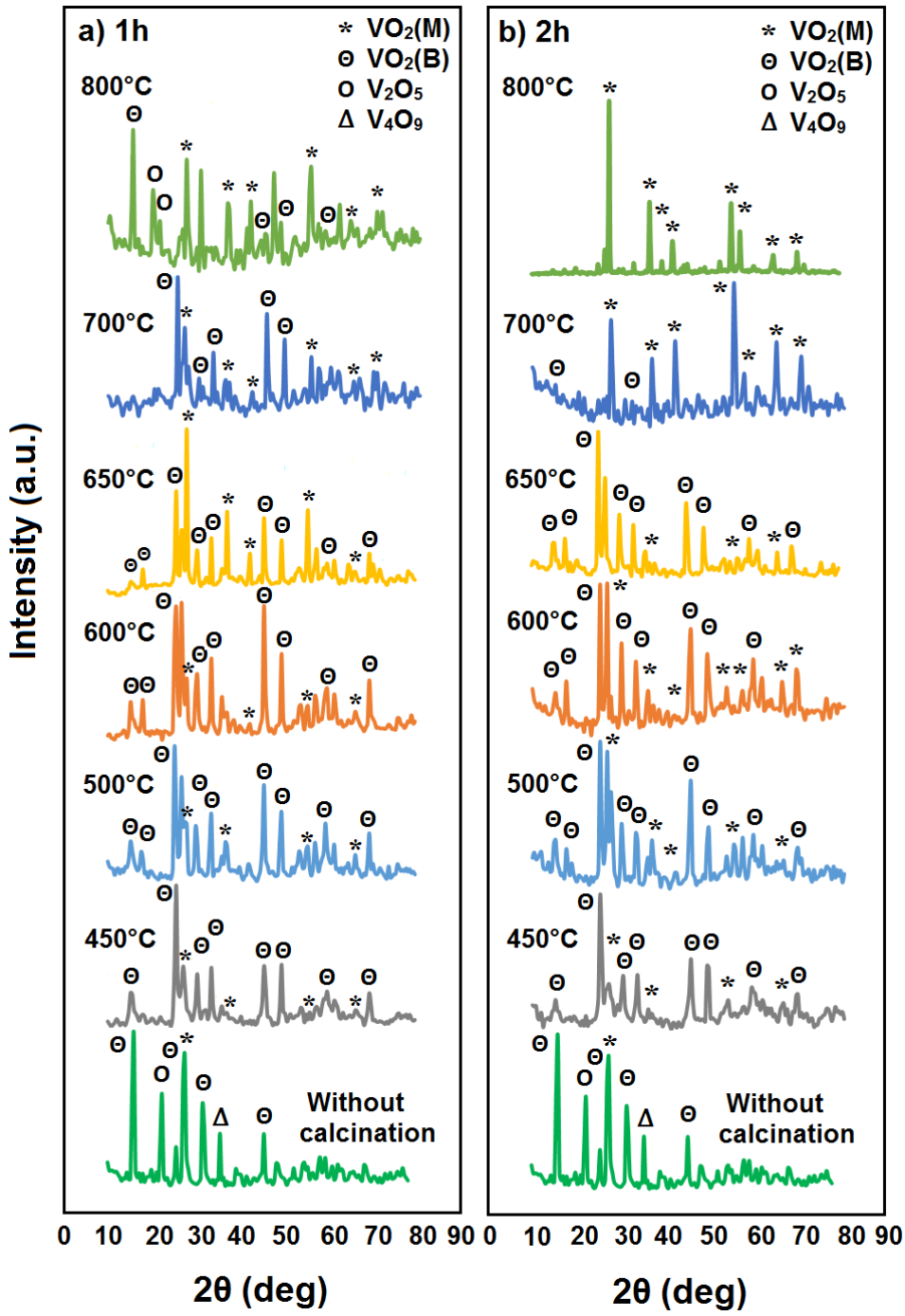

Figure 2.2 XRD spectra of the "0.6/1" samples before and after annealing for (a) 1 h and (b) 2 h at temperatures from 450 °C to 800 °C. * indicate the Bragg peaks of VO_2(M), Θ of VO_2(B), O of V_2O_5 and Δ of V_4O_9.

The phase transition (T_c) of VO_2 was characterized with DSC by monitoring the changes in latent heat [33]. DSC spectra of VO_2 prepared with varying molar ratios of aspartic acid/ NH_4VO_3 from 1.3/1 to 0.2/1, and calcined at 800 °C for 1 h, 2 h and 4 h were taken (Figure 2.3a-c). Figure 2.3d shows a DSC of 0.7/1 and 0.6/1 molar ratio samples, annealed for 2 h, and are compared to a commercially available sample of VO_2 (latent heat 26J/g, Aldrich).

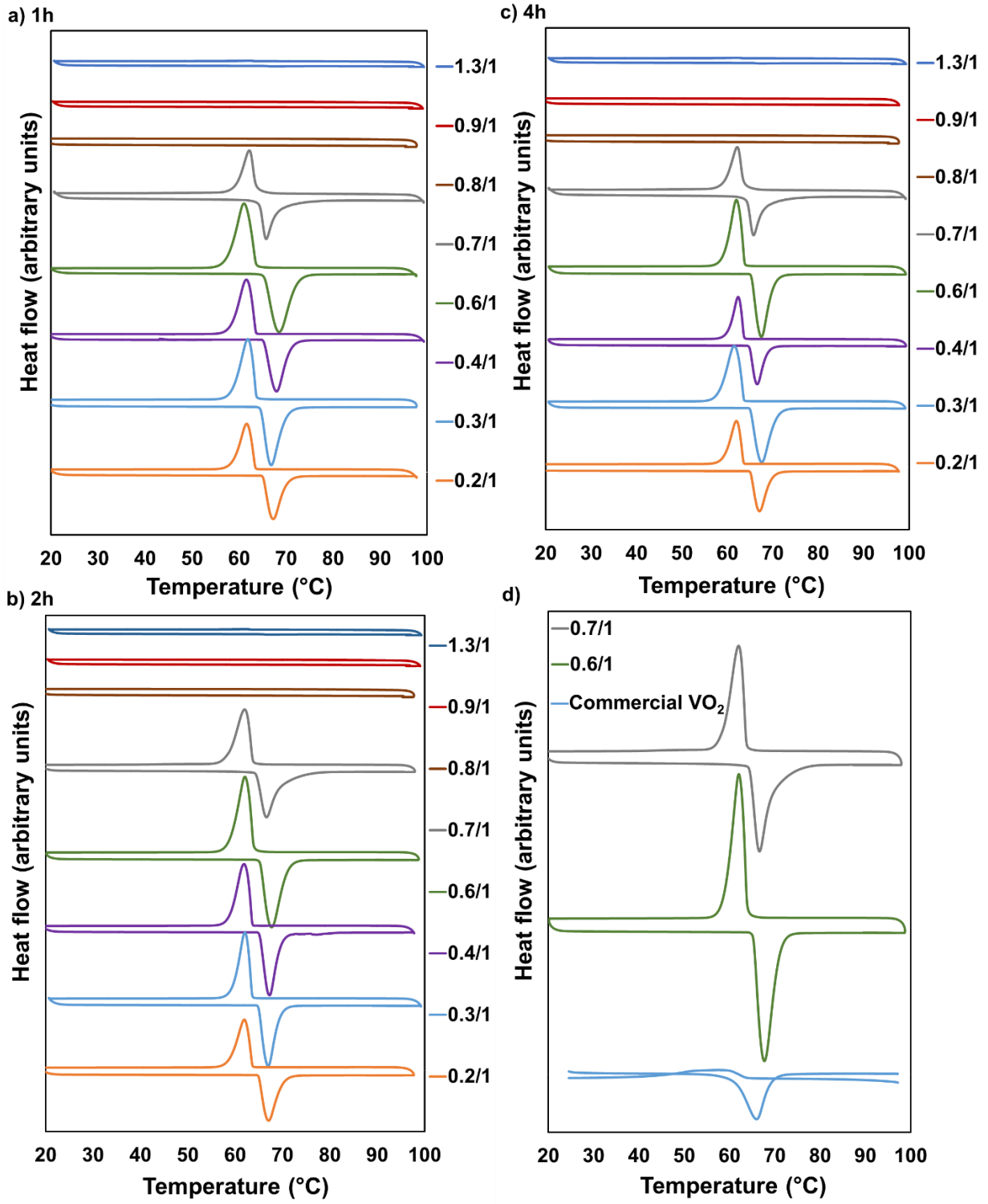

Figure 2.3 DSC spectra of VO_2 prepared at aspartic acid/ NH_4VO_3 molar ratios from 1.3/1 to 0.2/1, annealed at 800 °C for (a) 1 h, (b) 2 h, and (c) 4 h. d) DSC spectra of VO_2 prepared at aspartic acid/ NH_4VO_3: 0.7/1 and 0.6/1 molar ratio, and annealed at 800 °C for 2 h compared to commercially available sample of VO_2 (Aldrich, 99.9%). All DSC measurements are in the same y-scale.

The “0.6/1 (2 h)” sample shows the most pronounced DSC peak (Figure 2.3b) at the critical temperature (Tc) of 68°C, as this sample does not contain V_2O_5 (Table 2.1a) (data from EVA analysis of XRD spectra (Figure 2.1)). Table 2.1b summarizes the results of all DSC measurements for samples prepared with aspartic acid/ NH_4VO_3 molar ratios from 0.7/1 to 0.2/1 and annealed at 800 °C for 1 h, 2 h and 4 h. It also depicts the highest latent heat (49.5 J/g) for the “0.6/1 (2 h)” sample which is higher than the latent heat of commercial VO_2(M) samples (i.e., 41.87 J/g, Alfa Aesar) [34]. This indicates that the “0.6/1 (2 h)”-VO_2 material is highly crystalline [35]. For all samples, the latent heat decreased with increasing annealing time to 4 h (Table 2.1b). A similar decrease in latent heat (from 23.9 to 11.2 J/g) was previously reported by Dong et al. when the annealing time was increased from 6 to 48 h [36]. Reducing the hysteresis (ΔT) is necessary to increase the switching speed between the two phases (VO_2(M) $\leftrightarrow$ VO_2(R)) in response to a temperature change, ΔT (the difference in the peak position in the heating and the cooling cycle) [37]. A hysteresis larger than ~6 °C is not suitable for smart window applications with rapid switching response as it was shown in powder-based films prepared in previous studies which exhibited large hysteresis’s [7]. The transition temperature and the hysteresis of the “0.6/1 (2 h)” VO_2 sample are 68 °C and 5.9 °C, respectively. This small hysteresis of 5.9 °C is noticeably lower than values between 7.1-15.9 °C reported in literature [1, 7, 37-39].

Table 2.1 (a) sample composition of the "0.7/1" and "0.6/1" for all calcination times (data from EVA analysis of XRD spectra (Figure 2.1)), and (b) DSC results for all samples prepared with aspartic acid/ NH_4VO_3 molar ratios from 0.7/1 to 0.2/1 and annealed at 800 °C for 1 h, 2 h and 4 h. Samples without endothermic or exothermic peaks are omitted.

a)

Molar ratio of aspartic acid/ NH_4VO_3(mol/mol)	Calcination time (h)	Amount in % VO_2(M)	Amount in % V_2O_5	Amount in % triclincVO_2(T)
0.7/1	1	72.3	27.7	
0.7/1	2	91.6	8.4	
0.7/1	4	50.6	33	
0.6/1	1	84.5	15.5	
0.6/1	2	71		29
0.6/1	4	44.9	55.1	

b)

Molar ratio of aspartic acid/ NH_4VO_3(mol/mol)	Calcination time (h)	$T_{c\text{-heating}}$ (°C)	$T_{c\text{-cooling}}$ (°C)	Hysteresis Delta T (°C)	Latent heat (J/g)
0.7/1	1	67.0	62.0	5.0	33.8
0.7/1	2	66.6	62.0	4.6	38.3
0.7/1	4	65.9	62.1	3.8	24.5
0.6/1	1	68.7	61.1	7.6	47.5
0.6/1	2	68.0	62.1	5.9	49.5
0.6/1	4	67.5	61.9	5.6	37.9
0.4/1	1	68.0	61.5	6.5	34.4
0.4/1	2	67.4	62.0	5.4	34.2
0.4/1	4	66.5	62.4	4.1	18.8
0.3/1	1	66.8	62.0	4.8	37.8
0.3/1	2	67.0	62.1	4.9	34.8
0.3/1	4	67.6	61.5	6.1	37.8
0.2/1	1	67.2	61.6	5.6	26.5
0.2/1	2	67.3	62.0	5.3	28.9
0.2/1	4	67.1	62.0	5.1	23.2

DSC spectra of the "0.6/1(2 h)" samples were measured both in the un-calcined state and calcined at temperatures between 450 °C and 800 °C as shown in Figure 2.4. The heights of the endothermic and exothermal peaks considerably increased with increasing calcination temperature. In parallel, the latent heat increased from 0.08 to 49.5J/g (Figure 2.4), and the hysteresis decrease from 8.7 to 5.9 °C (Table 2.2). The lower latent heat with wider hysteresis at

the low annealing temperature is due to smaller average particle sizes of the VO_2 (Table 2.3) [12, 32]. Appropriate, high annealing temperature and time are essential for obtaining highly crystalline VO_2(M). Based on the above analysis and discussion, "optimized conditions" for pure monoclinic VO_2 is an aspartic acid/ NH_4VO_3 ratio of 0.6/1, calcined at 800 °C for 2 h.

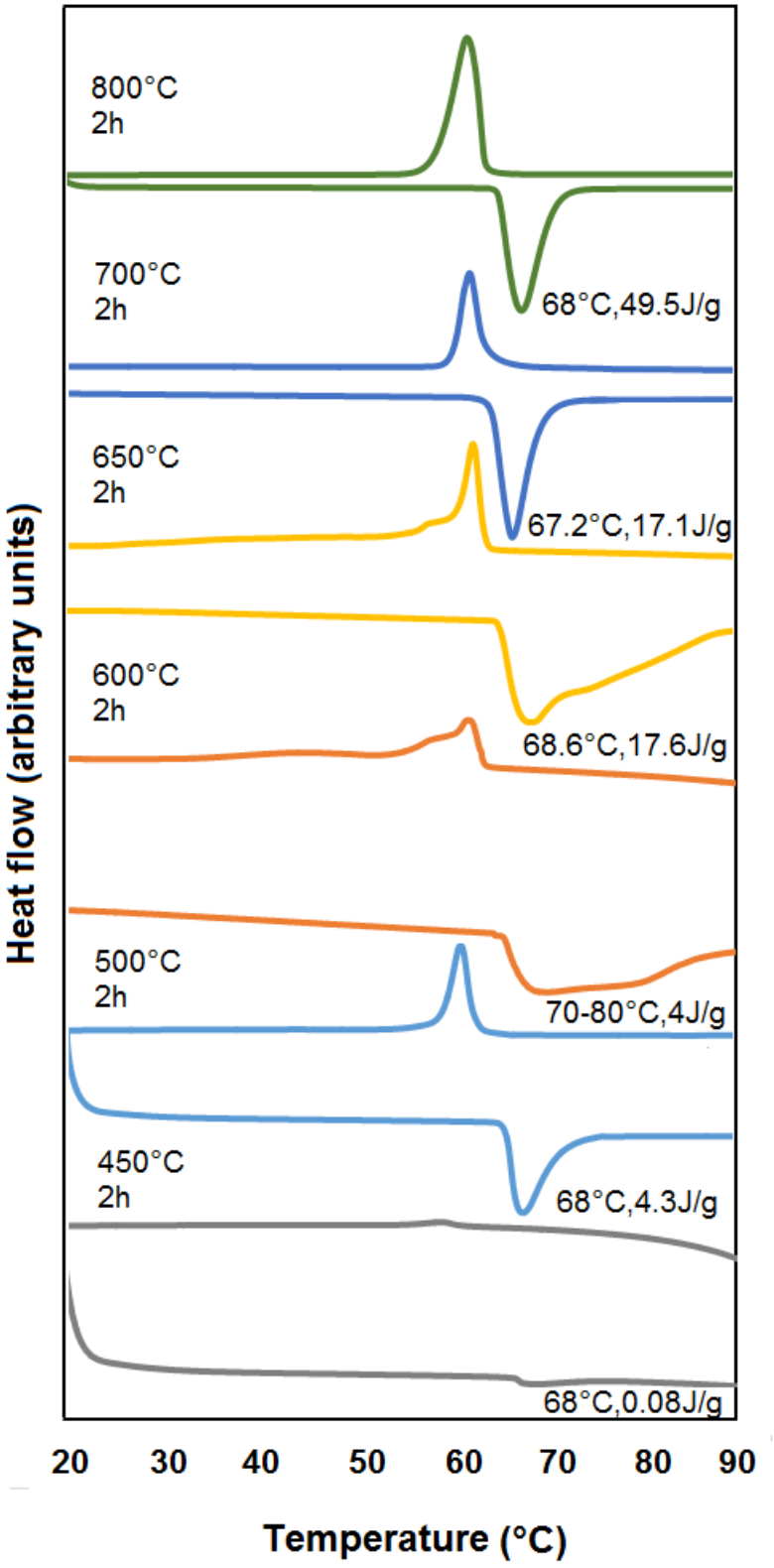

Figure 2.4 DSC spectra of the "0.6/1 (2 h)" samples for calcination from 450 °C-800 °C. All DSC measurements are in the same y-scale.

Table 2.2 DSC results of VO_2 prepared at an aspartic acid/ NH_4VO_3 of 0.6/1, annealed at different temperatures for 2 h.

Annealing Temperature (°C)	$T_{c\text{-heating}}$(°C)	$T_{c\text{-cooling}}$(°C)	Hysteresis Delta T (°C)
800	68.0	62.1	5.9
700	67.2	62.5	4.7
650	68.6	63.0	5.6
600	70.0	62.0	8.0
500	68.0	62.0	6.0
450	68.0	59.3	8.7

The average size of VO_2 particles were measured with the nanosizer and the polydispersity index (PdI) calculated using nanosizer software (Table 2.3). For this purpose, the materials were dispersed in distilled water and ultrasonicated (B2500A-MTH, VWR) for 10-15 min to "dissolve" the agglomerates and yield individual particles.

Table 2.3 Average size of VO_2(M), annealed at 450-800 °C for 2 h. Polydispersity Index (PdI).

Annealing temperature (°C)	Average size (nm)	Average PdI
450	209.0 ± 0.4	0.18±0.02
500	232.0 ± 1.4	0.27±0.03
600	264.0 ± 1.2	0.32±0.04
650	290.0 ± 2.2	0.35±0.03
700	305.0 ± 2.9	0.28±0.01
800	325.0 ± 2.4	0.40±0.05

2.3.2 The Effect of Tungsten Doping on the Monoclinic Phase and Transition Temperature of VO_2

Tungsten (W)-doping has been well documented to lower VO_2's T_c [13]. However, it is not clear from the literature on how the VO_2(M) phase is affected by W doping at different concentrations or on the role of synthesis for dopant integration. This section examines the

green reflux water-based method instead of doping by using the high-energy consumption, hydrothermal method. W-doped VO_2 samples were prepared using W-concentrations of 0 (un-doped), 1, 2, 3 and 4 at. % at the "optimized conditions". The XRD spectra of W-doped samples (all nominal concentrations at annealing temperatures of 450 °C, 500 °C and 800 °C) are depicted in Figure 2.5. The peaks of VO_2(B) disappear when doped with W and a pure VO_2(M) phase was achieved using lower annealing temperatures and shorter times (Figure 2.5a). For example, a pure VO_2(M) phase (without any additional diffraction peaks), is obtained for 1 and 3 at. % W-doping with an annealing temperature of 450 °C for 2 h, and 3 at. % W-doping annealed at 500 °C for 30 min, which was not possible without doping. Pure VO_2(M) was also obtained for 2 and 3 at. % W-doping annealed at 800 °C for 2 h (Figure 2.5b). These results agree with Chen et al. [1] and other previous reports [40, 41], indicating that certain doping levels of W could avoid the VO_2(B) phase. The angular position of the strongest XRD peak, the (011)-peak of VO_2(M) located at 27.7°, was stable with doping, except for the 3 at. %W-doped sample annealed at 450 °C for 2 h, which is shifted by 0.3° to 28°. This small shift to a higher angle indicates a decrease in the crystal lattice spacing according to Bragg's equation ($d = \lambda/2\sin\theta$: d spacing, λ wavelength of x-ray, θ diffraction angle) [42]. The stability of the diffraction peak position implies a small real doping level of W, systematically below the nominal values, and, therefore, no or very minor lattice distortions. XPS studies were performed (Figure 2.6) to measure the real W-concentrations. The real W-concentration for the nominal 3 at. % sample is 0.26 at. % (annealed at 800 °C for 2 h), less than 10% of the nominal value, confirming the hypothesis on the stable Bragg peaks. The Bragg peaks of W-doped VO_2 samples are not intense and rather wide, indicating smaller size particles according to Scherrer's equation [43]. This behavior is associated and

in accordance with the ability of W in restricting the growth process and aggregation of VO_2 particles [13].

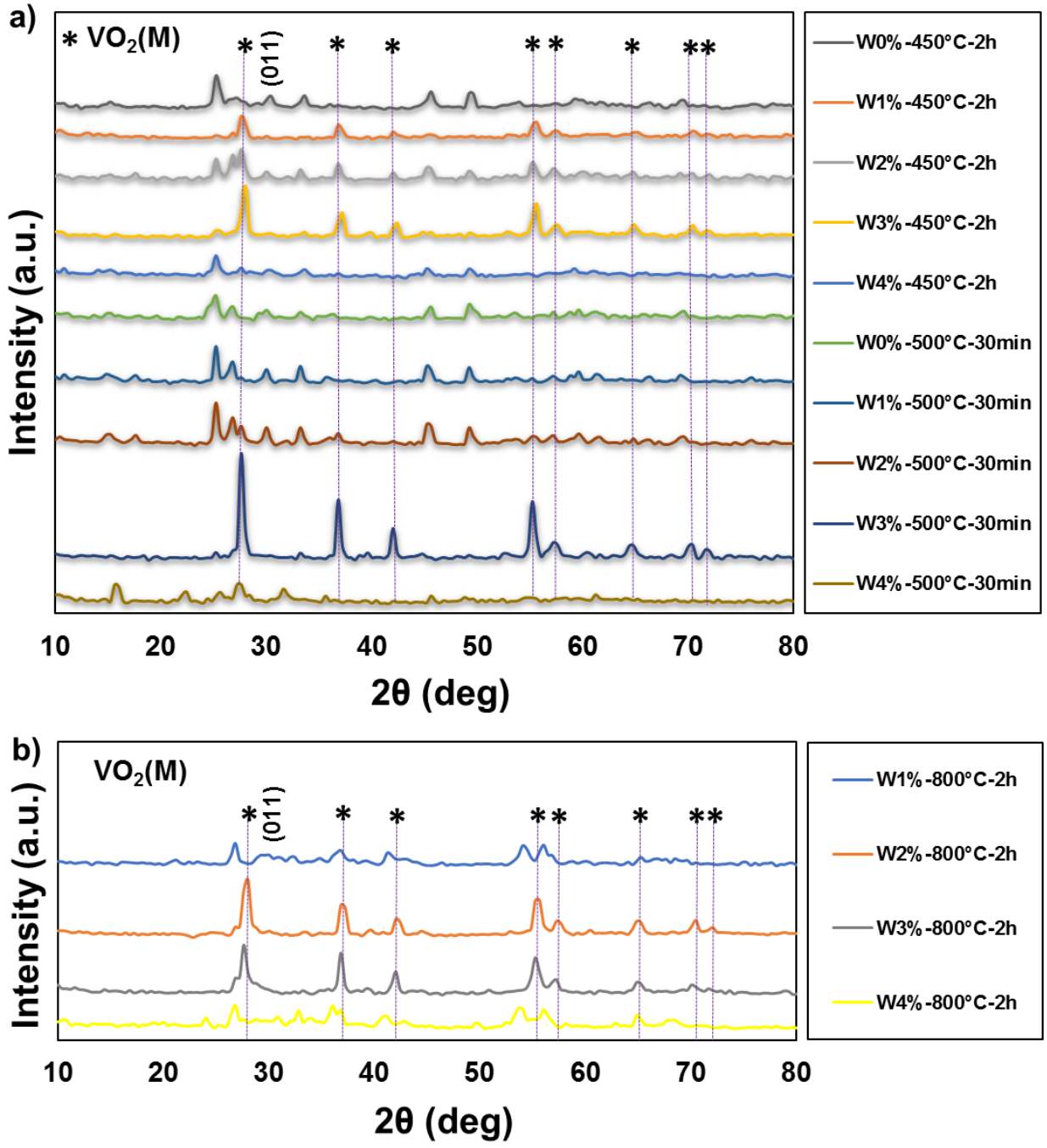

Figure 2.5 XRD spectra of W-doped VO_2 with W-concentrations of 0-4 at. %, synthesized at an aspartic acid/ NH_4VO_3 molar ratio of 0.6/1: (a) calcined at 450 °C for 2 h and 500 °C for 30 min, and (b) calcined at 800 °C for 2 h.

XPS analysis was used to investigate the V and W valence states on the surface of the nominal 3 at. % W-doped VO_2(M) (annealed at 800 °C for 2 h) (Figure 2.6). (The choice for this particular sample was its best performance in luminous transmittance and solar modulation efficiency: see below). The small peaks of carbon, nitrogen, sodium and silicon are attributed to surface contaminations. Three peaks appear in the O_{1s} region with the major peak at 530.3 eV, assigned to O^{2-} ions in the V-O bonding [44] (Figure 2.6b). The other two peaks are assigned to oxygen in H_2O and to hydroxide. The $V2_{p1/2}$ peak splits into three peaks at 525.3 eV, 524.0 eV (major peak) and 522.9 eV (weak peak) ascribed to V(V), V(IV) (majority with 59.5%) and V(III). The $V2_{p3/2}$ peak also splits into three peaks at 518.0 eV [V(V)], 516.6 eV [V(IV)] and 515.5 eV [(V(III)]. The peak energy of $V2_{p3/2}$ at 516.6 eV for V(IV) agrees well with the literature (516.3 eV) [45]. Weak peaks of $W_{4f7/2}$ in Figure 2.6a,c reveal a W(VI) oxidation state, indicating that W was successfully doped into the VO_2 lattice structure.

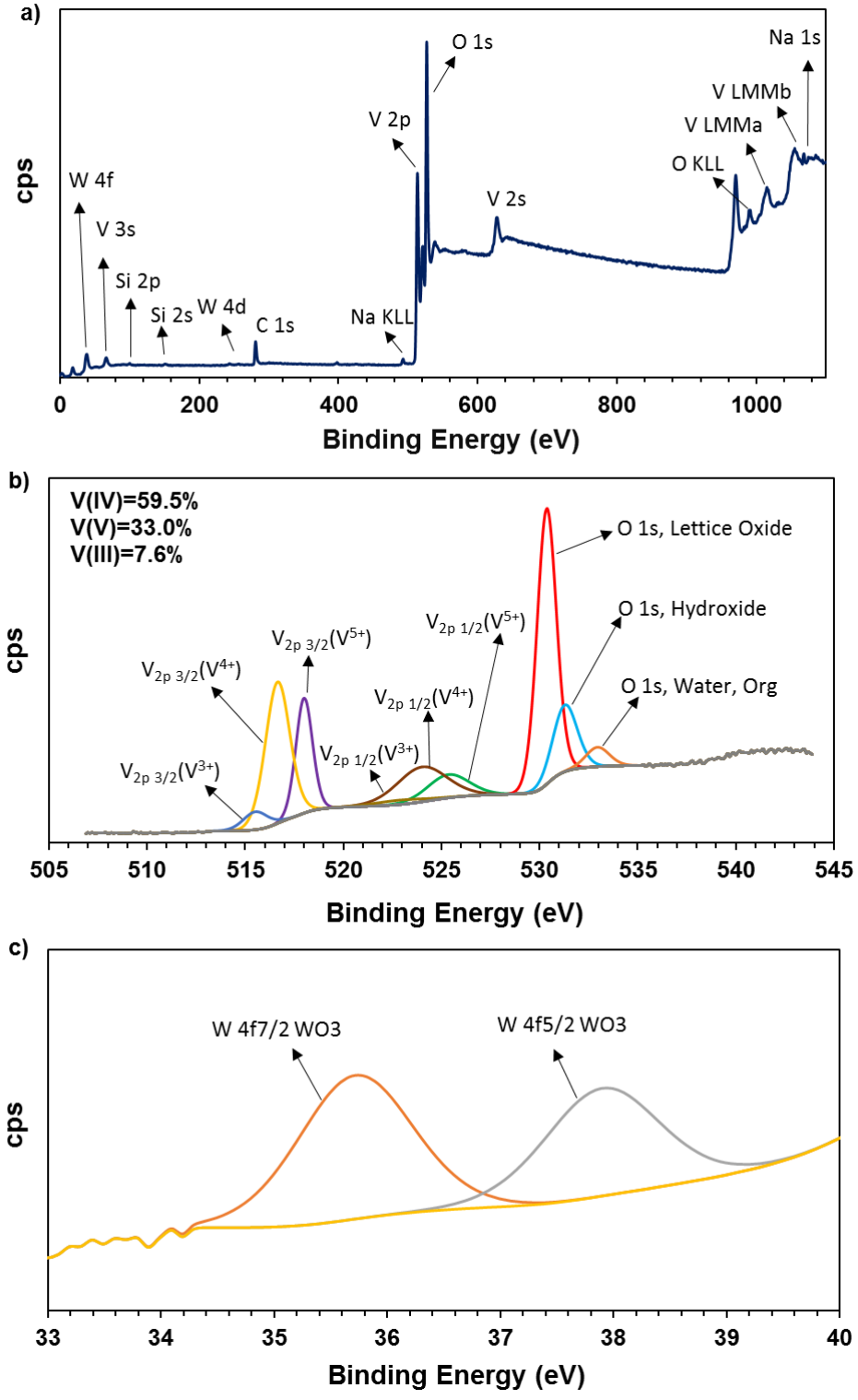

Figure 2.6 XPS spectra for a 3 at. % W-doped VO_2 (M) sample annealed at 800 °C for 2 h: (a) survey spectrum, (b) core-level spectrum for V_{2p} and O_{1s}, and (c) core-level spectrum for W_{4f}.

The effect of W-doping on T_c of VO_2 was investigated by DSC (Figure 2.7). The DSC data are summarized in Table 2.4. An influence of the presence of W on T_c can only be detected in samples with 2 and 3 at. % nominal W concentration that are annealed at 800 °C for 2 h. For example, a very weak endothermic peak of the 3 at. % W-doped VO_2 (annealed at 800 °C for 2 h) sample was detectable at 53.6 °C, which is lower than the "classical" 68 °C for pure VO_2. Based on literatures, responsible for this decrease in T_c is the band gap reduction and phase destabilization of VO_2 [46]. There is only a small reduction of T_c by doping with the reflux method in comparison to the hydrothermal method [47]. This is due to the low real W-concentration in the samples synthesized with the reflux method. The intensity and the latent heat of the endothermic DSC peak for W-dope d VO_2 (annealed at 800 °C for 2 h) sample decrease with increasing nominal W-concentration, however, this is not the case for samples annealed at lower temperatures (Figure 2.7 and Table 2.4). The DSC data for the low annealing temperature samples look like an increase in pure VO_2(M) phase with W-doping at small annealing temperatures.

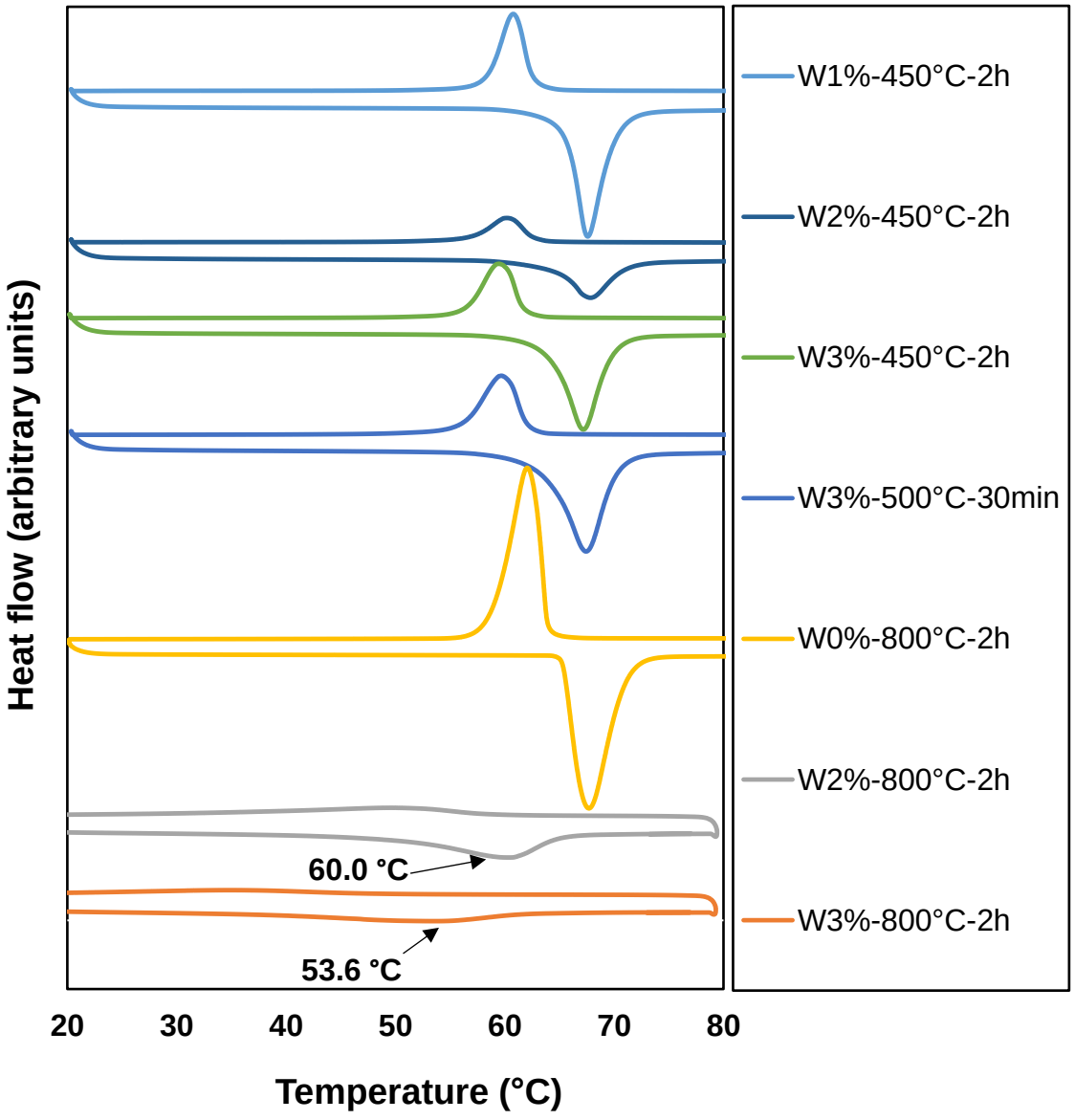

Figure 2.7 DSC spectra of W-doped VO_2 samples synthesized with an aspartic acid/ NH_4VO_3 molar ratio of 0.6/1 annealed with various combinations of temperature (450, 500, 800 °C) and times (30 min, 2 h). Samples without (or not clear) endothermic and exothermic peaks are omitted. All DSC measurements are in the same y-scale.

Table 2.4 DSC results for all W-doped samples prepared at different annealing temperatures and times. Samples without endothermic or exothermic peaks are omitted. The bold material shows the smallest transition temperature.

Samples	$T_{c\text{-heating}}$ (°C)	$T_{c\text{-cooling}}$ (°C)	Hysteresis Delta T (°C)	Latent heat (J/g)
W0%-800°C-2h	68.0	62.1	5.9	49.5
W2%-800°C-2h	60.0	50.0	10.0	24.4
W3%-800°C-2h	**53.6**	**35.2**	**18.4**	**14.0**
W4%-800°C-2h	58.4	46.4	12.0	0.4
W3%-500°C-30min	67.4	59.6	7.8	43.3
W1%-450°C-2h	67.6	60.7	6.9	40.0
W2%-450°C-2h	67.9	60.2	7.7	17.0
W3%-450°C-2h	67.2	59.5	7.7	36.3

2.3.3 The Effect of Polyvinylpyrrolidone on the Monoclinic Phase of VO_2

Polyvinylpyrrolidone (PVP) acts as a film-forming promoter by improving physical gelation through interactions between opposite charges (carbonyl groups (-) and amine groups (+)) [48]. The interaction between aqua vanadium ions (VO^{2+}) and negatively charged carbonyl groups of PVP in solution can improve the uniformity and dispersion of the precursor film, which should lead to the formation of a relatively pure monoclinic VO_2 phase [48, 49]. As discussed above, pure VO_2(M) cannot be obtained at low annealing temperatures without doping. However, when VO_2 is blended with PVP in ethanol, coated onto a glass substrate, dried in oven at 80 °C for 30min and calcined in coating format at 500 °C for 30 min, a pure monoclinic VO_2 was found in the coating's XRD spectra (Figure 2.8). This result suggests that the decomposition of PVP polymer effectively induced the formation of monoclinic VO_2, probably due to interactions between VO^{2+} and PVP at

the atomic scale [48, 49]. When the film is annealed at 500°C, degradation of PVP releases reductive gases such as NH_3 and prevent the oxidation of vanadium(IV). Conversely, when annealing at lower temperatures (400 and 300°C), the effect of the reductive gas NH_3 essentially disappears. A similar impact of polymer degradation on crystallization in other systems was previously reported in literature [48, 50-53].

In Figure 2.8 all VO_2(M) peaks are indexed [15]. The Bragg peaks are shifted considerably to higher diffraction angles, indicating a contraction of crystal lattice spacing. The underlying amorphous halos in the XRD spectra stem from the glass substrates. Mixing the PVP with the as synthesized VO_2 and annealing them together seems to have an influence on the phase purity of the VO_2(M) material [48]. This behavior was found for all samples imbedded in PVP, where annealing is ≥ 500°C.

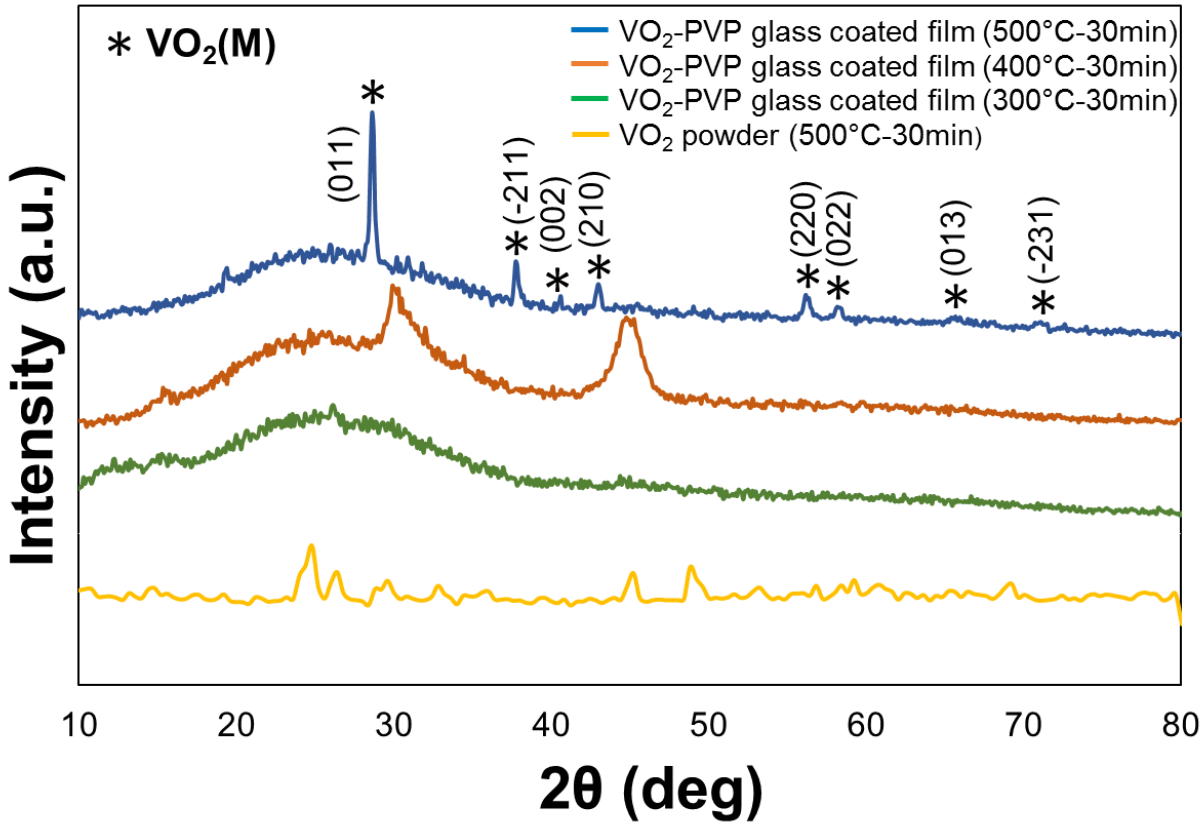

Figure 2.8 XRD spectra of VO_2 powder and VO_2-PVP (un-doped) coatings on glass annealed together at 300, 400 and 500 °C for 30 min.

2.3.4 Chemical Stability of W-doped VO_2

VO_2(M) is thermodynamically unstable [15]. Therefore, switchable VO_2 can gradually oxidize into un-switchable V_2O_5 when it is exposed to air or other oxygen containing environments at room temperature for long periods (i.e., 6 months). Oxygen treatment at elevated temperatures above 300 °C yields the same oxidation process [15]. Gao et al. were able to enhance the chemical stability of VO_2(M) by synthesizing a core/shell VO_2/SiO_2 composite, encapsulating VO_2 by SiO_2 [14]. However, they calcined their samples only 2 h in air. Here, 3 at. % W-doped material was subjected to a heat treatment in air for 0 to 8 h and then examined by XRD (Figure 2.9). The W-doped samples depicted a monoclinic phase until 7 h of heat-treatment. The 8 h-sample started to show a V_2O_5 portion. The Bragg peaks of the heat-treated materials were stable in angular position. A significantly longer exposure time, longer than 30 min [54] or 5 h [55], reported in literature without oxidation, was achieved by W-doping.

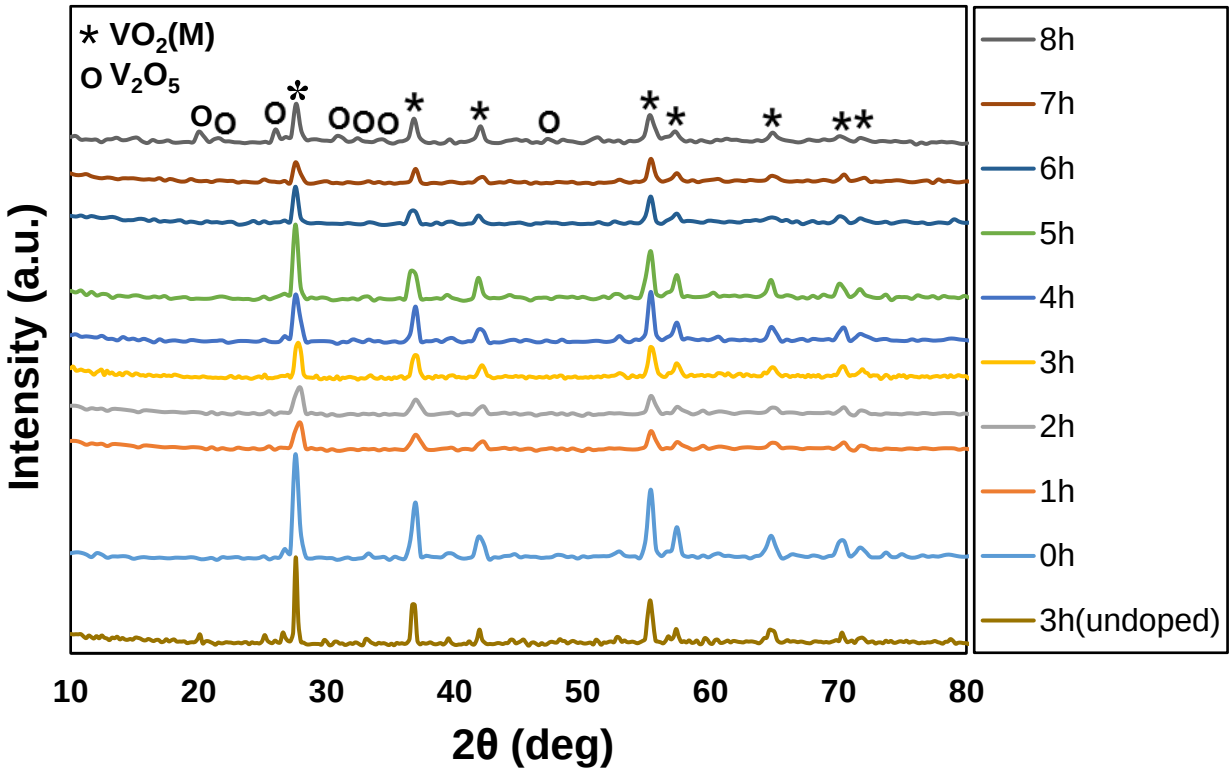

Figure 2.9 XRD spectra of 3 at.% W-doped VO_2 powders (annealed at 800 °C for 2 h) after heat treatment at 300 °C in air for 0 (blue) and 8 h (grey). * indicate the Bragg peaks of VO_2(M) and O of V_2O_5.

2.3.5 Optical Property of VO_2-PVP Coatings

Implementation of the VO_2 in smart windows requires a high IR switching efficiency while keeping the visible transmission as high as possible. However, literature states for VO_2 and W-doped VO_2 that when visible transparency (T_{lum}) is high, the solar modulation efficiency (ΔT_{sol}) is low and vice versa [56]. The optical modulation properties of VO_2/PVP and W-doped VO_2/PVP coatings on glass were investigated to evaluate their potential for usage in smart windows by measuring the optical transmittance at 22 °C and 80 °C (Figure 2.10). The integral solar transmittances, T_{sol} (250–2500 nm), and luminous transmittance, T_{lum} (380–780 nm) were calculated via equation (2.1):

$$T_{lum/sol} = \frac{\int \varphi_{lum/sol}(\lambda) T(\lambda) d\lambda}{\int \varphi_{lum/sol}(\lambda) d\lambda} \quad (2.1)$$

where T(λ) is the spectral transmittance at wavelength λ, $\varphi_{sol}(\lambda)$ is the solar irradiance spectra for an air mass of 1.5. (An air mass of 1.5 corresponds to the sun positioned 37° above the horizon with a 1.5 atmosphere thickness. That corresponds to a solar zenith angle of 48.2°). $\varphi_{lum}(\lambda)$ denotes the standard luminous efficiency function of photopic vision in the wavelength range of 380–780 nm [57]. Solar modulation efficiency (ΔT_{sol}) is obtained by the difference of T_{sol} (eq. 2.1) at 22 °C and 80°C. Table 2.5 summarizes the optical properties of coatings on glass fabricated with two un-doped and two W-doped samples (The bold line depicts the data for the material with the most efficient optical characteristics for smart window application). The W3% 800 °C-2 h-PVP-coating showed improved optical properties with respect to the un-doped samples, and with substantially improved optical properties ($T_{lum,best}$ = 47.6% and $\Delta T_{sol,best}$ = 20.37%) compared to previously published W-doped VO_2 synthesized with different strategies [13, 23, 57, 58]. (A brief overview can be found in Appendix A.)

The addition of W under these synthetic conditions hinders the growth of VO_2(M) particles, hence reducing the scattering of photons and leading to better optical properties and enhanced performance [13]. Despite, the un-doped VO_2 having a higher crystallinity and higher latent heat than the doped one, the thermo-chromicity of the (W3% 800 °C-2 h) coating is higher. A higher phase purity of the VO_2(M) in the doped coatings is claimed to be responsible. Figure 2.11 shows clear Bragg peaks arising from the W-doped VO_2/PVP coating which are missing in the XRD spectrum of the un-doped VO_2 /PVP coating. This suggests that both PVP and W-doping provoked an improvement of the VO_2's crystallinity. Photographs of un-doped and W-doped VO_2/PVP coatings on glass at room temperature placed on white paper with black capital letters (UWO) are

shown in Figure 2.10c,d. The 800 °C coatings (calcined powder) show a light blue color wheras the calinced VO_2/PVP coatings (500 °C) are brown for both doped and undoped sampels. The brown color stems probably from an onset of PVP pyrolysis and an accumulation of carbon during the annealing process.

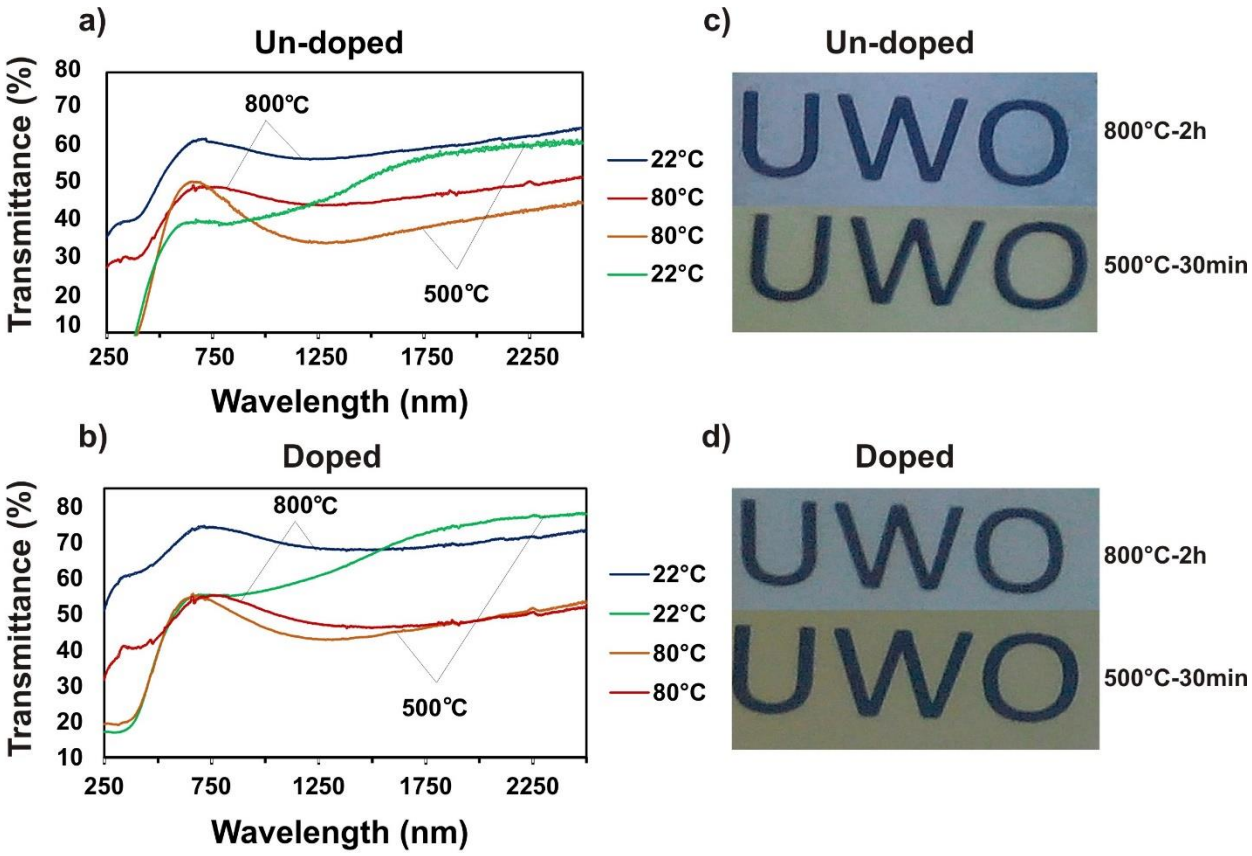

Figure 2.10 Transmittance spectra of: (a) un-doped and (b) 3 at. % W-doped VO_2/PVP coatings on glass. The coatings with only VO_2 is being annealed at 800 °C for 2 h in powder form (red and blue data) and the calcined VO_2/PVP coatings at 500 °C for 30 min (green and brown data). Photographs of VO_2/PVP coatings on glass (800 °C: calcined in powder form, 500 °C: calcined in coating form) against white paper with black letters (UWO) with (c) un-doped and (d) 3 at. % W-doped VO_2.

Table 2.5 Optical properties of un-doped and W-doped VO_2/PVP coatings on glass. The bold line depicts the data for the material with the efficient optical characteristics for smart window application.

Sample	T_{sol} (%)		ΔT_{sol} (%)	T_{lum} (%)		ΔT_{lum} (%)
	22 °C	80 °C		22 °C	80 °C	
W0%800°C-2h	56.07	43.98	12.09	55.69	43.43	12.25
W3%800°C-2h	**69.29**	**48.92**	**20.37**	**68.30**	**47.60**	**20.70**
W0%500°C-0.5h	37.55	38.05	-0.50	36.17	42.98	-6.81
W-3%500°C-0.5h	50.81	45.10	5.71	47.13	47.88	-0.75

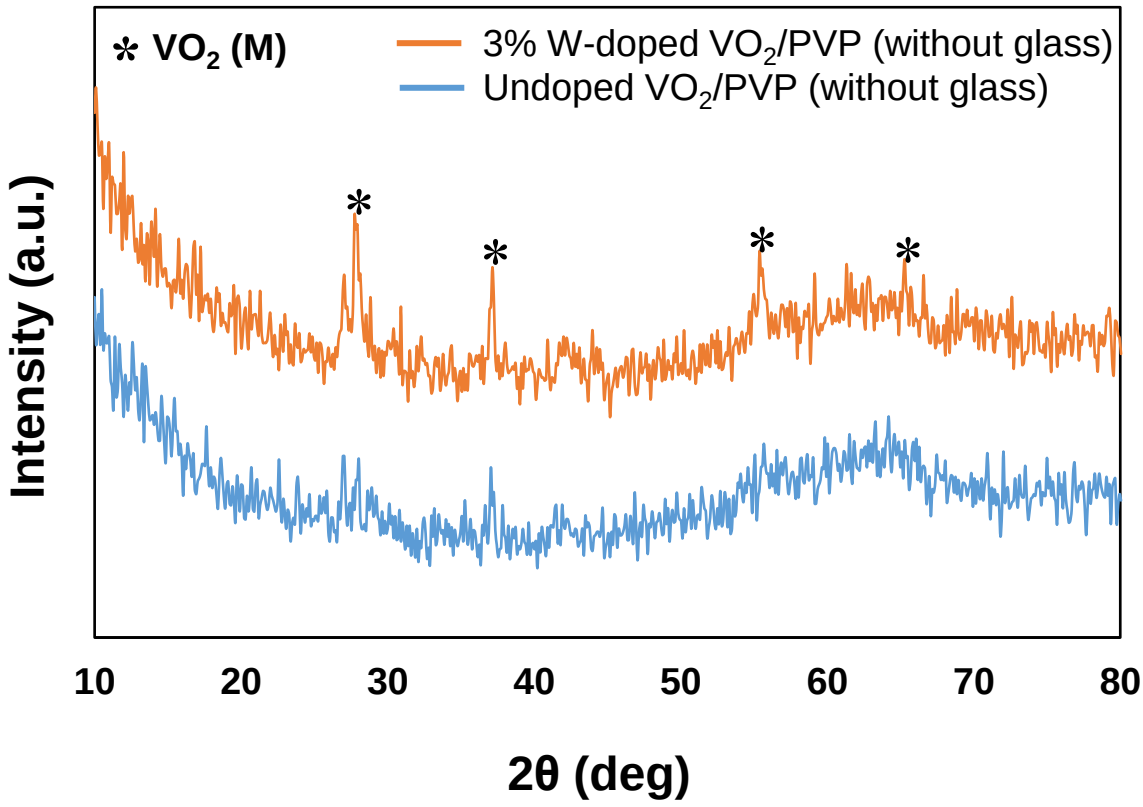

Figure 2. 11 XRD spectra of un-doped and W-doped VO_2/PVP films. Powders annealed at 800 °C for 2 h.

Figure 2.12 shows optical microscopy images of 3 at. % W-doped VO_2/PVP coatings on glass, powders calcined at 800 °C for 2 h and coating calcined at 500 °C for 30 min. The calcined coating in (b) with the smaller calcination temperture show a higher dispersion of the particles and smaller particle aggregates than the coating in (a), powder calcined at 800 °C. Higher annealing temperatures obviously leads to larger particle aggregation in the PVP coating.

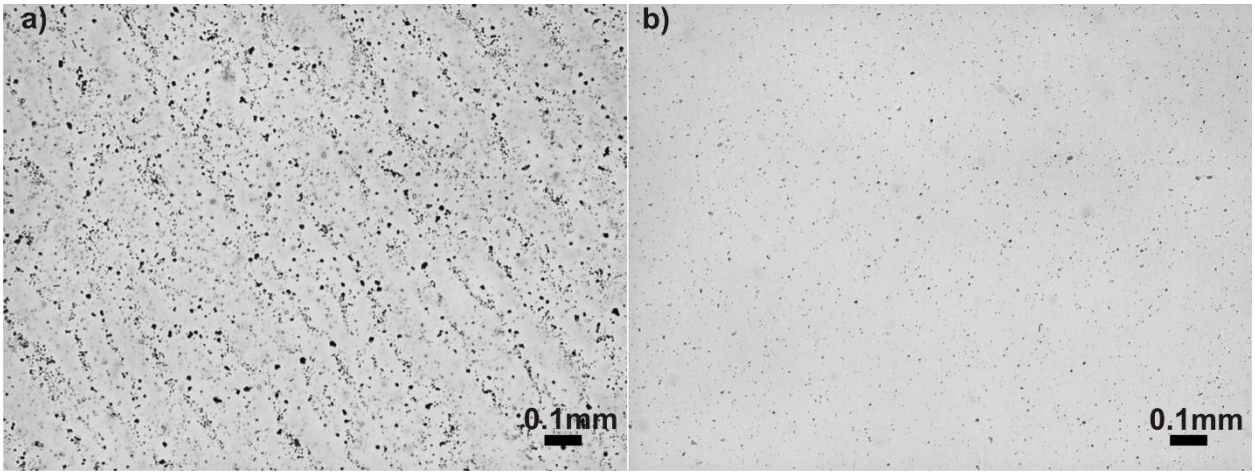

Figure 2. 12 Optical micrographs of 3 at.% W-doped VO_2/PVP coatings on glass (a) with powders calcined at 800 °C for 2 h and (b) with coating calcined at 500 °C for 30 min.

2.4 CONCLUSION

A synthesis strategy was examined for preparing VO_2(M) by reacting ammonium metavanadate with aspartic acid in water under reflux. This simple, green chemistry-based approach was found scalable, giving a reproducible large batch of W-doped VO_2 with a high yield (> 90%). The material exhibited a low transition temperature of 53 °C. The effect of W-doping and PVP on the phase purity of VO_2(M) was investigated. The method required a high 800 °C calcination temperature to synthesize material with a pure monoclinic VO_2 phase. The preparation of W-doped VO_2(M)/PVP coatings on glass with a relative uniform distribution, however in aggregated form,

was achieved at much lower temperatures. It was found that W-doping improved the stability against oxidation in air of the VO_2(M) to a non-switchable material. This is important for practical reasons like shelf-time before usage in a coating. An improvement in the optical properties, luminous transparency and solar modulation, in comparison to recent literature were achieved: $T_{lum,best}$ = 68.30% at 22 °C and $T_{lum,best}$ = 47.6% at 80 °C with an exceptionally high $\Delta T_{sol,best}$ of 20.37%. Consequently, the environmentally friendly synthesized W-doped VO_2 material attained meets for the first time the target criteria for smart windows: a luminous transmittance (T_{lum}) and a solar transmittance modulation efficiency (ΔT_{sol}) exceeding 40% and 10%, respectively [22]. Unfortunately, the critical temperature is not yet close to room temperature.

REFERENCES

1. Chen, R., et al., *Shape-controlled synthesis and influence of W doping and oxygen nonstoichiometry on the phase transition of VO2.* Scientific reports, 2015. **5**: p. 14087.
2. Park, J.H., et al., *Measurement of a solid-state triple point at the metal-insulator transition in VO2.* Nature, 2013. **500**: p. 431-434.
3. Budai, J.D., et al., *Metallization of vanadium dioxide driven by large phonon entropy.* Nature, 2014. **515**(7528): p. 535.
4. Nakano, M., et al., *Collective bulk carrier delocalization driven by electrostatic surface charge accumulation.* Nature, 2012. **487**(7408): p. 459.
5. Li, Y., et al., *Modification of Mott phase transition characteristics in VO2@ TiO2 core/shell nanostructures by misfit-strained heteroepitaxy.* ACS applied materials & interfaces, 2013. **5**(14): p. 6603-6614.
6. Skuza, J., et al., *Electro-thermal control of aluminum-doped zinc oxide/vanadium dioxide multilayered thin films for smart-device applications.* Scientific reports, 2016. **6**.
7. Li, Y., et al., *Core-shell VO2@ TiO2 nanorods that combine thermochromic and photocatalytic properties for application as energy-saving smart coatings.* Scientific reports, 2013. **3**.
8. Chen, S., et al., *The visible transmittance and solar modulation ability of VO 2 flexible foils simultaneously improved by Ti doping: an optimization and first principle study.* Physical Chemistry Chemical Physics, 2013. **15**(40): p. 17537-17543.
9. Zhang, J., et al., *Hydrothermal growth of VO2 nanoplate thermochromic films on glass with high visible transmittance.* Scientific reports, 2016. **6**: p. 27898.
10. Antunez, E., et al., *Porous silicon-VO2 based hybrids as possible optical temperature sensor: wavelength-dependent optical switching from visible to near-infrared range.* Journal of Applied Physics, 2015. **118**(13): p. 134503.
11. Zhang, C., et al., *Simple and facile synthesis W-doped VO2 (M) powder based on hydrothermal Pathway.* Int. J. Electrochem, 2015. **10**: p. 6014-6019.
12. Cao, X., et al., *Solution-based fabrication of VO 2 (M) nanoparticles via lyophilisation.* RSC Advances, 2015. **5**(33): p. 25669-25675.
13. Liang, Z., et al., *Tungsten-doped vanadium dioxide thin films as smart windows with self-cleaning and energy-saving functions.* Journal of Alloys and Compounds, 2017. **694**: p. 124-131.
14. Gao, Y., et al., *Enhanced chemical stability of VO 2 nanoparticles by the formation of SiO 2/VO 2 core/shell structures and the application to transparent and flexible VO 2-based composite foils with excellent thermochromic properties for solar heat control.* Energy & Environmental Science, 2012. **5**(3): p. 6104-6110.
15. Zhao, L., et al., *Solution-processed VO2-SiO2 composite films with simultaneously enhanced luminous transmittance, solar modulation ability and anti-oxidation property.* Scientific reports, 2014. **4**.
16. Mlyuka, N., G. Niklasson, and C.-G. Granqvist, *Thermochromic multilayer films of VO 2 and TiO 2 with enhanced transmittance.* Solar Energy Materials and Solar Cells, 2009. **93**(9): p. 1685-1687.
17. Jin, P., et al., *A VO2-based multifunctional window with highly improved luminous transmittance.* Japanese journal of applied physics, 2002. **41**(3A): p. L278.

18. Mlyuka, N.R., G.A. Niklasson, and C.G. Granqvist, *Thermochromic VO2-based multilayer films with enhanced luminous transmittance and solar modulation.* physica status solidi (a), 2009. **206**(9): p. 2155-2160.
19. Gao, Y., et al., *VO 2–Sb: SnO 2 composite thermochromic smart glass foil.* Energy & Environmental Science, 2012. **5**(8): p. 8234-8237.
20. Cao, Z., et al., *A simple and low-cost combustion method to prepare monoclinic VO2 with superior thermochromic properties.* Scientific reports, 2016. **6**.
21. Wang, N., et al., *Terbium-doped VO2 thin films: Reduced phase transition temperature and largely enhanced luminous transmittance.* Langmuir, 2016. **32**(3): p. 759-764.
22. Wu, X., et al., *Enhancement of VO 2 thermochromic properties by Si doping.* Surface and Coatings Technology, 2015. **276**: p. 248-253.
23. Hu, L., et al., *Porous W-doped VO2 films with simultaneously enhanced visible transparency and thermochromic properties.* Journal of Sol-Gel Science and Technology, 2016. **77**(1): p. 85-93.
24. Zhu, J., et al., *Vanadium dioxide nanoparticle-based thermochromic smart coating: high luminous transmittance, excellent solar regulation efficiency, and near room temperature phase transition.* ACS applied materials & interfaces, 2015. **7**(50): p. 27796-27803.
25. Zhang, J., et al., *Mesoporous SiO 2/VO 2 double-layer thermochromic coating with improved visible transmittance for smart window.* Solar Energy Materials and Solar Cells, 2017. **162**: p. 134-141.
26. Dou, S., et al., *Facile preparation of double-sided VO 2 (M) films with micro-structure and enhanced thermochromic performances.* Solar Energy Materials and Solar Cells, 2017. **160**: p. 164-173.
27. Zhu, J., et al., *Hybrid films of VO 2 nanoparticles and a nickel (ii)-based ligand exchange thermochromic system: excellent optical performance with a temperature responsive colour change.* New Journal of Chemistry, 2017. **41**(2): p. 830-835.
28. Sherigara, B., et al., *Oxidation of L-aspartic acid and L-glutamic acid by manganese (III) ions in aqueous sulphuric acid, acetic acid, and pyrophosphate media: A kinetic study.* International journal of chemical kinetics, 1995. **27**(7): p. 675-690.
29. Booth, J.M. and P.S. Casey, *Production of VO2 M1 and M2 nanoparticles and composites and the influence of the substrate on the structural phase transition.* ACS applied materials & interfaces, 2009. **1**(9): p. 1899-1905.
30. Biesinger, M.C., et al., *Resolving surface chemical states in XPS analysis of first row transition metals, oxides and hydroxides: Cr, Mn, Fe, Co and Ni.* Applied Surface Science, 2011. **257**(7): p. 2717-2730.
31. Hou, Z., et al., *Nitrogen-doped reduced graphene oxide intertwined with V 2 O 3 nanoflakes as self-supported electrodes for flexible all-solid-state supercapacitors.* RSC Advances, 2017. **7**(41): p. 25732-25739.
32. Chen, Y.-F., et al., *The effect of calcination temperature on the crystallinity of TiO 2 nanopowders.* Journal of crystal growth, 2003. **247**(3): p. 363-370.
33. Alivio, T.E., et al., *Postsynthetic Route for Modifying the Metal□ Insulator Transition of VO2 by Interstitial Dopant Incorporation.* Chemistry of Materials, 2017. **29**(12): p. 5401-5412.
34. Fang, B., et al., *Optical properties of vanadium dioxide thin film in nanoparticle structure.* Optical Materials, 2015. **47**: p. 225-230.

35. Lan, S.-D., et al., *Heteroepitaxial TiO 2@ W-doped VO 2 core/shell nanocrystal films: preparation, characterization, and application as bifunctional window coatings.* RSC Advances, 2015. **5**(90): p. 73742-73751.
36. Dong, B., et al., *An abnormal phase transition behavior in VO 2 nanoparticles induced by an M1–M2–R process: two anomalous high (> 68° C) transition temperatures.* RSC Advances, 2016. **6**(56): p. 50521-50528.
37. Li, W., et al., *Preparation and characterization of VO 2 (M)–SnO 2 thermochromic films for application as energy-saving smart coatings.* Journal of Colloid and Interface Science, 2015. **456**: p. 166-173.
38. Song, Z., et al., *Controllable synthesis of VO 2 (D) and their conversion to VO 2 (M) nanostructures with thermochromic phase transition properties.* Inorganic Chemistry Frontiers, 2016. **3**(8): p. 1035-1042.
39. Dong, B., et al., *An intermediate phase (NH 4) 2 V 4 O 9 and its effects on the hydrothermal synthesis of VO 2 (M) nanoparticles.* CrystEngComm, 2016. **18**(4): p. 558-565.
40. Katzke, H., P. Tolédano, and W. Depmeier, *Theory of morphotropic transformations in vanadium oxides.* Physical Review B, 2003. **68**(2): p. 024109.
41. Li, J., C.-y. Liu, and L.-j. Mao, *The character of W-doped one-dimensional VO 2 (M).* Journal of Solid State Chemistry, 2009. **182**(10): p. 2835-2839.
42. Chen, L., et al., *Synthesis of thermochromic W-doped VO 2 (M/R) nanopowders by a simple solution-based process.* Journal of nanomaterials, 2012. **2012**: p. 3.
43. Srirodpai, O., et al., *Preparation, Characterization and Thermo-Chromic Properties of EVA/VO2 Laminate Films for Smart Window Applications and Energy Efficiency in Building.* Materials, 2017. **10**(1): p. 53.
44. Cui, C.-j., et al., *Synthesis and electrochemical performance of lithium vanadium oxide nanotubes as cathodes for rechargeable lithium-ion batteries.* Electrochimica Acta, 2010. **55**(7): p. 2536-2541.
45. Li, W., et al., *Synthesis of VO 2 nanoparticles by a hydrothermal-assisted homogeneous precipitation approach for thermochromic applications.* Rsc Advances, 2014. **4**(25): p. 13026-13033.
46. Ye, J., et al., *Preparation, characterization and properties of thermochromic tungsten-doped vanadium dioxide by thermal reduction and annealing.* Journal of Alloys and Compounds, 2010. **504**(2): p. 503-507.
47. Chen, R., et al., *One-step hydrothermal synthesis of V 1− x W x O 2 (M/R) nanorods with superior doping efficiency and thermochromic properties.* Journal of Materials Chemistry A, 2015. **3**(7): p. 3726-3738.
48. Kang, L., Y. Gao, and H. Luo, *A novel solution process for the synthesis of VO2 thin films with excellent thermochromic properties.* ACS applied materials & interfaces, 2009. **1**(10): p. 2211-2218.
49. Gao, Y., et al., *Nanoceramic VO 2 thermochromic smart glass: a review on progress in solution processing.* Nano Energy, 2012. **1**(2): p. 221-246.
50. Luo, H., et al., *Optical and Structural Properties of Single Phase Epitaxial p-Type Transparent Oxide Thin Films.* advanced Materials, 2007. **19**(21): p. 3604-3607.
51. Jia, Q., et al., *Polymer-assisted deposition of metal-oxide films.* Nature materials, 2004. **3**(8): p. 529.

52. Burrell, A.K., T.M. McCleskey, and Q. Jia, *Polymer assisted deposition.* Chemical Communications, 2008(11): p. 1271-1277.
53. Bai, H., et al., *The preparation of a plasmonically resonant VO2 thermochromic pigment.* Nanotechnology, 2009. **20**(8): p. 085607.
54. Shen, N., et al., *Solid-state-reaction synthesis of VO 2 nanoparticles with low phase transition temperature, enhanced chemical stability and excellent thermochromic properties.* RSC Advances, 2015. **5**(130): p. 108015-108022.
55. Shen, N., et al., *Lowered phase transition temperature and excellent solar heat shielding properties of well-crystallized VO 2 by W doping.* Physical Chemistry Chemical Physics, 2016. **18**(40): p. 28010-28017.
56. Zhao, L., et al., *Solution-processed VO 2-SiO 2 composite films with simultaneously enhanced luminous transmittance, solar modulation ability and anti-oxidation property.* Scientific reports, 2014. **4**: p. 7000.
57. Yang, Y.-S., et al., *Tungsten doped VO 2/microgels hybrid thermochromic material and its smart window application.* RSC Advances, 2017. **7**(13): p. 7758-7762.
58. Wang, N., et al., *Single-Crystalline W-Doped VO2 Nanobeams with Highly Reversible Electrical and Plasmonic Responses Near Room Temperature.* Advanced Materials Interfaces, 2016. **3**(15).

Chapter 3

Hydrothermal synthesis of W- and Mo-doped VO_2 (M) and their Optical Coatings

ABSTRACT

The high yield synthesis of monoclinic vanadium dioxide (VO_2(M)) in a short time with a room temperature transition temperature (T_c) is of interest to design and fabricate VO_2-based smart windows with controlled/ automatically infrared transmission. We report in this work a novel VO_2(M) polymorph synthesis with a batch size of 2g by reducing ammonium metavanadate (NH_4VO_3) with hydrazine using a hydrothermal method followed by a short time heat treatment. Flower-like and stick-shaped morphologies of W(tungsten)-doped VO_2 and Mo(molybdenum)-doped VO_2 particles were obtained, respectively. Tungsten doping was more effective for lowering the phase transition temperature of VO_2 (68 °C) to an ambient temperature (23 °C) compared to molybdenum doping (54.4 °C). Further, a high transition reduction efficiency of 23 K/at. % was attained for W-doped VO_2 crystals. The thermochromic properties of VO_2/PVP (polyvinylpyrrolidone) coatings on glass were investigated with un-doped coatings exhibiting high infrared modulation (up to 35% at 2000 nm), and simultaneously high visible light transmittance (> 62%). However, for the 1at. % W-doped coatings, high infrared modulation obtained (up to 28% at 1500 nm) with visible transmittance (> 75%). This could open an economical way to large-scale VO_2 (M) particles synthesis to produce low cost smart windows.

KEYWORDS: monoclinic vanadium dioxide, VO_2(M), ammonium metavanadate (NH_4VO_3), hydrothermal method, W-doped VO_2, Mo-doped VO_2, transition reduction efficiency, infrared modulation, visible light transmittance, PVP.

3.1 INTRODUCTION

Commercial, residential and institutional buildings consume approximately 40% of total global primary energy mainly by space heating and cooling [1, 2], leading to a high carbon footprint. A substantial share of this energy is lost through windows by means of conduction and radiation. According to the Department of Energy of the United States, between 25-35% of energy in buildings is lost through windows [3]. Saving this energy requires new smart window designs, utilizing the available solar energy. Low emissivity energy efficient products, such as "Low-E" windows, have been developed, but they cannot alter their optical properties (wavelength depended transmission characteristics) in response to environmental temperature changes, thus limiting their energy efficiency [4, 5]. Electrochromic and gasochromic windows have been designed to save energy, but they are not able to intelligently change their optical properties in response to environmental conditions without an externally controlled stimulation [6, 7]. However, thermochromic vanadium dioxide (VO_2) coated windows can automatically control their wavelength dependent transmission in direct response to environmental temperature changes [5]. VO_2 undergoes a reversible first-order semiconductor-metal transition (SMT) at a phase transition temperature (T_c) of 68 °C [8]. When the temperature is below T_c, VO_2(M) is a semiconductor with monoclinic crystalline structure which is transparent to infrared radiation (IR). However, when the temperature is above T_c, VO_2(R) is a metal with rutile tetragonal crystalline structure which is reflective to IR [9]. Vapor-based deposition techniques are used to fabricate VO_2 smart coatings or films, but these methods are expensive and complex due to high cost equipment and the

difficulty to control the various valances of vanadium ions [1]. Thus, solution-based techniques are preferable due to their low cost and scalability. Hydrothermal methods for example, have many advantages, such as low temperature processing, controllable crystalline size, ease of use at industrial scale, utilization of many substrates and being environmentally friendly [1, 4]. However, a T_c of 68 °C is not ideal for application at room temperature. Therefore, T_c of VO_2 needs to be decreased to an ambient temperature for indoor comfort. This can be achieved by doping VO_2 with high valance cations [10], such as $W^{6+,}$ Mo^{5+} and Nb^{5+}. For example, Ji et al. [11] prepared VO_2 films with high optical thermo-chromic properties by implementing a hydrothermal method for coating VO_2 nanoparticles on a high transparency Teflon tape. However, they used a small scale synthesis; only 0.3 g of V_2O_5 was used as precursor (that is highly toxic [4], therefore undesirable for scale-up). Their T_c reduction efficiency by tungsten doping was in the order of 21.96 K/at. %w in the doping range from 0 to 2.5 at. %w [11]. Lianget al. [12] used a one-step hydrothermal synthesis of W-doped VO_2(M) nanorods at 240 °C for 48 h. A good transition reduction efficiency of 24.52 °C/at. %w was obtained, despite only 1.092 g of V_2O_5 being introduced to produce 0.996 g of VO_2 (M) using a 100 mL Teflon-lined stainless steel autoclave [12]. Gonçalves et al. [13] produced VO_2 nanoparticles by hydrothermal synthesis assisted by microwave irradiation in 20 ml of distilled water. However, the final transition temperature obtained was only 49 °C for a 3% WO_3 sample. Lei, et al. [14] used a hydrothermal synthesis at 180 °C for 48 h to fabricate VO_2-based films with a high transition temperature. Here only 0.5 g of NH_4VO_3 precursor was used which is less toxic than V_2O_5[14-16]. Dong et al. [17] also used a small scale hydrothermal reaction (0.25g of V_2O_5) with a W^{6+} dopant efficiency rate of 19.8 K/at%. Chen et al. [2, 18], Shen et al. [19], and Dai et al. [20] synthesized VO_2 with a small batch size in the order of 0.114 g using a 50 mL Teflon-lined stainless steel autoclave.

In this study, the reaction parameters (i.e., concentration, temperature and time) were investigated for the synthesis of VO_2 (M) using a hydrothermal synthetic system by reducing NH_4VO_3 with N_2H_4 in the green solvent, water. The influence of the parameters including calcination temperature and ramping rate were examined on the size, morphology, phase purity, phase transition temperature, latent heat and thermal hysteresis of Mo and W-doped VO_2 (M) with Mo and W contents from 0 to 4 at. % . The optical and thermochromic properties of (0-4 at. %)W-doped VO_2/PVP coated glasses were measured by analyzing the visible and near infra-red transmittance at low (below T_c) and high (above T_c) temperatures. Our objective in this study was to synthesize a large batch of W-doped VO_2(M) under hydrothermal conditions, with high yield and low Tc, providing a high IR switching efficiency in the heat concentrated region of the electromagnetic spectrum (300-1500 nm range). In contrast to other research groups, our experiments utilized a large-batch hydrothermal synthesis of pure-phase VO_2(M) by reacting 3g of non-toxic NH_4VO_3 precursor with hydrazine. Up to 2g of VO_2(M) was produced using a 125 mL Teflon-lined stainless-steel autoclave at 260 °C for 24 h. Hence, we can state that the batch size of VO_2 produced is between 2-18 times more than that obtained by other groups. Additionally, the T_c was lowered to room temperature (17 °C, 21 °C and 23 °C), while the transition reduction efficiency of W-doped VO_2 crystals was 23 K/at. %w, which is comparable with the literature efficiencies. We prepared VO_2/PVP coatings on glass which exhibited excellent thermochromic properties, showing good visible transmittance and high infrared (IR) modulation efficiency. A high infrared modulation of 28% was obtained for W-doped VO_2 at 1500 nm. The presented method is facile, scalable, low cost which can potentially help commercialize the application of VO_2 in smart windows.

3.2 EXPERIMENTAL SECTION

3.2.1 Materials

Ammonium metavanadate (NH_4VO_3, ≥99%, A.C.S. reagent), hydrogen peroxide solution (H_2O_2, 30 wt. % in H_2O, A.C.S. reagent), hydrazine solution (N_2H_4, 35 wt. % in H_2O), tungstic acid (H_2WO_4, 99%) and molybdic acid (H_2MoO_4, ≥ 85.0% MoO_3 basis, ACS reagent) and polyvinylpyrrolidone (PVP, average molecular weight 40 kDa) were purchased from Sigma-Aldrich, Canada. Ultra-high purity Argon (99.9%) was purchased from Praxair, Canada. Anhydrous ethyl alcohol was purchased from Commercial Alcohols, Inc., Canada Microscope glass slides were purchased from VWR International (Radnor, PA, USA). All chemicals were used as received without further purification.

3.2.2 Synthesis of VO_2, W-doped VO_2 and Mo-doped VO_2 particles

Briefly, 2.5 mL (0.48 mol/L) of 30 wt. % H_2O_2 was added dropwise to an aqueous solution containing 3.0 g (0.50 mol/L) of NH_4VO_3 and 47.5 mL of deionized water. The orange solution turned viscous after stirring at room temperature for 24 h. After that, 1 mL (0.22 mol/L) of 35 wt. % N_2H_4 was added dropwise to the above viscous solution, and after 20 min, a rigorous bubbling occurred while the solution turned to black, indicating reduction of vanadium (V) to vanadium (IV). For the synthesis of W-doped VO_2 or Mo-doped VO_2 particles, various amounts of H_2WO_4 or H_2MoO_4 were added into the black solution. The black solution, whether doped or not, was hydrothermally treated at 260 °C for 24 h in a 125-mL of Teflon-lined stainless-steel autoclave. Subsequently, the black product was isolated from the reaction mixture by centrifugation, washed with water and ethanol, then dried in a vacuum oven at 60 °C overnight. The dried powder was further calcined at 450 °C or 650 °C under argon gas for 1 h in a tube furnace prior to

characterization (yield > 89%). The expected chemical reduction of vanadium (V) to vanadium (IV) is shown in the reaction equation (3.1).

$$4\ NH_4VO_3 + N_2H_4 \rightarrow 4\ VO_2 + N_2 \uparrow + 4\ NH_3{\bullet}H_2O \qquad (3.3)$$

3.2.3 Fabrication of VO_2(M) and $W_xV_{(1-x)}O_2$(M) based coatings

To prepare coatings on glass slides, 0.16 g of VO_2(M) or of W(1-4 at. %)-doped VO_2(M) particles (calcined at 450 °C) were dispersed in 2 mL of ethanol in a small vial, to which 0.08 g of PVP was added followed by sonication at 50 °C for 60 min. Subsequently, 0.3 - 0.5 mL of the above VO_2/PVP solution was spin coated at 1500 rpm (revolutions per minute) for ca. 10 s onto a glass slide. The coating (thickness ~200 nm) samples were dried in a vacuum oven at 80 °C for 30 min.

3.2.4 Characterization

The crystallinity of the synthesized VO_2 particles was examined by X-ray diffraction (XRD; Bruker D2 phaser powder diffractometer, Billerica, MA, USA) using Cu Kα radiation ($\lambda_{K\alpha}$ = 1.54059 Å) with a scanning rate of 0.25°/second. The 2θ data was collected between 10° and 80° using a continuous scanning mode. The transition temperatures of VO_2 were determined by differential scanning calorimetry (DSC; SDT Q600, TA Instruments, USA) using a cooling-second heating-cycle between 0-90 °C. The data were analyzed via the instrument's software (Universal Analysis 2000, TA Instruments, USA). The optical transmittance was measured using a Shimadzu UV-3600 UV-Vis-NIR (Shimadzu, Kyoto, Japan) spectrophotometer in the wavelength range of 250 – 2500 nm. The temperature was controlled using a Julabo F12-Refrigarated/Heating Circulator (Julabo GmbH, Seelbach, Germany). The infrared modulation at wavelengths 2000 nm and at 1500 nm can be obtained from equation $\Delta T(\lambda)=T(\lambda)_s-T(\lambda)_m$ [21], where s and m represent the semiconductor (at 22 °C) and metal (80 °C) phases, respectively. Scanning electron

microscopy (SEM, Quanta 200) was used to study the morphologies and dimensions of the particles. The particle aggregates in the polymer coating on glass substrates were investigated using a Hitachi S-4500 field emission SEM (Hitachi, Tokyo, Japan). Elemental analysis of the samples was studied using energy dispersive X-ray spectrometry (EDX) combined with scanning electron microscopy (SEM, Quanta 200). A Veeco MultiMode V (Veeco, Plainview, N, USA) atomic force microscope (AFM) was used to image the surface topography of VO_2 coatings and to measure the thickness of the coatings via the Nanoscope V7.30 software. The particle sizes of VO_2 particles were measured using the Malvern Zeta-sizer Nano-ZS (Dynamic Light Scattering instrument (Malvern, UK).

3.3 RESULTS AND DISCUSSION

3.3.1 Characterization of VO_2 particles

The reaction parameters (i.e., concentration, temperature and time) were investigated for the synthesis of VO_2 (M) by reducing NH_4VO_3 with N_2H_4 in aqueous solution. Various concentrations of NH_4VO_3 (0.33, 0.50, 0.67 and 0.83 mol/L), N_2H_4 (0.22, 0.42 and 0.62 mol/L) and H_2O_2 (0, 0.48 and 0.96 mol/L) as a function of N_2H_4 (0.22 mol/L), NH_4VO_3 (0.50 mol/L) and ((N_2H_4 (0.22 mol/L), NH_4VO_3 (0.50 mol/L)), respectively were examined for the synthesis of VO_2(M) as shown by XRD (Figure 3.1a-c). All samples in Figure 3.1 were calcined at 650 °C for 1 h. A rigorous bubbling during nitrogen release with a color change from white (without H_2O_2) to black solution was observed after adding N_2H_4, indicating reduction of vanadium (V) to vanadium (IV) [11]. As identified by XRD (Figure 3.1a), only the characteristic peaks of NH_4VO_3 (0.50 and 0.67 mol/L) samples agree with those of VO_2(M) (JCPDS card no. 82-0661) [22], exhibiting a latent heat of 35 J/g and 33 J/g, respectively. The Bragg peaks of VO_2 (M) are indexed by stars (*). As for Figure 3.1b, a good crystallinity phase of VO_2(M) was only obtained for the N_2H_4 (0.22 mol/L) sample. To control the valance of vanadium and produce a vanadium precursor solution ($NH_4VO_3.nH_2O$) with uniform reduction, various concentrations of H_2O_2 (0, 0.48 and 0.96 mol/L) were examined as presented by XRD (Figure 3.1c) [11]. Notably, only minor oxygen release was observed when H_2O_2 was first added to an aqueous solution of NH_4VO_3 due to the decomposition of H_2O_2 while forming the V(V) peroxo complexes [11]. As shown in Figure 3.1c, additional reflection peaks were presented in the XRD pattern of the H_2O_2 (0 mol/L) sample corresponding to VO_2(B) phase (JCPDS data card 01-081-2392) [23]. However, when H_2O_2 (0.48 mol/L) was added, the VO_2(B) phase disappeared and the latent heat increased from 35 J/g to 39 J/g, respectively. The Bragg peaks of VO_2 (M) are indexed by stars (*) and the ones from VO_2(B) by triangles (Δ). Meanwhile,

the intensity of the diffraction peaks at high concentration of H_2O_2 (0.96 mol/L) decreased tremendously due to low crystallinity. Various reaction temperatures (140 °C, 200 °C and 260 °C) were examined for 1 day, however, a good VO_2(M) phase was only obtained at 260 °C (Figure 3.1e). Since a high purity VO_2(M) phase can only be synthesized at 260 °C with NH_4VO_3 (0.50 mol/L), N_2H_4 (0.22 mol/L) and H_2O_2 (0.48 mol/L) concentrations, this reaction conditions were chosen to be continued for a more in-depth examination. Figure 3.1d provides the XRD patterns of VO_2(M) for the reaction times 1, 3 and 6 days. The latent heat of SMT increased from 35 J/g to 50 J/g and 52 J/g with increasing reaction time from 1day to 3 and 6 days, respectively. This change is attributed to a high crystallinity at longer reaction times [24]. Further, as the reaction time increases from 1day to 3 and 6 days, the width of the XRD diffraction peaks compressed, and the size of particles increased from 174 nm(±0.21) to 210 nm(±0.26) and 308 nm(±0.4), respectively.

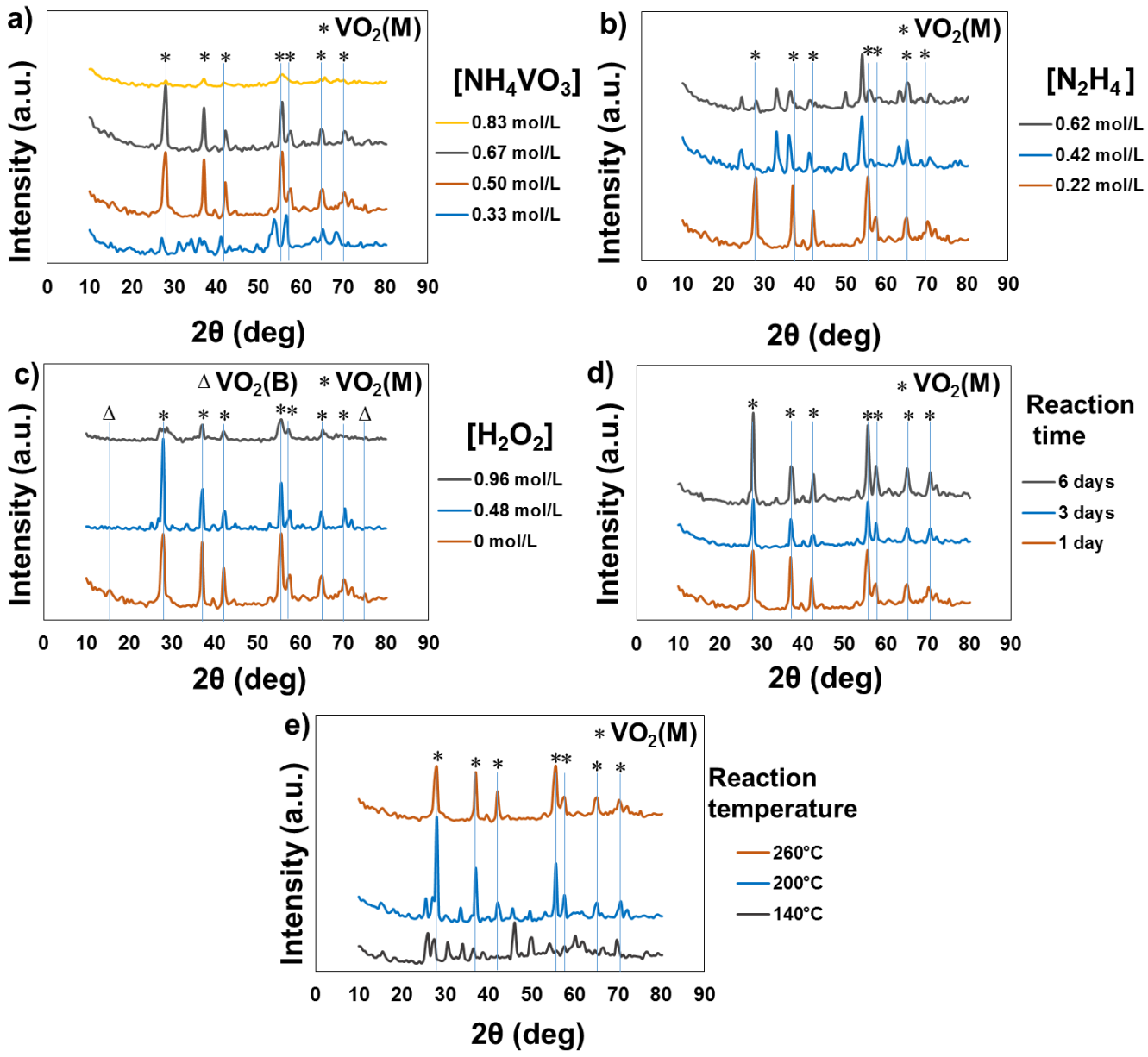

Figure 3. 1 XRD spectra of VO_2 (M) annealed at 650 °C for 1 h with variable reaction parameters. (a) Various concentrations of NH_4VO_3 as a function of N_2H_4 (0.22 mol/L), (b) various concentrations of N_2H_4 as a function of NH_4VO_3 (0.50 mol/L), and (c) various concentrations of H_2O_2 as a function of N_2H_4 (0.22 mol/L) and NH_4VO_3 (0.50 mol/L). Reaction of NH_4VO_3 (0.50 mol/L) with N_2H_4 (0.22 mol/L) at various (d) times and (e) temperatures.

The influences of the calcination parameters including temperature and ramping rate on the size, morphology and phase purity of Mo and W-doped VO_2 (M) with various nominal Mo and W contents from 0 to 4 at. % were investigated. W-doped VO_2 and Mo-doped VO_2 particles were synthesized by adding H_2WO_4 and H_2MoO_4, respectively. The XRD spectrum of VO_2 after calcination at different temperatures and ramping rates containing various amounts of tungsten (0 -4 at. %) are shown in Figure 3.2. Most diffraction peaks in Figure 3.2a are indexed to the crystal planes of VO_2 (M) [22]. In the spectra of W-doped VO_2 (1 at. %, 2 at. % and 4 at. %), some peaks of VO_2 (B) are detected. The reason for the appearance of the VO_2 (B) peaks is due to the low utilized annealing temperature of 450 °C with a low ramping rate of 10 °C/min. When the ramping rate was increased to 20 °C/min, the number of VO_2 (B) peaks decreased. Only a few VO_2 (B) peaks are seen for the 2 and 4 at. % W-doped samples (Figure 3.2b). Essentially, VO_2 (B) is a precursor of VO_2 (M). It can be transformed into VO_2 (M) if calcined at higher temperatures under inert gas [25]. As seen in Figure 3.2c, when the annealing temperature was increased to 650 °C, the XRD peaks for samples at all tungsten concentrations could be indexed to a pure VO_2 (M) phase. As seen in the enlargement of the (011) diffraction peak between 26° and 30° (Figure 3.2d-f), there is no effect on the spectral position of the diffraction peaks at low tungsten concentration (1 at. %). However, with increasing tungsten concentration, the (011) diffraction peak shifted slightly toward lower angles. When the W concentration was increased, more substitution of W for V ions occurred in the VO_2 (M) lattice. Since the radius of V cations (V^{4+} for 6-coordinate) is 58 pm, and that of W cations (W^{6+} for 6-coordinate) is 60 pm, the interplanar distance in the W-doped VO_2 must expand and the diffraction peaks shift to smaller angles [26, 27]. Hence the observed shifting of XRD spectra toward lower angles according to Bragg's law [$d = \lambda/(2\sin\theta)$] suggests a successful W-doping into the VO_2 (M) crystal lattice [26].

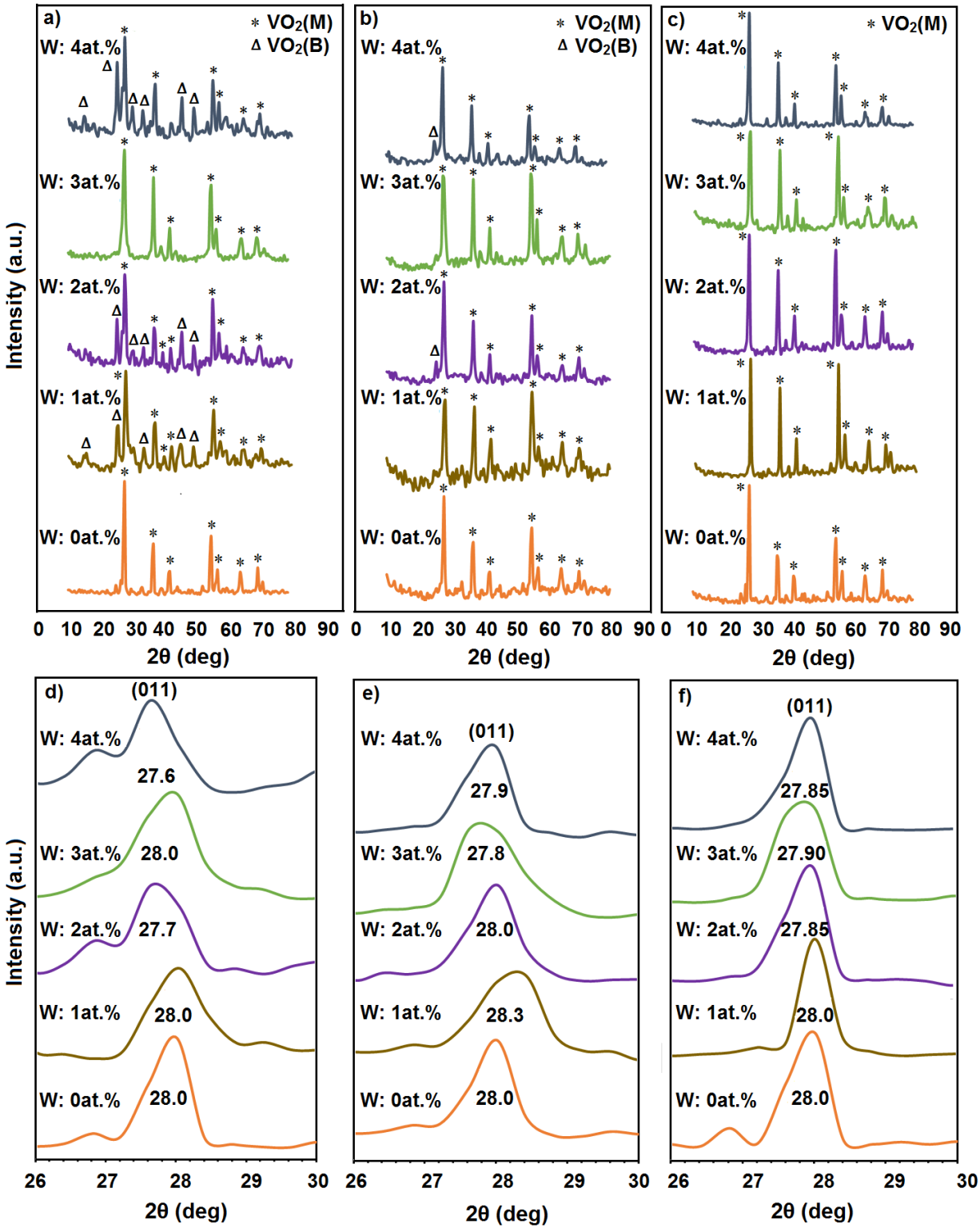

Figure 3.2 XRD spectra of VO_2 (M) with nominal contents of W (0 - 4 at. %). (a) Annealed at 450 °C with ramping rate of 10 °C/min, (b) annealed at 450 °C with ramping rate of 20 °C/min, and (c) annealed at 650 °C with ramping rate of 20 °C/min. Enlarged (011) diffraction peak

between 26° and 30° for VO_2 (M) with W concentrations 0 -4 at. %. (d) Annealed at 450 °C with ramping rate of 10 °C/min, (e) annealed at 450 °C with ramping rate of 20 °C/min, and (f) annealed at 650 °C with ramping rate of 20 °C/min.

Despite the success with the higher calcination temperature to synthesize W-doped VO_2 (M), the same calcination condition (650 °C) did not lead to a conversion of VO_2 (B) into VO_2 (M) for the Mo-doped VO_2; a significant quantity of VO_2 (B) phase remained (Figure 3.3).

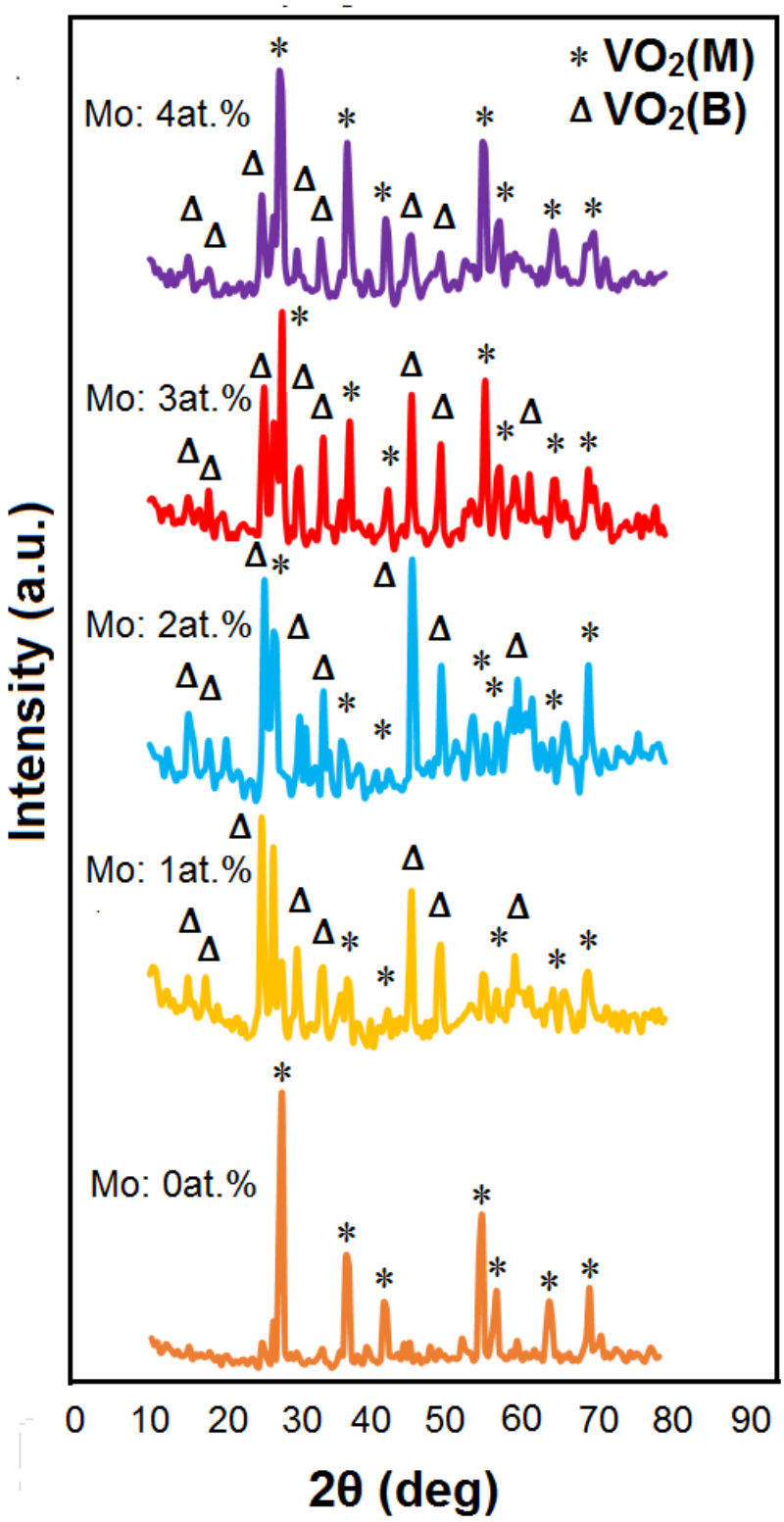

Figure 3.3 XRD pattern of VO_2(M) with nominal contents of Mo (0-4 at. %) after calcination at 650 °C with a ramping rate of 20 °C/min.

The XRD spectra of VO_2 with Mo-doping concentrations of 0-4 at. % after annealing at 450 °C with a ramping rate of 10 °C/min are shown in Figure 3.4a. The diffraction peaks can be indexed to the known crystal planes of VO_2 (M) [22]. However, there were some diffraction peaks of VO_2 (B) detected for all Mo concentrations (except for Mo: 2 at. %). Surprisingly, the VO_2 (B) phase decreased with increasing Mo concentration (the number of VO_2 (B) phase peaks decreased with increasing concentration). Overall, the remains of VO_2 (B) phase is much less than that of 650 °C. The enlarged (011) diffraction peaks for the different Mo concentrations are shown in Figure 3.4b. The Mo-doping shows only a small effect on the spectral position of the peak. Only the highest concentration of 4 at. % led to a slight shift to smaller angles: an increased interplanar distance. According to Shannon. [27] the radius of molybdenum cations (Mo^{6+} for 6-cooordinate) is 59 pm. This Mo-cation radius is less than that of the W-cation but still larger than that of V cation, leading to an increased interplanar distance.

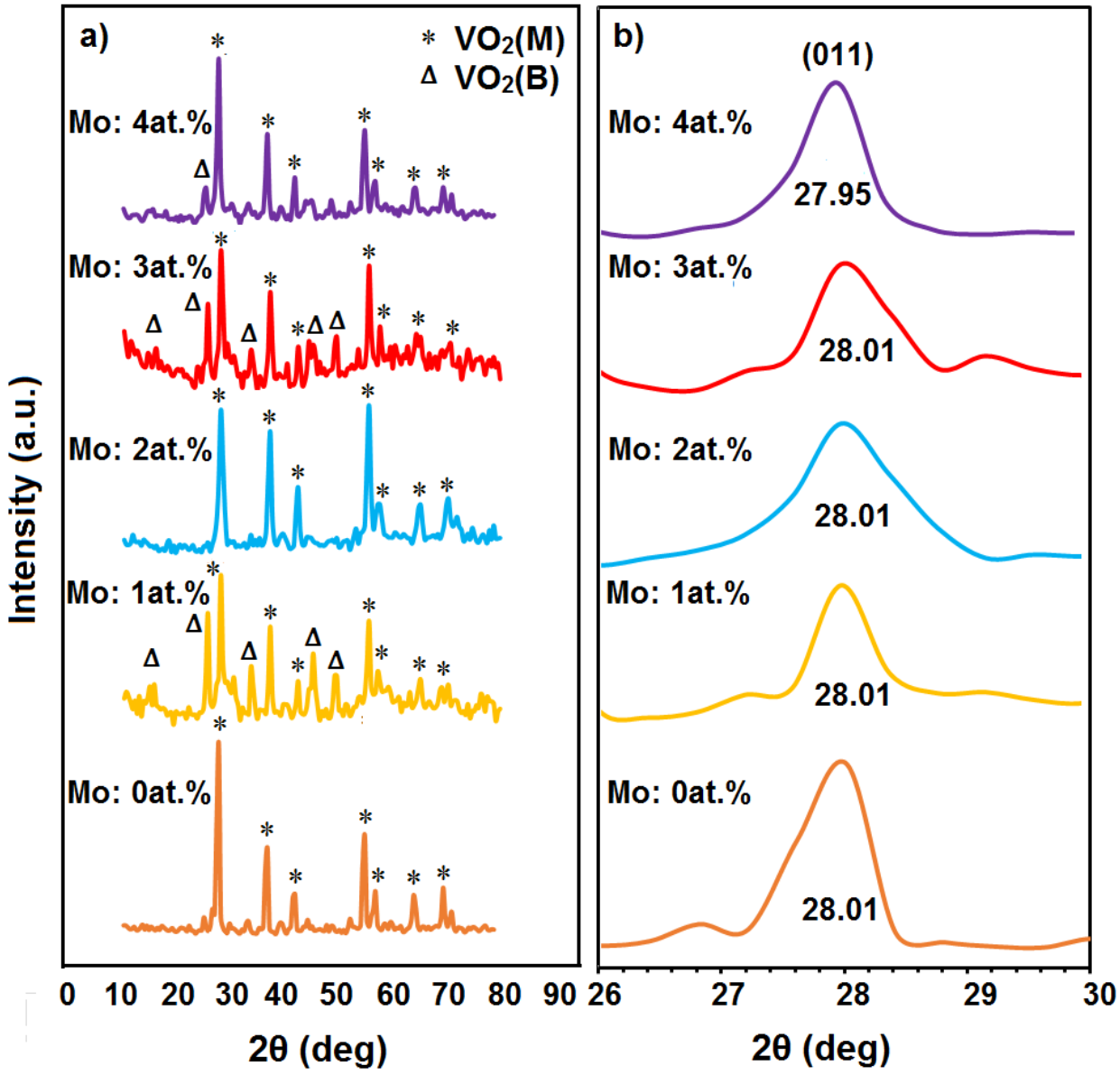

Figure 3.4 XRD patterns of VO_2(M) with nominal contents of Mo (0-4 at. %) after annealing at 450 °C and ramping rate of 10 °C/min. (a) Full XRD pattern, and (b) enlargement of the (011) diffraction peak between 26° and 30°.

SEM images (Figure 3.5) show the morphology of un-doped (Figure 3.5a-c) and W-doped (Figure 3.5d-f) VO_2 particles calcined at different temperatures. The SEM images show materials with nanoscopic structures. These images show that both calcination and W-doping change the

overall appearance. The 450 °C calcination of the un-doped VO_2 leads to the disappearance of the flaky agglomerate structures and to the appearance of a nano-stick agglomerate structure. The most obvious morphology change appeared with the annealing of the un-doped material at 650 °C. A substantial increase in the size of the "individual" nanoobjects and a clear appearance of crystallinity is observed (Figure 3.5c). This nanoobject size growth due to a high annealing temperature mainly by Ostwald-ripening (dissolution of small grains and re-precipitation onto large grains) agrees well with the results obtained by Yueyan et al. [28]. Completely different morphologies were obtained for the W-doped VO_2. Flaky structures are seen for the un-calcined W-doped VO_2 (Figure 3.5d). This flaky morphology did not change when annealed at 450 °C (Figure 3.5e). However, at a 650 °C calcination, a flower like structure with lots of individual crystalline needles was obtained (Figure 3.5f). We assume that the differences in morphology stems from the W-doping. The size of the W-doped VO_2 nanoobject is decreased due to reduction in crystallization ability for these particles with W-doping (i.e., intensified heterogeneous nucleation process) [10, 29]. Semi-crystalline structure with un-identified peaks were obtained for the un-calcined non-doped VO_2 and 3% W-doped VO_2 as shown by XRD spectra in Figure B1.

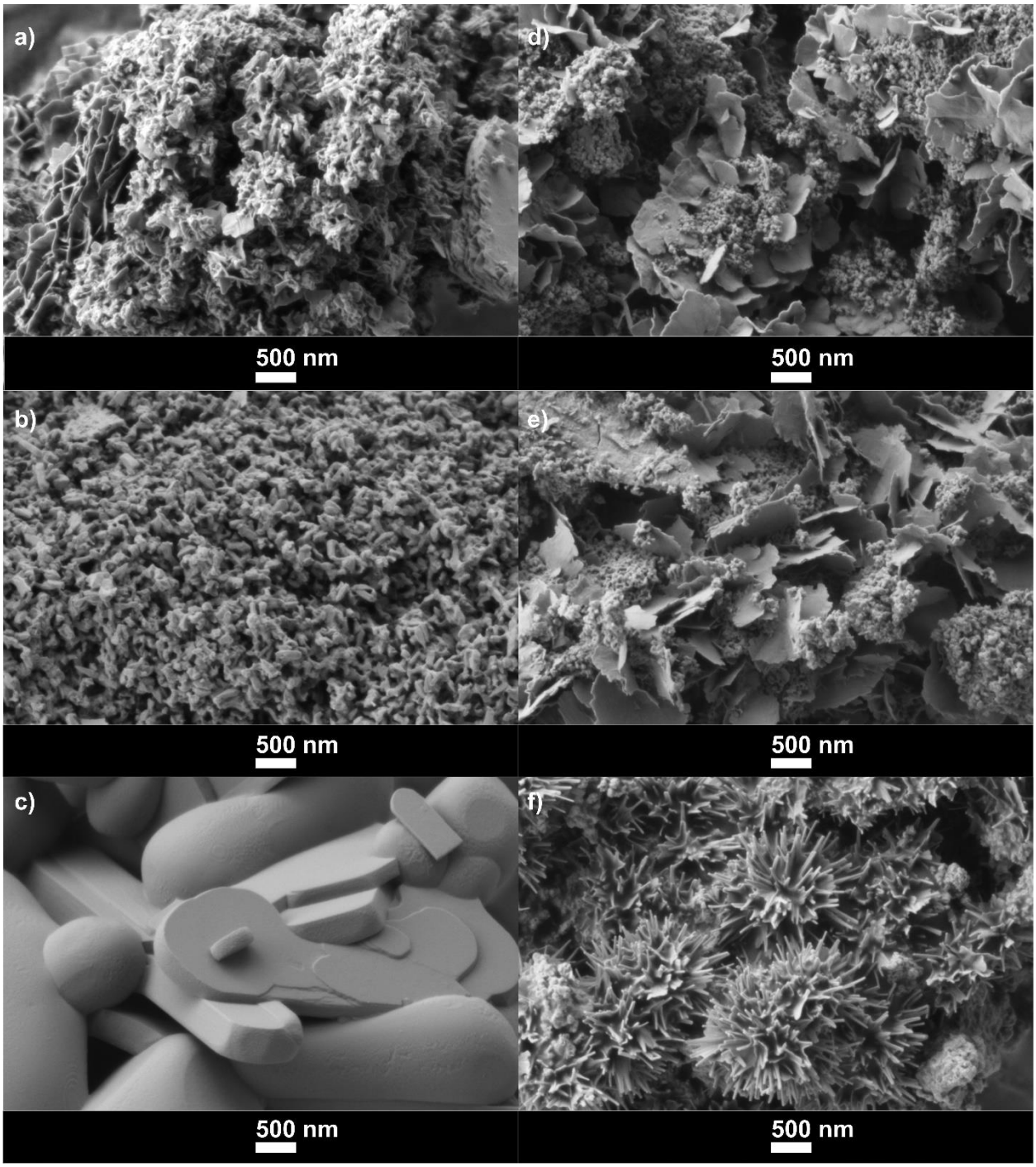

Figure 3.5 SEM images of un-doped and W-doped VO_2 particles at different calcination temperatures. (a)VO_2 before calcination, (b) VO_2 (M) after calcination at 450 °C and (c) at 650 °C. (d) 3 at. % W-doped VO_2 before calcination, (e) 3 at. % W-doped VO_2 after calcination at 450 °C, and (f) at 650 °C.

The presence and amount of V, W, and O in the synthesized materials was confirmed by quantitative EDX analysis (Figure 3.6). V and O peaks appeared in all samples, both doped and un-doped VO_2. The existence of stoichiometric VO_2 was confirmed by the intensities of the major peaks of V and O for un-doped VO_2 (Figure 3.6a). Tungsten was found present for all W-doped VO_2 samples. As an example, Figure 3.6b shows an EDX spectrum of a 3 at. % W-doped VO_2 sample. The real doping concentrations, c(W), of all W-doped samples are summarized in Table 3.1.

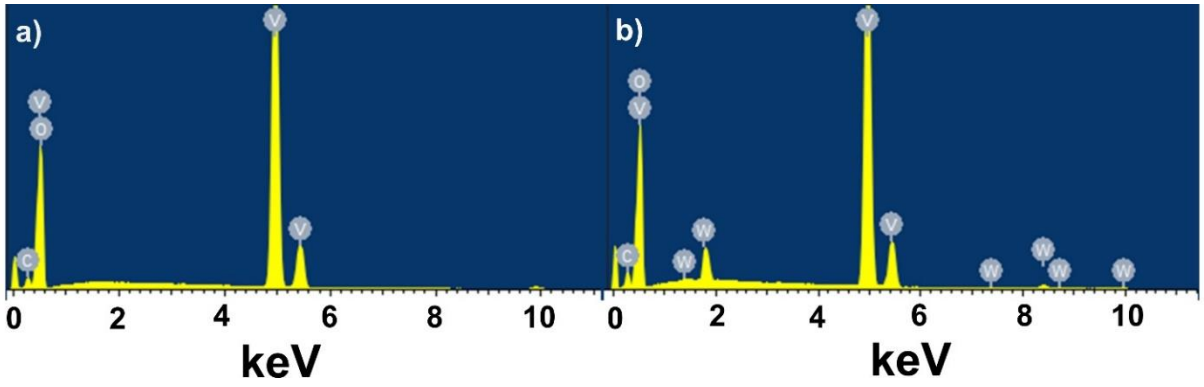

Figure 3.6 EDX spectra for (a) un-doped VO_2 and (b) 3 at. % W-doped VO_2.

Table 3.1 Real W and Mo concentrations, c, for doped VO_2 at different nominal contents (quantitative EDX data).

Nominal content [at.%]	c(W) [at.%]	c(Mo) [at.%]
0	0.0±0	0.0±0
1.0	1.10±0.1	0.34±0.0
2.0	1.59±0.2	0.39±0.0
3.0	2.73±0.1	1.10±0.1
4.0	3.30±0.2	1.31±0.1

For the Mo doped samples, SEM images of 3 at. % Mo-doped VO_2 are shown in Figure 3.7. The morphology is different from the W-doped VO_2. The SEM image shows an agglomerate of needle

like-structures. This needle-like morphology may limit the dispersity of particles, leading to light scattering, hence, negatively impacting the optical performance of the film. Surprisingly, there is no difference in the morphologies for the Mo-doped VO_2, calcined or not, besides that the average length of the needles is smaller for the calcined material (Figure 3.7b). Mo doping was confirmed by quantitative EDX via the representative peaks of Mo as shown in Figure 3.8. The real concentrations of Mo, c(Mo), for all Mo-doped samples are summarized in Table 3.1. It was found that a much lower Mo was present at a given nominal content in comparison to the W-doped samples (Table 3.1). Mo-doping was less effective than W-doping using this synthetic strategy.

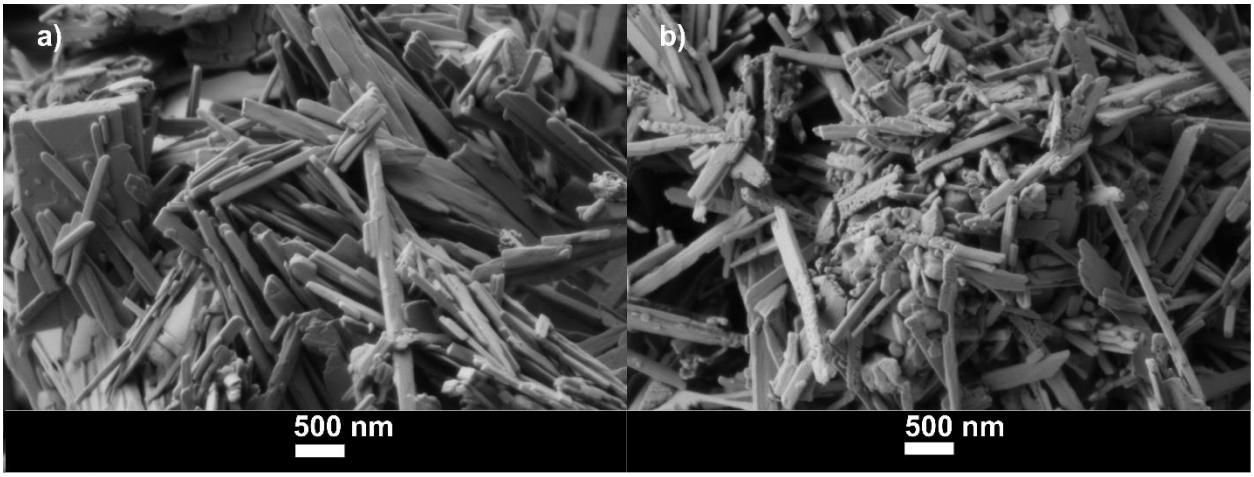

Figure 3.7 SEM images of 3 at. % Mo-doped VO_2: (a) before calcination, and (b) after calcination at 450 °C.

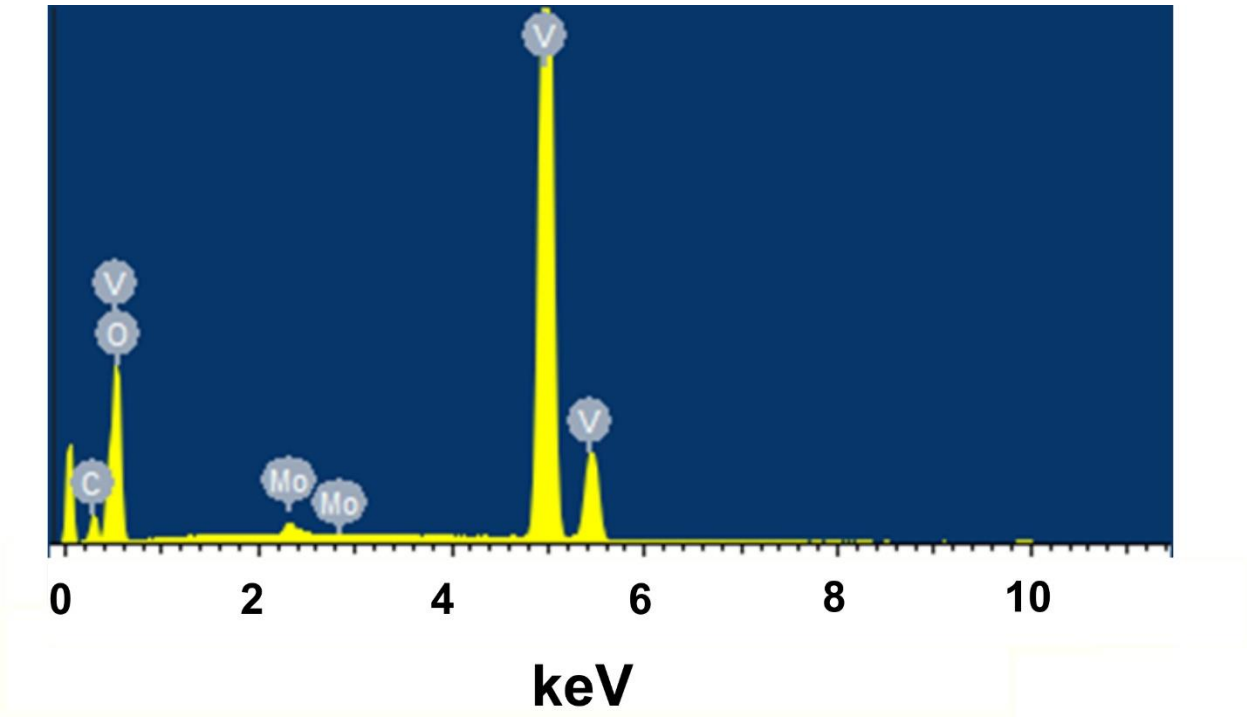

Figure 3.8 EDX spectrum for 3 at. % Mo-doped VO_2.

The average size of W-doped VO_2 particles was obtained using light scattering (Table 3.2). For this purpose, the materials were dispersed in distilled water and ultrasonicated for 10-15 min to "dissolve" the agglomerates and yield individual objects. The average particle size decreased with increasing W concentration from 0 to 3 at. %, but increased substantially for the 4 at. % sample, likely due to an enhanced heterogeneous nucleation process by doping with W [10, 30, 31].

Table 3.2 Average size of W-doped VO_2 particles with nominal W content (annealed at 450 °C with ramping rate of 10 °C/min). Polydispersity Index (PdI).

W content [at. %]	Average size (nm)	Average PdI
0	261.4±0.8	0.310±0.015
1	222.4±0.5	0.289±0.019
2	194.4±2.0	0.289±0.017
3	185.4±0.2	0.400±0.008
4	259.1±2.7	0.433±0.005

3.3.2 Thermochromic Properties of VO_2 particles

The effects of the calcination parameters including temperature and ramping rate on the phase transition temperature, latent heat and thermal hysteresis of Mo and W-doped VO_2 (M) were investigated using Mo and W contents from 0 to 4 at. %. The desirable temperature for human comfort is in the range of 20–25 °C while the transition temperature (T_c) of VO_2 can be lowered to this range when doped with metal ions, such as W^{6+}, Mo^{6+} and Nb^{5+} [32]. On a per-atomic-percent-basis, W ions are well known to be the most effective dopant to decrease T_c of VO_2 to ambient temperature. DSC data of W-doped VO_2 (M) with various nominal W contents from 0 to 4 at. % are shown in Figure 3.9 with respect to calcination temperature and ramping rates. W-doped VO_2 (M) materials which are annealed at 450 °C with ramping rate of 10 °C/min, showed a continuous endothermic T_c decline from 68 °C to 20 °C with increasing nominal W content (0 to 3at. %, Figure 3.9a). When a nominal W content of 4 at. % was reached, the endothermic T_c increased slightly back to 23 °C. This behavior is attributed to the average particle size (Table 3.2) which depicts the same trend as T_c. In the pure VO_2 sample annealed at 450 °C (Figure 3.9a), two endothermic phase transition peaks appear. This effect is ascribed to size effects, shape-dependences and interfacial defects [33]. Coexistence of two different size populations of VO_2 particles is shown by SEM image in Figure 3.10 after calcination at 450 °C. VO_2 (M) is considered as an excellent candidate for application in smart window design and production as long as the T_c is < 40 °C [26]. Upon increasing the ramping rate to 20 °C/min while maintaining the calcination temperature at 450 °C, a sharp endothermic peak at 69 °C for T_c is observed for un-doped VO_2 (Figure 3.9b) which decreased to 15.6 °C with increasing W concentration (0-3 at. % samples). A slight increase to 21 °C is observed for the 4 at. % sample. The 650 °C calcination data shows a continuous decrease of T_c from 68 °C to 17 °C along the entire W concentration range (Figure

3.9c). At 650 °C calcination, T_c continuously decreased upon increasing W content due to size reduction of particles with W doping up to 4 at. %. T_c is also depended on the ramping rate: T_c decreased with increasing ramping rate (Figure 3.9b). Increasing the calcination temperature also decreased T_c (Figure 3.9c) with the exception of the 3 at. % sample. The causes for lowering T_c of W-doped VO_2 with increasing calcination temperature is attributed to the higher crystallinity (Figure 3.2), a lower energy band gap [34] and higher real W concentration (i.e., 3.30 at. % at 450 °C and 3.70 at. % at 650 °C for W 4.0 at. % sample).

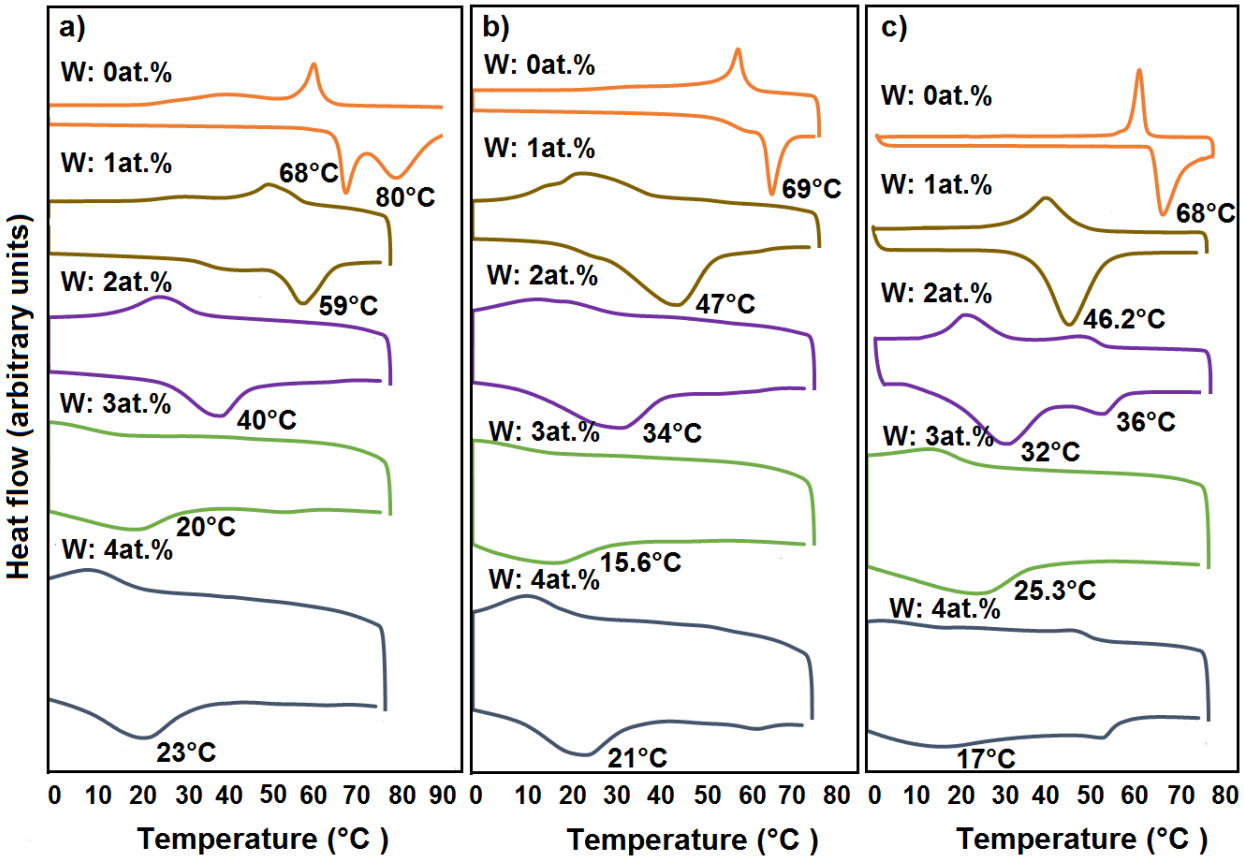

Figure 3.9 DSC data of VO_2(M) with nominal contents of W (0-4 at. %). (a) Annealed at 450 °C with ramping rate of 10 °C/min, (b) annealed at 450 °C with ramping rate of 20 °C/min and (c) annealed at 650 °C with ramping rate of 20 °C/min. All DSC measurements are in the same y-scale.

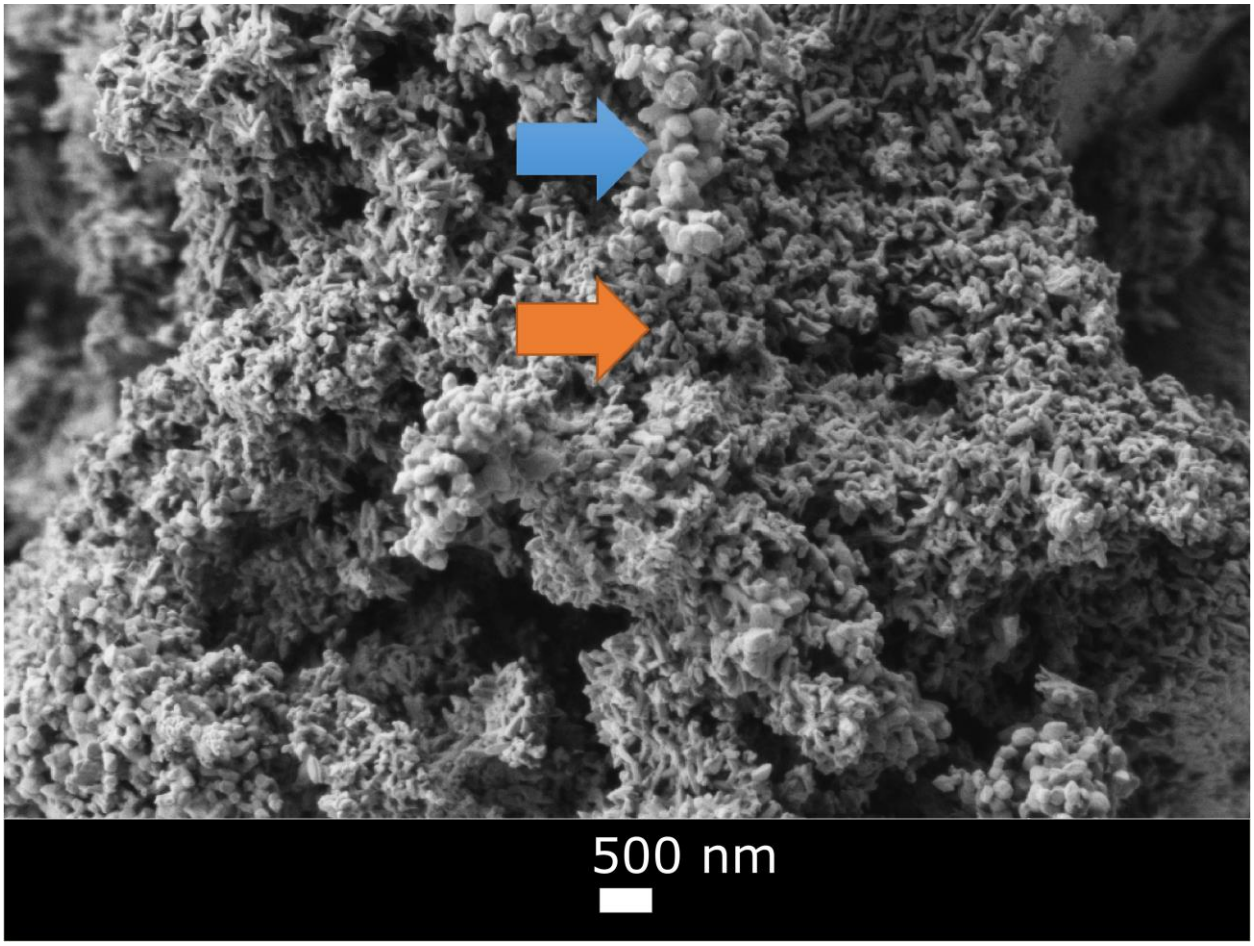

Figure 3.10 SEM image for un-doped VO_2. Existence of VO_2 particles with larger size are emphasized by blue arrow and smaller size by orange arrow.

Despite the significant improvement in reducing T_c by W-doping, increasing the W concentration (1-4 at. %) decreased the latent heat from 10, 29 and 41 J/g to 7.4, 8 and 3 J/g, respectively (Table 3.3), agreeing with Shenet al. [35]. This effect is probably due to less crystallinity [24] with doping enhancement upon inspection of the XRD spectra (Figure 3.2). An annealing temperature increase from 450 °C to 650 °C led to a latent heat increase for the W-doped VO_2 samples, with the exception of the 4 at. % sample. The reason for the high latent heat suggests

that the VO_2 particles with 0-3 at. % W-doping are highly crystalline in their crystalline structure when annealed at 650 °C [24].

Table 3.3 Latent heat (J/g) of VO_2 at different nominal W content, ramping rates and calcination temperatures.

W content [at. %]	0	1	2	3	4
calcination at 450°C, ramping rate at10°C/min	7.0, 8.5	10.0	11.0	7.6	7.4
calcination at 450°C, ramping rate at 20°C/min	9.2	29.0	11.0	4.5	8.0
calcination at 650°C, ramping rate at 20°C/min	39.0	41.0	12.0	11.8	3.0

For VO_2 thermochromic window coating applications, a narrow thermal hysteresis, ΔT_c, is required. Thermal hysteresis here is meant as the difference between endothermic and exothermic DSC peak position. In other words, it is the difference between the transition temperatures during the heating and cooling cycles, respectively. This is important to allow a fast response to temperature change. The thermal hysteresis rises from 7.2 °C to 23.6 °C and from 7.1 °C to 18.9 °C when the W concentrations increase to 3 at. % (Table 3.4). The increase in thermal hysteresis with increasing W concentration can be explained by an enhancement in the number of defects in the crystals when calcined at a low temperature. At the highest W concentration (4 at. %), the hysteresis declines substantially for the 450 °C samples. We assume this is caused by the relative larger size of the particles (Table 3.2); hence, a smaller number of defects should exist, what is in agreement with Lopez's work [36, 37]. A similar rise behavior for the thermal hysteresis with increasing W concentration is observed for the 650 °C samples (Table 3.4, except 1 at. %). In general, a smaller thermal hysteresis is obtained at 650 °C annealing in comparison to the 450 °C annealing (except for 4at. %), again, due to reduced number of defects at high annealing

temperature for bigger particles. The reason for lower T_c at 650 °C than 450 °C annealing is due to better W integration at 650 °C.

Table 3.4 Thermal hysteresis, ΔT_c(°C) of VO_2 at different W concentrations, ramping rates and calcination temperatures.

W content [at. %]	0	1	2	3	4
calcination at 450°C, ramping rate at10°C/min	7.2	8.0	13.7	23.6	12.2
calcination at 450°C, ramping rate at 20°C/min	7.1	22.0	16.0	18.9	8.1
calcination at 650°C, ramping rate at 20°C/min	5.4	4.3	8.7	9.8	14.0

It has been previously reported that Mo doping can be effective for depressing the T_c of VO_2 [38]. DSC data for VO_2(M) with nominal Mo contents 0-4 at. % are shown in Figure 3.11a upon calcination at 450 °C with a ramping rate 10 °C/min. Also in the case of Mo, T_c decreased, but only from 68 °C to 64.5 °C and 55.4 °C when the Mo content increased to 1 at. % and 2 at. %, respectively. This is accompanied by a particle size reduction (Table 3.5). However, T_c increased to 60.5 °C and 59 °C when Mo-doping reached concentrations of 3 and 4 at. %, due to a particle size increase (Table 3.5). DSC data of VO_2(M) with increasing Mo concentration upon calcination at 650 °C with ramping rate 20 °C/min (Figure 3.11b) show a decrease in T_c to 62.5 °C at 4 at. %. The reasons for the higher T_c values of the Mo-doped VO_2(M) samples in comparison to the W-doped VO_2(M) material lies in the overall smaller real Mo concentration (Table 3.1). Table 3.6 summarizes the latent heat increase with increasing Mo-doping concentration. This behavior is opposite to the latent heat development in W-doped VO_2 (Table 3.3). The inversed latent heat change is probably due to lower Mo concentration (Table 3.1). Besides some deviation, the thermal hysteresis of Mo-doped VO_2 also increased with Mo concentration up to 2 at. %; with the two highest doping concentrations the hysteresis decreased (Table 3.7). A smaller thermal hysteresis

was achieved at 650 °C compared to 450 °C calcination temperature. Again, defects through doping are attributed for this behaviour. Overall, lower thermal hysteresis values were obtained for Mo-doped VO_2 (except for Mo 2 at. %) than for W-doped VO_2, leading to the conclusion that less defects exist in the Mo-doped VO_2 particles. This is not surprising, given the lower real concentration and the smaller ion-radius.

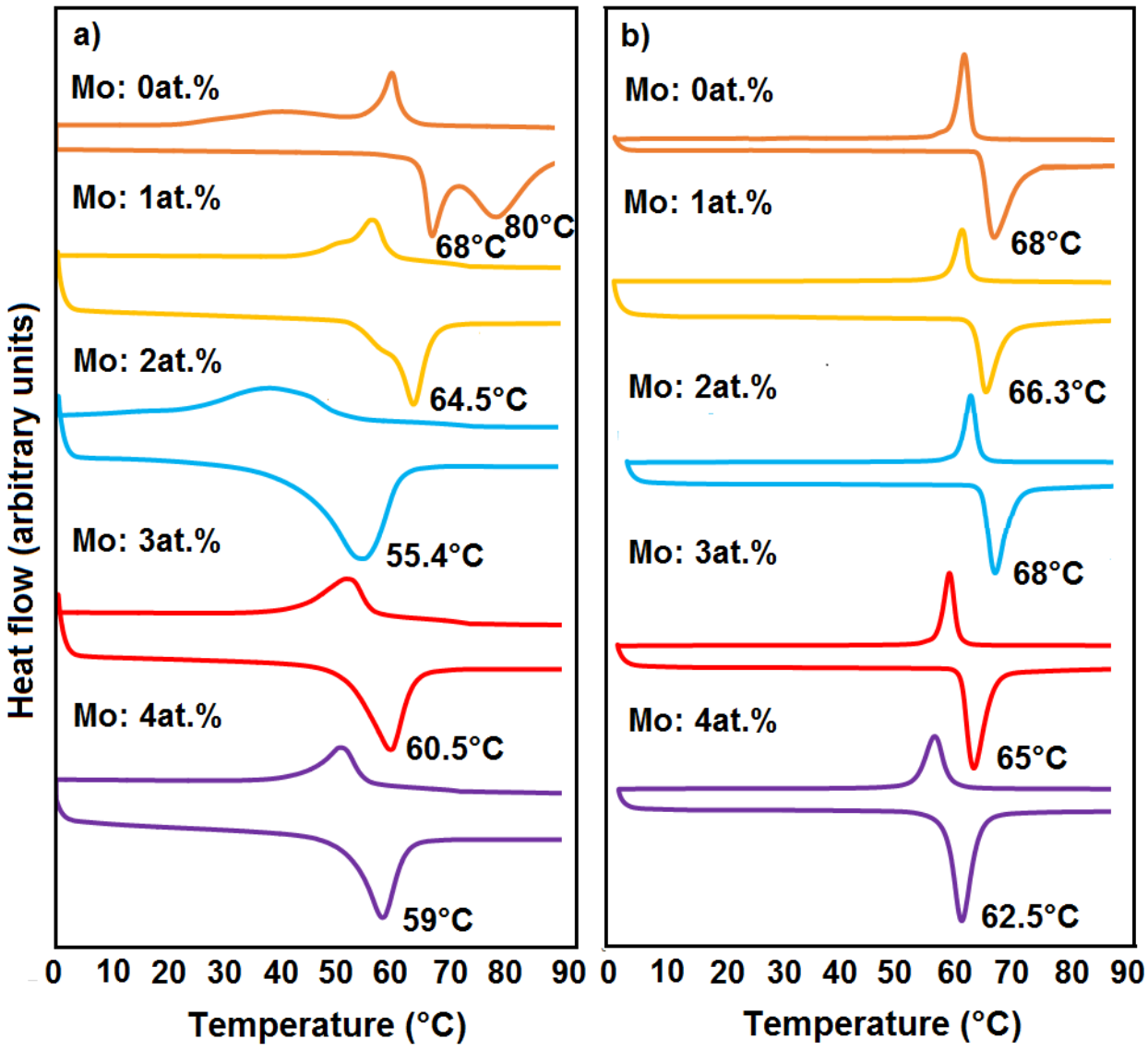

Figure 3.11 DSC data for VO_2 (M) with nominal contents of Mo (0-4 at. %) after annealing (a) at 450 °C and (b) at 650 °C. All DSC measurements are in the same y-scale.

Table 3.5 Average size of Mo-doping VO_2 particles corresponding to different nominal Mo content (annealed at 450 °C with ramping rate of 10 °C/min). Polydispersity Index (PdI).

Mo content [at. %]	Average size (nm)	Average PdI
0	261.4±1.0	0.340±0.006
1	253.3±3.3	0.297±0.011
2	236.2±2.2	0.395±0.004
3	249.7±1.3	0.343±0.007
4	236.2±1.0	0.358±0.001

Table 3.6 Latent heat (J/g) of VO_2 at different nominal Mo content, ramping rates and calcination temperatures.

Mo content [at. %]	0	1	2	3	4
calcination at 450°C, ramping rate at 10°C/min	7.0, 8.5	11.5	29.5	15.0	17.5
calcination at 650°C, ramping rate at 20°C/min	39.0	10.9	15.0	21.5	29.5

Table 3.7 Hysteresis width (°C) of VO_2 at different Mo concentrations, ramping rates and calcination temperatures.

Mo content [at. %]	0	1	2	3	4
calcination at 450°C, ramping rate at 10°C/min	7.2	7.5	16.7	7.7	7.5
calcination at 650°C, ramping rate at 20°C/min	5.4	4.1	5.8	4.3	4.7

To determine the T_c reduction coefficient, T_c was plotted versus the real doping concentration for W (Figure 3.12a) and Mo (Figure 3.12b). For both cases, a linear relationship is observed. The slopes provide the T_c reduction efficiency. For W, an efficiency of 23 K/at. % was found and for Mo, 8.74 K/at. % is obtained. The W-doped material is comparable to literature data where T_c reduction coefficients in order of 21-24 K/at. % were achieved [11, 39](Figure B2). For the Mo-doped material's reduction coefficient (8.74 K/at. %), a slight diminution was obtained. Literature

reports values of 11 K/at. % [40, 41]. Overall, W-doped material showed a better T_c reduction than the Mo-doped material, which is in agreement with Cui et al. [41].

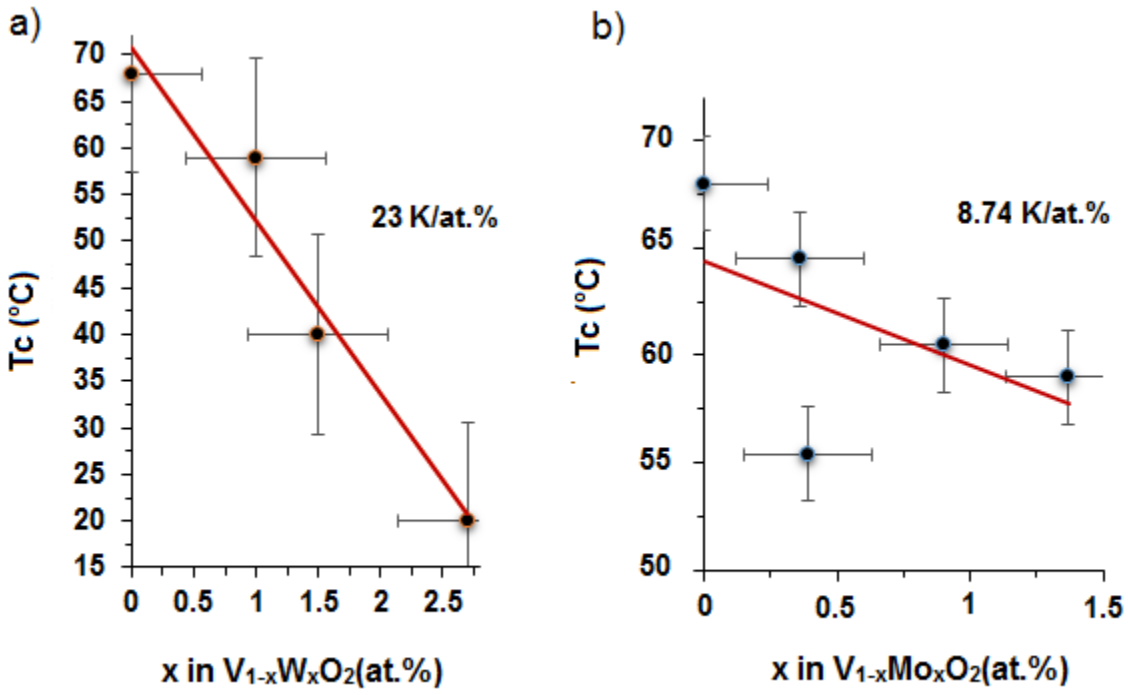

Figure 3.12 Relationship between T_c and real dopant concentration: (a) W and (b) Mo (both calcined at 450 °C with a ramping rate of 10 °C/min).

3.3.3 VO_2-PVP films

The optical and thermochromic properties of the (0-4 at. %) W-doped VO_2/PVP coated glasses were measured by analyzing the visible and near infrared transmittance at low (below Tc) and high (above Tc) temperatures, as shown in Figure 3.13 and 3.14. The optical and thermochromic properties of the VO_2/PVP coated glasses were analyzed to assess their applicability for smart windows. The challenge is to achieve a high IR modulation, meaning a high change in IR transmission upon temperature variation ($\Delta T_{@IR}$, Figure 3.13), while maintaining transmittance in

the visible (T_{vis}) above 60% [42]. Ji et al. [11] reported VO_2 films with values of T_{vis} and $\Delta T_{max@2000\ nm}$ of 50% and 50% for un-doped VO_2, and 59% and 28% for 0.924 at. % W-doped VO_2 material, respectively. Unfortunately, their visible transmittance was < 60% and the ΔT_{max} of the doped VO_2 decreased by reducing the wavelength to 1000 nm. This behavior results in a small solar modulation efficiency since most of the heat in the solar irradiance is concentrated in the 300-1500 nm range. The spectral transmittance of the un-doped and W-doped VO_2/PVP coatings on glass were characterized at 22 °C and 80 °C in the spectral region 250-2500 nm (Figure 3.13). The un-doped VO_2 film show a visible transmittance of 62% above T_c with a $\Delta T_{max@2000nm}$ of 35%. The reason for reversing the transmittance at high temperature in the visible region (solid dark red line), is mainly due to the lower refractive index (2.0–2.5) for rutile VO_2 phase than monoclinic VO_2 phase (2.7–2.8) [43]. The 1 at. % W-doped VO_2/PVP coating exhibited T_{vis} and $\Delta T_{max@2000nm}$ values of 75% and 25%, respectively (Figure 3.13). The maximum infrared modulation occurred at 1500 nm with a value of 28%. Smaller infrared modulations were observed at 1000 nm (17%), 1250 nm and 1750 nm (26%) and 2000 nm (25%). Increasing the nominal W content from 1 to 4 at. %, the visible transparency was improved substantially (up to 95%) but the IR modulation decreased from a maximum of 28% for the 1 at. % with increasing W-doping concentration to less than 10% for 4 at. % as shown in Figure 3.14, which is due to T_c being near or less than measured comfort temperature (22 °C). The dopant has triggered a blue-shift of the absorption edge by widening the band gap of VO_2 [7, 32, 44]. Photographs of un-doped and W-doped VO_2/PVP coated glass lying on a piece of white paper are shown in Figure 3.13, inset (bottom) and inset (top), respectively.

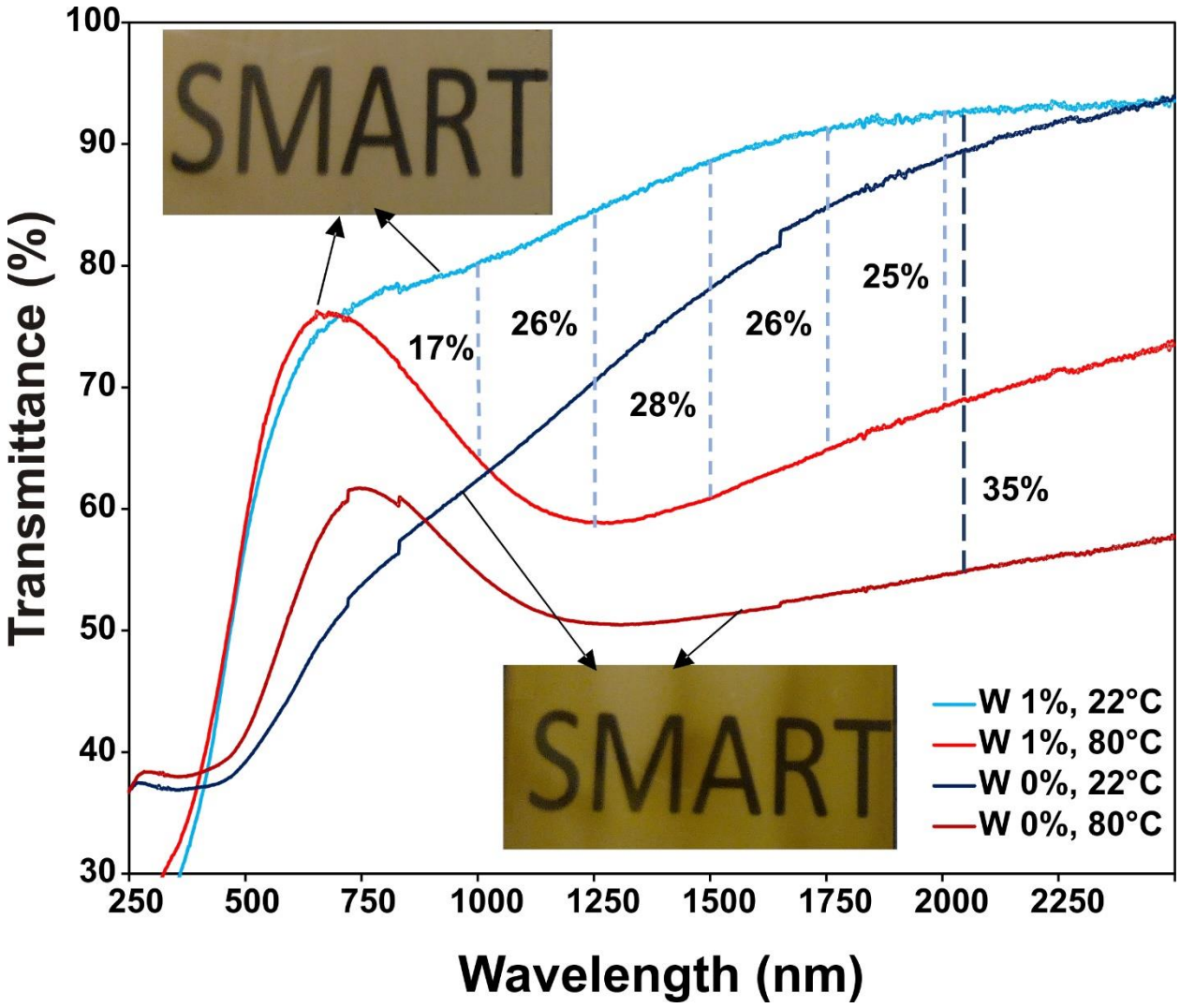

Figure 3. 13 Optical transmittance spectra of un-doped and 1 at. % W-dopedVO_2/PVP coatings on glass at 22 °C and 80 °C. Photographs of VO_2/PVP coated glass lying on a piece of white paper with non-doped (inset, bottom) and 1 at. % W doping (inset, top) in the VO_2.

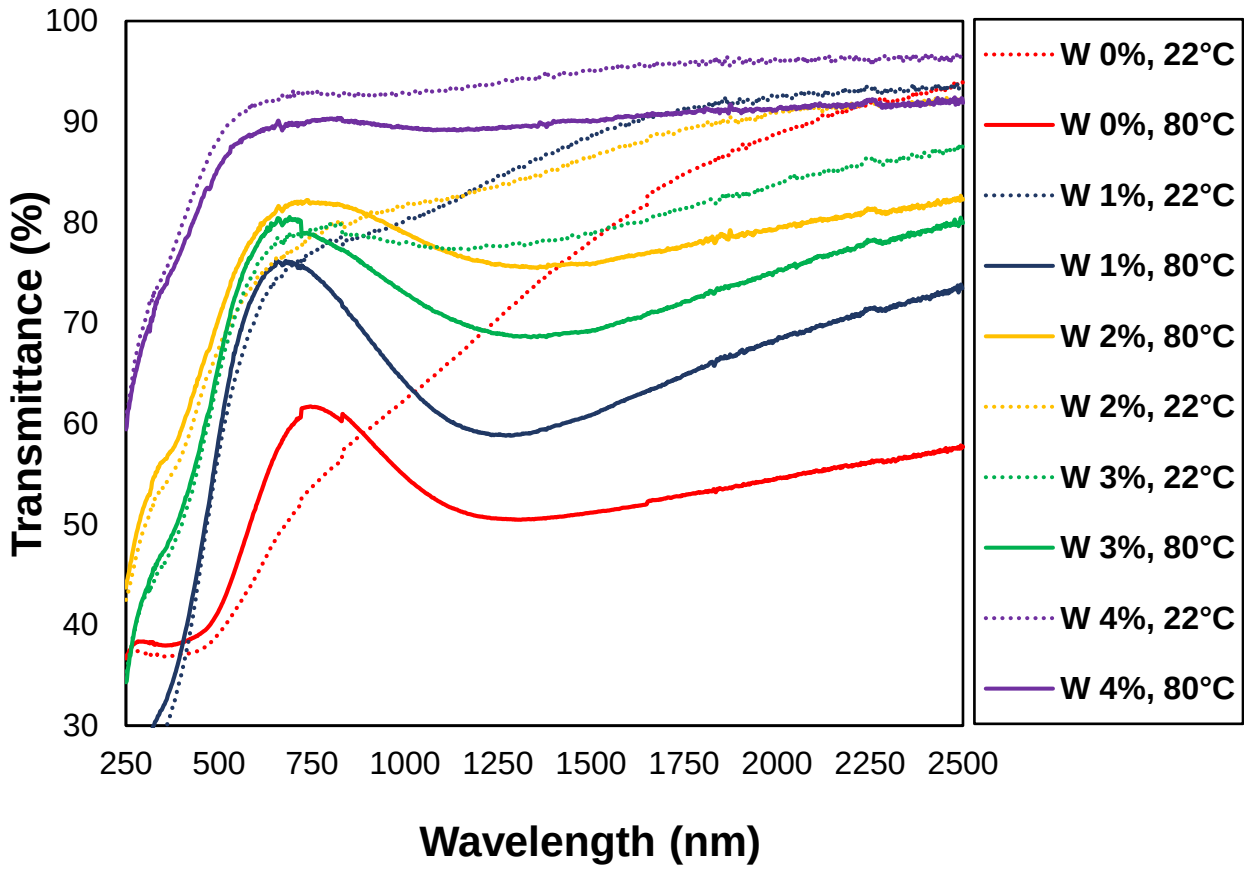

Figure 3. 14 Optical transmittance spectra for the un-doped and W (1-4 at. %)-doped VO_2 films measured at 22 °C (semiconductor phase) and 80 °C (metallic phase).

SEM images of VO_2 and W-doped VO_2 in PVP coated on glass are shown in Figure 3.15 (coating thickness ~200 nm). Agglomeration of particles occurred in both coatings, however, the un-doped VO_2(M) dispersed better in the PVP than the W-doped VO_2. The reason might be the higher hydrophilicity of the material at low W concentration [45]. AFM investigations confirmed these results and show that the films are rough (Figure B3).

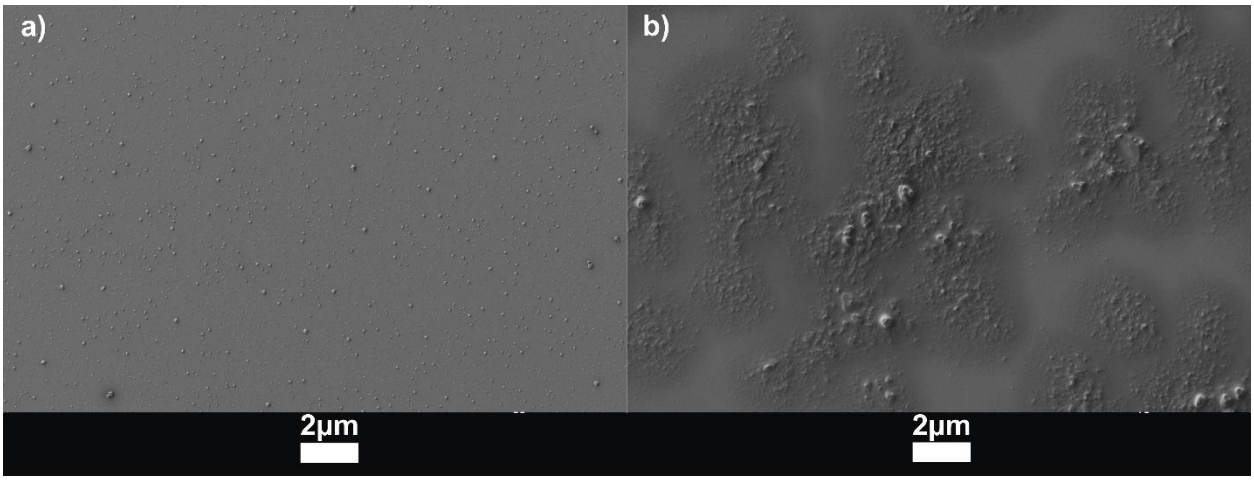

Figure 3. 15 SEM images of (a) VO_2 and (b) 1 at. % W-doped VO_2 in PVP coated on glass.

3.4 CONCLUSIONS

Using a hydrothermal method with a short time annealing, VO_2(M) crystals were synthesized with a high yield in a relative large batch size (2g) by reducing ammonium metavanadate (NH_4VO_3) with hydrazine. Both W- and Mo-doped VO_2 were synthesized. It was found that W was more effective than Mo to reduce T_c of VO_2 down to room temperature, being useful for smart windows. A high transition reduction efficiency of 23 K/at. % was achieved for W-doped VO_2 crystals. The thermochromic properties of VO_2/PVP coated glass exhibited an excellent visible light transmittance above 62% and high infrared modulation up to 35% at 2000 nm. The highest infrared modulation of 28% at 1500 nm was obtained for 1 at. % W-doped VO_2/PVP coating with a visible transmittance above 75%. These values are promising for an application of W-doped VO_2 crystals in smart window designs. This simple and green synthetic method can open avenues for an economic and commercial large-scale VO_2 (M) production for affordable smart windows.

REFERENCES

1. Zhang, J., et al., *Hydrothermal growth of VO2 nanoplate thermochromic films on glass with high visible transmittance.* Scientific reports, 2016. **6**: p. 27898.
2. Chen, S., et al., *The visible transmittance and solar modulation ability of VO 2 flexible foils simultaneously improved by Ti doping: an optimization and first principle study.* Physical Chemistry Chemical Physics, 2013. **15**(40): p. 17537-17543.
3. Casini, M. *Smart windows for energy efficiency of buildings*. in *Proceedings of the Second International Conference on Advances in Civil, Structural, and Enviro nmental Engineering*. 2014.
4. Li, Y., et al., *Core-shell VO2@ TiO2 nanorods that combine thermochromic and photocatalytic properties for application as energy-saving smart coatings.* Scientific reports, 2013. **3**.
5. Granqvist, C.G., *Transparent conductors as solar energy materials: A panoramic review.* Solar energy materials and solar cells, 2007. **91**(17): p. 1529-1598.
6. Baetens, R., B.P. Jelle, and A. Gustavsen, *Properties, requirements and possibilities of smart windows for dynamic daylight and solar energy control in buildings: A state-of-the-art review.* Solar Energy Materials and Solar Cells, 2010. **94**(2): p. 87-105.
7. Zhou, J., et al., *VO2 thermochromic smart window for energy savings and generation.* Scientific reports, 2013. **3**.
8. Cao, Z., et al., *A simple and low-cost combustion method to prepare monoclinic VO2 with superior thermochromic properties.* Scientific reports, 2016. **6**.
9. Chen, R., et al., *Shape-controlled synthesis and influence of W doping and oxygen nonstoichiometry on the phase transition of VO2.* Scientific reports, 2015. **5**: p. 14087.
10. Wu, Y., et al., *Decoupling the lattice distortion and charge doping effects on the phase transition behavior of VO2 by titanium (Ti4+) doping.* Scientific reports, 2015. **5**: p. 9328.
11. Ji, S., F. Zhang, and P. Jin, *Preparation of high performance pure single phase VO 2 nanopowder by hydrothermally reducing the V 2 O 5 gel.* Solar Energy Materials and Solar Cells, 2011. **95**(12): p. 3520-3526.
12. Liang, S., et al., *One-Step Hydrothermal Synthesis of W-Doped VO2 (M) Nanorods with a Tunable Phase-Transition Temperature for Infrared Smart Windows.* ACS Omega, 2016. **1**(6): p. 1139-1148.
13. Gonçalves, A., et al., *Smart optically active VO 2 nanostructured layers applied in roof-type ceramic tiles for energy efficiency.* Solar Energy Materials and Solar Cells, 2016. **150**: p. 1-9.
14. Miao, L., et al., *Depressed haze and enhanced solar modulation capability for VO 2-based composite films with distinct size effects.* RSC Advances, 2016. **6**(93): p. 90813-90823.
15. Chen, L., et al., *Synthesis of thermochromic W-doped VO 2 (M/R) nanopowders by a simple solution-based process.* Journal of nanomaterials, 2012. **2012**: p. 3.
16. Zhang, C., et al., *Simple and facile synthesis W-doped VO2 (M) powder based on hydrothermal Pathway.* Int. J. Electrochem, 2015. **10**: p. 6014-6019.

17. Dong, B., et al., *Phase and morphology evolution of VO 2 nanoparticles using a novel hydrothermal system for thermochromic applications: the growth mechanism and effect of ammonium (NH 4+).* RSC Advances, 2016. **6**(85): p. 81559-81568.
18. Chen, S., et al., *Unraveling mechanism on reducing thermal hysteresis width of VO2 by Ti doping: a joint experimental and theoretical study.* The Journal of Physical Chemistry C, 2014. **118**(33): p. 18938-18944.
19. Shen, N., et al., *The synthesis and performance of Zr-doped and W–Zr-codoped VO 2 nanoparticles and derived flexible foils.* Journal of Materials Chemistry A, 2014. **2**(36): p. 15087-15093.
20. Dai, L., et al., *F-doped VO 2 nanoparticles for thermochromic energy-saving foils with modified color and enhanced solar-heat shielding ability.* Physical Chemistry Chemical Physics, 2013. **15**(28): p. 11723-11729.
21. Ma, Y., et al., *Synthesis of flake-like VO 2 (M) by annealing a novel (NH 4) 0.6 V 2 O 5 phase and its thermochromic characterization.* Ceramics International, 2016. **42**(14): p. 16382-16386.
22. Li, Y., et al., *A novel inorganic precipitation–peptization method for VO2 sol and VO2 nanoparticles preparation: Synthesis, characterization and mechanism.* Journal of colloid and interface science, 2016. **462**: p. 42-47.
23. Popuri, S.R., et al., *Rapid hydrothermal synthesis of VO2 (B) and its conversion to thermochromic VO2 (M1).* Inorganic chemistry, 2013. **52**(9): p. 4780-4785.
24. Lan, S.-D., et al., *Heteroepitaxial TiO 2@ W-doped VO 2 core/shell nanocrystal films: preparation, characterization, and application as bifunctional window coatings.* RSC Advances, 2015. **5**(90): p. 73742-73751.
25. Zhang, Y., *VO2 (B) conversion to VO2 (A) and VO2 (M) and their oxidation resistance and optical switching properties.* Materials Science-Poland, 2016. **34**(1): p. 169-176.
26. Huang, A., et al., *Preparation of V x W 1− x O 2 (M)@ SiO 2 ultrathin nanostructures with high optical performance and optimization for smart windows by etching.* Journal of Materials Chemistry A, 2013. **1**(40): p. 12545-12552.
27. Shannon, R.D., *Revised effective ionic radii and systematic studies of interatomic distances in halides and chalcogenides.* Acta crystallographica section A: crystal physics, diffraction, theoretical and general crystallography, 1976. **32**(5): p. 751-767.
28. Liu, Y., et al., *Effect of annealing temperature on the structure and properties of vanadium oxide films.* Optical Materials Express, 2016. **6**(5): p. 1552-1560.
29. Wu, Y., et al., *A novel route to realize controllable phases in an aluminum (Al 3+)-doped VO 2 system and the metal–insulator transition modulation.* Materials Letters, 2014. **127**: p. 44-47.
30. Brown, B., et al., *Electrical and optical characterization of the metal-insulator transition temperature in Cr-doped VO2 thin films.* Journal of Applied Physics, 2013. **113**(17): p. 173704.
31. Du, J., et al., *Significant changes in phase-transition hysteresis for Ti-doped VO 2 films prepared by polymer-assisted deposition.* Solar Energy Materials and Solar Cells, 2011. **95**(2): p. 469-475.
32. Zhao, L., et al., *Solution-processed VO2-SiO2 composite films with simultaneously enhanced luminous transmittance, solar modulation ability and anti-oxidation property.* Scientific reports, 2014. **4**.

33. Dong, B., et al., *An abnormal phase transition behavior in VO 2 nanoparticles induced by an M1–M2–R process: two anomalous high (> 68° C) transition temperatures.* RSC Advances, 2016. **6**(56): p. 50521-50528.
34. Mioduska, J., et al., *The effect of calcination temperature on structure and photocatalytic properties of WO3/TiO2 nanocomposites.* Journal of Nanomaterials, 2016. **2016**.
35. Shen, N., et al., *Lowered phase transition temperature and excellent solar heat shielding properties of well-crystallized VO 2 by W doping.* Physical Chemistry Chemical Physics, 2016. **18**(40): p. 28010-28017.
36. Lopez, R., et al., *Synthesis and characterization of size-controlled vanadium dioxide nanocrystals in a fused silica matrix.* Journal of applied physics, 2002. **92**(7): p. 4031-4036.
37. Song, Z., et al., *Controllable synthesis of VO 2 (D) and their conversion to VO 2 (M) nanostructures with thermochromic phase transition properties.* Inorganic Chemistry Frontiers, 2016. **3**(8): p. 1035-1042.
38. Dey, A., et al., *Nanocolumnar Crystalline Vanadium Oxide-Molybdenum Oxide Antireflective Smart Thin Films with Superior Nanomechanical Properties.* Scientific reports, 2016. **6**: p. 36811.
39. Tang, C., et al., *Local atomic and electronic arrangements in W x V 1− x O 2.* Physical Review B, 1985. **31**(2): p. 1000.
40. Zhang, J., et al., *Giant reduction of the phase transition temperature for beryllium doped VO 2.* Physical Chemistry Chemical Physics, 2013. **15**(13): p. 4687-4690.
41. Cui, Y., et al., *Hydrogen-doping induced reduction in the phase transition temperature of VO 2: a first-principles study.* Physical Chemistry Chemical Physics, 2015. **17**(32): p. 20998-21004.
42. Zhou, M., et al., *Periodic porous thermochromic VO 2 (M) films with enhanced visible transmittance.* Chemical Communications, 2013. **49**(54): p. 6021-6023.
43. Li, W., et al., *Preparation and characterization of VO 2 (M)–SnO 2 thermochromic films for application as energy-saving smart coatings.* Journal of Colloid and Interface Science, 2015. **456**: p. 166-173.
44. Zhou, J., et al., *Mg-doped VO2 nanoparticles: hydrothermal synthesis, enhanced visible transmittance and decreased metal–insulator transition temperature.* Phys. Chem. Chem. Phys, 2013. **15**: p. 7505-7511.
45. Liang, Z., et al., *Tungsten-doped vanadium dioxide thin films as smart windows with self-cleaning and energy-saving functions.* Journal of Alloys and Compounds, 2017. **694**: p. 124-131.

Chapter 4

Synthesis of Chemically Stable VO_2/SiO_2 Composite with High IR Modulation Coating

ABSTRACT

This work provides a new approach for the rapid and green synthesis of VO_2/SiO_2 composite structures by reducing ammonium metavanadate with maleic acid using water as solvent. The synthesis examined various (maleic acid/NH_4VO_3) and (Si/V) molar ratios, various tungsten concentrations and various annealing temperatures. The results showed that the VO_2/SiO_2 composite was found to prevent the agglomeration and improve the anti-oxidation of the VO_2 sample left in air at room temperature for up to seven months. In addition, the infrared (IR) switching transmittance was examined using a VO_2/SiO_2 composite film at a wavelength of 2500 nm, and compared to plain VO_2 film coated under similar conditions. The composite film demonstrated an excellent IR switching quality (20%), 4X greater than plain VO_2 film (5%), while retaining high visible transmittance (70%) at a wavelength of 680 nm. Furthermore, using this reflux synthetic process at low temperatures, the phase transition temperature (T_c) of 2 at.% W-doped VO_2 was reduced considerably to 23 °C, when tungstic acid (as the W-doping source) was pre-dissolved in hydrogen peroxide (H_2O_2) before addition.

KEYWORDS: chemical stability, thermochromic, VO_2/SiO_2 composite, maleic acid, anti-oxidation, IR switching, reflux process, phase transition temperature, H_2O_2.

4.1 INTRODUCTION

Buildings are responsible for nearly 40% of the worldwide use of primary energy [1]. A large component of this energy is consumed by space heating and space cooling to balance the energy lost through the windows to maintain thermal comfort in buildings [2]. Electrochromic and gasochromic energy-saving windows have been traditionally used in buildings. These methods normally require an external electric field and gas, while their optical performance cannot be changed in response to environmental modulation [3, 4]. Another popular and versatile building technology used today is low-E windows, where energy is saved by reflecting the infrared light. Similar to electrochromic windows, they cannot adjust their response to environment temperature changes [5, 6].

Thermochromic smart windows provide a new approach that can help reduce energy consumption of buildings by regulating their solar irradiation through a building glass [7]. Monoclinic VO_2 (M) is a promising thermochromic material for smart windows due to its ability to modulate the NIR transparency [8, 9]. VO_2 undergoes a fully reversible first-order semiconductor-metal transition (SMT) at a critical temperature (T_c) of 68 °C. This SMT is accompanied by a change in the electrical and optical properties in the infrared (IR) region [10, 11]. VO_2 is monoclinic semiconductor phase (M-phase, space group $P2_1/c$) at temperatures below T_c, but at temperatures above T_c, VO_2 is tetragonal rutile metallic phase (R-phase, space group $P4_2/mnm$) [12]. In the semiconductor state, the vanadium atoms pair and open an energy gap of 0.6 eV, allowing high infrared transmission. In the metallic state, the band gap is eliminated due to an overlapping between the V3d band and Fermi level, hence blocking or reflecting any near-infrared (NIR) light [8, 13-15]. The crystal structure of VO_2 (M) is characterized by alternating V−V distances of 2.65 and 3.12 Å to form a zigzag chain and distorted VO_6 octahedral. In contrast, VO_2 (R) contains a

single V−V distance of 2.85 Å forming linear chains of edge-shared Jahn−Teller and less distorted VO_6 octahedral [16]. The T_c can be regulated by doping with ions and this depends on the relative valence and relative size of the dopant ions compared to that of the V^{4+} ions. For example, T_c can be lowered to room temperature by doping with high valence-large ions such as W^{6+}, Mo^{5+} and Nb^{5+}, or increased by doping with low valence-small ions (Al^{3+}, Cr^{3+}, and Ga^{3+}) [17, 18].

Various techniques have been used to prepare VO_2 (M) coatings on transparent substrates to advance the application of VO_2 based smart windows. Based on some studies [19, 20], powder-based solution coating techniques have many advantages over vapor deposition methods, including simple coating systems, large-scale production, low-cost and flexibility for substrate selection. These make them an excellent alternative for the latter methods [21]. However, VO_2 (M) is not thermodynamically stable in dry air, and it oxidizes into V_2O_5 if annealed at 300 °C in air or stored in air for a long time [22, 23]. The chemical and mechanical stability of VO_2 particles can be enhanced by coating with an inert barrier shell such as silica [24]. The silica layer is optically transparent and can decrease the scattering caused by the refractive index (RI) mismatch between the VO_2 (M) particles and their polymer matrix [25]. According to some optical calculations [17, 26], VO_2 particles dispersed in a dielectric matrix (i.e., SiO_2, ZrO_2, TiO_2) can provide better visible light transmission (T_{vis}) and solar modulation ability (ΔT_{sol}) than pure VO_2 films. Previous studies on VO_2-SiO_2 core-shell composites mainly focused on a prior synthesis of VO_2 followed by the fabrication of a core-shell composite [20, 27, 28]. Hence, many steps are required which inevitably increases the time and complexity of the process and raises the fabrication cost. Recently, VO_2-SiO_2 composites are fabricated, but these methods are complex too, thus increasing the time and cost of the preparation process [17, 29].

In this work, we examined reducing ammonium metavanadate with maleic acid using a reflux method in water for the rapid synthesis of chemically stable VO_2-SiO_2 composite structure. Various molar ratios of (Si/V) were examined while the reaction mechanism of the optimized molar ratio of maleic acid/NH_4VO_3 is explored. In addition, the effect of SiO_2 on the size, morphology, dispersion, latent heat, hysteresis, anti-oxidation and thermochromic property of VO_2 (M) are investigated. The effect of W on T_c using tungstic acid for W-doping was also investigated. This methodology was found to provide composite films with simultaneously high visible transmittance of 70% at the wavelength of 680 nm and good infrared (IR) modulations of 20% at 2500 nm (transmittance difference across SMT). The addition of SiO_2 was found to significantly enhance the anti-oxidation property of the composite and inhibited VO_2 from being oxidized to V_2O_5. Furthermore, using reflux at low temperature was found to provide VO_2 materials with a phase transition temperature (T_c) of 2 at. % W-doped VO_2 depressed significantly to 23 °C, when tungstic acid as the W-doping source is dissolved in H_2O_2 prior to use.

4.2 EXPERIMENTAL SECTION

4.2.1 Materials

Maleic acid ($C_4H_4O_4$, ≥ 99.0%, Reagent Plus®), fumed silica (SiO_2, 99.9%), ammonium metavanadate (NH_4VO_3, ≥ 99%, A.C.S. reagent), tungstic acid (H_2WO_4, 99%), hydrogen peroxide solution (H_2O_2, 30 wt.% in H_2O, A.C.S. reagent) and polyvinylpyrrolidone (PVP, K 29-32, average molecular weight 40 kDa) were purchased from Sigma-Aldrich, Canada. Anhydrous ethyl alcohol was purchased from Commercial Alcohols, Inc., Canada. Microscope glass slides were purchased from VWR International (Radnor, PA , USA). Ultra-high purity Argon (99.9%) was purchased from Praxair, Canada. All chemicals were used as received without further purification.

4.2.2 Synthesis of VO_2 and W-doped VO_2 particles

For the preparation of VO_2, the maleic acid ($C_4H_4O_4$) and ammonium metavanadate (NH_4VO_3) powders were directly added using a 1.5:1 molar ratio to 50 mL of deionized water containing 0.0085 mol vanadium, and maintained under reflux and stirred for 2 h at 100 °C. For the preparation of W-doped VO_2, different concentrations of H_2WO_2 (1-4 at. %) containing ammonium metavanadate were used. Additionally, 2 at. % W-doped VO_2 was also prepared by dissolving the tungstic acid first in 0.5 mL of H_2O_2 and sonicated for 10 minutes prior to use. Further, the solution was cooled to RT, and the resulting black precipitate, doped or un-doped, was collected by centrifugation and washed several times with deionized water, before drying in an oven at 60 °C overnight. Subsequently, the dried powder was calcined (500-800 °C) under argon gas for 1 h in a tube furnace prior to characterization. Calcination for a short time (1 h) was used to avoid agglomeration due to the sintering effect.

4.2.3 Synthesis of VO_2-SiO_2 composite particles

Maleic acid (0.0129 mol) was first refluxed with fumed silica (molar ratio of Si/V=0.05, 0.1 or 0.2) in 50 ml of deionized water at 100 °C for 20 min. Then ammonium metavanadate (0.0085 mol) was added and the mixture was further refluxed for 4.75 h. The VO_2-SiO_2 composite was collected by centrifugation and washed several times with deionized water, before drying in an oven at 60 °C overnight. Further, the composite annealed under argon in a tube furnace at 500 °C or 600 °C for 1 h. Calcination with low temperature and short time was used to avoid agglomeration due to sintering.

4.2.4 Fabrication of VO_2(M) and VO_2-SiO_2 based coatings

In a small vial, 0.08 g of VO_2 or VO_2-SiO_2 calcined material and 0.08 g of polyvinylpyrrolidone (PVP-40) were mixed in 2 mL of ethanol and ultrasonicated at 50 °C for 60 min.

To prepare the coatings, 0.3-0.5 mL of the VO_2/PVP or VO_2-SiO_2/PVP solution was spin-coated on glass substrates at 1500 rpm for ca. 10 s. Sucessively, the films were dryed in the oven at 80 °C for 30 min. The approximate thickness of the coatings were ~250-350 nm.

4.2.5 Characterization

The crystallinity of the synthesized VO_2 and VO_2-SiO_2 particles was examined by X-ray diffraction (XRD; Bruker D2 phaser powder diffractometer, Billerica, MA, USA) using Cu Kα radiation ($\lambda_{K\alpha}$ = 1.54059 Å) with a scanning rate of 0.25°/second. The 2θ data was collected between 10° and 80° using continuous scan mode. The transition temperature (T_c) of VO_2, W-doped VO_2 and VO_2-SiO_2 were determined by differential scanning calorimetry (DSC; SDT Q600, TA Instruments, USA) using a cooling-second heating-cycle between 10-80 °C. The data was analyzed via the instrument's software (Universal Analysis 2000, TA Instruments, USA). The

optical transmittance of the coated films was measured using a Shimadzu UV-3600 UV-Vis-NIR (Shimadzu, Kyoto, Japan) spectrophotometer in the wavelength range of 250 – 2500 nm. The temperature was controlled using a Julabo F12-Refrigarated/Heating Circulator (Julabo GmbH, Seelbach, Germany). The infrared (IR) modulation at wavelengths 2500 nm was obtained using the equation $\Delta T(\lambda)=T(\lambda)_s-T(\lambda)_m$ [30], where s and m represent the semiconductor (at 22 °C) and metal (80°C) phases, respectively. The morphologies and dimensions of the VO_2 and VO_2-SiO_2 particles were examined with a Hitachi S-4500 field emission SEM (Hitachi, Tokyo, Japan). The thickness of the coatings was measured via the Nanoscope V7.30 software using Veeco MultiMode V (Veeco, Plainview, N, USA) atomic force microscope (AFM). A Malvern Zetasizer Nano-ZS (Dynamic Light Scattering instrument (Malvern, UK) was used to measure the size of the VO_2 particles. X-ray photoelectron spectroscopy (XPS) analysis was carried out using a Kratos Axis Ultra spectrometer (Kratos, Manchester, UK) equipped with a monochromatic Al Kα source (15 mA, 14 kV). Prior to measurements, the instrument was calibrated using the $Au_{4f7/2}$ line (83.96 eV) of metallic gold. For calibration of the spectrometer's dispersion, the $Cu_{2p3/2}$ line (932.62 eV) of metallic copper was used. The Kratos charge neutralizer system was used for all specimens. Survey scan analyses and high resolution analyses were carried out evaluating analysis areas of 300 x 700 μm with a pass energy of 160 eV and 20 eV, respectively. Spectra have been charge corrected to the main line of the carbon 1s spectrum (adventitious carbon) set to 284.8 eV and analyzed via the XPS software (CASA, version 2.3.14). V_{2p} and O_{1s} were curve-fitted following the procedures described by Biesinger et al. [31].

4.3 RESULTS AND DISCUSSION

4.3.1 Molar ratio optimization of maleic acid/ NH_4VO_3

For the synthesis of VO_2(M), various molar ratios of maleic acid/ NH_4VO_3 (1/1.5-1.5/1) were investigated. The solution-based synthesis of VO_2 from maleic acid and ammonium metavanadate was found to be sensitive to the molar ratio (which is defined as the mole percent of acid to vanadium precursor); and by adjusting this reaction parameter a monoclincVO_2 can be obtained. Figure 4.1 exhibits the X-ray diffraction (XRD) patterns of VO_2(M), prepared with different molar ratios of maleic acid/ NH_4VO_3, which are annealed at 500 °C for 1 h. For a molar ratio of 1:1.5 (maleic acid/ NH_4VO_3), the product is mixture of V_5O_9, V_6O_{13} and VO_2(M) [17]. As the molar ratio of maleic acid/ NH_4VO_3 increased to 1:1, all the diffraction peaks match well with that of the standard XRD pattern of VO_2 (M) (JCPDS card No. 82-0661, space group $P2_1c$) [32]. Upon further increasing the molar ratio of maleic acid/ NH_4VO_3 to 1.5:1, the intensity of the diffraction peaks significantly increased, with an absence of impurity or other phases, indicating an improved crystallinity, which illustrates that the ratio 1.5:1 is an optimal for the synthesis of pure monoclinic VO_2. Therefore, this ratio was selected for further investigation.

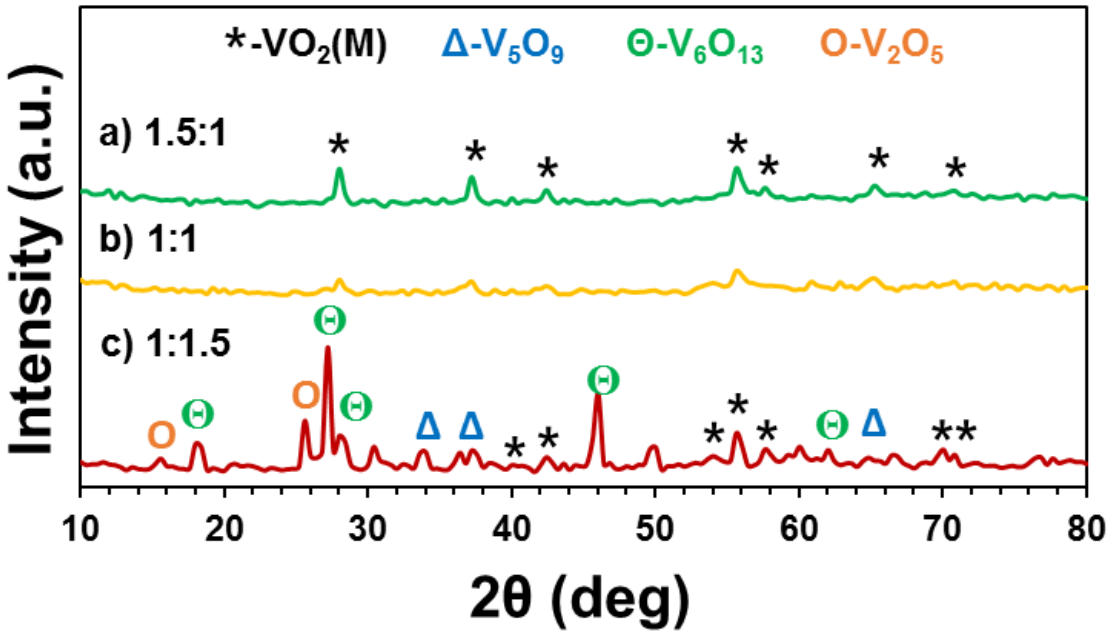

Figure 4.1 The XRD spectra of VO_2 prepared with different molar ratios of maleic acid/ NH_4VO_3: (a) 1.5:1, (b) 1:1 and (C) 1:1.5. * indicate the Bragg peaks of VO_2(M). Δ, Θ and O indicate the Bragg peaks of V_5O_9, V_6O_{13} and V_2O_5, respectively.

4.3.2 Study of reaction mechanisms

The reaction mechanism of the optimized molar ratio (1.5:1) of maleic acid/ NH_4VO_3 for the synthesis of VO_2(M) was further investigated. Based on the literature and our XPS, FTIR and XRD results, the as synthesized product obtained by reduction of NH_4VO_3 with maleic acid is a mixture of $(NH_4)0.5V_2O_5$ and $(NH_4)_2V_4O_9$ (molar ratio: 6.8:1). However, it transforms to a mixture of VO_2 and V_2O_5 (molar ratio: 3:1) after calcination. To investigate the elemental composition and valence state of the as-prepared and as-calcined (at 500 °C for 1 h) product, the samples were examined using X-ray photoelectron spectroscopy (XPS) as shown in Figure 4.2. The peaks in the XPS survey spectrum for the as-synthesized (Figure 4.2a) and as-calcined (Figure 4.2b) samples, correspond to elements (N, C, Na, Si, V and O), where Na and Si peaks are attributed to surface

contamination. The XPS peaks at 516.65 and 524.00 eV for the as-synthesized (Figure 4.2c, Table 4.1), and at 516.44 and 523.79 eV for the as-calcined (Figure 4.2d, Table 4.1) samples, are associated with the spin-orbit splitting of $V2_{p3/2}$ and $V2_{p1/2}$, respectively, which agree with V^{4+} in the literature [8, 33, 34]. Meanwhile, the peaks at 517.79 and 525.14 eV for the as-synthesized (Figure 4.2c, Table 4.1), and at 517.82 and 525.17 eV for as-calcined (Figure 4.2d, Table 4.1) for $V2p_{3/2}$ and $V2p_{1/2}$, respectively, are attributed to the V^{5+} valence state. From the as-synthesized (Figure 4.2c) and as-calcined (Figure 4.2d) samples, the peaks of O1s respectively appeared at 530.36 and 530.26 eV, which can be assigned to O^{2-} in the V-O [35]. After calcination, the percent of V^{5+} decreased from 58.0% to 40.6%, while V^{4+} increased from 42.0% to 59.4% (Table 4.1). The growing of VO_2% after annealing is a result of V_4O_9 and V_2O_5 having the organics removed from the [$(NH_4)0.5V_2O_5$; $(NH_4)_2V_4O_9$] mixture, which is accompanied by a release of CO_2 and NH^{4+}, respectively. Supporting the argument of CO_2 and NH^{4+} release, the atomic ratio (C/V) for all organics are decreased after calcination (Table 4.2, Figure 4.2e, f), and the overall removal ratio of (C/V) and (N/V) is 32 and 100%, respectively (Table 4.3, Figure 4.2a, b).

After collecting the deposited VO_2 at the bottom by centrifugation, the residual solute in the top clear solution was freeze-dried and then further characterized by ^{1}H NMR and ^{13}C NMR (Figure C1, C2). The NMR spectra of the solute matches well with maleic acid signals, suggesting no other organics. Thus, the NMR spectrum further confirms the release of CO_2, which is consistent with XPS analysis. Furthermore, the X-ray diffraction (XRD) pattern of the as-synthesized product is shown in Figure C3 and all diffraction peaks can be clearly indexed to $(NH_4)_{0.5}V_2O_5$ and $(NH_4)_2V_4O_9$ [36].

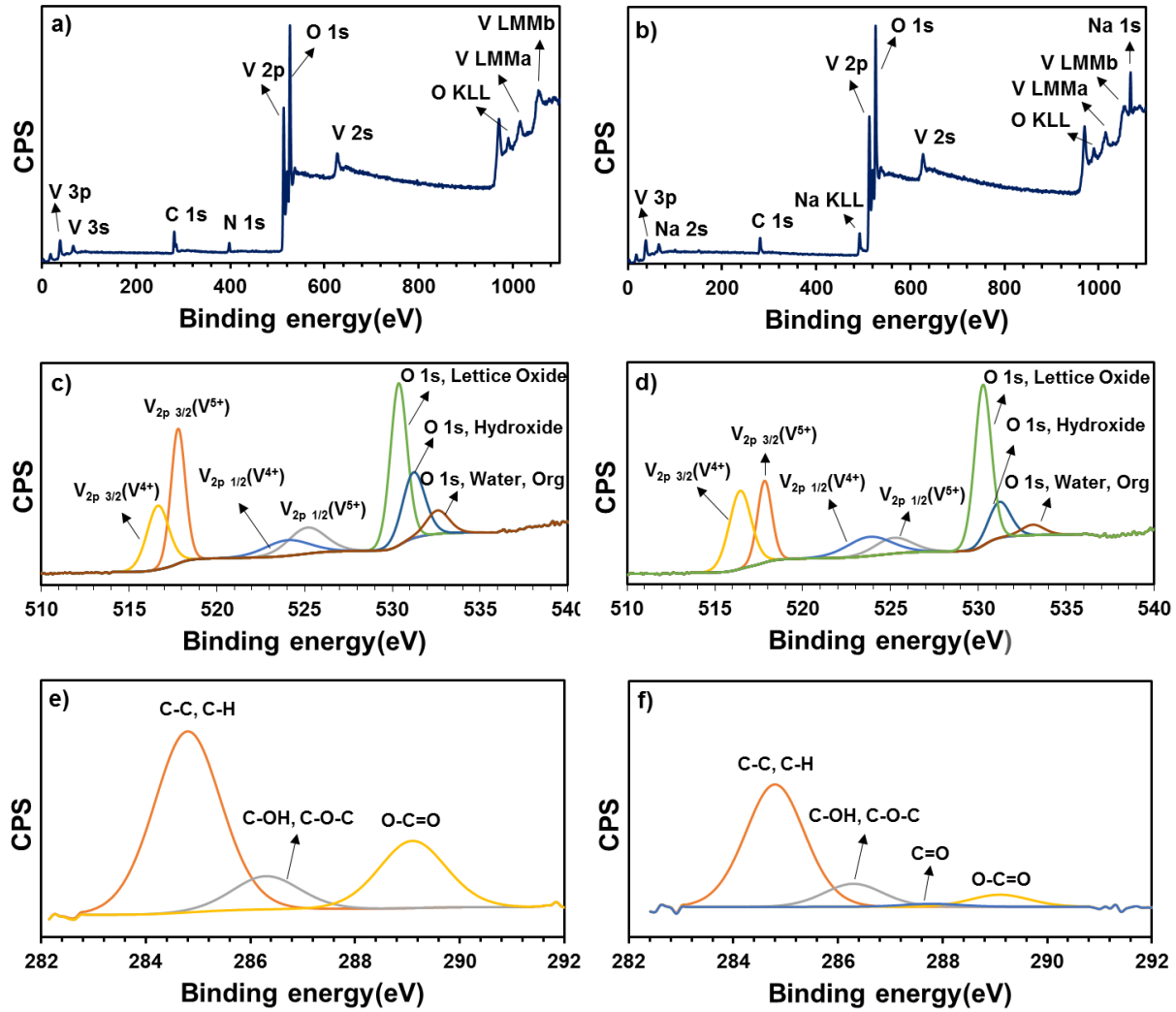

Figure 4.2 XPS spectra of sample before and after annealing at 500 °C: (a, b) survey spectrum; (c, d) V 2p and O 1s core-level spectra; (e, f) C 1s core-level spectra, respectively.

Table 4.1 XPS analysis of as-synthesized and as-calcined product.

Name	Before calcination		After calcination	
	Position	Percent (%)	Position	Percent (%)
V2p ½ (V)	525.14	0	525.17	0
V2p ½ (IV)	524.00	0	523.79	0
V2p 3/2 (V)	517.79	58.0	517.82	40.6
V2p 3/2 (IV)	516.65	42.0	516.44	59.4

Table 4.2 XPS analysis of atomic ratio(C/V) for as-synthesized and as-calcined product.

Bond name	Before calcination		After calcination	
	Position	Atomic ratio(C/V)	Position	Atomic ratio(C/V)
O-C=O	289.10	0.31	289.10	0.07
C=O	NA	0	287.80	0.02
C-OH, C-O-C	286.30	0.15	286.30	0.12
C-C, C-H	284.80	0.84	284.80	0.67

Table 4.3 XPS of total atomic ratio of (C/V) and (N/V) for as-synthesized and as-calcined product.

Name	Atomic ratio	Before calcination	After calcination	% removal
C 1s	(C/V)	1.3	0.88	32
N 1s	(N/V)	0.25	0	100

For further investigation on the phase composition, the Fourier transform infrared (FTIR) spectra was measured between 400 and 4000 cm^{-1} for the as-synthesized and as-calcined samples. The samples were prepared by grinding the dried sample with potassium bromide (KBr) powder, in the ratio of ~1:200 (sample: KBr) and then compressed into discs. The FTIR spectrum of the as-synthesized and as-calcined (at 500 °C for 1 h) samples are shown in Figure 4.3a and Figure 4.3b, respectively. Figure 4.3a shows that the absorption bands for non-calcined product at (987, 758) cm^{-1} and 542 cm^{-1} are respectively assigned to V=O and V–O–V. Meanwhile the peaks at 3132 and 1400 cm^{-1} are attributed to NH^{4+} stretching and umbrella modes, respectively, which disappear after annealing. This implies that the as-synthesized product is a mixture of $(NH_4)_{0.5}V_2O_5$ and $(NH_4)_2V_4O_9$ [36-38]. Figure 4.3b shows that the absorption bands for as-calcined product at (1022, 739) cm^{-1} and at (534 and 469) cm^{-1} are intrinsic to VO_2 and are respectively assigned to V=O stretching and V–O–V deformation modes [39, 40]. Meanwhile, the bands in the (3435, 1631) cm^{-1} region are attributed to ν(O–H) of H_2O [41]. The above results of the FTIR analysis confirm that the as-calcined sample corresponds to the VO_2 phase, which is consistent with the XPS and XRD

results. Moreover, the residual solute in the clear solution after freeze-drying was also characterized using FTIR analysis (Figure 4.4). The bands of solute (Figure 4.4a) matches well with signals of maleic acid (Figure 4.4b) and this results further confirms CO_2 release, which is in agreement with the results from NMR and XPS analysis.

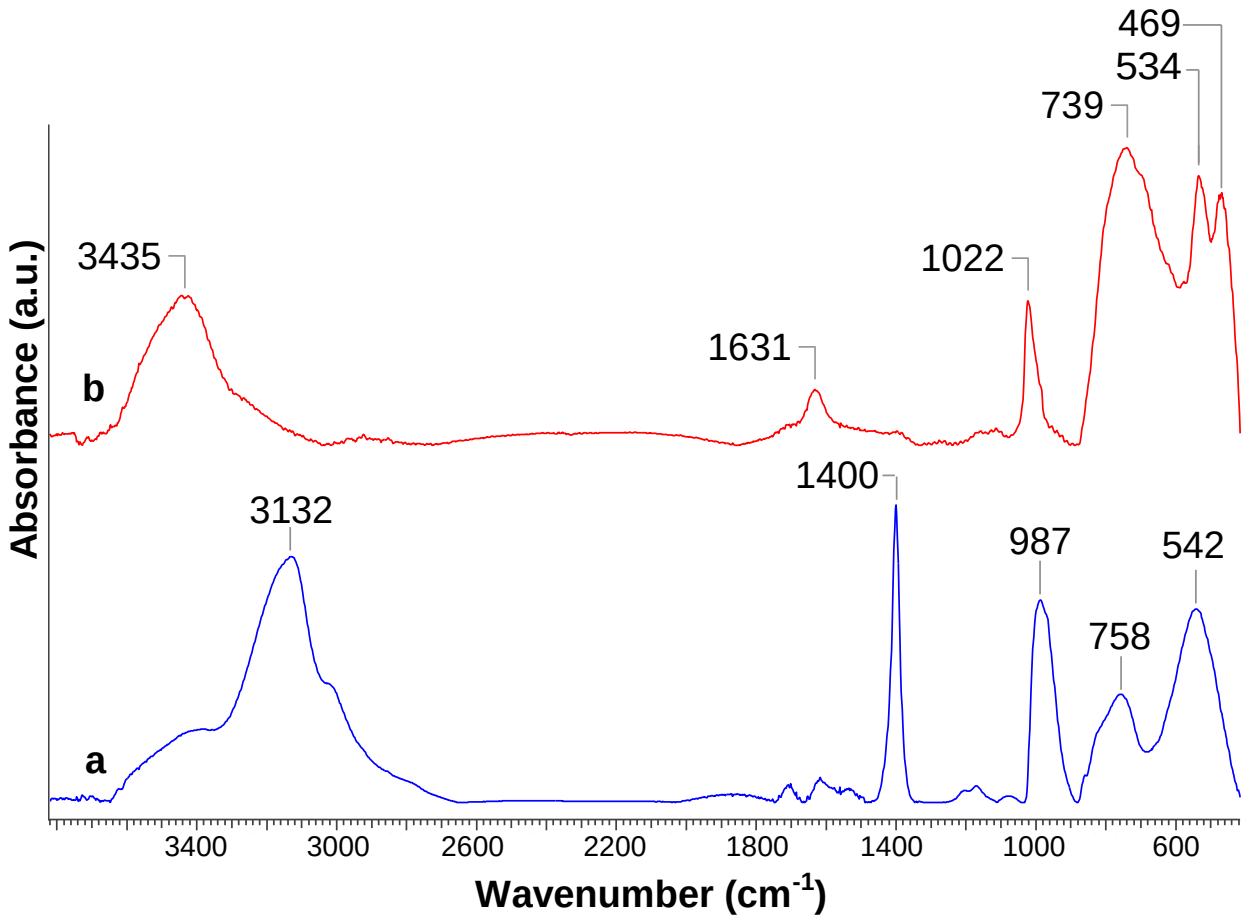

Figure 4.3 FTIR spectra of (a) as-synthesized and (b) as-calcined sample obtained from reaction of maleic acid with NH_4VO_3.

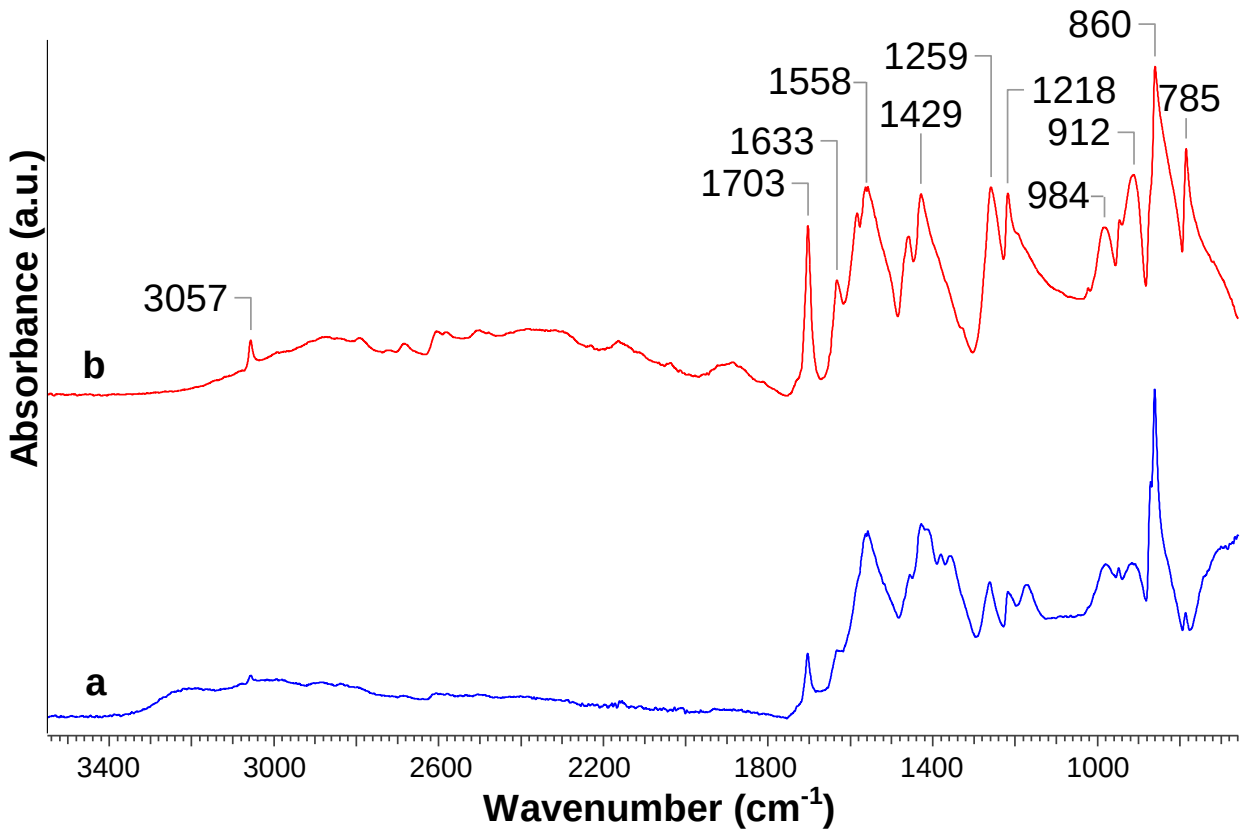

Figure 4.4 FTIR spectra of (a) the residual solute in the clear solution after freeze-drying and (b) maleic acid.

4.3.3 The effect of annealing temperature

To investigate the influence of annealing temperature from 500 °C to 800 °C on the phase transition temperature (T_c), hysteresis width and latent heat (J/g) of VO_2(M), measurements were conducted using differential scanning calorimetry (DSC). The DSC results of the VO_2 obtained at various annealing temperatures (500-800 °C) for 1 h are summarized in Table 4.4. We can see that when the annealing temperature was increased from 500 °C to 700 °C, the T_c(°C) exhibited a decrease from 67.3 °C to 66.7 °C during the heating cycle and an increase from 62.0 °C to 63.4 °C during the cooling cycle. Meanwhile, the hysteresis width (ΔT°C) (difference between heating and cooling DSC peaks) showed a decrease from 5.3 °C to 3.3 °C. The hysteresis width is narrow when T_c is low,

which agrees with M. Li (2014) and X. Li's (2017) work [42-44]. A small ΔT(°C) signifies a fast response and high sensitivity of the VO_2 to the temperature changes and this may be associated to the high crystallinity at high annealing temperatures [44]. Thermal analysis reveals that the latent heat (which is calculated as the area under heating) escalates from 27.0J/g to 47.8J/g during phase transition when annealing temperature increases from 500 °C to 800 °C, respectively (Table 4.4). This effect is mainly due to high crystallinity of large grain size of VO_2 particles at high annealing temperatures [45] as shown in Figure 4.5 and Table 4.5. The average size of particles was examined by light scattering (Nanosizer).

Table 4.4 DSC results for the heating and cooling cycles of monoclinic VO_2 obtained at different calcination temperatures (500-800 °C) for 1 h.

Annealing temperature(°C)	$T_{c\text{-heating}}$(°C)	$T_{c\text{-cooling}}$(°C)	Hysteresis Delta T (°C)	Latent heat (J/g)
500	67.3	62.0	5.3	27.0
600	67.2	62.9	4.3	28.0
650	67.1	63.2	3.9	28.2
700	66.7	63.4	3.3	33.2
800	67.5	63.2	4.3	47.8

Table 4.5 Average size of VO_2(M), annealed (500-800 °C) for 1 h. Polydispersity Index (PdI).

Annealing temperature (°C)	Average size (μm)	Average PdI
500	0.650± 0.001	2.0±0.05
600	2.5 ± 0.4	0.54±0.02
650	4.0± 0.1	1.0±0.04
700	15± 0.3	3.0±0.01
800	19± 0.6	1.5±0.05

The morphologies of the as-synthesized VO_2 (Figure 4.5a) and as-calcined (Figure 4.5b-f) at various temperatures (500-800 °C) were examined by SEM as displayed in Figure 4.5. It can be seen that the morphology gradually changes from amorphous as prepared (Figure 4.5a) to globular, rod-like and large globular particles as annealing temperature increased (Figure 4.5b-f) mainly due to a sintering effect.

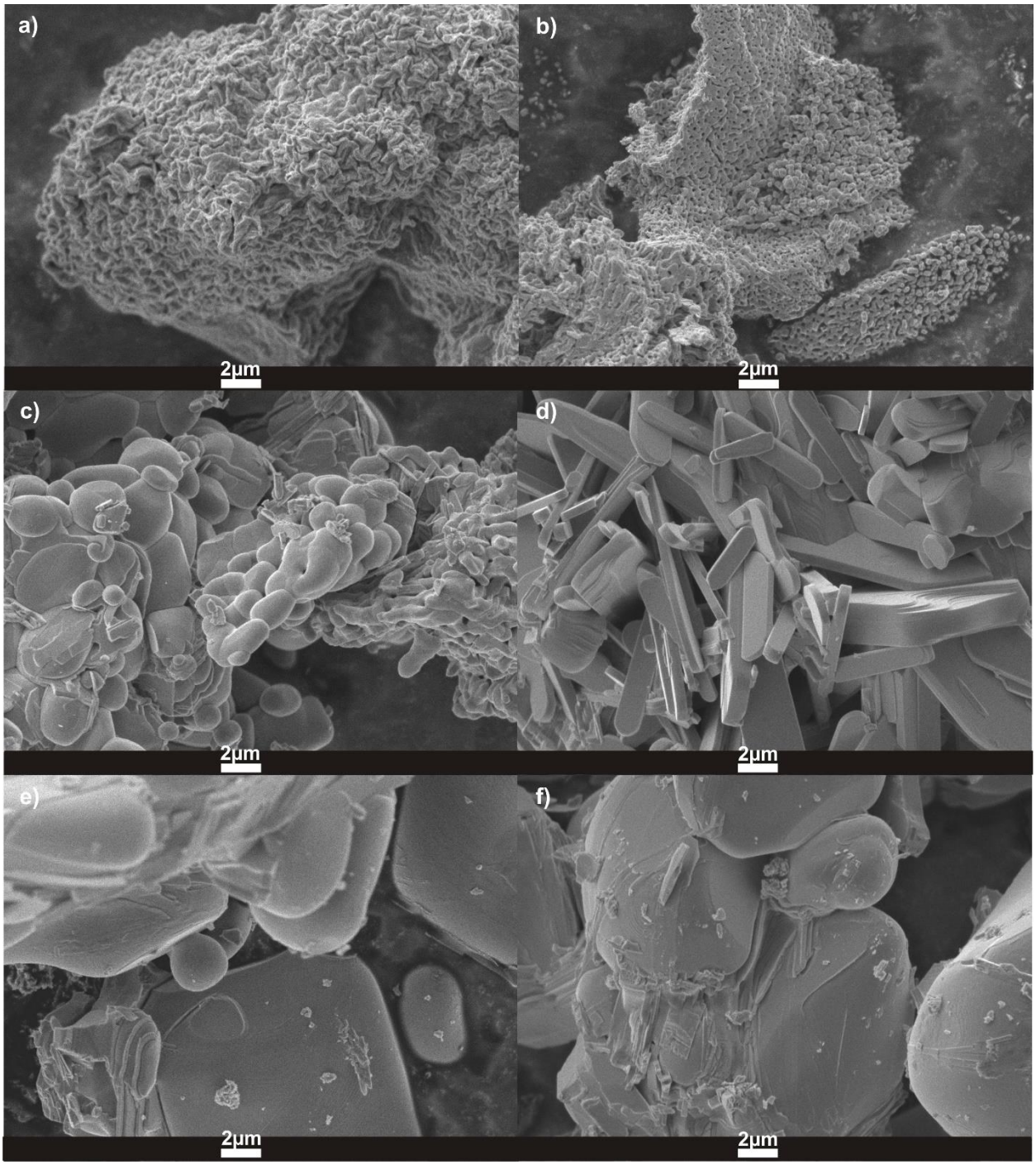

Figure 4.5 SEM images of VO_2 prepared at different annealing temperatures (heating rate = 10 °C min^{-1}). (a) as synthesized; (b) 500 °C; (c) 600 °C; (d) 650 °C; (e) 700 °C; (f) 800 °C.

4.3.4 The effect of W when tungstic acid is dissolved in H_2O_2

The effect of W-doping on the phase transition temperature (T_c) of VO_2 was analyzed as shown in Table 4.6 and Figure 4.6. For potential use of monoclinic VO_2 in smart windows, the phase transition temperature (T_c) in most occurrences should be reduced from 68 °C to near room temperature (21-25 °C). Among many elements, tungsten is reported to be the most effective dopant to produce a large shift in T_c with small content [46]. The phase transition temperatures of W (0-4 at. %)-doped samples (without H_2O_2) were characterized via differential scanning calorimetry (DSC) and the results are shown in Table 4.6. Upon increasing the W doping content from 0 to 3 at. %, the T_c was decreased from 67.3 to 48.8 °C, respectively, and the 4 at. %W sample was without peaks, therefore is omitted (Table 4.6). The unsuccessful doping is due to the actual amount of W in the substitution positions being less than the nominal doping content, with this mainly ascribed to undissolved tungstic acid in the water solution. However, when tungstic acid (as the source of W-doping) was dissolved in hydrogen peroxide (H_2O_2) prior to use, the phase transition temperature of 2 at. % W-doped VO_2 sample was lowered significantly to T_c=23 °C compare to T_c=49.5 °C of VO_2 sample without H_2O_2 having same content of W (Table 4.6). In comparison to the un-doped sample, the phase transition temperatures of W doped sample (H_2O_2) exhibited very low T_c as shown Figure 4.6. Moreover, the latent heat is inevitably depressed by W dopant, which dropped from 27.0 to 14.0 J/g at W doping level of 3 at. % (Table 4.6). This tendency in latent heat values is due to doping-induced retardation of phase transition [46]. Additionally, the hysteresis width (ΔT (°C)) decreased to 4.5 when W doping level increased to 3 at. %, mainly owing to low T_c and size effect of small doped particles [47].

Table 4.6 DSC results of (0-4 at. %) W-doped VO_2 and 2 at. %W-doped VO_2(using H_2O_2) samples annealed at 500 °C for 1 h. (4 at.%W sample was without endothermic peak, therefore is omitted).

W content [at. %]	$T_{c\text{-heating}}$(°C)	$T_{c\text{-cooling}}$(°C)	Hysteresis Delta T (°C)	Latent heat(J/g)
0	67.3	62.0	5.3	27.0
1	51.3	45.8	5.5	25.0
2	49.5	44.2	5.3	17.9
3	48.8	44.3	4.5	14.0
2(in H_2O_2)	23.0	9.0	14	9.0

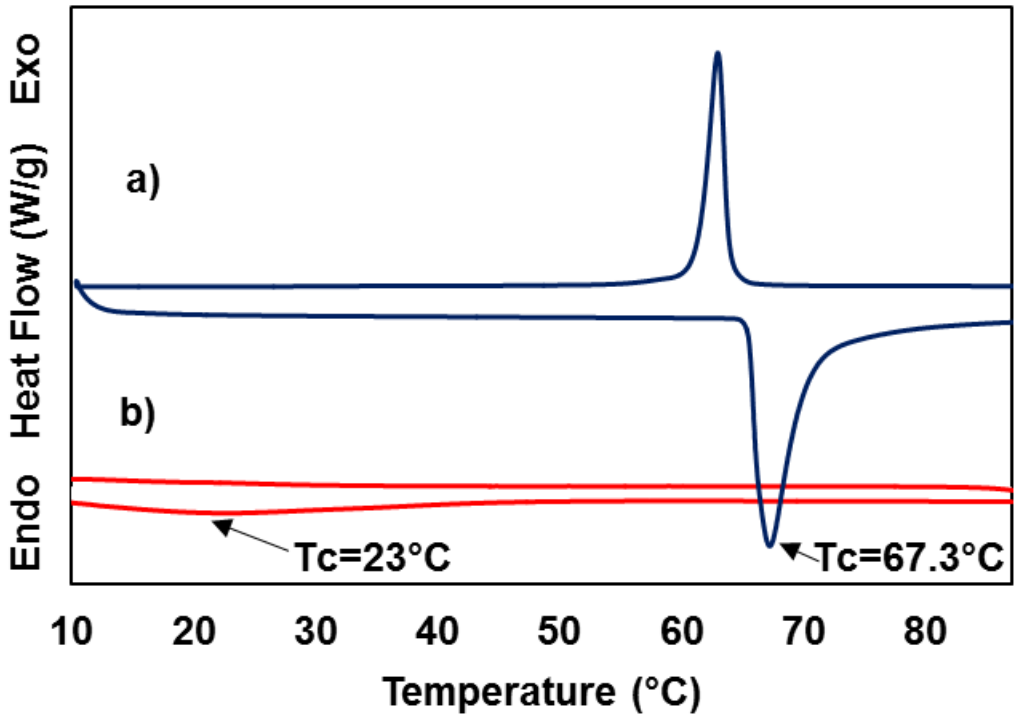

Figure 4.6 The phase transition properties of (a) VO_2 and (b) 2 at. %W-doped VO_2 using hydrogen peroxide(H_2O_2).

4.3.5 The effect of SiO_2 addition on the size and dispersion of VO_2

To study the effect of SiO_2 addition on the size, morphology, dispersion, hysteresis width and latent heat of VO_2, various molar ratios of Si/V (0-0.2) were examined. Table 4.7 shows a DSC analysis of samples annealed at 500 °C and 600 °C for 1 h. The hysteresis width decreased and the latent heat increased for all samples at 600 °C compared to samples at 500 °C. This suggests high crystallinity and large particle sizes at high annealing temperature, which agrees with Cao et al. work [45]. Further, the light scattering results confirm that the mean particle size of VO_2/SiO_2 composite (Si/V=0.05) are approximately 155.5 nm (Table 4.8) compared to 650 nm of VO_2 particles (Table 4.5) annealed under the same conditions (500 °C for 1 h). With verification by SEM, good dispersion of small particles was obtained for the composite compared to an agglomerated VO_2, while both samples annealed at same conditions (Figure 4.7). This tendency suggests that the addition of SiO_2 inhibits the agglomeration of VO_2 particles. However, the results show that the particle sizes of VO_2 increase as the molar ratio of the SiO_2 increases (Table 4.8).

Table 4.7 DSC results of VO_2/SiO_2 composite with different Si/V molar ratio annealed at 500 °C and 600 °C for 1 h. (Sample with molar ratio Si/V=0.2 at 600 °C was without endothermic peak, therefore is omitted).

Molar ratio(Si/V)	$T_{c\text{-heating}}$(°C)	$T_{c\text{-cooling}}$(°C)	Hysteresis Delta T(°C)	Latent heat (J/g)
0 at 500°C	67.3	62.0	5.3	27.0
0.05 at 500°C	68.0	61.1	6.9	28.3
0.05 at 600°C	67.4	62.5	4.9	36.7
0.1 at 500°C	67.5	57.2	10.3	10.7
0.1 at 600°C	66.5	63.0	3.5	11.6
0.2 at 500°C	67.8	60.8	7.0	15.5

Table 4.8 Average size of VO_2-SiO_2, annealed at 500 °C for 1 h. Polydispersity Index (PdI).

Molar ratio(Si/V)	Average size(nm)	Average PdI
0.05	155.5 ± 0.1	3.4±0.01
0.1	163.1± 0.2	0.32±0.01
0.2	186.7 ± 0.2	1.0±0.00

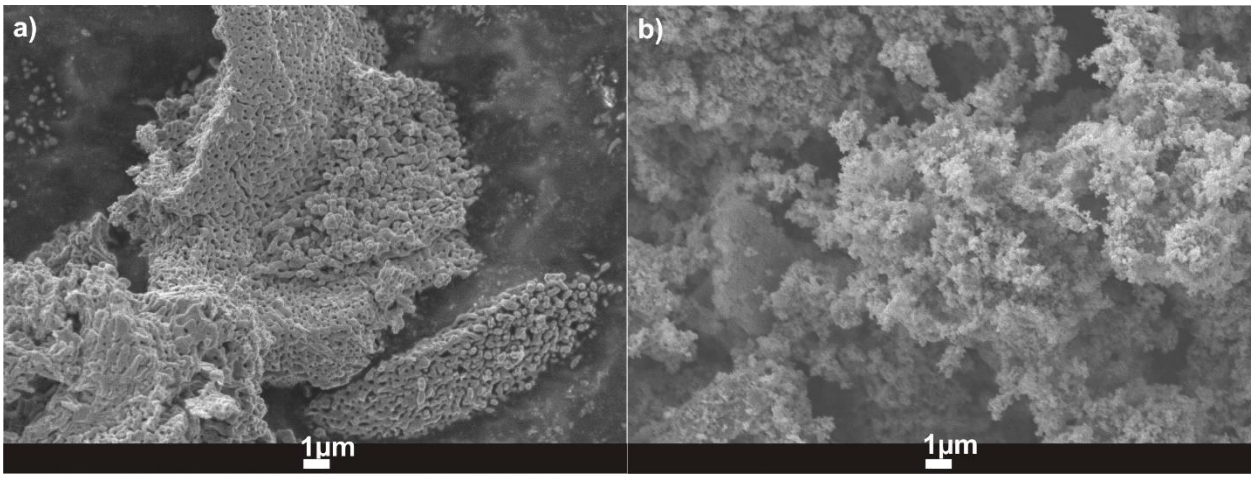

Figure 4.7 SEM photographs of (a) VO_2 and (b) VO_2/SiO_2 (Si/V= 0.05), while both samples annealed at 500 °C for 1 h.

4.3.6 The effect of SiO_2 addition on the chemical stability of VO_2

The impact of SiO_2 on the anti-oxidation property of VO_2(M) was inspected closely as shown in Figure 4.8. The structure of the VO_2/SiO_2 composite effectively enhanced the anti-oxidation property of VO_2. This hypothesis was confirmed by XRD comparative study of VO_2 (Figure 4.8a) and VO_2/SiO_2(Si/V molar ratio = 0.05) (Figure 4.8b) after exposing them to air for 7 months at room temperature, while having same annealing conditions (at 500 °C for 1 h). Evidently, VO_2 cannot maintain the original pure monoclinic phase in the air for long period of time. The (011)

peak disappeared while additional peaks assigned to V_2O_5 or other high valence vanadium oxides emerged (Figure 4.8a) [20]. In comparison, the Bragg diffraction of the composite maintained same position and all peaks are assigned to pure monoclinic VO_2 (Figure 4.8b).

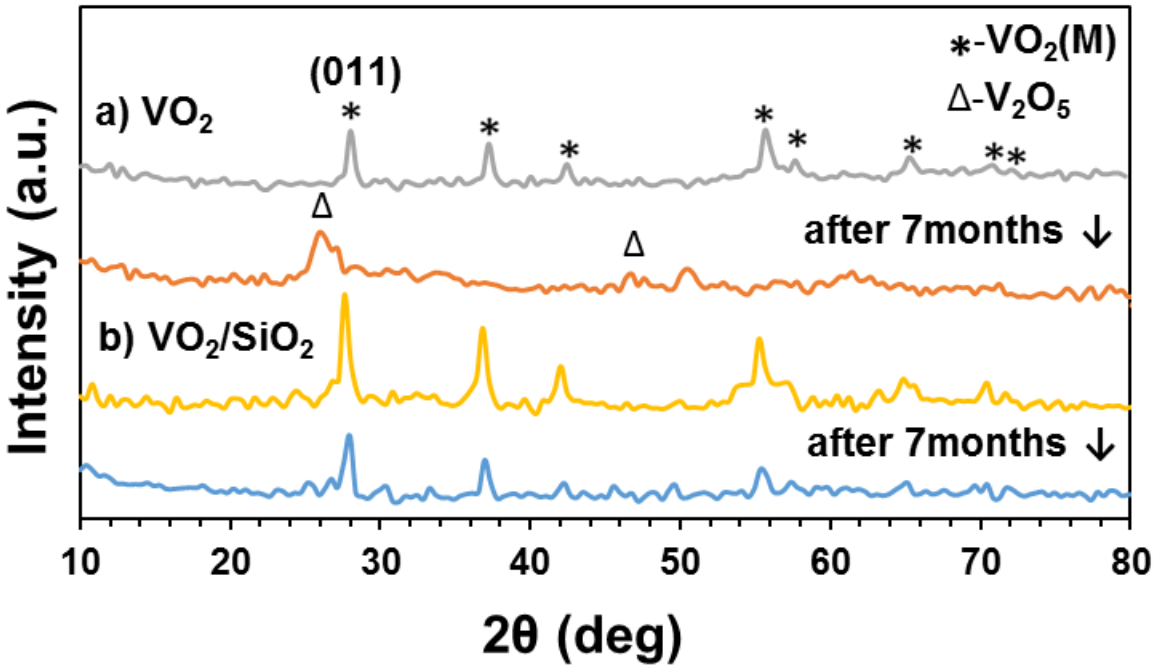

Figure 4.8 XRD spectra of (a) VO_2 and (b) VO_2/SiO_2 composite (Si/V molar ratio = 0.05) before and after depositing in air for 7 months at room temperature.

4.3.7 The effect of SiO_2 addition on the thermochromic property of VO_2 films

To investigate the influence of SiO_2 addition on the thermochromic behavior of VO_2, the UV-Vis–NIR transmittance of VO_2 and VO_2/SiO_2 composite (molar ratio of Si/V = 0.05) films were characterized. The films were coated on the glass using the same conditions and analyzed in the wavelength range between 250 nm and 2500 nm, while both samples were annealed at 500 °C for 1 h (Figure 4.9). The blue transmittance curves measured at 20 °C and the red transmittance curves at 80 °C correspond to the semiconductor phase (transparent for NIR light) and the metal phase

(blocks the IR light), respectively. The visible transmittance of the film is reduced from 82% for the VO_2 film to 70% for the composite film at a wavelength of 680 nm. This increased scattering of the composite after blending with polymer is attributed to agglomeration of particles. However, the thermochromic property of the film considerably improved due to the addition of SiO_2 which agrees with Zhao et al's. work [48]. For the composite film prepared at a Si/V (molar ratio=0.05), a significant transmittance change in the NIR spectrum across the phase transition was exhibited at the wavelength of 2500 nm (20%) compare to (5%) of the plain VO_2 film, which indicates good thermochromic performance for the composite.

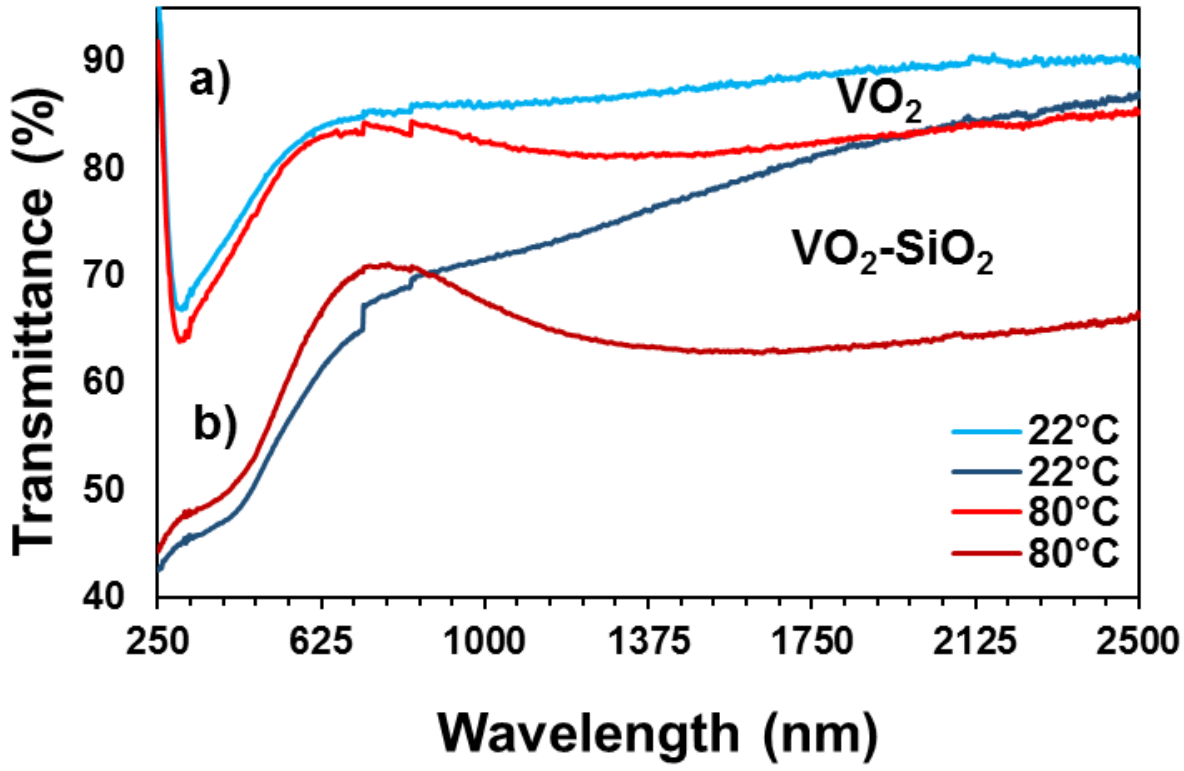

Figure 4.9 UV-Vis-NIR transmittance spectra of (a) VO_2 and (b) VO_2/SiO_2composite (Si/V molar ratio = 0.05) in the wavelength ranges from 250 nm to 2500 nm. Blue lines: semiconducting state at 20 °C; Red lines: metallic state at 80 °C.

4.4 CONCLUSIONS

A novel VO_2-SiO_2 composite was synthesized through a green process by reducing ammonium metavanadate with maleic acid in water. The SiO_2 remarkably improved the chemical stability of VO_2 sample deposited in air at room temperature for seven months. In addition, the VO_2/SiO_2 composite film demonstrated an excellent performance with IR switching ability (20%), four times greater than of the plain VO_2 film, while maintaining high visible transmittance (70%) at 680 nm. Further, using a condenser at low reaction temperature, the phase transition temperature of 2 at. % W-doped VO_2 was dramatically reduced to 23 °C, when tungstic acid was pre-dissolved in the hydrogen peroxide (H_2O_2) prior to use. Therefore, the composite could have a great potential for an application in smart window due to the promising properties of the IR switching and chemical stability.

REFERENCES

1. Zhang, J., et al., *Hydrothermal growth of VO2 nanoplate thermochromic films on glass with high visible transmittance.* Scientific reports, 2016. **6**: p. 27898.
2. Li, S.-Y., G.A. Niklasson, and C.-G. Granqvist, *Thermochromic fenestration with VO 2-based materials: three challenges and how they can be met.* Thin Solid Films, 2012. **520**(10): p. 3823-3828.
3. Zhou, J., et al., *VO2 thermochromic smart window for energy savings and generation.* Scientific reports, 2013. **3**.
4. Baetens, R., B.P. Jelle, and A. Gustavsen, *Properties, requirements and possibilities of smart windows for dynamic daylight and solar energy control in buildings: A state-of-the-art review.* Solar Energy Materials and Solar Cells, 2010. **94**(2): p. 87-105.
5. Chen, S., et al., *The visible transmittance and solar modulation ability of VO 2 flexible foils simultaneously improved by Ti doping: an optimization and first principle study.* Physical Chemistry Chemical Physics, 2013. **15**(40): p. 17537-17543.
6. Granqvist, C.G., *Transparent conductors as solar energy materials: A panoramic review.* Solar energy materials and solar cells, 2007. **91**(17): p. 1529-1598.
7. Dou, S., et al., *Facile preparation of double-sided VO 2 (M) films with micro-structure and enhanced thermochromic performances.* Solar Energy Materials and Solar Cells, 2017. **160**: p. 164-173.
8. Zhang, Z., et al., *Thermochromic VO2 thin films: solution-based processing, improved optical properties, and lowered phase transformation temperature.* Langmuir, 2010. **26**(13): p. 10738-10744.
9. Liu, M., et al., *Dual-Phase Transformation: Spontaneous Self-Template Surface-Patterning Strategy for Ultra-transparent VO2 Solar Modulating Coatings.* ACS nano, 2016. **11**(1): p. 407-415.
10. Qazilbash, M.M., et al., *Mott transition in VO2 revealed by infrared spectroscopy and nano-imaging.* Science, 2007. **318**(5857): p. 1750-1753.
11. Liang, S., et al., *One-Step Hydrothermal Synthesis of W-Doped VO2 (M) Nanorods with a Tunable Phase-Transition Temperature for Infrared Smart Windows.* ACS Omega, 2016. **1**(6): p. 1139-1148.
12. Zhang, Z., et al., *Solution-based fabrication of vanadium dioxide on F: SnO 2 substrates with largely enhanced thermochromism and low-emissivity for energy-saving applications.* Energy & Environmental Science, 2011. **4**(10): p. 4290-4297.
13. Goodenough, J.B., *The two components of the crystallographic transition in VO2.* Journal of Solid State Chemistry, 1971. **3**(4): p. 490-500.
14. Qazilbash, M.M., et al., *Electrodynamics of the vanadium oxides V O 2 and V 2 O 3.* Physical Review B, 2008. **77**(11): p. 115121.
15. Eyert, V., *The metal-insulator transitions of VO2: A band theoretical approach.* arXiv preprint cond-mat/0210558, 2002.
16. Wu, Y., et al., *Decoupling the lattice distortion and charge doping effects on the phase transition behavior of VO2 by titanium (Ti4+) doping.* Scientific reports, 2015. **5**: p. 9328.
17. Zhao, L., et al., *Solution-processed VO2-SiO2 composite films with simultaneously enhanced luminous transmittance, solar modulation ability and anti-oxidation property.* Scientific reports, 2014. **4**.

18. Wu, Y., et al., *Depressed transition temperature of W x V 1− x O 2: mechanistic insights from the X-ray absorption fine structure (XAFS) spectroscopy.* Physical Chemistry Chemical Physics, 2014. **16**(33): p. 17705-17714.
19. Li, Y., et al., *Core-shell VO2@ TiO2 nanorods that combine thermochromic and photocatalytic properties for application as energy-saving smart coatings.* Scientific reports, 2013. **3**.
20. Gao, Y., et al., *Enhanced chemical stability of VO 2 nanoparticles by the formation of SiO 2/VO 2 core/shell structures and the application to transparent and flexible VO 2-based composite foils with excellent thermochromic properties for solar heat control.* Energy & Environmental Science, 2012. **5**(3): p. 6104-6110.
21. Gao, Y., et al., *Phase and shape controlled VO 2 nanostructures by antimony doping.* Energy & Environmental Science, 2012. **5**(9): p. 8708-8715.
22. Lindström, R., et al., *Thin films of vanadium oxide grown on vanadium metal: oxidation conditions to produce V2O5 films for Li-intercalation applications and characterisation by XPS, AFM, RBS/NRA.* Surface and interface analysis, 2006. **38**(1): p. 6-18.
23. Fu, G., et al., *Annealing effects on VO 2 thin films deposited by reactive sputtering.* Thin Solid Films, 2006. **515**(4): p. 2519-2522.
24. Velikov, K.P. and A. van Blaaderen, *Synthesis and characterization of monodisperse core− shell colloidal spheres of zinc sulfide and silica.* Langmuir, 2001. **17**(16): p. 4779-4786.
25. Li, Y.-Q., et al., *Facile synthesis of highly transparent polymer nanocomposites by introduction of core–shell structured nanoparticles.* Chemistry of Materials, 2008. **20**(8): p. 2637-2643.
26. Li, S.-Y., G.A. Niklasson, and C.-G. Granqvist, *Nanothermochromics: calculations for VO 2 nanoparticles in dielectric hosts show much improved luminous transmittance and solar energy transmittance modulation.* Journal of Applied Physics, 2010. **108**(6): p. 063525.
27. Li, R., et al., *Synthesis and characterization of plate-like VO 2 (M)@ SiO 2 nanoparticles and their application to smart window.* Materials Letters, 2013. **110**: p. 241-244.
28. Lu, X., et al., *A novel method to modify the color of VO 2-based thermochromic smart films by solution-processed VO 2@ SiO 2@ Au core–shell nanoparticles.* RSC Advances, 2016. **6**(53): p. 47249-47257.
29. Cao, Z., et al., *Tunable simultaneously visible-light and near-infrared transmittance for VO2/SiO2 composite films to enhance thermochromic properties.* Materials Letters, 2017. **209**: p. 609-612.
30. Ma, Y., et al., *Synthesis of flake-like VO 2 (M) by annealing a novel (NH 4) 0.6 V 2 O 5 phase and its thermochromic characterization.* Ceramics International, 2016. **42**(14): p. 16382-16386.
31. Biesinger, M.C., et al., *Resolving surface chemical states in XPS analysis of first row transition metals, oxides and hydroxides: Cr, Mn, Fe, Co and Ni.* Applied Surface Science, 2011. **257**(7): p. 2717-2730.
32. Wu, C., et al., *Direct hydrothermal synthesis of monoclinic VO 2 (M) single-domain nanorods on large scale displaying magnetocaloric effect.* Journal of Materials Chemistry, 2011. **21**(12): p. 4509-4517.
33. Xu, C.-l., et al., *A novel reduction–hydrolysis method of preparing VO 2 nanopowders.* Materials Research Bulletin, 2004. **39**(7): p. 881-886.

34. Chen, S.-E., et al., *Effects of annealing on thermochromic properties of W-doped vanadium dioxide thin films deposited by electron beam evaporation.* Thin Solid Films, 2017. **644**: p. 52-56.
35. Silversmit, G., et al., *Determination of the V2p XPS binding energies for different vanadium oxidation states (V 5+ to V 0+).* Journal of Electron Spectroscopy and Related Phenomena, 2004. **135**(2): p. 167-175.
36. Wu, X., et al., *Synthesis and characterization of self-assembling (NH 4) 0.5 V 2 O 5 nanowires.* Journal of Materials Chemistry, 2004. **14**(5): p. 901-904.
37. Dong, B., et al., *An intermediate phase (NH 4) 2 V 4 O 9 and its effects on the hydrothermal synthesis of VO 2 (M) nanoparticles.* CrystEngComm, 2016. **18**(4): p. 558-565.
38. Dobley, A., et al., *Manganese vanadium oxide nanotubes: synthesis, characterization, and electrochemistry.* Chemistry of materials, 2001. **13**(11): p. 4382-4386.
39. Ji, H., et al., *Infrared thermochromic properties of monoclinic VO 2 nanopowders using a malic acid-assisted hydrothermal method for adaptive camouflage.* RSC Advances, 2017. **7**(9): p. 5189-5194.
40. Chen, W., et al., *Synthesis and characterization of novel vanadium dioxide nanorods.* Solid state communications, 2004. **132**(8): p. 513-516.
41. Schnetzer, F., et al., *Unraveling the coupled processes of (de) hydration and structural changes in Na+-saturated montmorillonite.* The Journal of Physical Chemistry C, 2016. **120**(28): p. 15282-15287.
42. Li, M., et al., *Defect-mediated phase transition temperature of VO 2 (M) nanoparticles with excellent thermochromic performance and low threshold voltage.* Journal of Materials Chemistry A, 2014. **2**(13): p. 4520-4523.
43. Zhong, L., et al., *Star-shaped VO 2 (M) nanoparticle films with high thermochromic performance.* CrystEngComm, 2015. **17**(30): p. 5614-5619.
44. Li, X., et al., *A convenient way to reduce the hysteresis width of VO 2 (M) nanomaterials.* New Journal of Chemistry, 2017. **41**(24): p. 15260-15267.
45. Cao, X., et al., *Solution-based fabrication of VO 2 (M) nanoparticles via lyophilisation.* RSC Advances, 2015. **5**(33): p. 25669-25675.
46. Shen, N., et al., *Lowered phase transition temperature and excellent solar heat shielding properties of well-crystallized VO 2 by W doping.* Physical Chemistry Chemical Physics, 2016. **18**(40): p. 28010-28017.
47. Hu, L., et al., *Porous W-doped VO 2 films with simultaneously enhanced visible transparency and thermochromic properties.* Journal of Sol-Gel Science and Technology, 2016. **77**(1): p. 85-93.
48. Zhao, L., et al., *Solution-processed VO 2-SiO 2 composite films with simultaneously enhanced luminous transmittance, solar modulation ability and anti-oxidation property.* Scientific reports, 2014. **4**: p. 7000.

Chapter 5

Water Based Synthesis at RT for VO_2 Polymer Coatings with Enhanced IR Modulation

ABSTRACT

The preparation of monoclinic vanadium dioxide (VO_2(M)) using an economical and green methodology is of high interest for applications in smart windows and coatings. This work reports a novel synthetic strategy for preparing un-doped and W-doped VO_2 particles based on the hydrolysis of vanadyl acetylacetonate ($VO(acac)_2$) with HCl in water at RT. It was found that vanadium(V)oxide NPs can promote dispersion of VO_2(M) (IV) particles in hydrophilic polymers including poly(4-vinylpyridine) (P4VP) and polyvinylpyrrolidone (PVP), helping to switch their IR transmission on demand. The effect of coating thickness and concentration ratios of VO_2/polymer on the optical characteristics of the coatings was systematically evaluated. The resulting VO_2(M)/P4VP films exhibited an excellent infrared (IR) transmission switch, $\Delta T_{IR@2500nm}$, of 47% (transmission change due to the temperature-triggered phase transition) with a high visible transmittance, $T_{vis@680nm}$, of 41%. Hydrophobic VO_2/poly methyl methacrylate (PMMA) films gave a $\Delta T_{IR@2500nm}$ of 30% and a $T_{vis@680nm}$ of 29%. The superb performance of the VO_2(M)/P4VP coating is ascribed to the uniform dispersion of VO_2(M) particles within the matrix. The proposed synthetic strategy was found scalable, allowing the potential large-scale production of VO_2(M).

KEYWORDS: monoclinic vanadium dioxide, economical, energy consumption, doping process, vanadium(V)oxide, dispersion, green chemistry, hydrophobic, PMMA, hydrophilic, P4VP, thicknesses, concentrations.

5.1 INTRODUCTION

Heating and cooling buildings to comfortable temperatures consumes up to 40% of our total energy usage in developed countries [1]. A major part of this energy is lost through windows by heat conduction, radiation and convection effects. Low emissivity (E) glass can be used to minimize energy losses through windows. However, the optical transmission properties of low E glass cannot be modified or switched in response to changing temperature or lighting conditions, thereby limiting its effectiveness [2]. The use of thermochromic windows provides another intriguing option, which automatically regulates solar/heat transmission in response to environmental temperature changes [3]. Of the potential thermochromic materials, vanadium dioxide, VO_2, is known to display a fully reversible semiconductor-metal transition (SMT) at a phase transition temperature (T_c) of 68 °C [4]. At temperatures below T_c, VO_2 is a semiconductor with a monoclinic crystalline structure (M phase, space group $P2_1/c$; transparent to infrared radiation (IR)). When the temperature is above T_c, VO_2 is metallic with a tetragonal crystalline structure (R phase, space group $P4_2/mnm$) a state in which the material is reflective to IR radiation [5-7]. Visible transparency is maintained through the SMT-phase transition, making VO_2 a potential candidate for energy efficient windows [8]. However, VO_2 has a rather high T_c of 68 °C, limiting its effectiveness. The T_c value can be lowered by doping with cations such as tungsten (W) or molybdenum (Mo). A green scalable approach to synthesize VO_2(M)

particles with or without dopants has been elusive [9, 10]. Various methods have been previously utilized to fabricate transparent VO_2-containing coatings for windows [7]. Vapor based deposition techniques are generally used to produce VO_2 films, but require high vacuum conditions [11]. These deposition methods are rather complex and not amendable to preparing nanoparticles in high volumes for polymer film integration [11]. Wet chemistry methods can be used to fabricate VO_2 thin films at lower costs [9]. For example, Liang et al. [12] utilized a one-step hydrothermal synthesis method to fabricate W-doped VO_2 (M) nanorods. These nanorods when mixed into composite films showed mid-infrared transmission switching of up to 31% and a phase-transition temperature of 37.3 °C. However, the utilized hydrothermal process used rather long reaction times (48 hours) at 240 °C. Chen et al. [13] prepared a coating of 0.5 at. % W-doped VO_2 nanorods and obtained a visible transmittance of T_{vis} = 57.1% and a solar modulation efficiency of ΔT_{sol} = 8.1% with a T_c at 47 °C. But again, the W-doped VO_2 nanorod synthesis method required a relatively long time (72 h) at 280 °C. Li et al. [14] have synthesized Mo-doped VO_2/TiO_2 composite nanocrystals and prepared a film with a T_c of 38.7 °C and a ΔT_{sol} of 35%, but similarly, a long hydrothermal heating process of 48 h at 220 °C was required. To the best of our knowledge, there are no systematic studies regarding preparing W doped VO_2 using a scalable room temperature (RT) method followed by a short time annealing process.

The present study aimed to examine a simple scalable RT method in water to prepare VO_2 (M) materials suitable to improve the infrared switching efficiency and visible transparency of polymeric coatings. This study began with the optimization of vanadyl acetylacetonate ($VO(acac)_2$) concentration in aqueous solution and annealing time conditions for the synthesis of VO_2 monoclinic phase (i.e. VO_2(M)) via the hydrolysis of ($VO(acac)_2$) with HCl in water at RT. Then, the effect of dispersion quality of VO_2(M) and its concentration in hydrophilic (P4VP, PVP)

and hydrophobic (PMMA) polymers was examined on the optical performace of the coatings. VO_2(M)/P4VP and VO_2(M)/PVP films demonstrated excellent IR modulation ($\Delta T_{IR@2500nm}$=47% and 40%) with high visible transmittance ($T_{vis@680nm}$=41% and 35%), respectively, better than the VO_2(M)/PMMA films with ($\Delta T_{IR@2500nm}$=30%, $T_{vis@680nm}$=29%), formulated under the same conditions. The excellent performance of hydrophilic coatings is attributed to the well dispersed VO_2(M) particles in P4VP and PVP, driven by repulsion between the VO_2(M) (IV) target particles and vanadium(V) oxide small nanoparticles which are always co-synthesized in the un-doped case.

5.2 EXPERIMENTAL SECTION

5.2.1 Materials

Vanadyl acetylacetonate ($VO(acac)_2$, 98%), hydrochloric acid (HCl, 37% in H_2O), ammonium tungstate (99.99% trace metals basis), polyvinylpyrrolidone (PVP, average molecular weight 40 kDa), poly(methyl methacrylate) (PMMA, average molecular weight ~120 kDa) and poly(4-vinylpyridine) (P4VP, average molecular weight ~60 kDa) were purchased from Sigma-Aldrich, Canada. Ultra-high purity argon (99.9%) was purchased from Praxair. Anhydrous ethyl alcohol (95%) was purchased from Commercial Alcohols, Inc., Canada. Glass substrates (VWR Microscope Slides) were purchased from VWR International. All chemicals were used as received without any further purification.

5.2.2 Synthesis of VO_2(M) and W-doped VO_2 particles

VO_2 and W-doped VO_2 particles were synthesized via a hydrolysis step followed by a calcination process. Briefly, 1.0 g $VO(acac)_2$ was dissolved in 28 mL of deionized (DI) water in a round-bottom flask, to which 6 mL of HCl was added dropwise resulting in a blue solution. For the

synthesis of W-doped VO_2, various amounts of ammonium tungstate were subsequently added to the solution. Afterwards, whether doped or un-doped, the solution was stirred continuously at room temperature for 24 h. After evaporation of the solvent using a rotary evaporator, the crude products were harvested and dried in a vacuum oven at 65 °C for 12 h. Crude products were also obtained using a freeze-drying process. The product first frozen for 12 h, then the solvent (water) is removed by sublimation, diffusion and desorption drying process using a freeze-dryer for 24 h. Thereafter, the respective crude was calcined at 450 °C for different times under inert gas (argon) in a tube furnace (yield > 80%). The proposed hydrolysis reaction is depicted in Figure 5.1.

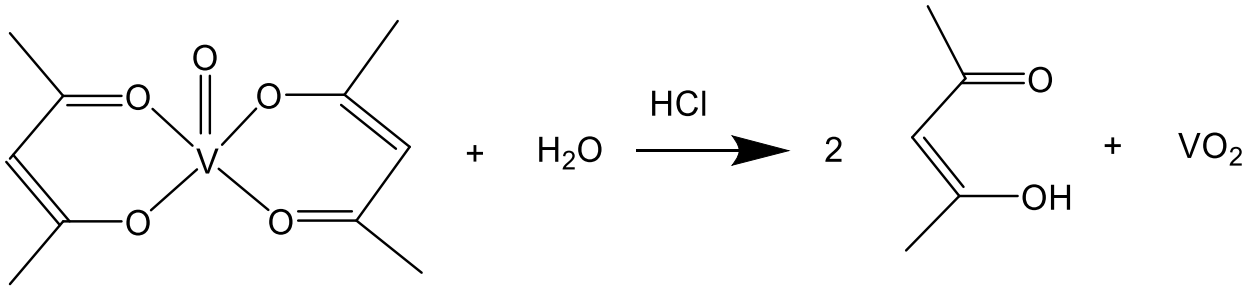

Figure 5. 1 Hydrolysis of $VO(acac)_2$ into VO_2 via HCl catalysis.

5.2.3 Fabrication of VO_2/PVP and W-doped VO_2/PVP coated glass

To prepare VO_2(M)/polyvinylpyrrolidone(PVP) coatings on glass, 0.16 g of W-doped or un-doped VO_2 (M) was dispersed in 2mL of ethanol to which 0.08 g of polyvinylpyrrolidone (PVP) was added, then followed by sonication at 50 °C for 60 min. 0.3-0.5 mL of the above solution was coated on a glass slide using a spin-coater at 3000 rpm for ca. 10 s. The coatings were dried in a vacuum oven at 80 °C for 30 min. The thicknesses of the coatings were approximately 250 - 350 nm according to SEM analysis (Hitachi, Tokyo, Japan).

5.2.4 Fabrication of VO_2/PMMA coated glass

To prepare VO_2(M)/poly methyl methacrylate (PMMA) coatings on glass, VO_2 was dispersed in a small vial containing 2 mL toluene to which PMMA was added (ratios see below), followed by sonication at 50 °C for 60 min. The weight % ratios of VO_2:PMMA (wt. %:wt. %; in toluene solvent) were 2.3:4.6, 4.5:4.5, 2.2:8.9 and 4.3:8.7, respectively. Subsequently, 0.3-0.5 mL of these VO_2/PMMA solutions was spin coated each at 1000, 2000 and 3000 rpm for ca. 10s onto a glass slide. The coated glass samples were dried in a vacuum oven at 80 °C for 30 min. The coating thicknesses are in the range of 0.6 to 2.1 μm, measured by SEM (Hitachi, Tokyo, Japan).

5.2.5 Fabrication of VO_2/P4VP coated glass

VO_2(M)/poly 4-vinylpyridine (P4VP) coatings on glass slides were prepared by dispersing VO_2 in 2 mL acetic acid in a small vial, adding P4VP and sonicate the solution at 50 °C for 60 min. The ratios of VO_2:P4VP (wt. %:wt. %; in acidic acid solvent) were 2.3:4.6, 4.5:4.5, 2.2:8.9 and 4.3:8.7, respectively. Subsequently, 0.3-0.5mL of the above VO_2/P4VP solution were spin coated at 1000, 2000 and 3000 rpm, respectively, for ca. 10s onto glass slides. The coated glass samples were dried in a vacuum oven at 80 °C for 30 min, with coating thicknesses in the range of 1 to 2.5 μm (measured by SEM (Hitachi, Tokyo, Japan)).

5.2.6 Characterization

The crystallinity of the synthesized VO_2 particles was examined by X-ray diffraction (XRD; Bruker D2 phaser powder diffractometer, Billerica, MA, USA) using Cu Kα radiation ($\lambda_{K\alpha}$ = 1.54059 Å) with a scanning rate of 0.25°/second. The transition temperatures of VO_2 were determined by differential scanning calorimetry (DSC; SDT Q600, TA Instruments, Dallas, TX, USA) using a cooling-heating-cycle between 0-90 °C, with both rates set at 10 °C/min. The data was analyzed via the instrument's software (Universal Analysis 2000, TA Instruments, Dallas,

TX, USA). The optical transmittances were measured with a UV-3600 UV-VIS-NIR spectrophotometer (Shimadzu, Kyoto, Japan) at a wavelength range of 250 – 2500 nm. The temperature was controlled using a Julabo F12-refrigarated/heating circulator (Julabo, Seelbach, Germany). The infrared modulation at 2500 nm was obtained from the equation $\Delta T(\lambda) = T(\lambda)_s - T(\lambda)_m$, where s and m represent semiconductor (sample at 22 °C) and metal (sample at 80 °C), respectively [15]. Scanning electron microscopy (SEM, Quanta 200) was used to study the morphologies and dimensions of particles and their aggregates in the PVP polymer coating (on glass substrates). The particle aggregates in the PMMA and P4VP polymer coatings and their coating thicknesses on the glass substrates were investigated with a Hitachi S-4500 field emission SEM (Hitachi, Tokyo, Japan). The elemental analysis of the samples was carried out by energy dispersive X-ray spectrometry (EDX) combined with scanning electron microscopy (SEM, Quanta 200). The average particle sizes of VO_2 particles were measured using Malvern Zeta-sizer Nano-ZS DLS (dynamic light scattering, Malvern, UK) instrument.

5.3 RESULTS AND DISCUSSION

5.3.1 Characterization of VO_2(M) reacted for 24 h at RT

To obtain a pure monoclinic phase of VO_2 (synthesized at RT, 24 h), the aqueous solution of $VO(acac)_2$ at variable concentrations between 0.00005 mol/L(pH=3) and 0.19 mol/L(pH=-0.6) were examined (Figure 5.2). As shown in Figure 5.2a,b, the concentrations between (0.19-0.05mol/L) produced blue solutions of VO^{2+} ions (V(IV)) [16]. However, when the concentration decreased to 0.03 mol/L, a solution of mint green color was obtained, which is an indication of V(V) ion formation [16](Figure 5.2c). The green color was distinct at 0.01 mol/L (Figure 5.2d) and lower concentrations (i.e. Figure 5.2e).

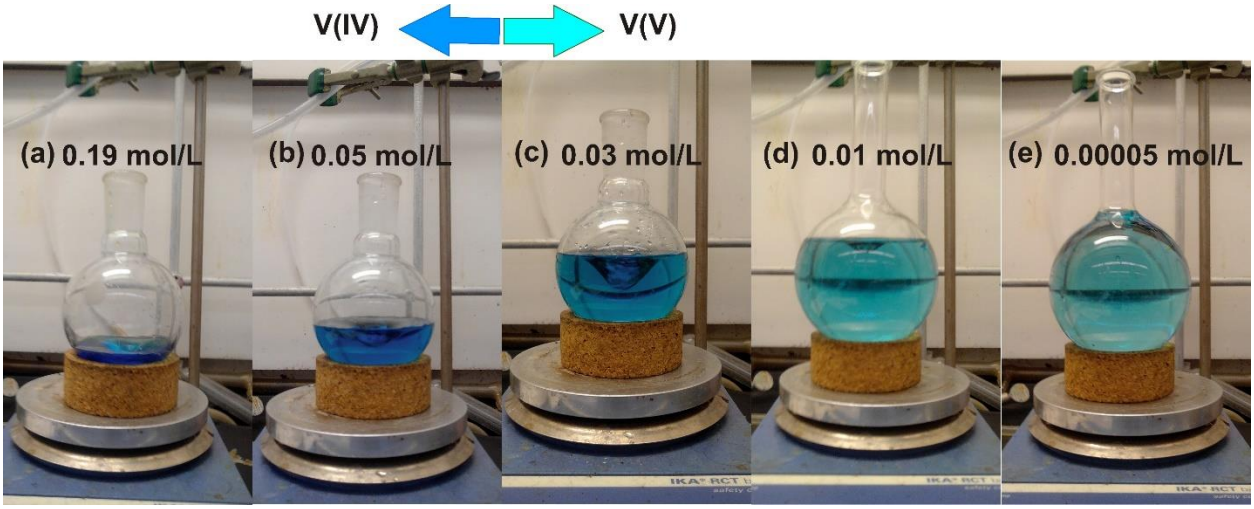

Figure 5. 2 Solution of $VO(acac)_2$ at different concentrations.

The produced VO_2 samples were examined using various annealing times (1-5 h) by XRD analysis for phase identification (Figure 5.3). Un-calcined samples do not show any diffraction peaks, indicating the amorphous nature of the material. The Bragg peaks for samples calcined for 1-3 h suggest a metastable VO_2(B) phase of vanadium dioxide [17]. A pure monoclinic VO_2 phase

is only obtained after 4 h of calcination with diffraction peaks at 28°, 37.2°, 40.4°, 42.4°, 55.6°, 57.6°, 65.7° and 70.9°, which represent the planes (011), (-211), (002), (210), (220), (022), (013) and (-231) of monoclinic VO_2, respectively [11]. The small unidentified peaks in the XRD spectra may represent some unknown phases of nonstoichiometric vanadium oxides [18]. VO_2(M) at 4 h calcination was chosen to be continued for more in-depth study. The as-synthesized sample was further investigated at various calcination temperatures (450-800 °C) for 1 h, but without any success.

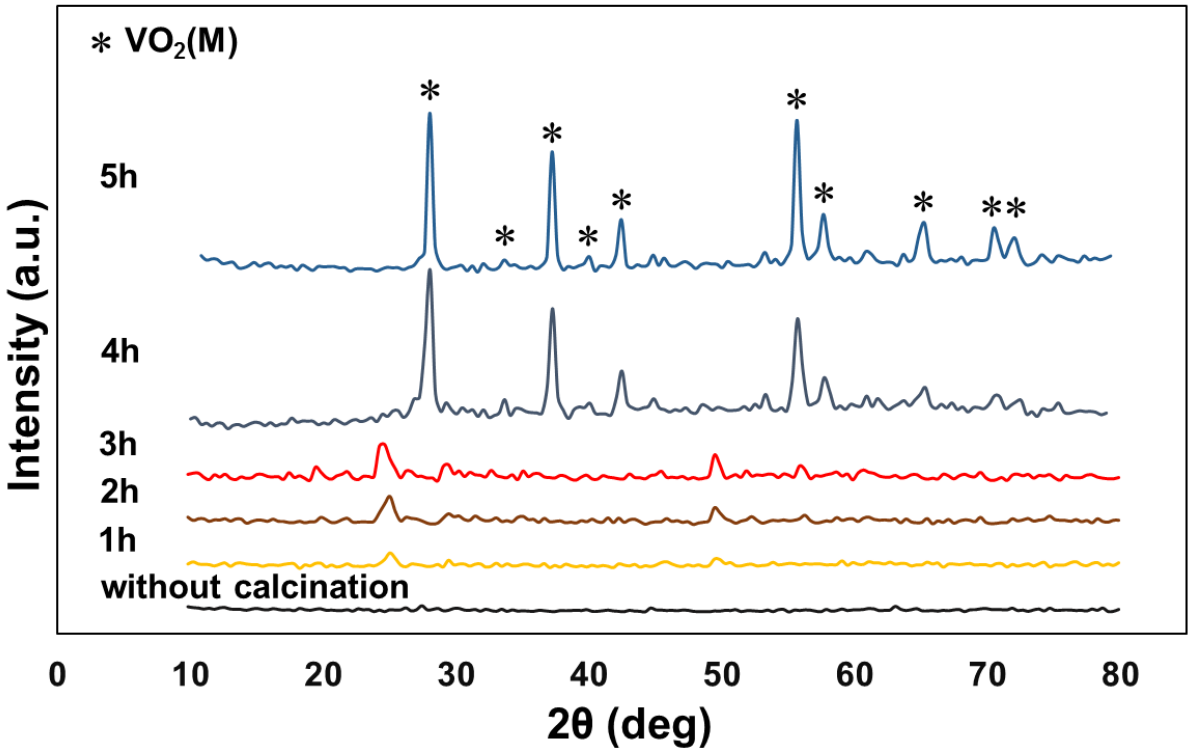

Figure 5. 3 XRD spectra of un-doped VO_2 reacted for 24 h at RT before and after calcination at 450 °C for 1-5 h. The stars depict diffraction peaks of the monoclinic VO_2(M) phase.

FTIR investigation (Figure 5.4) was conducted to verify the synthesis of VO_2(M) via the hypothesized room temperature (RT) strategy followed by a calcination at 450 °C for 4 h. The

samples were prepared by grinding the dried sample with potassium bromide (KBr) powder in the ratio of ~1:200 (sample: KBr) and then compressed to form discs. The FTIR result before calcination (Figure 5.4b), shows a broad absorption band at 3386 cm^{-1} and a medium band at 1628 cm^{-1} which are assigned to the stretching and bending vibrations of hydroxyl groups, ν(O-H), respectively. These vibrations occur due to absorbed water molecules on the sample surfaces [12]. They are reduced substantially in the FTIR spectrum of the calcined sample, indicating that a dehydration process occurred during calcination (Figure 5.4c). Before calcination, the VO_2 shows stretching vibrations at 499 cm^{-1} for ν(V-O-V) and 997 cm^{-1} for ν(V=O) [19], typical for the amorphous material (Fig 1b). After annealing, the peak at 997 cm^{-1} shifts to 1003 cm^{-1}, while the peak at 499 cm^{-1} splits into three peaks (744, 544, and 449 cm^{-1}). The latter indicates the characteristic stretching vibrations of VO_2(M), which agrees well with the findings by Xia et al. [20] and confirms the effect of O–H stretching produced by lattice water [21]. The precursor, $VO(acac)_2$, shows vibrations (Figure 5.4a) similar to those reported by Ndwandwe et al. [19].

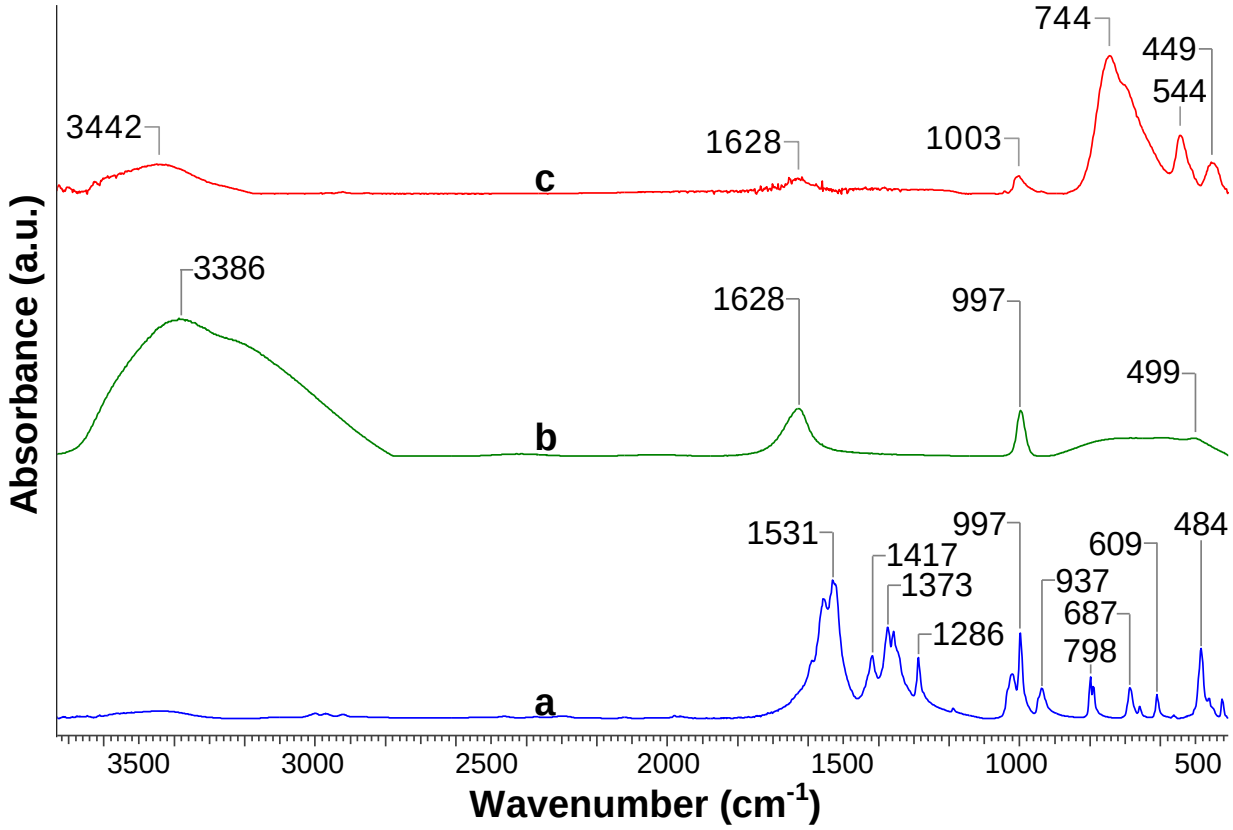

Figure 5. 4 FTIR spectra of (a) $VO(acac)_2$ (blue), (b) VO_2 before calcination (green) and (c) VO_2(M) after calcination (red).

To examine if the water based synthesis at RT would work with Tungsten (W) doping, the samples were reacted for 24 h at RT and then calcined at 450 °C for 4 h before XRD analysis. Diffraction patterns of W-doped VO_2 (W content: 0 at. %, 2.5 at. %, 5 at. % and 10 at. %) are shown in Figure 5.5. In Figure 5.5a, the diffraction peaks can be assigned to the crystal planes of VO_2(M) (JCPDS card no. 82-0661) [15] which are marked with a star (*). Figure 5.5b shows a section (26°-30°) of the XRD spectra of samples containing different amounts of W. These spectra indicate the (011) peak of the monoclinic phase (0 and 2.5 at. % W) and the (110) peak of the rutile phase (5 and 10 at. % W). In the enlarged spectra, there is no spectral shift in the position of (011) peak between the un-doped and 2.5 at. % W-doped VO_2 . The incorporation of W into the VO_2(M)

crystal lattice led to a narrower and less intense (011) M peak, an indication that large particle sizes with deteriorated crystallinity were formed during calcination of 2.5 at. % W-doped VO_2 samples (see Table 5.1 for particle sizes). With increasing W concentration (5 at. % and 10 at. %), the diffraction peaks are shifted toward a lower angle (from 28° to 27.4°). This significant peak shift depicts a different crystal phase, i.e. rutile phase (JCPDS card No. 79-1655). It was previously reported that rutile VO_2(R) phase can be formed at room temperature [13, 22], a result also indicating that W may dramatically stabilize the rutile phase VO_2(R) at room temperature. The ionic radius of the tungsten cation (W^{6+} for 6-coordinate: 60 pm) is slightly larger than the ionic radius of vanadium cation (V^{4+} for 6-coordinate: 58 pm). Consequently, exchanging V by W leads to an expansion of the interplanar distance, d, and thus, according to Bragg's law [$d = \lambda/(2\sin\theta)$], to a shift towards lower diffraction angles [23].

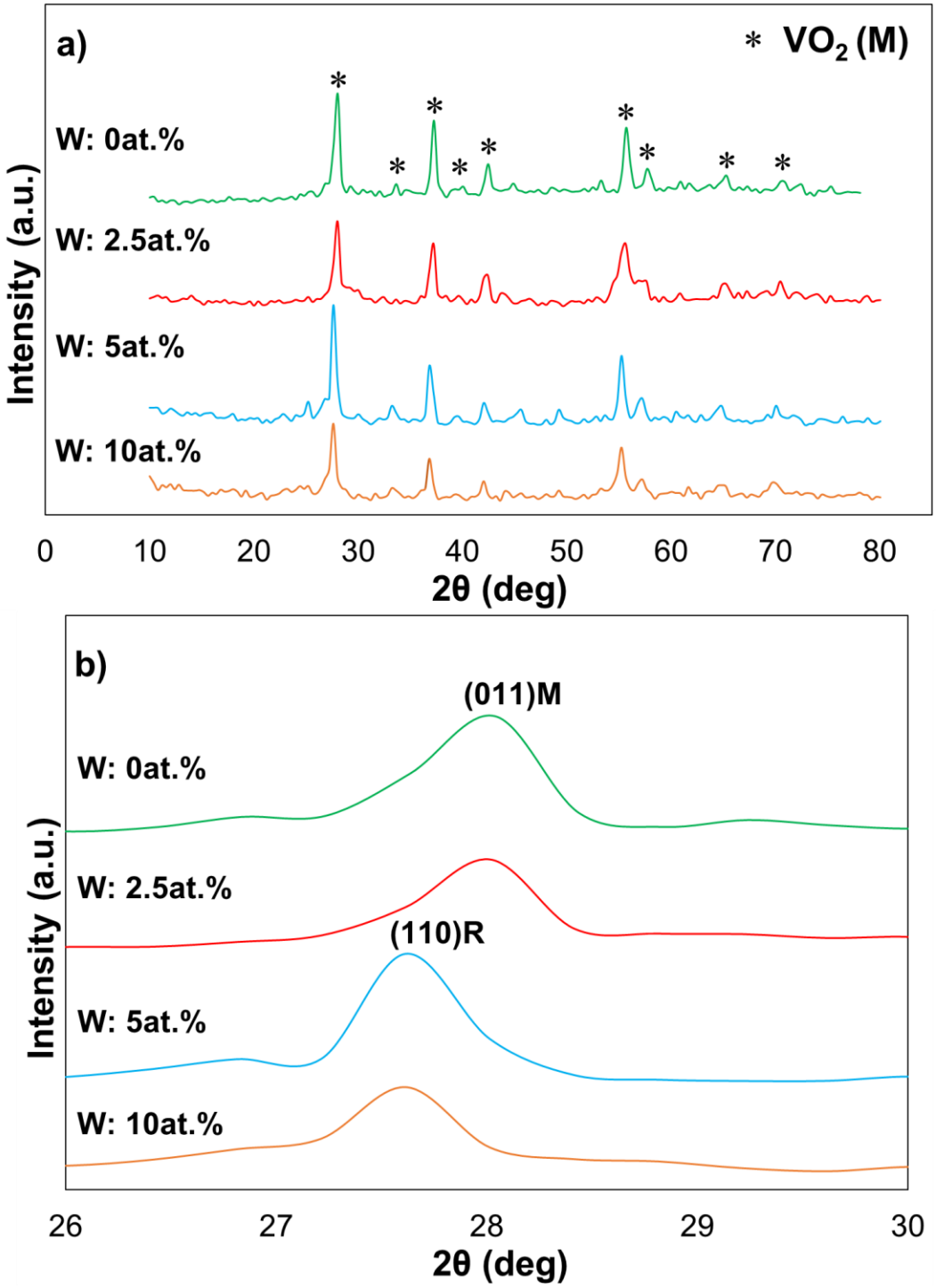

Figure 5. 5 XRD spectra of VO_2 (M) with various nominal contents of tungsten: (a) the entire XRD spectrum and (b) an enlargement of the spectra between 26° and 30°.

Tungsten is well known to be an effective dopant to decrease the phase transition temperature of VO_2 close to RT. W-doped VO_2(M) samples shown in Figure 5.5 were examined by differential scanning calorimetry (DSC) (Figure 5.6). The endothermic phase transition temperature (T_c) of VO_2(M) decreased from 68 °C to 45 °C with increasing W-content. Based on Wu, Y. et al., this is due to the de-twisting of the monoclinic VO_2 lattice by W-doping stress, which reduces the band gap and hence lowers the potential energy barrier for phase transition [24]. Although the transition temperature of 5 at. % and 10 at. % was found at 52 °C and 45 °C, respectively, the transition shows an onset at much lower temperature (~at RT). This confirms the existence of some of the VO_2(R) phase at RT. A T_c of 45 °C for the 10 at. % W-doped VO_2 was achieved via the RT reaction, which is close to 40 °C, the "standard T_c" for an application in smart window design [23]. However, increasing the W content to 5 and 10 at. %, the system decreases the optical switching performance. As shown in Figure 5.6, the latent heat (calculated from the heating cycles of the DSC data) decreased from 30 J/g to 19.5 J/g, 10.8J/g and 8.5J/g with increasing W-content. This is due to the competition between doping-induced deferment of phase transition (Tc) and doping-induced crystallinity enhancement [22]. The appearance of two endothermic transition peaks for un-doped VO_2 in the DSC data (Figure 5.6), is due to a double population of particle sizes (see Figure 5.8a) [25, 26]. 10-cycles DSC heating/cooling scans for 2.5 at. % W-doped VO_2 sample is shown in Figure D1. To confirm that the hydrolysis of $VO(acac)_2$ occurs at RT, and not during rotary evaporation or during the drying process in an oven, the un-doped/doped samples were freeze-dried after reflux while maintaining identical synthesis conditions. The DSC peaks intensified, and the latent heat increased for all freeze-dried samples as shown in Figure 5.7, possibly due to moisture reduction (except for the 10 at. % W sample which shows no peak at all; not shown).

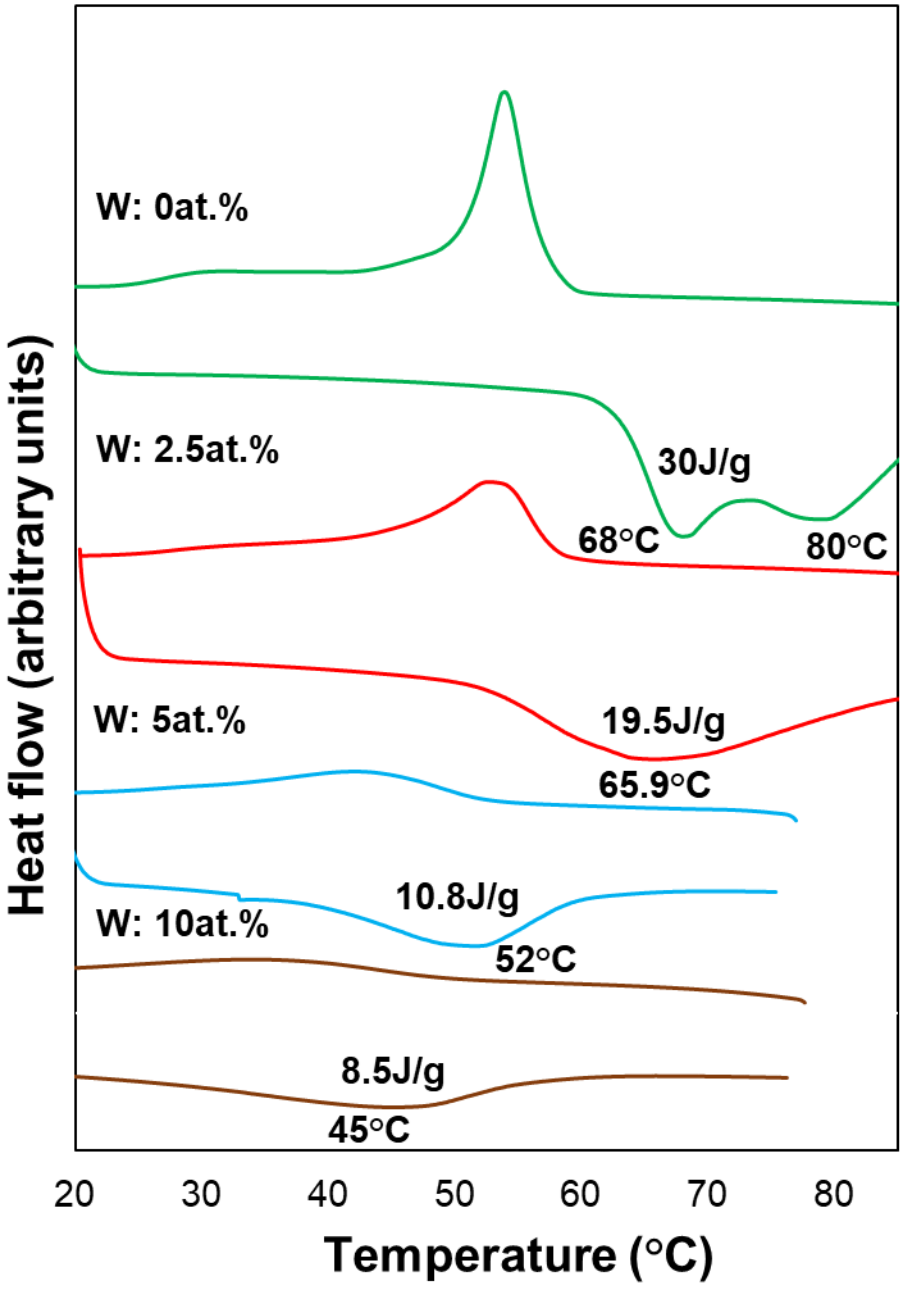

Figure 5. 6 DSC spectra of VO_2(M) at various nominal contents of tungsten after 24 h of reaction and calcination at 450 °C for 4 h.

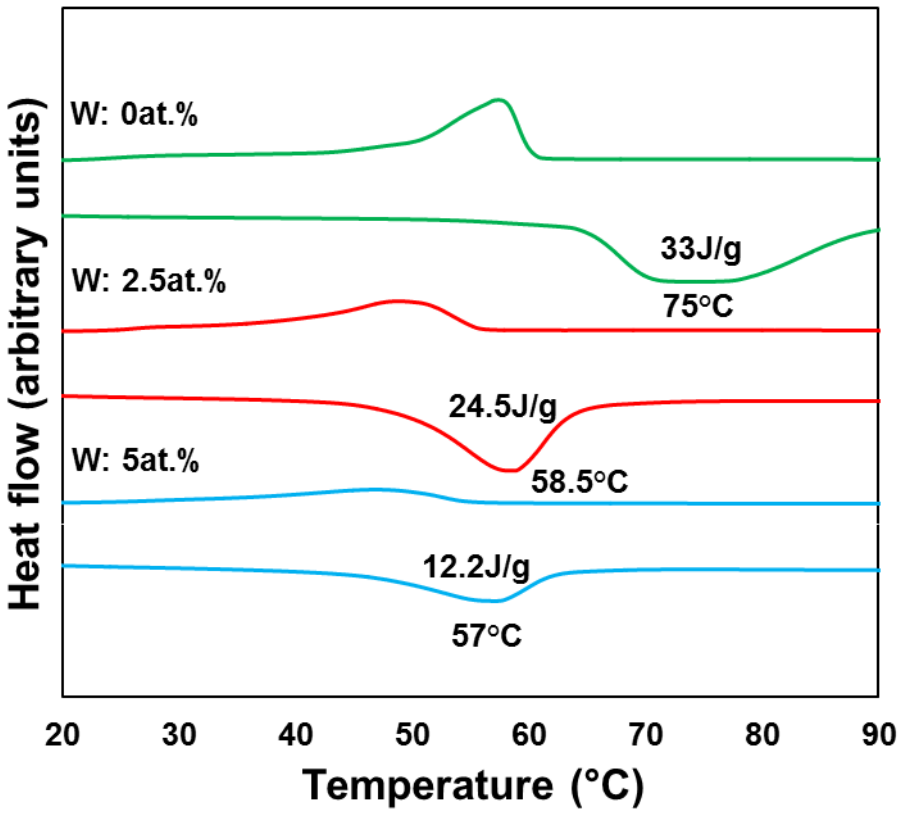

Figure 5. 7 DSC spectra of VO_2(M) at various nominal contents of tungsten after 24 h of reaction using freeze-drying process.

The morphologies of both the un-doped and W-doped VO_2 particles were characterized by SEM (Figure 5.8). The un-doped VO_2 (Figure 5.8a) depicts two particle populations with different sizes. Small NPs with diameters of ~50 nm are blended with particles of ~300 nm diameter (Figure 5.8a, red circles). To separate the small NPs from the large particles, ethanol was added to the un-doped VO_2 powder, then centrifuged (Thermo Scientific Sorvall Legend RT+ centrifuge) at 4500 rpm for 10 mins. The large VO_2(M) particles yielded a black color (vanadium(IV) oxide) that precipitated at the bottom (Figure 5.9a) while the yellow supernatant with the small NPs (vanadium(V) oxide) [27] were layered above (Figure 5.9b). Thermochromic behavior was not found for the coating

made with the small NPs from the yellow supernatant, confirming vanadium (V) oxide. The dynamic light scattering (DLS) data on average size for the VO_2 hence needs to be interpreted carefully. According to DLS data (Figure D2, in Appendix D), the size distribution histogram of VO_2 by intensity and volume shows bimodal-like distribution. One peak with an average size between 47-50 nm (2-13%) and the second with 309-392 nm (87-98%). This is further confirms the dual populations of the particle sizes. Doped VO_2, on the other hand, showed single particle population only (Figure 5.8b). Size uniformity of VO_2 particles with W-addition agrees well with Shen et al. [22]. The morphology of the 5 at. % sample shows agglomerated leaf-like structures (Figure 5.8c). Reaching a W-content of 10 at. %, a flower like morphology is seen, with needle like particles (Figure 5.8d). Obviously, the W-concentration controls the particle growth and morphology.

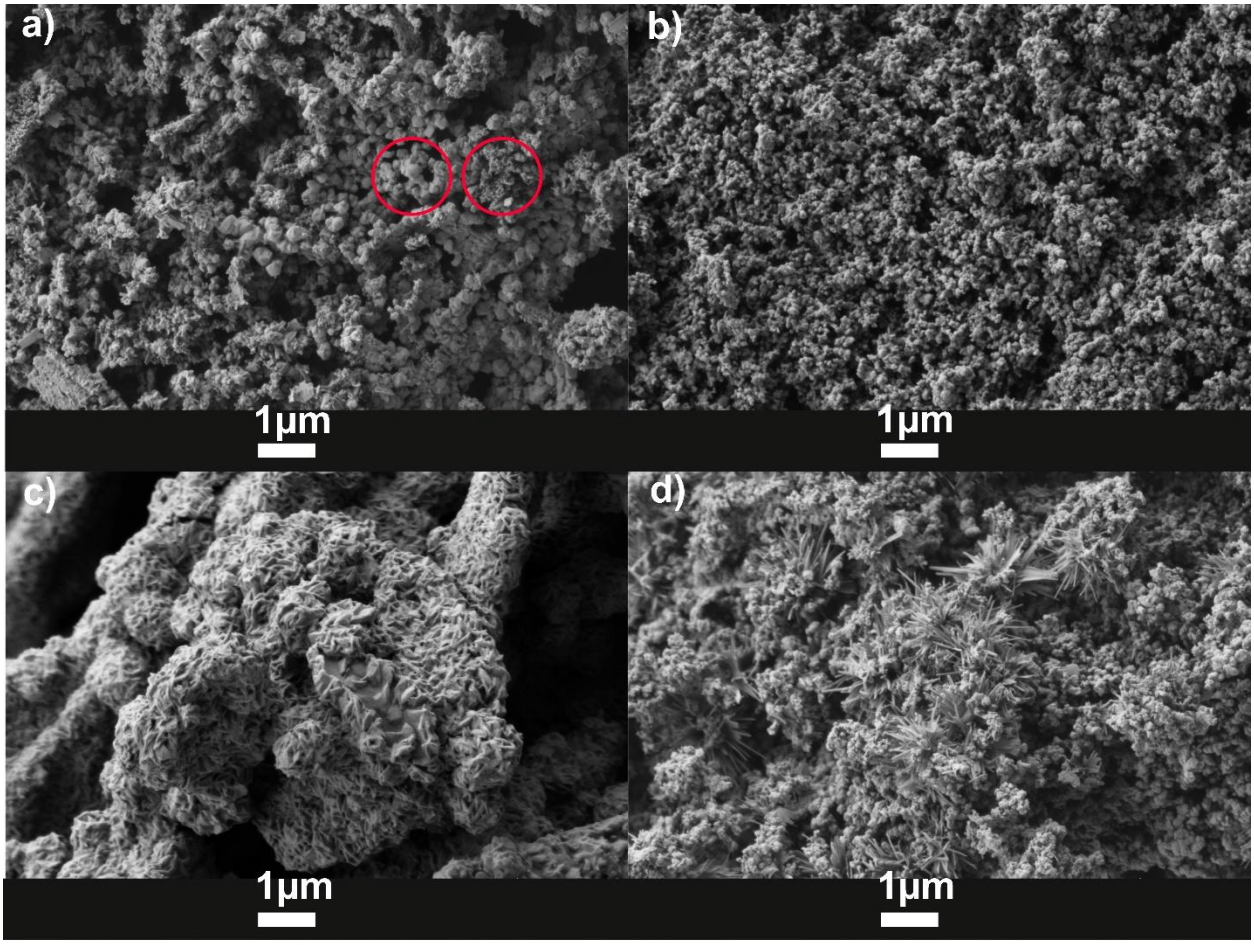

Figure 5. 8 SEM images of VO_2 (M) reacted for 24 h at RT for the nominal W-contents after calcination at 450 °C for 4 h. (a) 0 at. %, (b) 2.5 at. %, (c) 5 at. %, and (d) 10 at. %. The red circles indicate examples of each particle population.

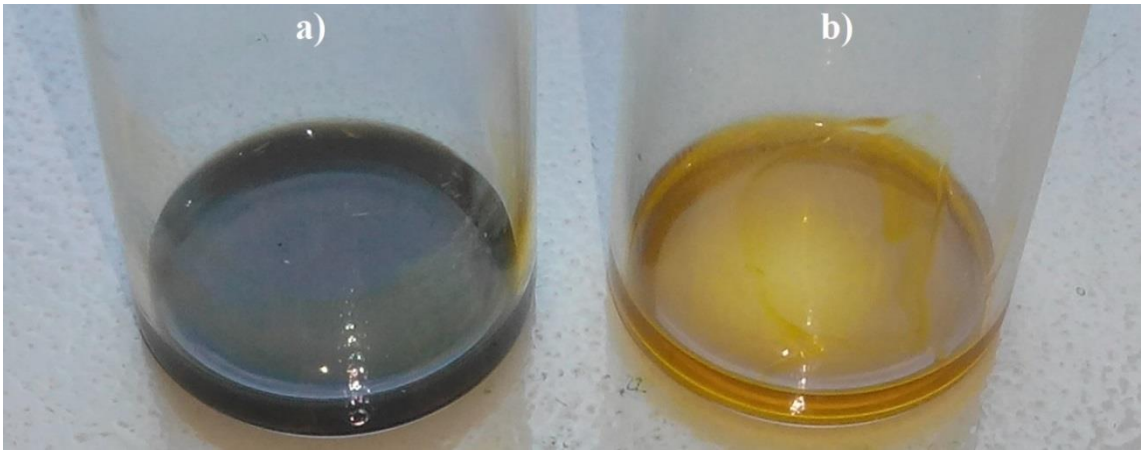

Figure 5. 9 Centrifuged un-doped VO_2 NPs in ethanol. (a) Large particle population precipitate yielding black color vanadium(IV) oxide, and (b) small NPs in the collected supernatant.

The average particle (aggregates) sizes were investigated with dynamic light scattering (DLS, Zeta-sizer, Table 5.1). Without calcination, the amorphous material shows an average object size of ~4 µm, obviously an agglomerate. Upon calcination at 450 °C for 4 h, the average particle size decreased to ~233 nm. With increasing W-content and identical calcination conditions, the average particle size increased to 440 nm. The average particle sizes agree with SEM (Figure 5.8). A similar trend of particle size increase was obtained with increasing W concentration using Scherrer's equation (Table 5.1), although the size of particles were much smaller. The reason for the size variance between the methods, is that the Zeta-sizer provides information on aggregate size and hydrodynamic volume [28]. The Scherrer technique is an approximation based on a crystallite (coherently scattering region) size present in the grain and measures domain rather than particle [29]. The particle size increase with W-content increase is due to the high valence of W-ions compared to V-ions. When (W^{6+}) replace (V^{4+}) sites in the monoclinic VO_2 crystal lattice, the negative charge defects on the surface of grains may increase driven by charge balance [30]. Increasing the concentration of these defects can create an electric dipole that speeds up the diffusion of the VO^{2+} ions in solution, thus leading to an enhanced growth of VO_2 grains [30].

Table 5. 1 Average diameter of W-doped VO_2 particles investigated with DLS (Zeta-sizer) and Scherrer equation.

Nominal content of W(at. %)	Calcination at 450°C for 4h	Average size (nm) using Zeta-sizer	Average size (nm) using Scherrer eq
0	No	3900.0 ± 4.9	
0	Yes	232.9 ± 1.3	81.9±1.2
2.5	Yes	255.0 ± 3.2	136.4±1.5
5	Yes	265.5 ± 1.0	204.7±1.3
10	Yes	440.3 ± 6.5	272.9±1.0

The hysteresis, ΔT (°C), in the DSC spectra is the difference between the temperature of the endothermic and the exothermic peak during heating and cooling cycles, respectively. Table 5.2 summarizes the hysteresis data for the W-doped samples reacted for 24 h at RT. ΔT (°C) decreases with increasing the W-content (except for the highest concentration). This is due to the decreasing of T_c, agreeing well with Li et al. [14].

Table 5. 2 T_c and hysteresis of the W-doped VO_2 samples reacted for 24 h at RT.

W [at.%]	$T_{c\text{-heating}}$ (°C)	$T_{c\text{-cooling}}$ (°C)	Hysteresis ΔT (°C)
0	68.0	54.4	13.6
2.5	65.9	53.4	12.5
5	52.0	42.7	9.3
10	45.0	34.8	10.2

The presence of W, V, and O are confirmed by EDX analysis (Figure 5.10). The V and O representative peaks are present in all samples. The representative peaks for W are present in all W-doped VO_2 samples. The intensity of the W-peaks is increasing with W-concentrations, confirming a successful W-doping into the VO_2 lattice. Table 5.3 shows the real W-concentrations obtained by EDX analysis. The real concentration is less than the nominal content which agrees

with findings of Chen et al. [13] and Huang et al. [23] but is in discrepancy with Shidong et al. [31].

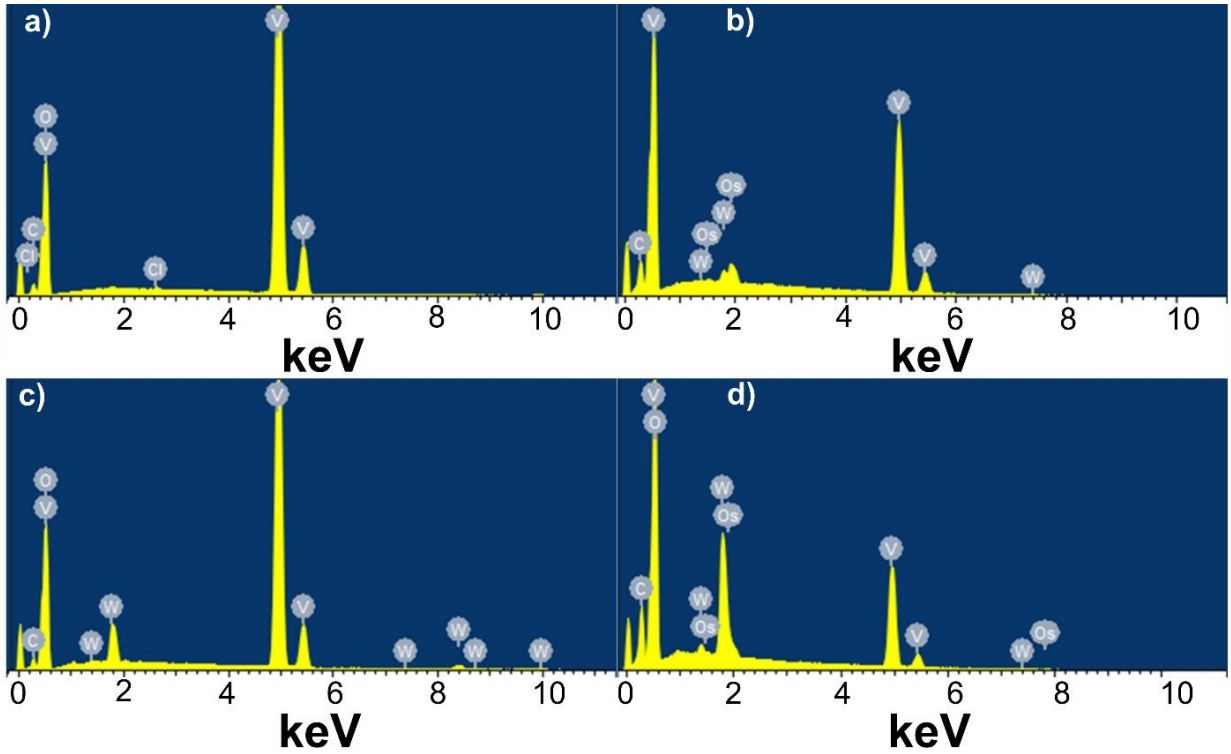

Figure 5. 10 EDX spectra of VO_2 (M) with various W-contents reacted for 24 h at RT after annealing at 450 °C for 4 h: (a) 0 at. %, (b) 2.5 at. %, (c) 5 at. % and (d) 10 at. %.

Table 5. 3 Real W-concentrations for doped VO_2 reacted for 24 h at RT at different nominal W-contents from EDX data evaluation.

Nominal content of W [at. %]	Real W concentration [at. %]
0	0
2.5	1.2 ±0.1
5	4.2 ±0.3
10.0	8.0 ±0.2

A T_c reduction efficiency of 5.42 K/at. % for W-doped VO_2 particles was found by plotting T_c versus the real W-concentration (Figure 5.11). The T_c reduction coefficient obtained here is low

compared to literature values. Dong et al. [32] achieved 19.8 K/at. %, and Wang et al. [33] achieved 17.2 °C/at. %, however, both used a high-energy consumption hydrothermal method.

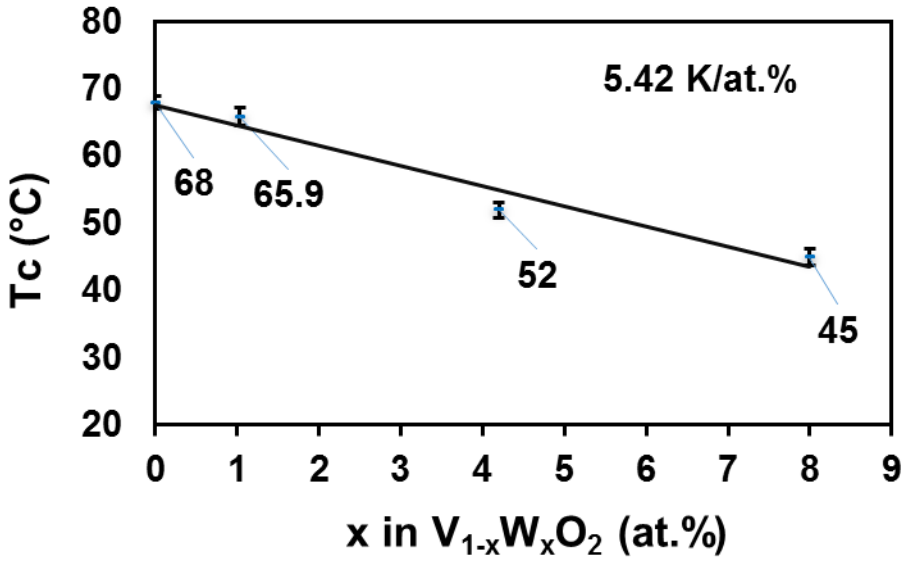

Figure 5. 11 T_c versus real W-concentration. The line is a least square linear fit.

5.3.2 Characterization of VO_2(M) reacted for 72 h at RT

The effect of reaction time (72 h) on the crystallinity and T_c of VO_2(M) was examined by XRD and DSC, respectively. The XRD spectra for un-doped and W-doped VO_2 reacted for 72 h at RT are shown in Figure 5.12a. A pure VO_2(M/R) spectra is obtained for all W-doped samples. The XRD peaks' full width at half maximum (FWHM) for W-doped VO_2 (72 h reaction) are much wider than the peaks' FWHM of W-doped VO_2 (24 h reaction). According to Scherrer's equation, this implies a small size particle synthesis. The strongest diffraction peak, (110)R, was present at 27.6° for all samples, suggesting that some VO_2(R) phase (JCPDS card No. 79-1655) was already formed at room temperature [13, 22].

The DSC spectra for doped and un-doped VO_2 reacted for 72 h at RT are shown in Figure 5.12b. Increased W-contents led to a decrease in latent heat (25 J/g, 4.8 J/g, 0 J/g and 0 J/g), probably due to poor crystallinity and a lower purity of monoclinic VO_2 phase with high W-doping concentration [34]. The endothermic T_c and ΔT (°C) decreased from 73 °C to 64 °C and from 16 °C to 9 °C, respectively with W-doping at 2.5 at. %. The thermo-chromic properties are deteriorated for 5 and 10 at. % W-doped VO_2.

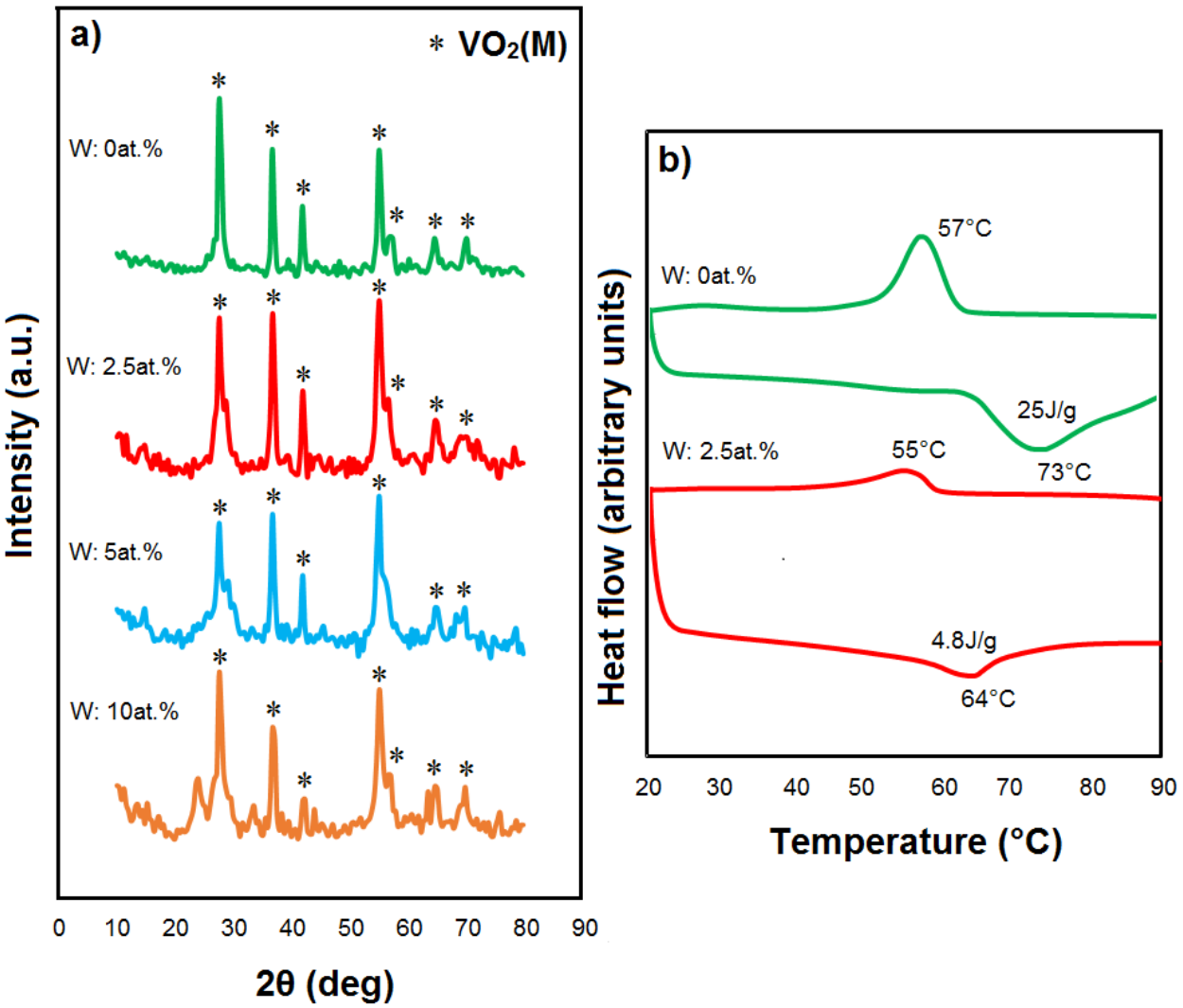

Figure 5. 12 (a) XRD spectra and (b) DSC spectra of VO_2(M) at various nominal contents of tungsten after 72 h of reaction. The stars (*) depict the VO_2 diffraction peaks of the monoclinic phase ((JCPDS card no. 82-0661).

5.3.3 Dispersion of VO_2 Particles in PVP coatings

Polyvinylpyrrolidone (PVP) was chosen to improve the physical gelation of the coating through the interactions between carbonyl groups (-) and amine groups (+) of PVP [35]. Additionally, the interaction between VO^{2+} ions and carbonyl groups (-) of PVP can potentially improve the dispersion of VO_2 particles and uniformity of the film [36]. VO_2/PVP coatings on glass were prepared by dispersing the VO_2 particles in ethanol to which PVP was added. Then the solution was sonicated, coated on a glass slide and dried in a vacuum oven. Dispersion of pristine and doped materials in PVP were examined by SEM. The SEM images of Figure 5.13a and b, images of un-doped VO_2 in PVP coatings on glass in two magnifications, show well dispersed particles, whereas the 2.5 at. % W-doped VO_2 particles in PVP (Figure D3) show agglomerated particle structures. The un-doped VO_2 sample consists of a double population of particles with respect to size and material (Figure 5.8a and Figure 5.9). A Coulomb repulsion between the large positively charged vanadium(IV) oxide particles and the small, also positively charged vanadium(V) oxide NPs might be responsible for the stable distances between the un-doped particles (Figure 5.13a and b). In the enlarged SEM image of Figure 5.13b, a ring of small NPs around large particles are depicted by a red circle. The particle number density per unit area in Figure 5.13a, was found to be 667 (±4) n/mm^2 (where "n" is the number of large particles). The uniformity of particle distributions in the film (Figure 5.13a) was estimated based on the number of large particles (n) per unit area (mm^2) at three different locations as shown by histogram in Figure D4. For the first time, VO_2 particles have shown a proper dispersion in a polymer coating which is necessary for smart window

application. Clusters and agglomerates of particles in a transparent coating lead to light scattering which will make the coating opaque with a milky appearance, unacceptable for window applications. As shown in Figure D5, bimodal distribution was also obtained using ImageJ software analysis for the SEM image of Figure 5.13. Unfortunately, agglomeration is observed for 2.5 at. % (Figure D3), probably due to a high hydrophilicity at low W content [37].

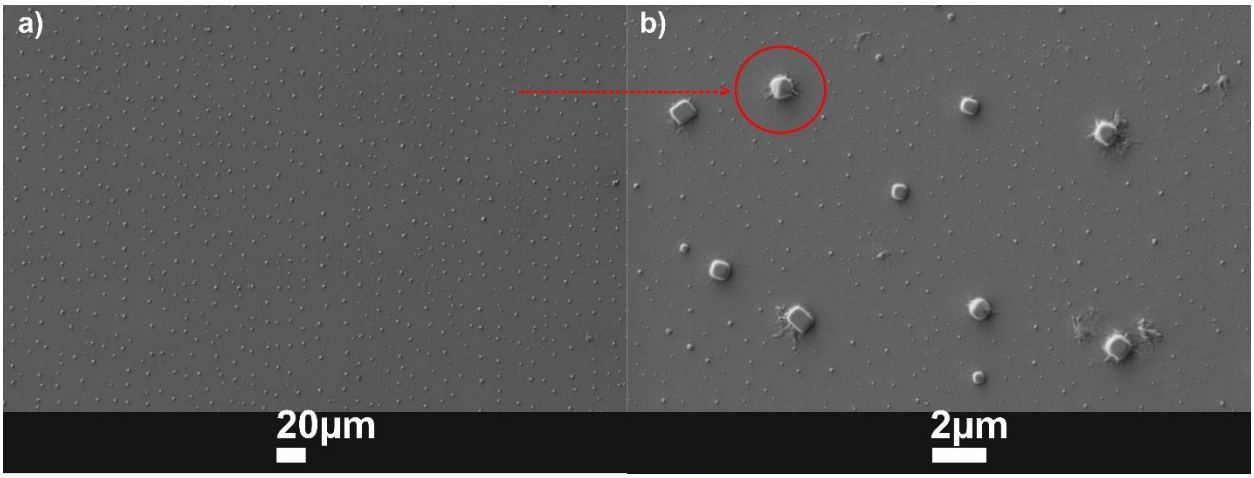

Figure 5. 13 SEM images of VO_2(M) dispersed in PVP coatings on glass. (a) and (b) un-doped with different magnification (see scale bar).

5.3.4 Thermo-chromic properties of VO_2 dispersed in PVP coatings on glass

Thermochromic properties of un-doped VO_2 (M) and W-doped VO_2 NP in PVP coatings on glass were investigated by UV-VIS-IR spectrophotometry. The transmittance spectra between 250 - 2500 nm at 22 °C and 80 °C are depicted in Figure 5.14a for the un-doped and in Figure 5.14b for the W-doped VO_2. The SMT was clearly observed in both coatings. The infrared (IR) transmittance modulation achieved, $\Delta T_{IR@2500nm}$, for the un-doped VO_2 coating was 40% with a visible transmittance, $T_{vis@680nm}$, of 35%. However, for 2.5 at. % W-doped VO_2 coating, $\Delta T_{IR@2500nm}$ was only 13% with a $T_{vis@680nm}$ of 42%. The visible transmittance was enhanced by

W-doping but a deteriorated switching behavior was observed. The reason might be a W-triggered a blue-shift of the absorption edge by widening the band gap of VO_2 [11, 38, 39]. We conclude, that the un-doped VO_2 coatings have suitable optical, thermo-chromic and dispersion properties for smart window applications. The main reason for the lower transmittance in the visible region at low temperature is due to higher refractive index (2.7–2.8) for monoclinic VO_2 phase in comparison to the rutile VO_2 phase (2.0–2.5) due to enhanced light scattering effects of the relatively large NPs [40]. Increasing the W-doping content in the coatings to 5 and 10 at. % showed little infrared (IR) modulation ability between 22 °C and 80 °C (Figure D6). UV-VIS-IR spectra were taken from PVP-coatings containing the individual small NP population (yellow supernatant). No thermochromic behavior was found for the coating made with the small NPs from the yellow supernatant, confirming vanadium (V) oxide.

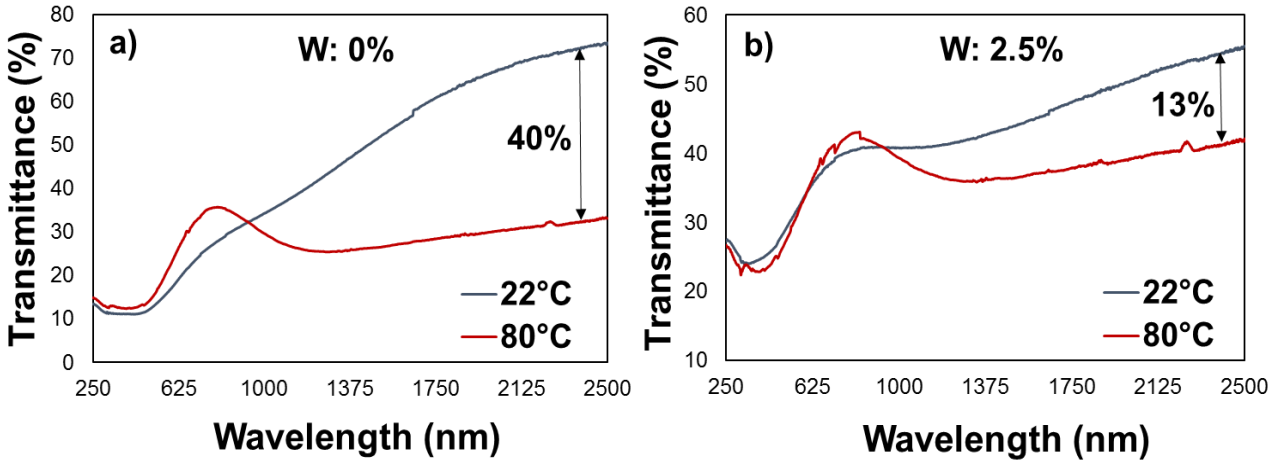

Figure 5. 14 Optical transmittance spectra of (a) un-doped VO_2/PVP coating and (b) 2.5 at.% W-doped VO_2/PVP coating.

For a fast phase transition response, a small hysteresis (ΔT_c) is a key requirement for VO_2 thermochromic coatings. The hysteresis of the VO_2/PVP and 2.5 at. % W-doped VO_2/PVP

coatings are 12.5 °C and 10 °C (Figure 5.15a and b) compare to 13.6 °C and 12.5 °C of VO_2 and 2.5 at. % W-doped VO_2 powders (Table 5.2), respectively. This indicates a reduction in hysteresis width when VO_2 powder is mixed with PVP. This hysteresis width (10 °C) is comparable to 15.8 °C and 10.7 °C for the films reported by Liang, Shan, et al. [12] and Li, Wenjing, et al. [40] respectively. However, it is higher than 8.6 °C reported by Chen, Ru, et al. [41].

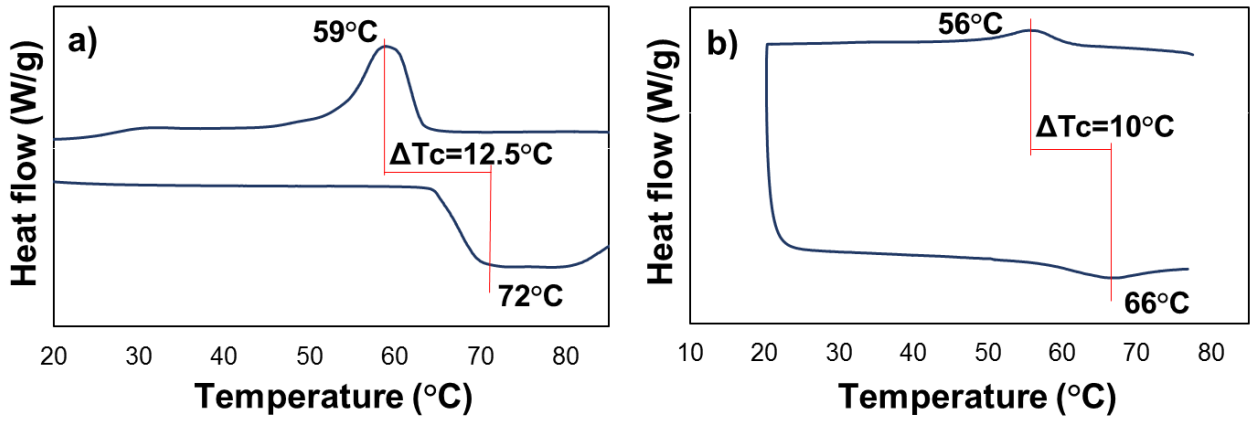

Figure 5. 15 DSC spectra of (a) VO_2/PVP coating and (b) 2.5 at. % W-doped VO_2/PVP coating.

5.3.5 FTIR studies on VO_2/PMMA films

The surface interaction between VO_2 particles and PMMA in the coating was examined using FTIR (Figure 5.16). To obtain a water repellent coating, hydrophobic PMMA was chosen for the fabrication and characterization of VO_2/PMMA films. PMMA is an highly optical transparent polymer with high impact strength, is lightweight and shatter-resistant, and possesses favorable processing properties [42, 43]. Figure 5.16a, b and c represent the FTIR spectra of VO_2, PMMA, and VO_2/PMMA films, respectively. The samples were prepared by coating a thin transparent layer of the sample on the compressed KBr disc, then dried in the oven to remove the solvent. All the characteristic absorption peaks assigned to PMMA are observed in PMMA and VO_2/PMMA [44, 45]. The peaks observed at

(2995 cm^{-1}, 2843cm^{-1}), (1485, 1448, 1387 cm^{-1}), (1149 cm^{-1}) and (1192 cm^{-1}) are attributed to stretching, deformation, twisting and wagging mode of the methyl (CH_3) group [45]. The intense peak at 1732 cm^{-1} is assigned to the characteristic stretch vibration of the ester carbonyl C=O of PMMA [45]. The position of this peak is maintained for VO_2/PMMA coating, suggesting no loosening of C=O due to an interaction with oppositely charged vanadium aqua ions [36]. The peaks at 750 cm^{-1} and (1242, 1271 cm^{-1}) are attributed to bending of C=O and stretching modes of C–O, respectively [45]. The FTIR bands of the VO_2/PMMA film exhibits indistinguishable features to that of pure PMMA, with no change in the band position. Nevertheless, if you look carefully, the magnitude of the absorption peaks are minimized little bit in the VO_2/PMMA, and this could be due to cooperation between VO_2 and PMMA by adsorption through methoxycarbonyl group (–C(O)OCH_3) of polymer. A peak intensity increase of 733 and 750 cm^{-1} with an new peak appeared at 536 cm^{-1} in the VO_2/PMMA films are attributed to stretching vibration of V=O and V-O, respectively. Thus, the coordination between VO_2 and PMMA is confirmed by FTIR spectra and is probably due to an interaction between (–C(O)OCH_3) of PMMA and surface hydroxyl (OH) of VO_2.

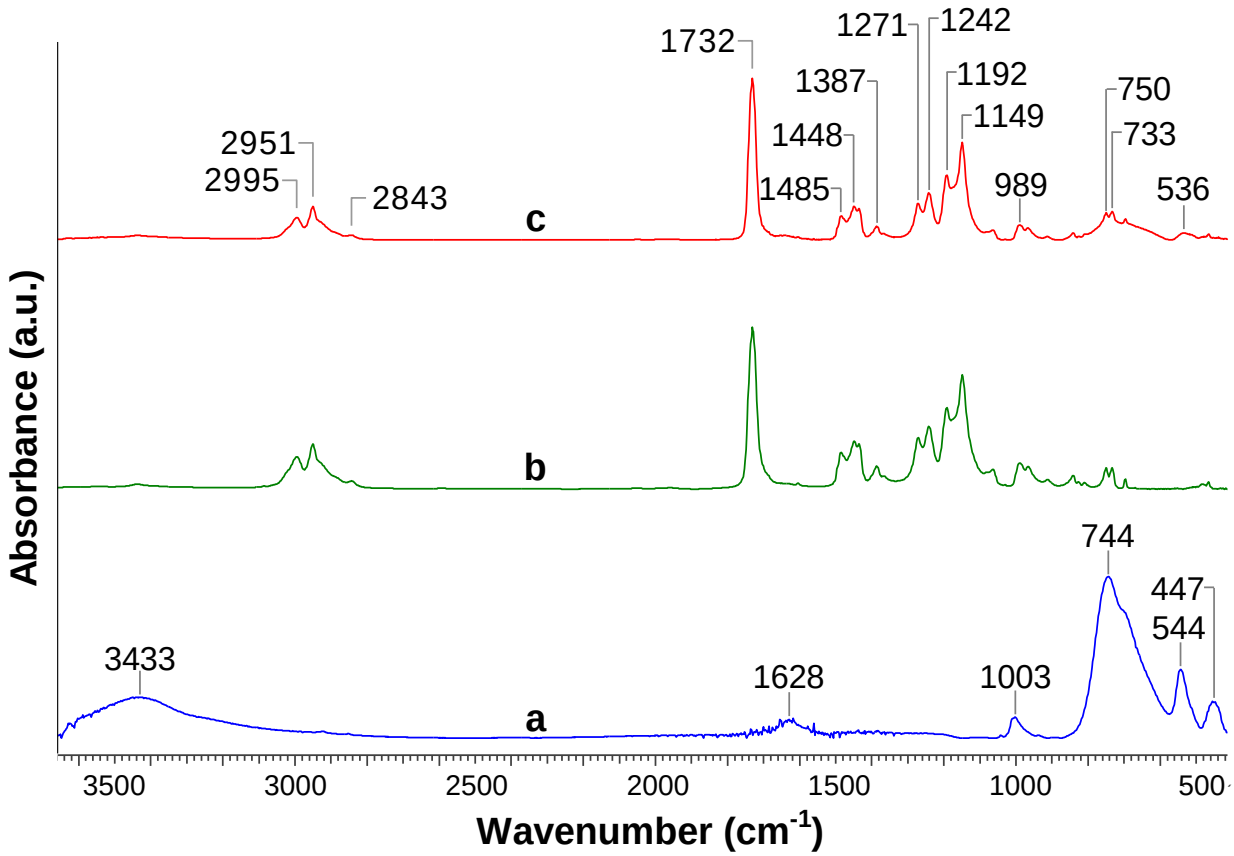

Figure 5. 16 FTIR spectra of (a) VO_2 (blue), (b) PMMA (green), and (c) VO_2/PMMA (red).

5.3.6 Thermochromic studies on VO_2/PMMA films with different thicknesses on glass

The effect of film thicknesses and concentration ratios of VO_2:PMMA on the optical and thermochromic performance of VO_2/PMMA films were investigated during phase transition by measuring the UV–VIS–NIR transmittance spectra from 250 to 2500 nm at 22 °C and 80 °C (Figure 5.17). Figure 5.17a shows VO_2:PMMA samples at weight percent ratios of 2.3:4.6, 4.5:4.5, 2.2:8.9 and 4.3:8.7 (wt. %:wt. %), in toluene solvent. The various mixtures were spin coated at 1000, 2000 and 3000 rpm onto glass slides to obtain coatings of different thicknesses hence, different visible transmittances and different IR transmittance switches. For all films, with increasing spin rate and thus decreasing film thicknesses (Figure 5.17b), an increase in visible

transmittance and a decrease in IR transmittance switching is observed (Figure 5.17a). When the concentration of VO_2 is low in VO_2:PMMA coating (i.e., 2.3:4.6 and 2.2:8.9), films show high visible transmittance and low IR transmittance switching, however, when concentration of VO_2 is high (i.e., 4.5:4.5 and 4.3:8.7), films show low visible transmittance and high IR transmittance switching (Figure 5.17a).

The dispersion of VO_2 (M) particles in PMMA for the (4.3:8.7) sample, spin coated at 1000 rpm, was characterized by SEM (Figure 5.18a). Agglomerated particles were observed (Figure 5.18a) in the 2 μm thick film (measured with SEM, Figure 5.22a) while visible transmittance, $T_{vis@680nm}$, and IR transmittance switching, $\Delta T_{IR@2500nm}$, were 29% and 30%, respectively (Figure 5.18b).

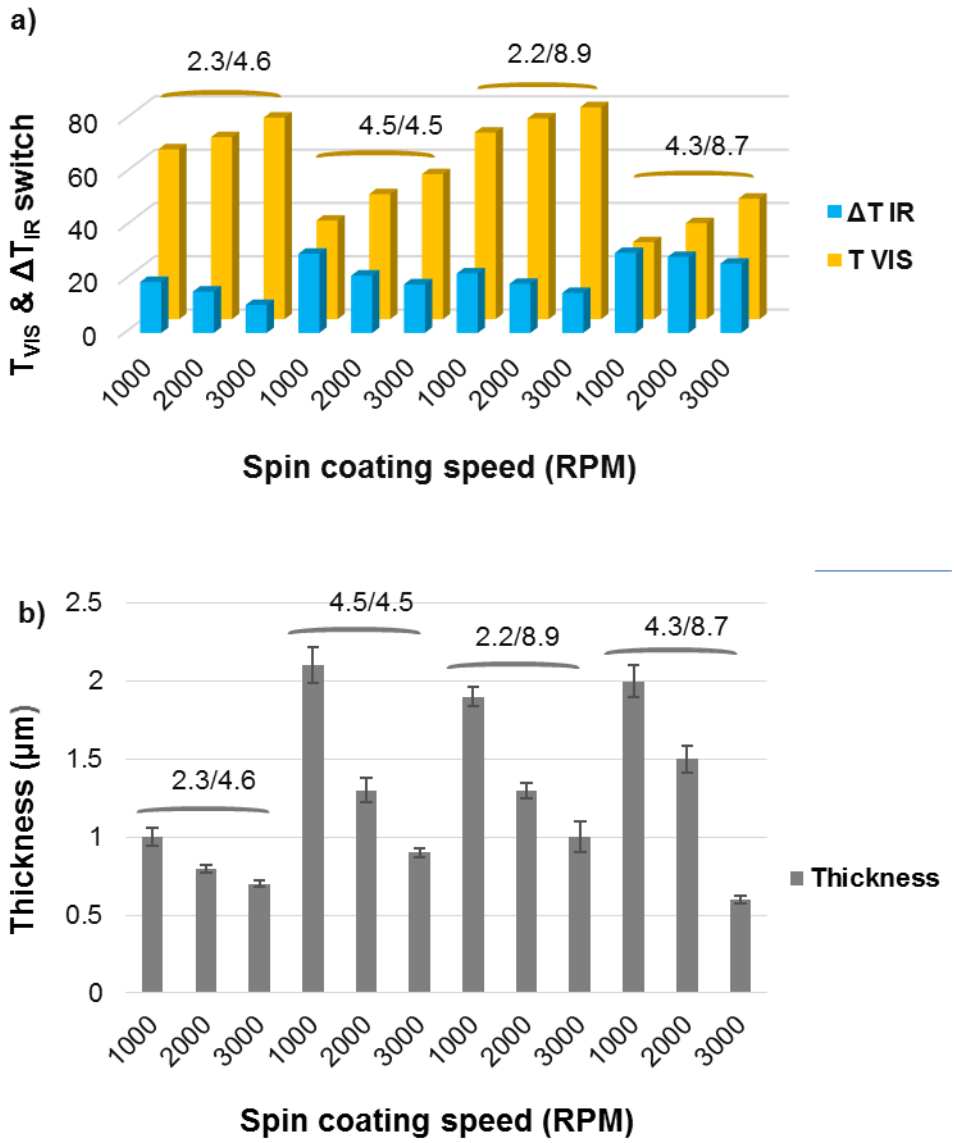

Figure 5. 17 UV–VIS–NIR analysis of the VO_2/PMMA films, spin coated at 1000, 2000 and 3000 rpm onto a glass and prepared at weight percent ratios of 2.3:4.6, 4.5:4.5, 2.2:8.9 and 4.3:8.7 (wt. %: wt. %), respectively. (a) Visible transmittance (orange bar) and IR switching (blue bar) with (b) various thickness (grey bar). The transmittances were obtained at 22 °C and 80 °C in the spectral range of 250 – 2500 nm.

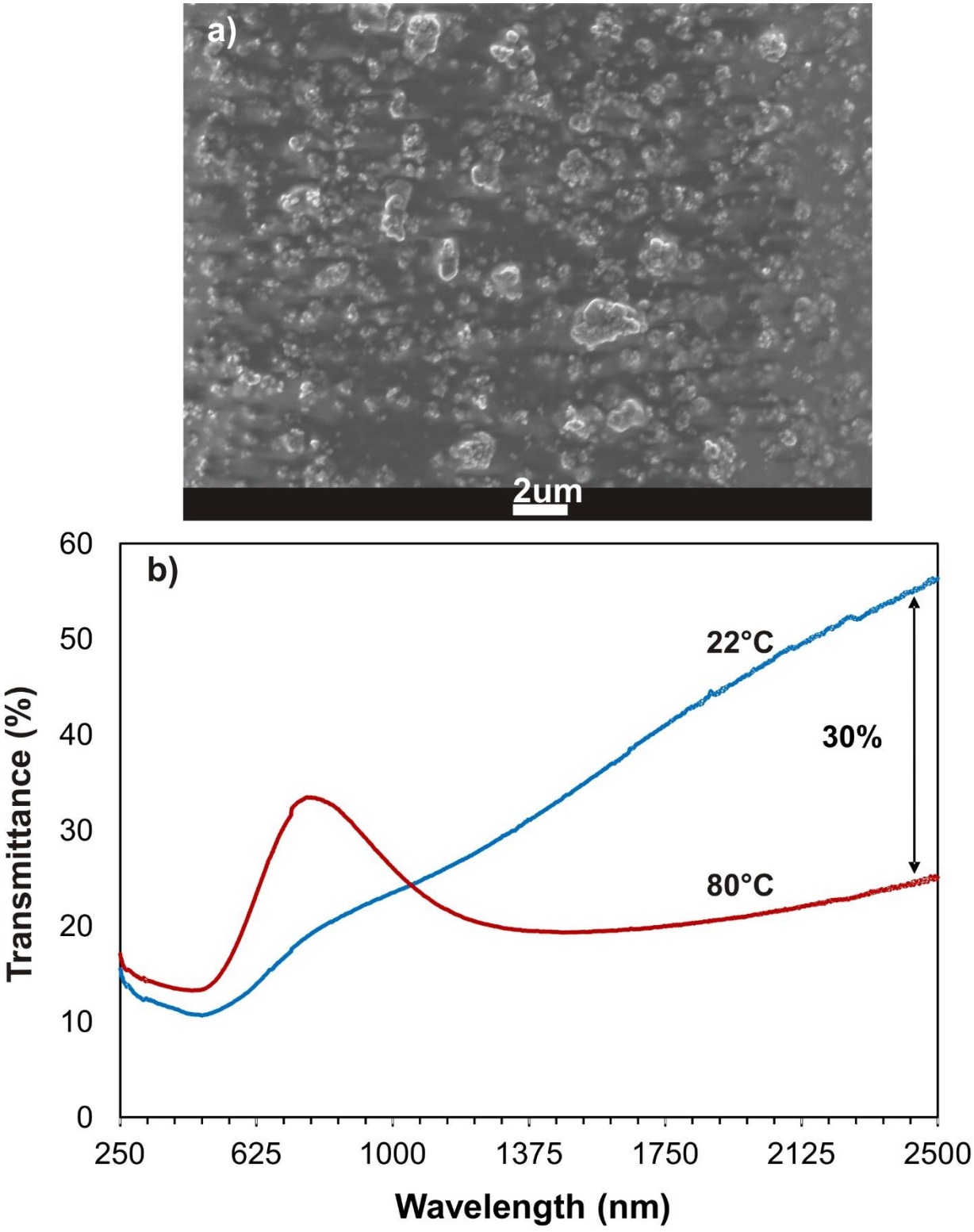
a)
2um
b)
22°C
80°C
30%
Transmittance (%)
Wavelength (nm)
0
10
20
30
40
50
60
250
625
1000
1375
1750
2125
2500

Figure 5. 18 VO_2/PMMA (4.3/8.7) (wt. %:wt. %) coating sample, spin coated at 1000 rpm. (a) SEM image depicting morphology and (b) UV–VIS–NIR transmittance spectra (250 – 2500 nm) at 22 °C (blue) and 80 °C (red).

5.3.7 FTIR studies on VO_2/P4VP films

The surface interaction between VO_2 and poly(4-vinylpyridine) (P4VP) in the coating was scrutinized using FTIR (Figure 5.19). P4VP is often used in the fabrication of coatings or as a matrix material for semiconductor particles. This polymer was chosen for coating studies with a hydrophilic property [46, 47]. Figure 5.19 depicts the FTIR spectra of VO_2, P4VP and VO_2/P4VP. The samples were prepared by coating a thin transparent layer of the sample onto compressed KBr discs, then dried in the oven to remove the solvent. P4VP IR-band positions are in agreement with the spectra reported by Esma et al. [48]. No shift in the band positions between P4VP and VO_2/P4VP was found. The characteristic vibrations of the pyridine rings are seen at 1601 cm^{-1}, assigned to C=N stretching, and at 1417 cm^{-1}, assigned to C=C stretching, indicating incoordination between the pyridine ring (pyridinic nitrogen atoms) and the VO_2 in the VO_2/P4VP [49-51] (Figure 5.19c). The FTIR vibration peaks at 2856, 2931, and 3028 cm^{-1} are attributed to the C–H vibrations of the aliphatic CH_2 in the vinyl chain [52]. The stretching vibration at 3406 cm^{-1} is due to the NH^+ of the pyridinium ion [48, 53]. The intensity of the bands at 3406 and 1637 cm^{-1} are increased in the VO_2/P4VP, while a slight reduction in the 3028 cm^{-1} peak was observed. This may be attributed to the loss of methyne protons and transfer to a side chain pyridine nitrogen with the formation of a pyridinium ion, suggesting that the mobile acidic acid solvent acted as a proton transfer vehicle [48, 53, 54]. High intensity with broad bands appeared in the FTIR spectra of the VO_2/P4VP sample at 744 cm^{-1} and (559 cm^{-1}, 447 cm^{-1}), which are ascribed to the stretching

vibrations of ν(V=O) and ν(V-O), respectively, indicating adsorption and an incorporation of VO_2 into the matrix.

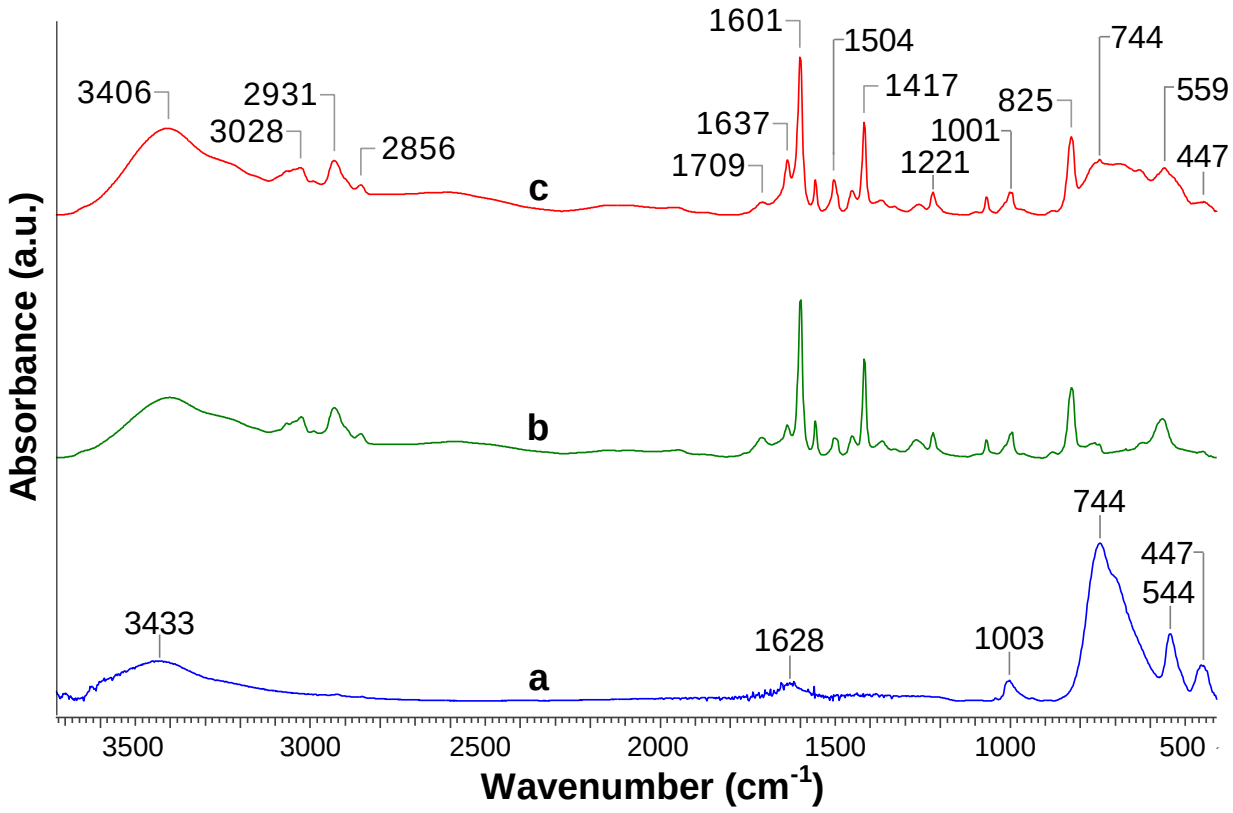

Figure 5. 19 FTIR spectra of (a) VO_2 (blue), (b) P4VP (green), and (c) VO_2/P4VP (red)

5.3.8 Thermo-chromic studies on VO_2/P4VP films with different thickness on glass

The effect of film thickness and concentrations ratios of VO_2:P4VP on the optical and thermochromic characteristics of VO_2/P4VP coatings on glass were investigated during phase transition by measuring UV–VIS–NIR transmittance from 250 to 2500 nm at 22 °C and 80 °C (Figure 5.20). Figure 5.20a shows VO_2:P4VP samples at weight percent ratios of 2.3:4.6, 4.5:4.5, 2.2:8.9 and 4.3:8.7 (wt. %:wt. %), in an acidic acid solvent. Spin speeds of 1000, 2000 and 3000 rpm were used. Decreasing film thicknesses was obtained by increasing the spinning speed (Figure

5.20b), hence influencing both the visible transmittance and the IR transmittance switching (Figure 5.20a). A decrease in coating thickness corresponds to an increase in the visible transmittance (at wavelength 680 nm) and a decrease in the IR transmittance switching (Figure 5.20a). When the concentration of VO_2 is low in VO_2:P4VP samples (i.e., 2.3:4.6 and 2.2:8.9), films show high visible transmittance, when the concentration of VO_2 is high (i.e., 4.5:4.5 and 4.3:8.7), films show low visible transmittance (Figure 5.20a). On the other hand, when the concentration of P4VP is low in VO_2:P4VP samples (i.e., 2.3:4.6 and 4.5:4.5), films show low IR switching, when concentration of P4VP is high (i.e., 2.2:8.9 and 4.3:8.7), films show high IR switching (Figure 5.20a).

The dispersion of VO_2 (M) particles in P4VP for the (4.3:8.7) sample, spin coated at 1000 rpm, was characterized by SEM (Figure 5.21a). The particles, relatively large aggregates, are distributed uniformly (Figure 5.21a) in the 2.1 µm thick film (Figure 5.22b). The visible transmittance of this sample, $T_{vis@680nm}$, and the IR transmittance switching, $\Delta T_{IR@2500nm}$, were 41% and 47%, respectively (Figure 5.21b). An estimation of a direct band gap of 1.75 eV was obtained for this film using Tauc plot (Figure D7). Uniform dispersion of VO_2 particles into P4VP matrix has been shown to have an important effect on enhancing the desired optical and thermochromic characteristics of the coatings which is in excellent agreement with Zhu et al.'s work [55].

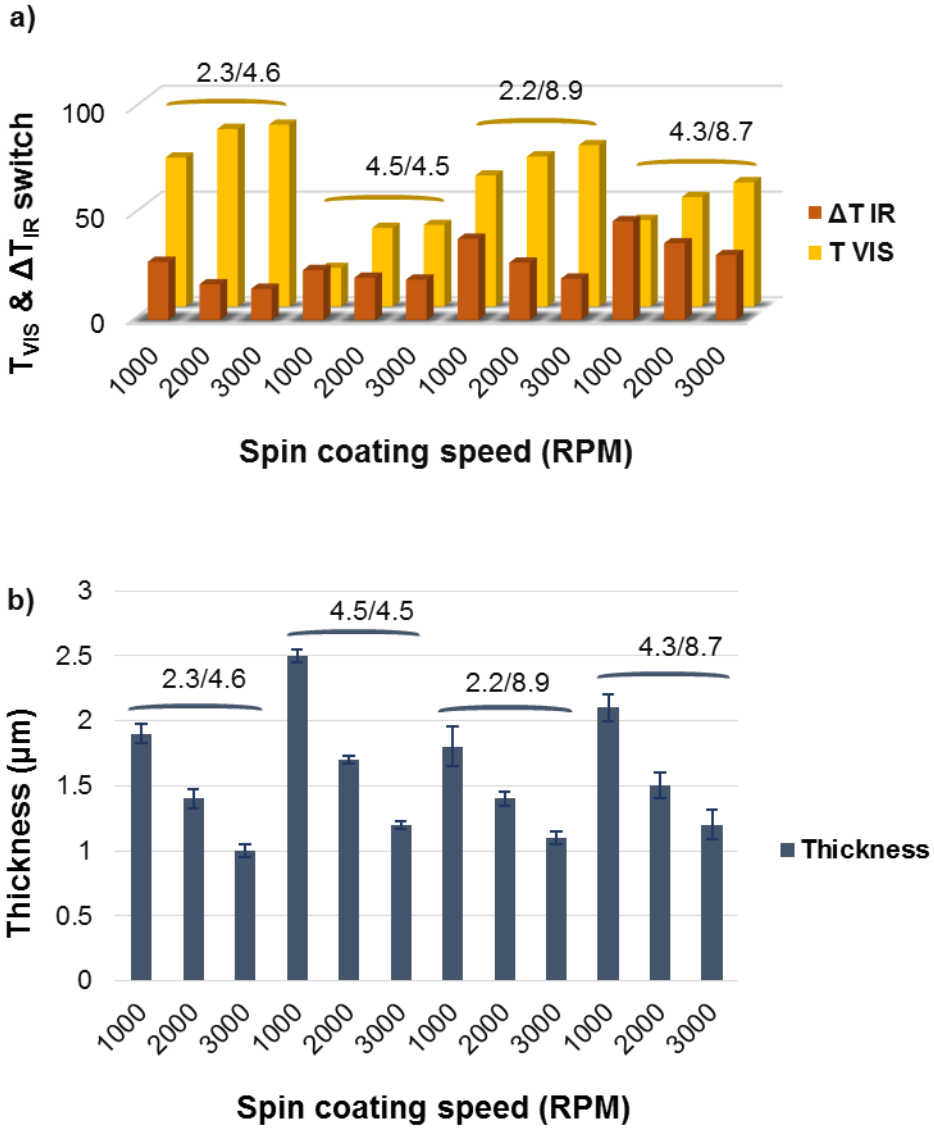

Figure 5. 20 UV–VIS–NIR analysis of the VO_2/P4VP films, spin coated at 1000, 2000 and 3000 rpm onto a glass and prepared at weight percent ratios of 2.3:4.6, 4.5:4.5, 2.2:8.9 and 4.3:8.7 (wt. %:wt. %). (a) Visible transmittance (orange) and IR switching (brown) with (b) thickness (blue). The transmittance was obtained at 22 °C and 80 °C in the spectral range of 250–2500 nm.

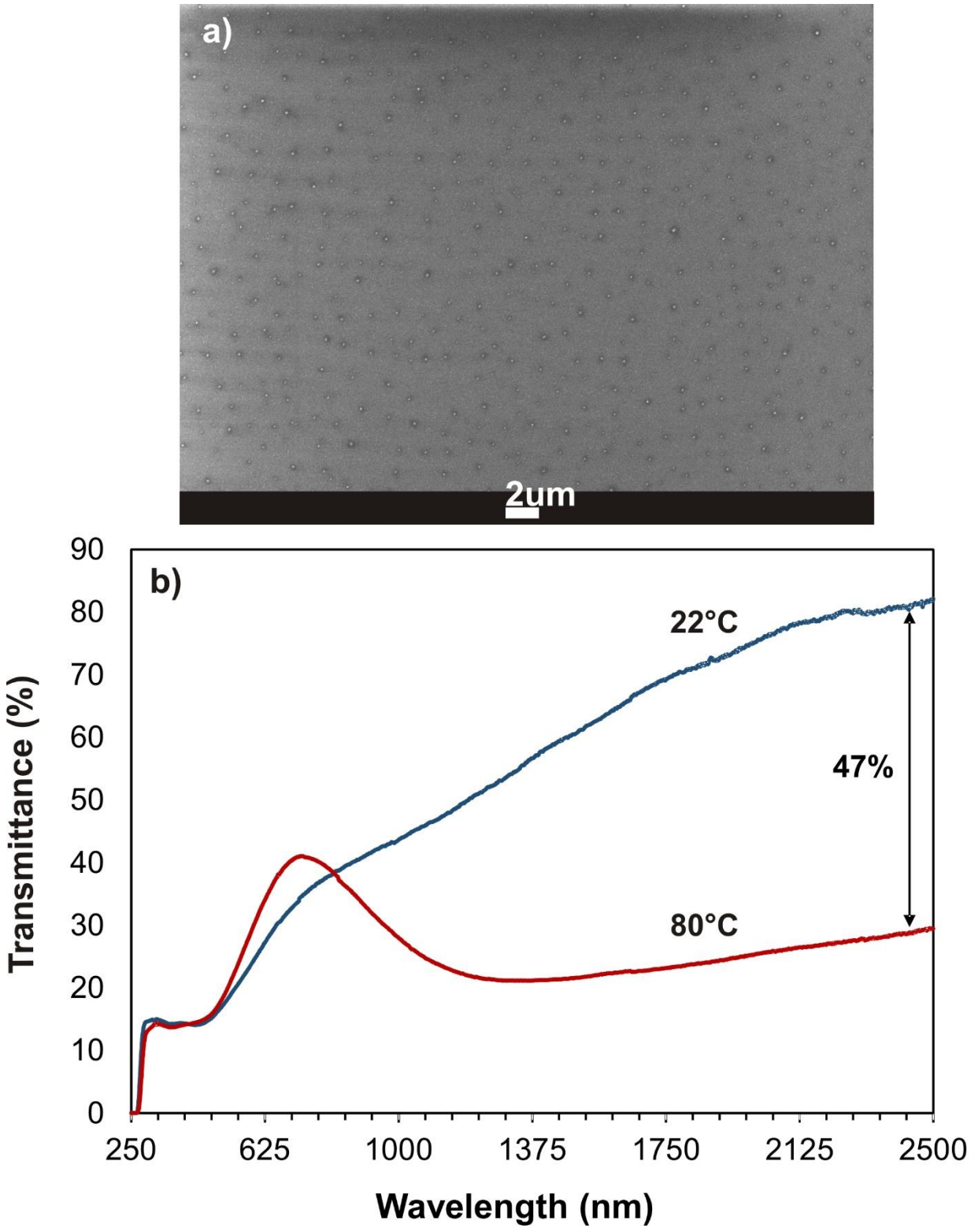
a)
2um
b)
22°C
47%
80°C
Transmittance (%)
Wavelength (nm)
0
10
20
30
40
50
60
70
80
90
250
625
1000
1375
1750
2125
2500

Figure 5. 21 VO_2/P4VP (4.3:8.7) (wt. %:wt. %) film sample, spin coated at 1000 rpm. (a) SEM morphology, (b) UV–VIS–NIR transmittance spectra (250–2500 nm) at 22 °C (blue) and 80 °C (red).

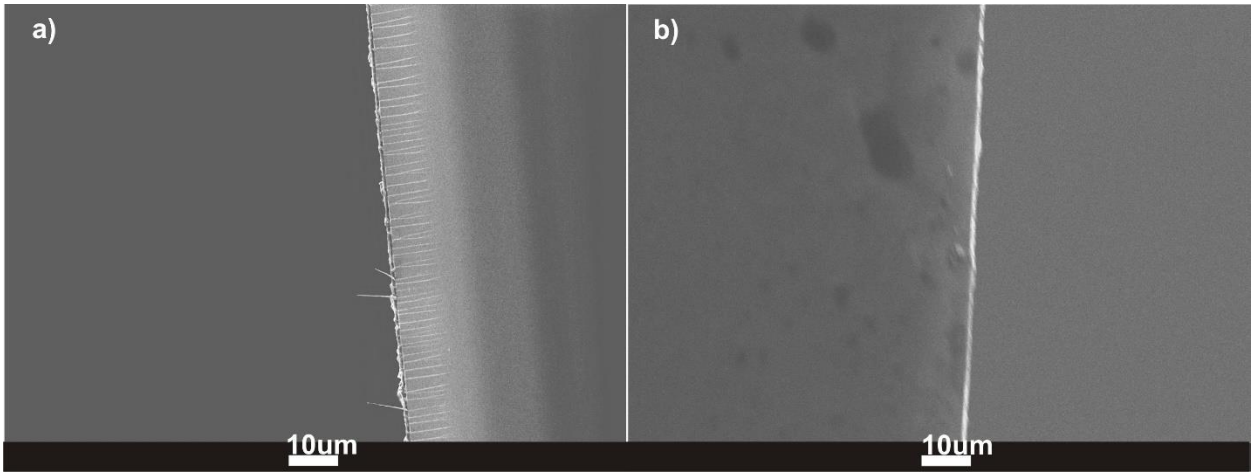

Figure 5. 22 SEM thicknesses of (a) VO_2/PMMA (4.3:8.7) (wt. %:wt. %) and (b) VO_2/P4VP (4.3:8.7) (wt. %:wt. %) film samples, spin coated at 1000 rpm.

5.4 CONCLUSIONS

Un-doped and W-doped VO_2 particles were synthesized in a green, low energy consumption RT approach which is easily up-scalable. An excellent dispersion of un-doped VO_2(M) (IV) particles in hydrophilic polymers, PVP and P4VP coatings was discovered driven by cationic Coulomb repulsion between the VO_2(M) target particles and vanadium(V) oxide NPs which are always co-synthesized in the un-doped case. An un-doped VO_2/PVP coated glass was fabricated with a high IR modulation ability of 40% at 2500 nm and a good visible transmittance of 35% at 680 nm. Hydrophobic VO_2/PMMA and hydrophilic VO_2/P4VP coatings with different thicknesses and VO_2-concentrations were investigated to simulate weather resistant and good dispersion of VO_2, respectively. The VO_2/P4VP film exhibited an excellent IR modulation ability (47% at 2500 nm) with good visible transmittance (41% at 680 nm) which is associated to the film' uniform dispersion of particles.

REFERENCES

1. Berardi, U., *Building energy consumption in US, EU, and BRIC countries.* Procedia engineering, 2015. **118**: p. 128-136.
2. Chen, S., et al., *The visible transmittance and solar modulation ability of VO 2 flexible foils simultaneously improved by Ti doping: an optimization and first principle study.* Physical Chemistry Chemical Physics, 2013. **15**(40): p. 17537-17543.
3. Ye, H., X. Meng, and B. Xu, *Theoretical discussions of perfect window, ideal near infrared solar spectrum regulating window and current thermochromic window.* Energy and Buildings, 2012. **49**: p. 164-172.
4. Qazilbash, M.M., et al., *Mott transition in VO2 revealed by infrared spectroscopy and nano-imaging.* Science, 2007. **318**(5857): p. 1750-1753.
5. Liu, M., et al., *Terahertz-field-induced insulator-to-metal transition in vanadium dioxide metamaterial.* Nature, 2012. **487**(7407): p. 345.
6. Nakano, M., et al., *Collective bulk carrier delocalization driven by electrostatic surface charge accumulation.* Nature, 2012. **487**(7408): p. 459.
7. Zhou, J., et al., *VO2 thermochromic smart window for energy savings and generation.* Scientific Reports, 2013. **3**.
8. Ji, Y., et al., *Role of microstructures on the M1-M2 phase transition in epitaxial VO2 thin films.* Scientific reports, 2014. **4**.
9. Zhang, J., et al., *Hydrothermal growth of VO 2 nanoplate thermochromic films on glass with high visible transmittance.* scientific reports, 2016. **6**: p. 27898.
10. Yu, J.-H., et al., *Enhanced visible transmittance of thermochromic VO2 thin films by SiO2 passivation layer and their optical characterization.* Materials, 2016. **9**(7): p. 556.
11. Zhao, L., et al., *Solution-Processed VO2-SiO2 Composite Films with Simultaneously Enhanced Luminous Transmittance, Solar Modulation Ability and Anti-Oxidation property.* Scientific Reports, 2014. **4**.
12. Liang, S., et al., *One-Step Hydrothermal Synthesis of W-Doped VO2 (M) Nanorods with a Tunable Phase-Transition Temperature for Infrared Smart Windows.* ACS Omega, 2016. **1**(6): p. 1139-1148.
13. Chen, R., et al., *One-step hydrothermal synthesis of V 1− x W x O 2 (M/R) nanorods with superior doping efficiency and thermochromic properties.* Journal of Materials Chemistry A, 2015. **3**(7): p. 3726-3738.
14. Li, D., et al., *Hydrothermal synthesis of Mo-doped VO2/TiO2 composite nanocrystals with enhanced thermochromic performance.* ACS applied materials & interfaces, 2014. **6**(9): p. 6555-6561.
15. Li, Y., et al., *A novel inorganic precipitation–peptization method for VO 2 sol and VO 2 nanoparticles preparation: Synthesis, characterization and mechanism.* Journal of colloid and interface science, 2016. **462**: p. 42-47.
16. Youn, S., S. Jeong, and D.H. Kim, *Effect of oxidation states of vanadium precursor solution in V2O5/TiO2 catalysts for low temperature NH3 selective catalytic reduction.* Catalysis Today, 2014. **232**: p. 185-191.
17. Wang, Q., et al., *VO 2 (B) nanosheets as a cathode material for Li-ion battery.* Journal of Materials Science & Technology, 2015. **31**(6): p. 630-633.

18. Wang, Y., M. Li, and L. Zhao, *The effects of vacuum annealing on the structure of VO2 thin films.* Surface and Coatings Technology, 2007. **201**(15): p. 6772-6776.
19. Ndwandwe, S., P. Tshibangu, and E.D. Dikio, *Synthesis of Carbon Nanospheres From Vanadium β-Diketonate Catalyst.* International Journal of Electrochemical Science, 2011. **6**: p. 749-760.
20. Xia, X., et al., *VO 2 nanoflake arrays for supercapacitor and Li-ion battery electrodes: performance enhancement by hydrogen molybdenum bronze as an efficient shell material.* Materials Horizons, 2015. **2**(2): p. 237-244.
21. Xu, H., et al., *From VO2 (B) to VO2 (A) nanorods: Hydrothermal synthesis, evolution and optical properties in V2O5H2C2O4H2O system.* Optik-International Journal for Light and Electron Optics, 2014. **125**(20): p. 6078-6081.
22. Shen, N., et al., *Lowered phase transition temperature and excellent solar heat shielding properties of well-crystallized VO 2 by W doping.* Physical Chemistry Chemical Physics, 2016. **18**(40): p. 28010-28017.
23. Huang, A., et al., *Preparation of V x W 1− x O 2 (M)@ SiO 2 ultrathin nanostructures with high optical performance and optimization for smart windows by etching.* Journal of Materials Chemistry A, 2013. **1**(40): p. 12545-12552.
24. Wu, Y., et al., *Depressed transition temperature of W x V 1− x O 2: mechanistic insights from the X-ray absorption fine structure (XAFS) spectroscopy.* Physical Chemistry Chemical Physics, 2014. **16**(33): p. 17705-17714.
25. Dai, L., et al., *Synthesis and phase transition behavior of undoped VO 2 with a strong nano-size effect.* Solar Energy Materials and Solar Cells, 2011. **95**(2): p. 712-715.
26. Xiao, X., et al., *A facile process to prepare one dimension VO 2 nanostructures with superior metal–semiconductor transition.* CrystEngComm, 2013. **15**(6): p. 1095-1106.
27. Nagabhushana, G. and G. Chandrappa, *Facile solution combustion synthesis of monoclinic VO 2: a unique and versatile approach.* Journal of Materials Chemistry A, 2013. **1**(38): p. 11539-11542.
28. Ungár, T., et al., *Correlation between subgrains and coherently scattering domains.* Powder Diffraction, 2005. **20**(4): p. 366-375.
29. James, A., J. Subrahmanyam, and K. Yadav, *Structural and electrical properties of nanocrystalline PLZT ceramics synthesized via mechanochemical processing.* Journal of Physics D: Applied Physics, 2006. **39**(10): p. 2259.
30. Gao, Y., et al., *Phase and shape controlled VO 2 nanostructures by antimony doping.* Energy & Environmental Science, 2012. **5**(9): p. 8708-8715.
31. Ji, S., F. Zhang, and P. Jin, *Preparation of high performance pure single phase VO 2 nanopowder by hydrothermally reducing the V 2 O 5 gel.* Solar Energy Materials and Solar Cells, 2011. **95**(12): p. 3520-3526.
32. Dong, B., et al., *Phase and morphology evolution of VO 2 nanoparticles using a novel hydrothermal system for thermochromic applications: the growth mechanism and effect of ammonium (NH 4+).* Rsc Advances, 2016. **6**(85): p. 81559-81568.
33. Wang, X., et al., *Fabrication of VO 2-based multilayer structure with variable emittance.* Applied Surface Science, 2015. **344**: p. 230-235.
34. Song, Z., et al., *Controllable synthesis of VO 2 (D) and their conversion to VO 2 (M) nanostructures with thermochromic phase transition properties.* Inorganic Chemistry Frontiers, 2016. **3**(8): p. 1035-1042.

35. Kang, L., Y. Gao, and H. Luo, *A novel solution process for the synthesis of VO2 thin films with excellent thermochromic properties.* ACS applied materials & interfaces, 2009. **1**(10): p. 2211-2218.
36. Gao, Y., et al., *Nanoceramic VO2 thermochromic smart glass: A review on progress in solution processing.* Nano Energy, 2012. **1**(2): p. 221-246.
37. Liang, Z., et al., *Tungsten-doped vanadium dioxide thin films as smart windows with self-cleaning and energy-saving functions.* Journal of Alloys and Compounds, 2017. **694**: p. 124-131.
38. Dai, L., et al., *F-doped VO 2 nanoparticles for thermochromic energy-saving foils with modified color and enhanced solar-heat shielding ability.* Physical Chemistry Chemical Physics, 2013. **15**(28): p. 11723-11729.
39. Zhou, J., et al., *Mg-doped VO 2 nanoparticles: hydrothermal synthesis, enhanced visible transmittance and decreased metal–insulator transition temperature.* Physical Chemistry Chemical Physics, 2013. **15**(20): p. 7505-7511.
40. Li, W., et al., *Preparation and characterization of VO 2 (M)–SnO 2 thermochromic films for application as energy-saving smart coatings.* Journal of Colloid and Interface Science, 2015. **456**: p. 166-173.
41. Chen, R., et al., *Shape-controlled synthesis and influence of W doping and oxygen nonstoichiometry on the phase transition of VO2.* Scientific reports, 2015. **5**: p. 14087.
42. Ali, U., K.J.B.A. Karim, and N.A. Buang, *A review of the properties and applications of poly (methyl methacrylate)(PMMA).* Polymer Reviews, 2015. **55**(4): p. 678-705.
43. Lu, Y., et al., *Functional transparent nanocomposite film with thermochromic and hydrophobic properties fabricated by electrospinning and hot-pressing approach.* Ceramics International, 2018. **44**(1): p. 1013-1018.
44. Jiang, J., *Ultrasonic-assisted synthesis of PMMA/Ni0. 5Zn0. 5Fe2O4 nanocomposite in mixed surfactant system.* European Polymer Journal, 2007. **43**(5): p. 1724-1728.
45. Singhal, A., et al., *UV-shielding transparent PMMA/In 2 O 3 nanocomposite films based on In 2 O 3 nanoparticles.* RSC Advances, 2013. **3**(43): p. 20913-20921.
46. Tenhaeff, W.E., L.D. McIntosh, and K.K. Gleason, *Synthesis of Poly (4-vinylpyridine) Thin Films by Initiated Chemical Vapor Deposition (iCVD) for Selective Nanotrench-Based Sensing of Nitroaromatics.* Advanced Functional Materials, 2010. **20**(7): p. 1144-1151.
47. Liu, Y., J.F. Flores, and J.Q. Lu, *Tailoring 1D ZnO Nanostructure Using Engineered Catalyst Enabled by Poly (4-vinylpyridine).* The Journal of Physical Chemistry C, 2014. **118**(33): p. 19387-19395.
48. Esma, C.-B., D. Zoulikha, and M. Ali, *Molecular weight effect on the quaternization of poly (4-vinylpyridine) with alkylbromide.* Journal of Macromolecular Science, Part A, 2012. **49**(12): p. 1084-1091.
49. Wen, X., L. Tang, and L. Qiang, *Stimuli-responsive one-dimensional copolymer nanostructures fabricated by metallogel template polymerization and their adsorption of aspirin.* Soft matter, 2014. **10**(22): p. 3960-3969.
50. Xue, Y. and H. Xiao, *Antibacterial/Antiviral Property and Mechanism of Dual-Functional Quaternized Pyridinium-type Copolymer.* Polymers, 2015. **7**(11): p. 2290-2303.
51. Chen, Y., W. Zhao, and J. Zhang, *Preparation of 4-vinylpyridine (4VP) resin and its adsorption performance for heavy metal ions.* RSC Advances, 2017. **7**(8): p. 4226-4236.

52. Chen, J., et al., *Ruthenium complex immobilized on poly (4-vinylpyridine)-functionalized carbon-nanotube for selective aerobic oxidation of 5-hydroxymethylfurfural to 2, 5-diformylfuran.* RSC Advances, 2015. **5**(8): p. 5933-5940.
53. Vaganova, E., et al., *Acidity of the methyne group of poly (4-vinylpyridine) leads to side-chain protonation in pyridine.* New Journal of Chemistry, 2015. **39**(8): p. 5920-5922.
54. Silverstein, R.M. and F.X. Webster, *Spectrometric identification of organic compounds.* 1998.
55. Zhu, J., et al., *Vanadium dioxide nanoparticle-based thermochromic smart coating: high luminous transmittance, excellent solar regulation efficiency, and near room temperature phase transition.* ACS applied materials & interfaces, 2015. **7**(50): p. 27796-27803.

Chapter 6

Conclusions and Recommendations

6.1 CONCLUSIONS

In this thesis, a green and novel energy maintaining process for the synthesis of VO_2(M) was found by reacting ammonium metavanadate with aspartic acid in water. Using a straightforward reflux wet chemical process, a consistent large batch of W-doped VO_2 with a high yield (>90%) and a low phase transition temperature of 53 °C was effectively synthesized. According to XRD and EVA, the "0.7/1" and "0.6/1" samples, have yielded the highest monoclinic VO_2(M) amounts for all calcination times, however, only "0.6/1(2 h)" sample contained no V_2O_5. Phase transition temperature, monoclinic phase purity and chemical stability of VO_2(M) were investigated as a function of the W-doping, besides, the phase purity was examined as a function of PVP as well. Based on DSC and XRD results, it was found that both W and PVP had a signification effect on the experimental parameters. As matter of fact, without W-doping or without blending with PVP is not possible to synthesize a material with a pure monoclinic VO_2 phase primary below 800 °C calcination temperature. Moreover, it was proved that W-doping have enhanced the anti-oxidation of the VO_2(M) in air, which is important for useful purposes like shelf-life before utilization in a smart coating. Further, tungsten was found to be more effective on T_c primarily for samples annealed at 800 °C for 2 h. The fabrication of W-doped VO_2(M)/PVP coatings on glass with a relative uniform dispersion, nonetheless in aggregated form, was obtained. Based on UV-Vis-NIR spectra, a simultaneous improvement in both luminous transparency and solar modulation in comparison to recent literatures was accomplished: $T_{lum,best}$ 68.30% at 22 °C and $T_{lum,best}$ = 47.6 % at 80 °C with an extraordinarily high $\Delta T_{sol,\ best}$ of 20.37%. Accordingly, the environmentally

friendly synthesized W-doped VO_2 material obtained for the first time satisfies the target criteria for smart windows.

VO_2(M) crystals were synthesized in a high yield with a relatively large batch (2g) by reducing ammonium metavanadate (NH_4VO_3) with hydrazine using a novel green hydrothermal method. Both Mo- and W-doped VO_2 were synthesized, and the morphology and phase transition were strongly affected by different doping as confirmed by SEM and DSC. It was found that W was more effective than Mo to reduce phase transition temperature of VO_2 down to an ambient temperature. According to XRD, for all W-doped samples, VO_2(B) phase was completely transformed into VO_2 (M), primarily after being annealed at 650 °C with heating rate of 20 °C/min. A high transition reduction efficiency of 23 K/at. % was obtained for W-doped VO_2 crystals. Additionally, the thermochromic properties of VO_2/PVP coated glass exhibited an excellent visible light transmittance above 62% and high infrared modulation up to 35% at 2000 nm. Meanwhile, the highest infrared (IR) switching of 28% at 1500 nm was obtained for 1 at. % W-doped VO_2/PVP coating with a visible transmittance above 75%. These results are promising for an application of W-doped VO_2 nanocrystals in smart window technology. This simple and green synthetic method can open avenues for an economic and commercial large-scale VO_2 (M) production for low-cost smart windows.

A VO_2-SiO_2 composite was synthesized through a novel reflux-process by reducing ammonium metavanadate with the maleic acid, already blended with fumed silica, using water solvent. According to XRD, the ratio of maleic Acid/ NH_4VO_3 at 1.5:1 was the optimum for the synthesis of a monoclinic VO_2. XPS, FTIR, ^{1}H NMR and ^{13}C NMR were used to study the reaction mechanisms, and the as synthesized product found to be a mixture of $(NH_4)0.5V_2O_5$ and $(NH_4)_2V_4O_9$ (molar ratio: 6.8:1), however, it transformed into a mixture of VO_2 and V_2O_5 (molar

ratio: 3:1) after annealing. Hysteresis width, latent heat and T_c of the pristine VO_2 were investigated as a function of various annealing temperatures using DSC. Typically, when annealing temperature is increased from 500 °C to 700 °C, the T_c exhibited a decrease from 67.3 °C to 66.7 °C during the heating cycle and an increase from 62.0 °C to 63.4 °C during the cooling cycle, causing the hysteresis width to decrease from 5.3 °C to 3.3 °C. Meanwhile, the latent heat increased from 27.0J/g to 47.8J/g during phase transition when annealing temperature increases from 500 °C to 800 °C. Further, using condenser at low reaction temperature, the phase transition temperature of 2 at. % W-doped VO_2 was dramatically reduced to 23 °C, when tungstic acid was pre-dissolved in hydrogen peroxide (H_2O_2) prior to use. To study the effect of SiO_2 addition on the size, morphology, dispersion and chemical stability of VO_2, different Si/V molar ratios were examined. The zeta-sizer results revealed that the mean particles size of VO_2/SiO_2 composite (Si/V=0.05) is approximately 155.5 nm compare to 650 nm of pristine VO_2 particle size annealed at the same conditions, suggesting that the addition of SiO_2 inhibits the agglomeration of VO_2 particles. Accordingly, as displayed by SEM, well dispersion of small particles is formed for the composite compare to an agglomerated VO_2. In addition, the SiO_2 significantly enhanced the anti-oxidation stability of VO_2, which was maintained in air, at room temperature for seven months. Further, the VO_2/SiO_2 composite film exhibited an excellent efficiency with IR modulation up to 20%, four times greater than 5% of plain VO_2 film, while retaining high visible transparency of 70% at the wavelength of 680 nm. Therefore, the composite could have a great potential for an application in smart window due to promising properties of IR switching and chemical stability.

A novel, green and low energy consumption RT process for the synthesis of un-doped and W-doped VO_2 NPs was achieved by hydrolysis of vanadyl acetylacetonate with HCl in aqueous solution after a short time calcination. Hydrolysis reaction was proposed and FTIR, XRD and DSC

investigations were conducted to verify the success of the RT synthetic strategy of VO_2. Various experimental parameters including reaction time, annealing time and W doping concentration were investigated. To confirm that the reaction didn't occur during rotary evaporation or during an oven drying, the samples were freeze-dried after reflux while maintaining same synthesis conditions. Accordingly, the DSC revealed that the peaks are intensified, and the latent heat increased for all W samples due to moisture reduction. Further, it was found that the particle size and latent heat decreased when increasing W for 72 h reaction. However, the particle size increased with less thermochromic deterioration when increasing W for 24 h reaction, hence this reaction was chosen for more in-depth study. A pure monoclinic VO_2 phase is primarily obtained after 4 h of calcination at 450 °C. The lowest T_c of 45 °C was achieved for the 10 at. % W-doped VO_2 sample. An excellent distribution of un-doped VO_2(M) (IV) NPs in PVP coatings was revealed and it is driven by positive-positive Coulomb repulsion between the VO_2(M) target NPs and vanadium(V) oxide NPs which are always co-synthesized in the un-doped case. An un-doped VO_2/PVP coated glass was fabricated with a high IR modulation ability of 40% at 2500 nm and a good luminous transmittance of 35%. Moreover, hydrophobic VO_2/PMMA and hydrophilic VO_2(M)/P4VP films with variable thicknesses and concentrations were investigated to obtain weather resistant films and films with good dispersion of VO_2, respectively. When concentration of VO_2 is low in VO_2/PMMA or VO_2/P4VP, films exhibit high visible transmittance and low IR switching, however, vise-versa results were obtained when concentration is high and this correspond to thickness factor as well. According to FTIR study, the coordination between VO_2 and PMMA is probably due to an interaction between (–C(O)OCH_3) of PMMA and surface hydroxyl(OH) of VO_2. However, new broad bands appeared in the FTIR spectra of the VO_2/P4VP at 744 and 447 cm^{-1}, which are ascribed respectively to stretching vibration of ν(V=O) and ν(V-O), indicating the adsorption and incorporation of VO_2 in

the P4VP matrix. Finally, VO_2(M)/P4VP film exhibited better IR switching (47%) with good visible transmittance (41%) compared to VO_2/PMMA film, which is associated to the film' uniform dispersion of particles. Overview of the methodologies used in this study and their results are shown in the Table 6.1

Table 6. 1 Overview of the methods and their results

Method	V source	Reducer	Solvent	Optical property	Chemical stability	T_c (°C)	ΔT_c (°C)	Dispersity
Reflux (Ch. 2)	NH_4VO_3	L-aspartic acid	Water	ΔT_{sol}=20.4 % T_{lum}=68.3%	7 h at 300 °C in air	53.6	5.9	Aggregate
Hydrothermal (Ch. 3)	NH_4VO_3	Hydrazine	Water	$\Delta T_{IR@2000nm}$ =35% T_{vis} =62%	n/a	17	4.3	Aggregate
Reflux (SiO_2 composite)(Ch. 4)	NH_4VO_3	Maleic acid	Water	$\Delta T_{IR@2000nm}$ =20% T_{vis} =70%	7 months at RT in air	23	3.3	n/a
Hydrolysis at RT (Ch. 5)	$VO(acac)_2$	Hydrolysis by HCl	Water	$\Delta T_{IR@2500nm}$ =47% Tvis =41%.	n/a	45	9.3	Excellent

6.2 RECOMMENDATIONS

In this thesis, new synthetic approaches were designed for the successful fabrication of VO_2-based films with excellent optical properties. However, further studies would be useful to help understand the underlying science while facilitating industrial implementation.

1. Enhancing the dispersion of NPs could lead to improving the optical properties of prepared films.
    - Agglomeration of nanoparticles in a transparent host reduces the light transmittance due to light scattering, and a uniform dispersion for these NPs remains a big challenge, which limit their intended applications. The excellent dispersion in this study, which is driven by positive-positive Coulomb repulsion between VO_2(M) and vanadium(V) oxide NPs,

can be further investigated to improve the distribution of other NPs.

- Rational design and synthesis of new polymer matrices to effectively stabilize the particles and enhance the optical property of the VO_2 based film.

2. Visible transmittance could be further improved by adding in an antireflection coating, i.e., ZnO, TiO_2 and Al_2O_3.
3. Average particles size of VO_2 can be reduced to NPs size in this study through reducing the reaction times (6-12 hours) primarily for hydrothermal process.
4. Optimized thermochromic polymers may be used in combination with VO_2, to improve color, transparency and IR switching of the films.
5. Examining new dopants, metal cations with large ionic radii or large valence state, that have less negative impact on thermochromicity of VO_2, while reducing T_c to room temperature.
6. Along with tremendous applications, VO_2 could be employed in medical area, by developing switchable biosensors established on the combining between VO_2 and Au NPs.
7. Information about the coordination structure of vanadium atoms in films can be revealed from synchrotron interpretation using X-ray absorption spectroscopy (XAS). X-ray absorption near-edge structure (XANES) can be used to obtain the chemical state and local symmetry of vanadium, tungsten or molybdenum.
8. More detailed application studies on forming films and coatings.
9. Designing multifunctional smart coating (i.e., VO_2/TiO_2 film) for energy saving and self-cleaning window.
10. For energy generation application, VO_2 material can be integrated with solar cell layer. This is achieved by increasing the phase transition temperature of VO_2 by doping with low-valent cations at high concentration such as Al^{3+}, Cr^{3+}, Ti^{+4}, Ga^{3+} and Fe^{3+}.

APPENDIX A

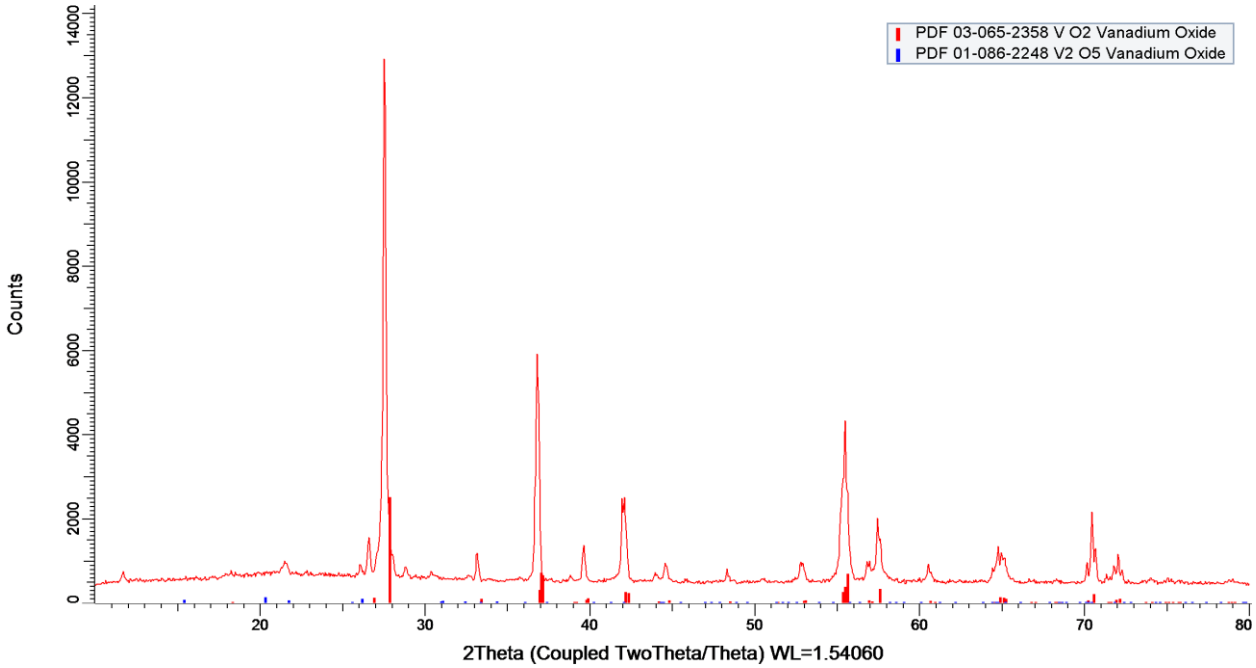

Figure A1 EVA spectrum and analysis of VO_2 for 0.7/1 molar ratio annealed at 800 °C for 2 h (red: 91.6%VO_2(M) and blue: 8.4%V_2O_5)

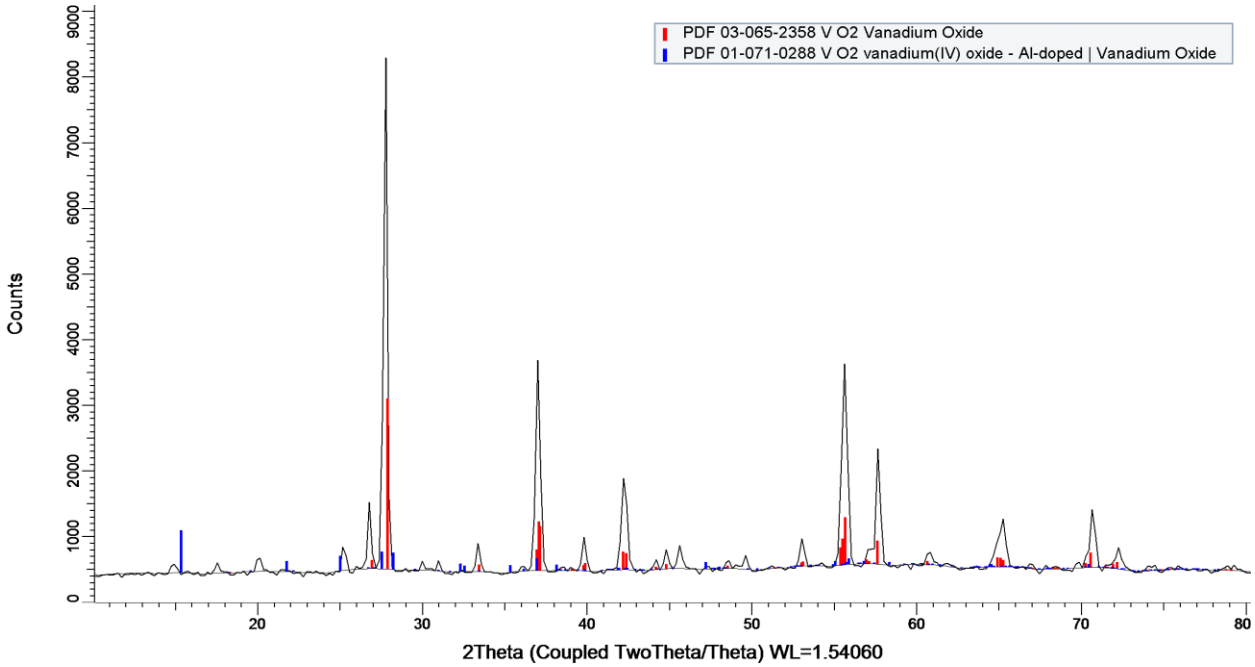

Figure A2 EVA spectrum and analysis of VO_2 for 0.6/1 molar ratio annealed at 800 °C for 2 h (red: 71%VO_2(M), blue: 29% triclincVO_2(T))

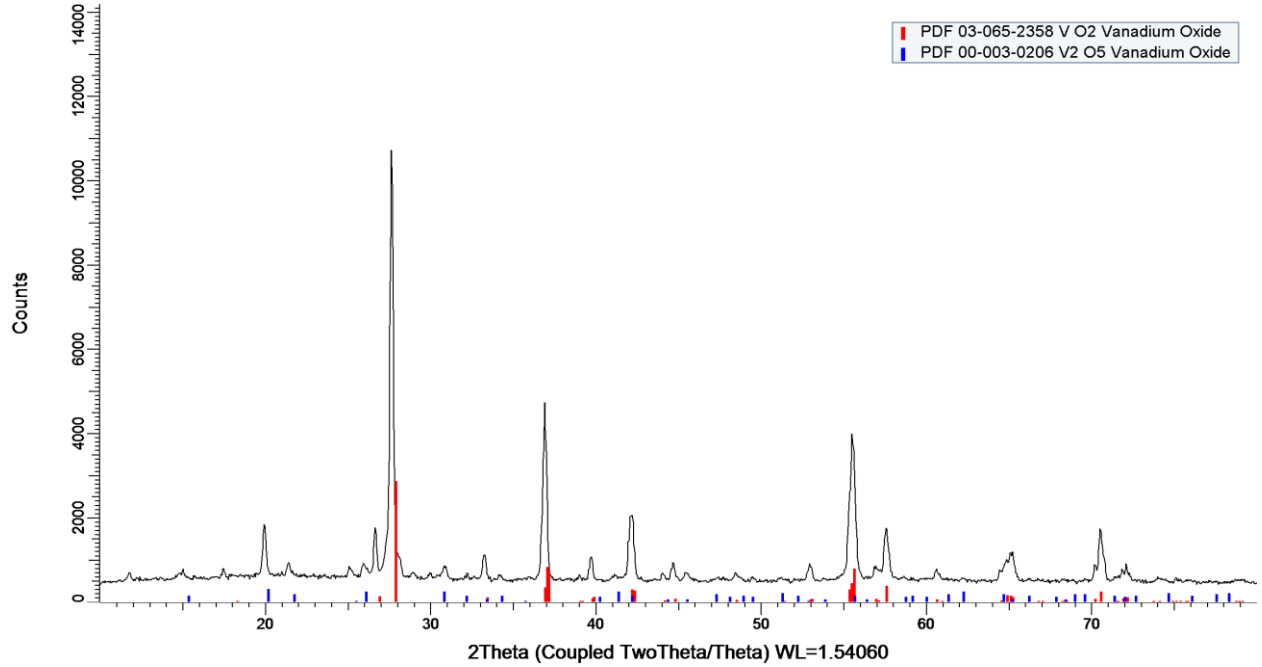

Figure A3 EVA spectrum and analysis of VO_2 for 0.7/1 molar ratio annealed at 800 °C for 1 h (red: 72.3%VO_2(M) and blue: 27.7%V_2O_5)

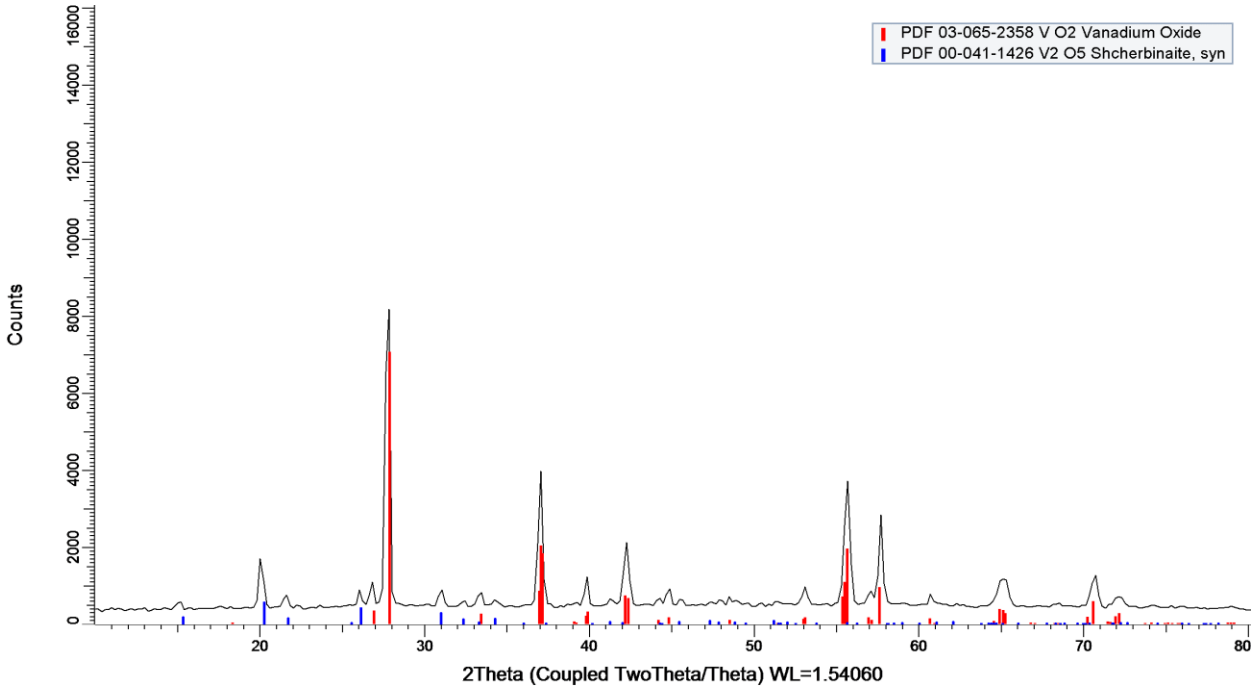

Figure A4 EVA spectrum and analysis of VO_2 for 0.6/1 molar ratio annealed at 800 °C for 1 h (red: 84.5%VO_2(M) and blue: 15.5%V_2O_5)

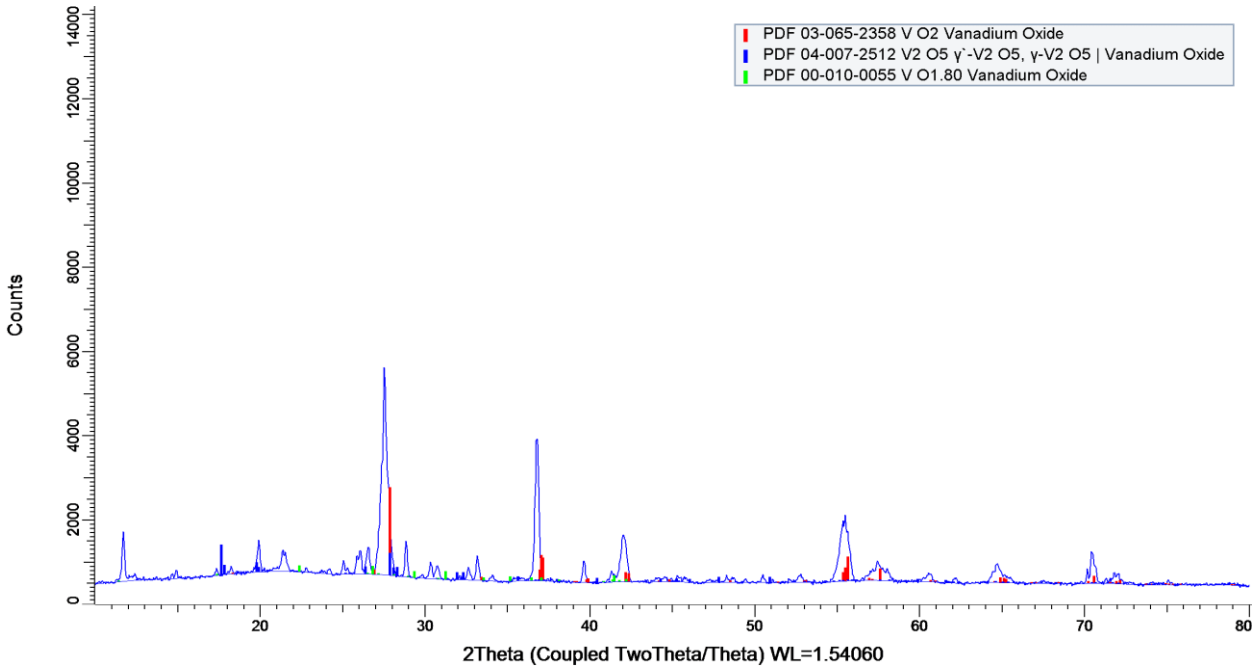

Figure A5 EVA spectrum and analysis of VO_2 for 0.7/1 molar ratio annealed at 800 °C for 4 h (red: 50.6% VO_2(M), blue: 33%V_2O_5 and green: 16.4% (V_5O_9)

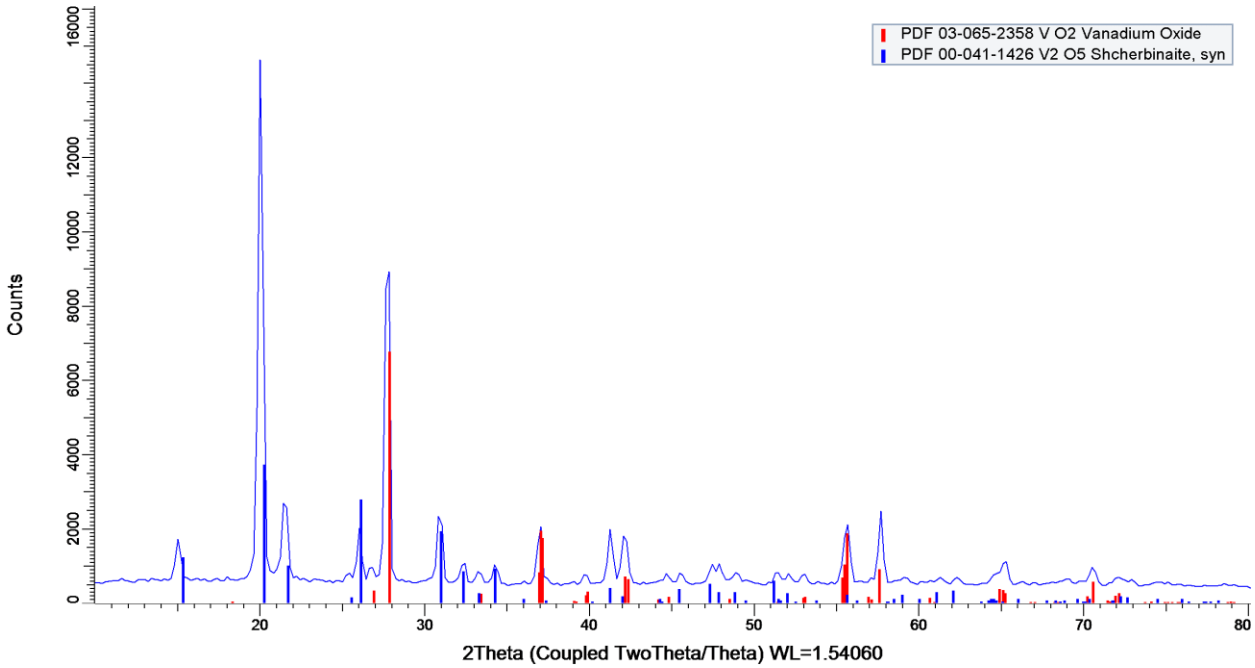

Figure A6 EVA spectrum and analysis of VO_2 for 0.6/1 molar ratio annealed at 800 °C for 4 h (red: 44.9%VO_2(M) and blue: 55.1%V_2O_5)

Short Overview on Previous Strategies Aiming for High Luminous Light Transmission and the Solar Modulation Efficiency

Li et al. casted hydrothermally synthesized VO_2 composite on transparent Teflon to obtain Core-shell VO_2(M)@SiO_2 films [1], but achieved only poor optical properties: T_{lum} of 35.96% and ΔT_{sol} of 8.4%. The values of T_{lum} and ΔT_{sol} reported for a typical single-layered VO_2 coating are 41.0% and 6.7% [2], respectively, and for a double-layered TiO_2/VO_2 film 46.0% and 7.0% [3]. For a five-layered $TiO_2/VO_2/TiO_2/VO_2/TiO_2$ film 44% and 12.1% [4], respectively were reported and for a composite VO_2-Sb: SnO_2 film is 49.8% and 11.7% [5]. Zhao et al. were able to improve the optical properties to T_{lum} = 48.5% and ΔT_{sol} = 15.7% for un-doped films, and T_{lum} = 43.3% and ΔT_{sol} =11.3% for W-doped films [1]. However, they implemented multi-step, time consuming procedures (refluxing at 120 °C for 10 hours, ageing for one day and calcination). More recently the following values for (T_{lum}, ΔT_{sol}) were reported: (70.3%, 9.3%) [6], (62.2%, 12.5%) [7], (73.6%, 2.9%) [8], (25.6%, 12.2%) [9], (45.7%, 6.9%) [10], (48.3%, 17.3%) [11], (80%, 10.2%) [12], (80.6%, 9.10%) [13] and (75.5%, 7.7%) [14]. Declining ΔT_{sol} can be observed when VO_2 is doped with other elements due to lattice distortion [13, 15].

Brief Overview of Visible Transparency (T_{lum}) and Solar Modulation Efficiency (ΔT_{sol}) from Literature

Liang et al. [16] obtained visible transparencies in the order of 70-79% however, their ΔT_{sol} values were low from 6 - 8.6% for un-doped, and between 0.5 - 1.5% for W-doped VO_2 samples. The optical transmittance of a 25 μm thick film of W-doped VO_2 HPCA composite microgel was investigated by Yang et al. [17]. They achieved a high ΔT_{sol} of 36%, but the film turned translucent at 60 °C, only showed a T_{lum} of 33%. Other examples of T_{lum} and ΔT_{sol} values for W-doped VO_2 films include (45.7%, 6.9%) [11], (56.0%, 8.7%) [12] and (31.2%, 6.4%) [18], respectively.

REFERENCES

1. Gao, Y., et al., *Enhanced chemical stability of VO 2 nanoparticles by the formation of SiO 2/VO 2 core/shell structures and the application to transparent and flexible VO 2-based composite foils with excellent thermochromic properties for solar heat control.* Energy & Environmental Science, 2012. **5**(3): p. 6104-6110.
2. Zhao, L., et al., *Solution-processed VO2-SiO2 composite films with simultaneously enhanced luminous transmittance, solar modulation ability and anti-oxidation property.* Scientific reports, 2014. **4**.
3. Mlyuka, N., G. Niklasson, and C.-G. Granqvist, *Thermochromic multilayer films of VO 2 and TiO 2 with enhanced transmittance.* Solar Energy Materials and Solar Cells, 2009. **93**(9): p. 1685-1687.
4. Jin, P., et al., *A VO2-based multifunctional window with highly improved luminous transmittance.* Japanese journal of applied physics, 2002. **41**(3A): p. L278.
5. Mlyuka, N.R., G.A. Niklasson, and C.G. Granqvist, *Thermochromic VO2-based multilayer films with enhanced luminous transmittance and solar modulation.* physica status solidi (a), 2009. **206**(9): p. 2155-2160.
6. Zhang, J., et al., *Hydrothermal growth of VO2 nanoplate thermochromic films on glass with high visible transmittance.* Scientific reports, 2016. **6**: p. 27898.
7. Gao, Y., et al., *VO 2–Sb: SnO 2 composite thermochromic smart glass foil.* Energy & Environmental Science, 2012. **5**(8): p. 8234-8237.
8. Cao, Z., et al., *A simple and low-cost combustion method to prepare monoclinic VO2 with superior thermochromic properties.* Scientific reports, 2016. **6**.
9. Wang, N., et al., *Terbium-doped VO2 thin films: Reduced phase transition temperature and largely enhanced luminous transmittance.* Langmuir, 2016. **32**(3): p. 759-764.
10. Wu, X., et al., *Enhancement of VO 2 thermochromic properties by Si doping.* Surface and Coatings Technology, 2015. **276**: p. 248-253.
11. Hu, L., et al., *Porous W-doped VO2 films with simultaneously enhanced visible transparency and thermochromic properties.* Journal of Sol-Gel Science and Technology, 2016. **77**(1): p. 85-93.
12. Zhu, J., et al., *Vanadium dioxide nanoparticle-based thermochromic smart coating: high luminous transmittance, excellent solar regulation efficiency, and near room temperature phase transition.* ACS applied materials & interfaces, 2015. **7**(50): p. 27796-27803.
13. Zhang, J., et al., *Mesoporous SiO 2/VO 2 double-layer thermochromic coating with improved visible transmittance for smart window.* Solar Energy Materials and Solar Cells, 2017. **162**: p. 134-141.
14. Dou, S., et al., *Facile preparation of double-sided VO 2 (M) films with micro-structure and enhanced thermochromic performances.* Solar Energy Materials and Solar Cells, 2017. **160**: p. 164-173.
15. Zhu, J., et al., *Hybrid films of VO 2 nanoparticles and a nickel (ii)-based ligand exchange thermochromic system: excellent optical performance with a temperature responsive colour change.* New Journal of Chemistry, 2017. **41**(2): p. 830-835.
16. Liang, Z., et al., *Tungsten-doped vanadium dioxide thin films as smart windows with self-cleaning and energy-saving functions.* Journal of Alloys and Compounds, 2017. **694**: p. 124-131.

17. Yang, Y.-S., et al., *Tungsten doped VO 2/microgels hybrid thermochromic material and its smart window application.* RSC Advances, 2017. **7**(13): p. 7758-7762.
18. Wang, N., et al., *Single-Crystalline W-Doped VO2 Nanobeams with Highly Reversible Electrical and Plasmonic Responses Near Room Temperature.* Advanced Materials Interfaces, 2016. **3**(15).

APPENDIX B

Semi-crystalline structure with un-identified peaks were obtained for the un-calcined non-doped VO_2 and 3% W-doped VO_2 as shown by XRD spectra in Figure B1.

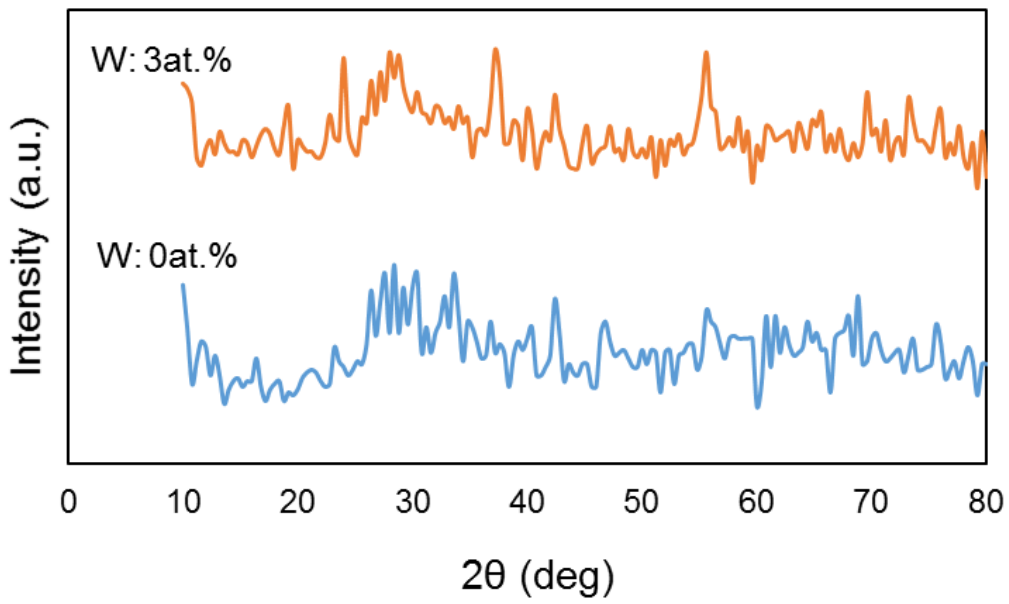

Figure B1 XRD spectra of un-doped and 3at.% W-doped VO_2 without calcinations.

T_c reduction coefficient of W-doped VO_2 for literature is shown in Figure B2.

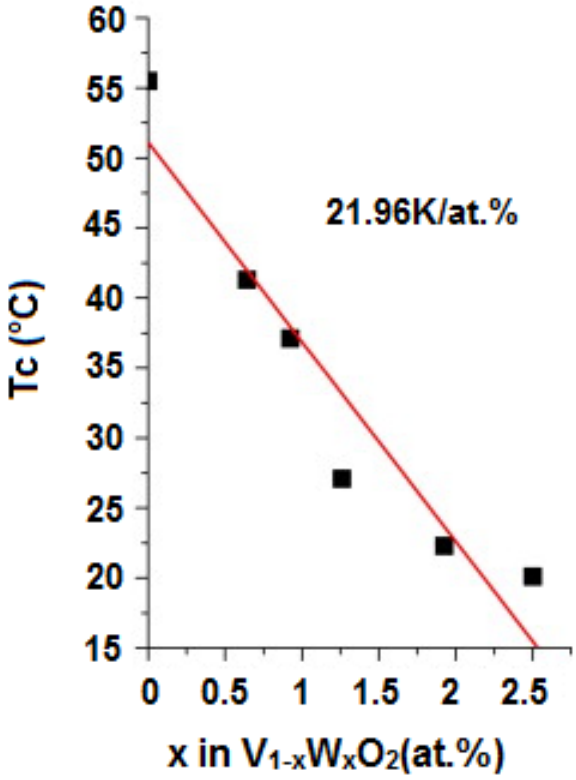

Figure B2 T_c reduction efficiency of W-doped VO_2 from Reference [11].

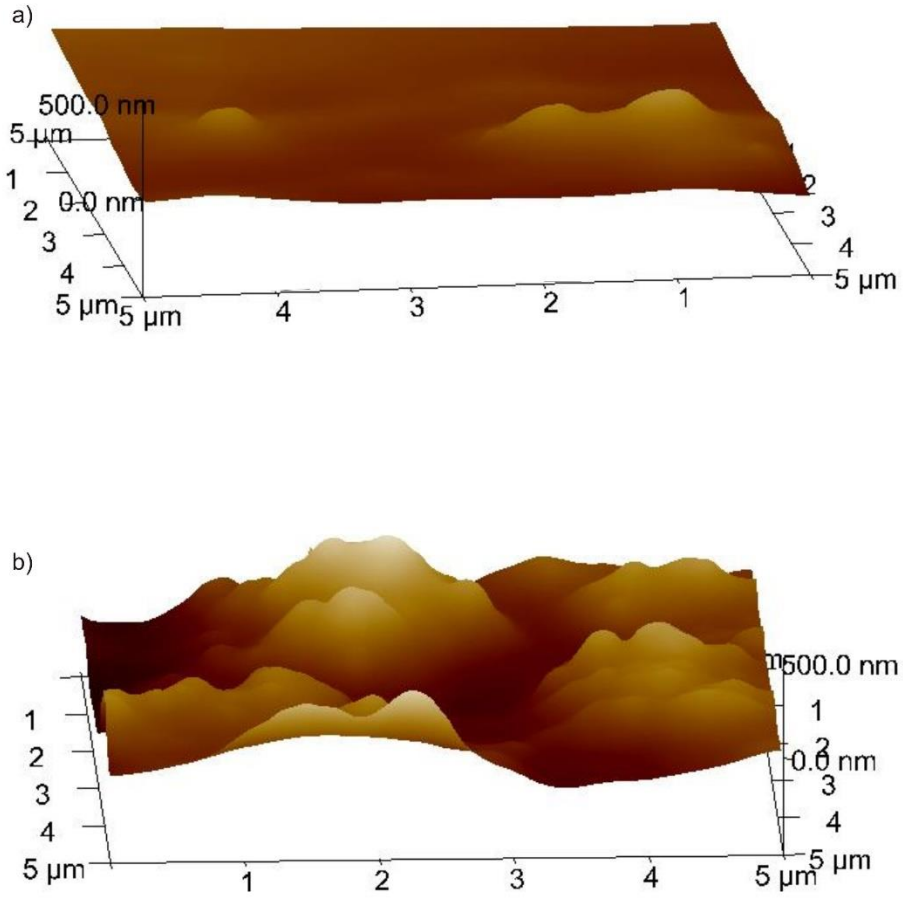

Figure B3 AFM images of the (a) VO_2 and (b) 1at. % W-doped VO_2 films.

APPENDIX C

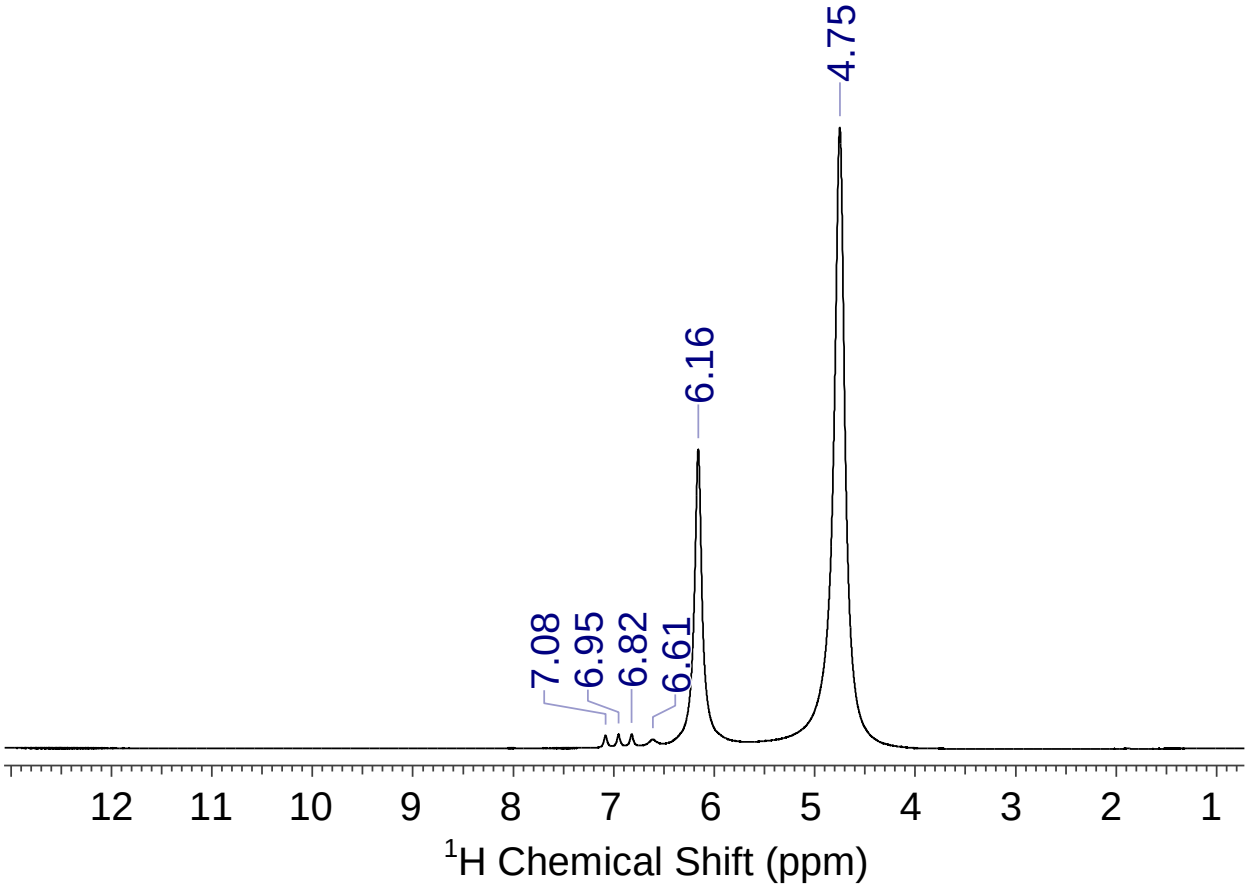

Figure C1 ^{1}H NMR spectra of the residual solute in the clear solution after freeze-drying.

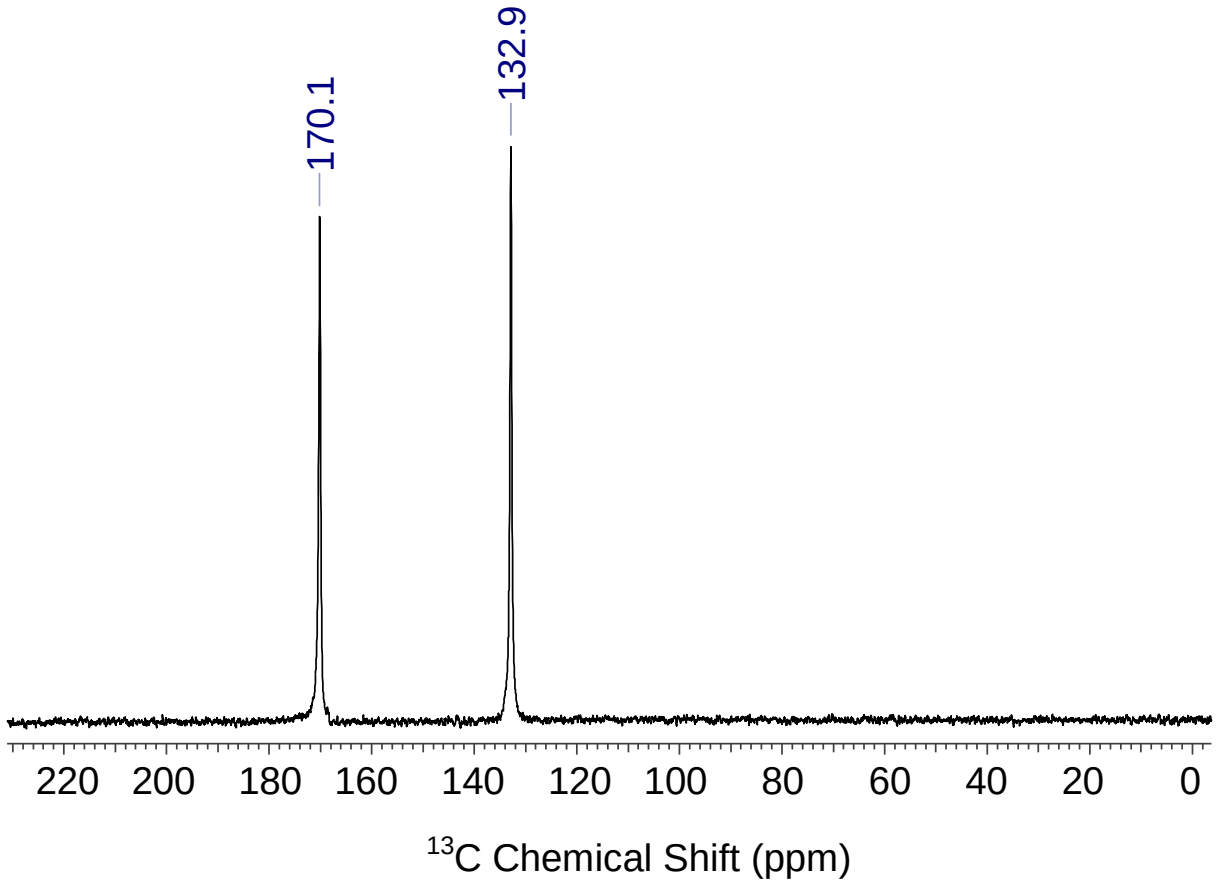

Figure C2 ^{13}C NMR spectra of the residual solute in the clear solution after freeze-drying.

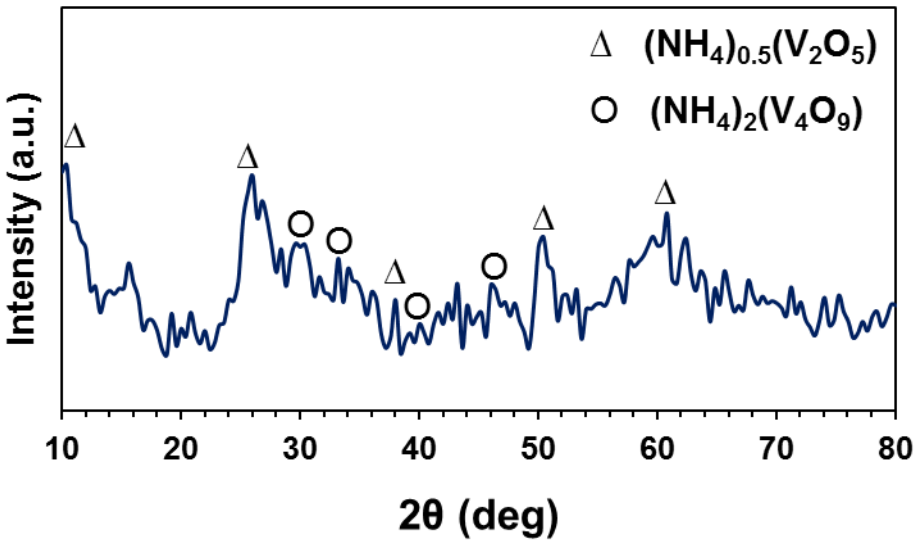

Figure C3 XRD spectra of as synthesized product without calcinations.

APPENDIX D

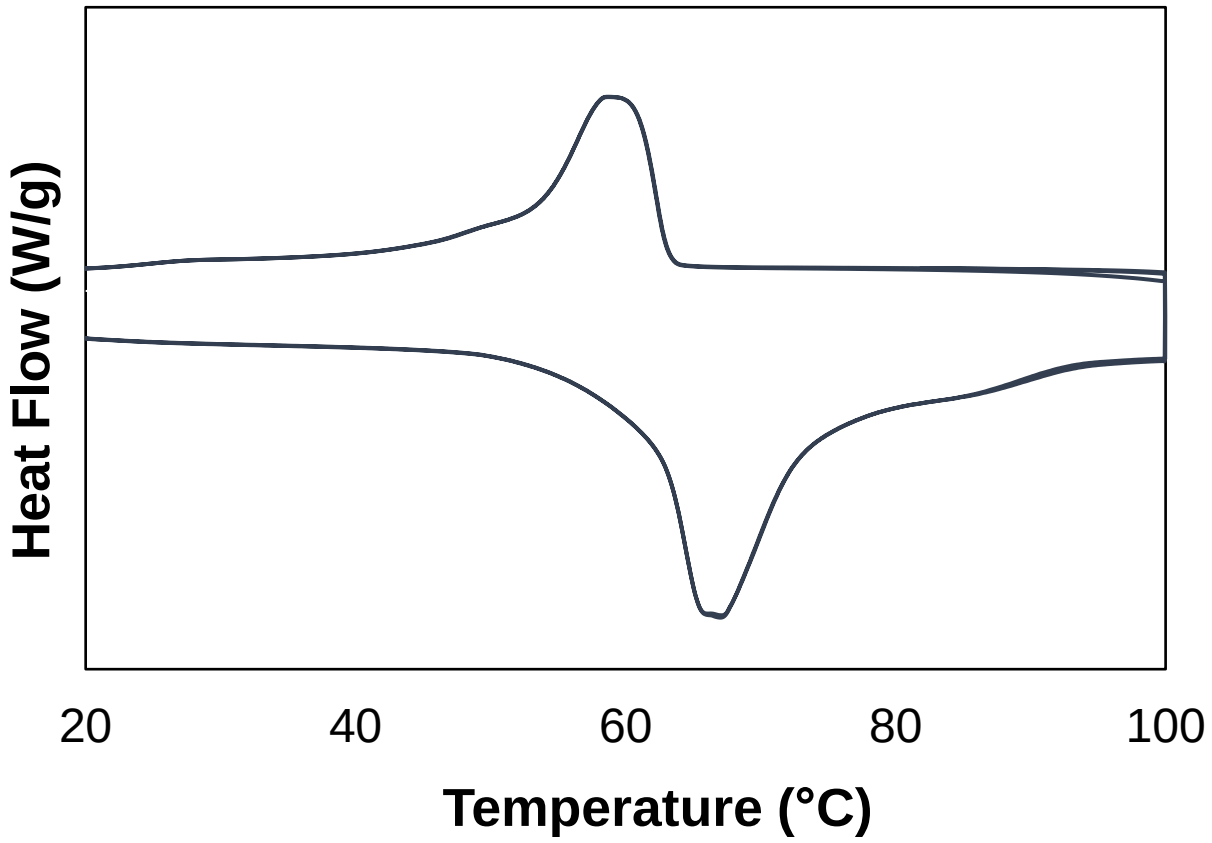

Figure D1 10-cycles DSC heating/cooling scans for 2.5 at. % W-doped VO_2 sample.

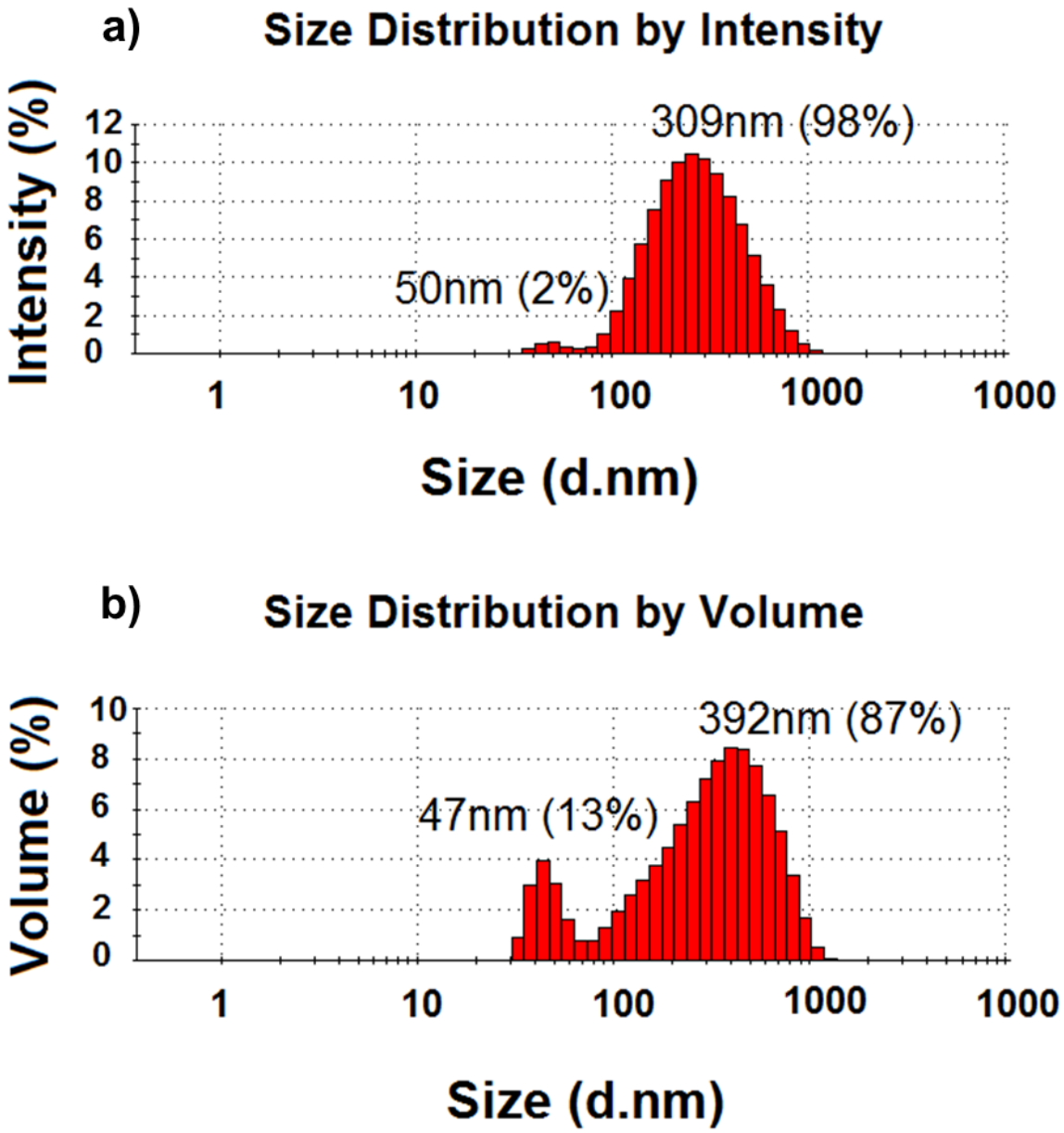

Figure D2 Size distribution histogram by (a) intensity and (b) volume for un-doped VO_2 determined by DLS.

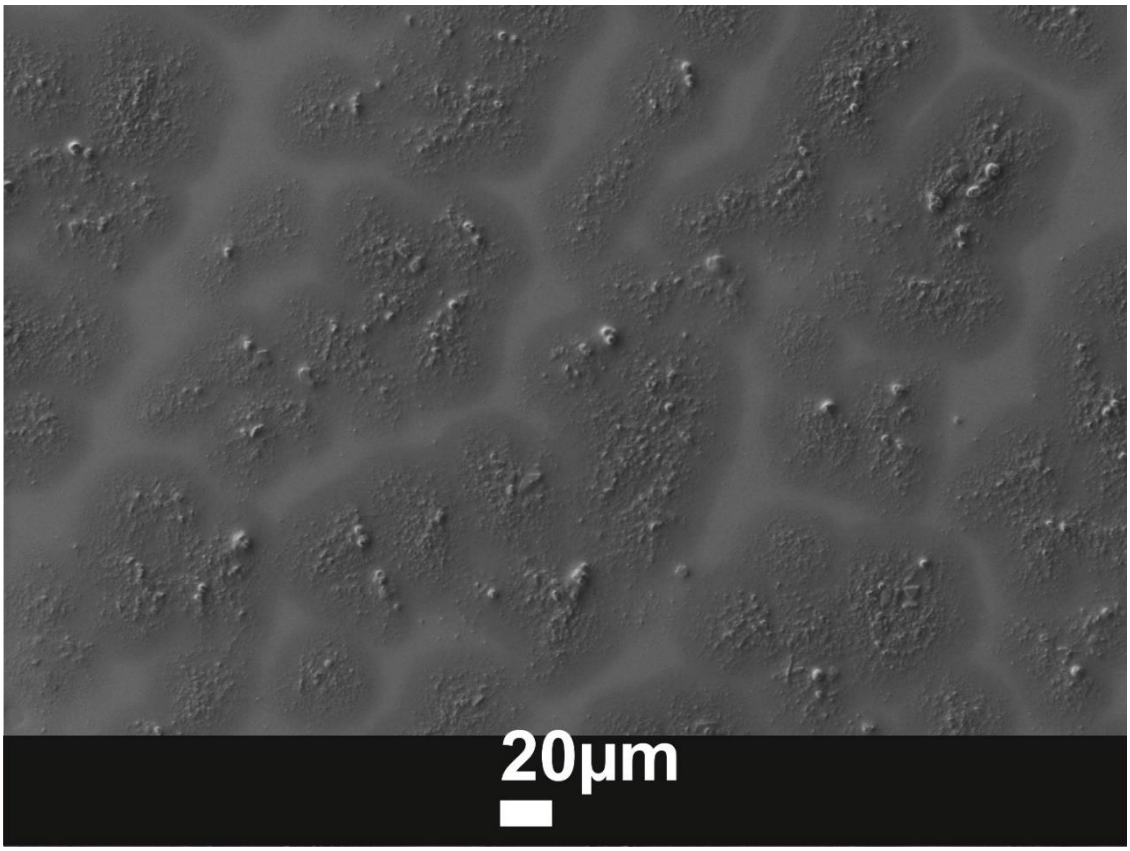

Figure D3 SEM image of 2.5 at. % W-doped VO_2 dispersed in PVP coatings on glass.

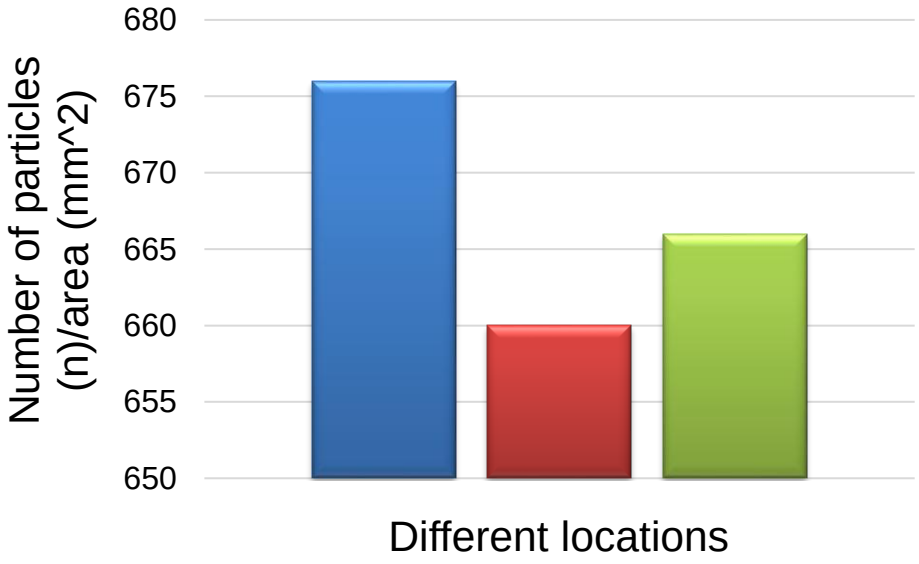

Figure D4 Histogram of spread of particles in the film estimated by the number of particles (n) per unit area (mm^2) at three different locations.

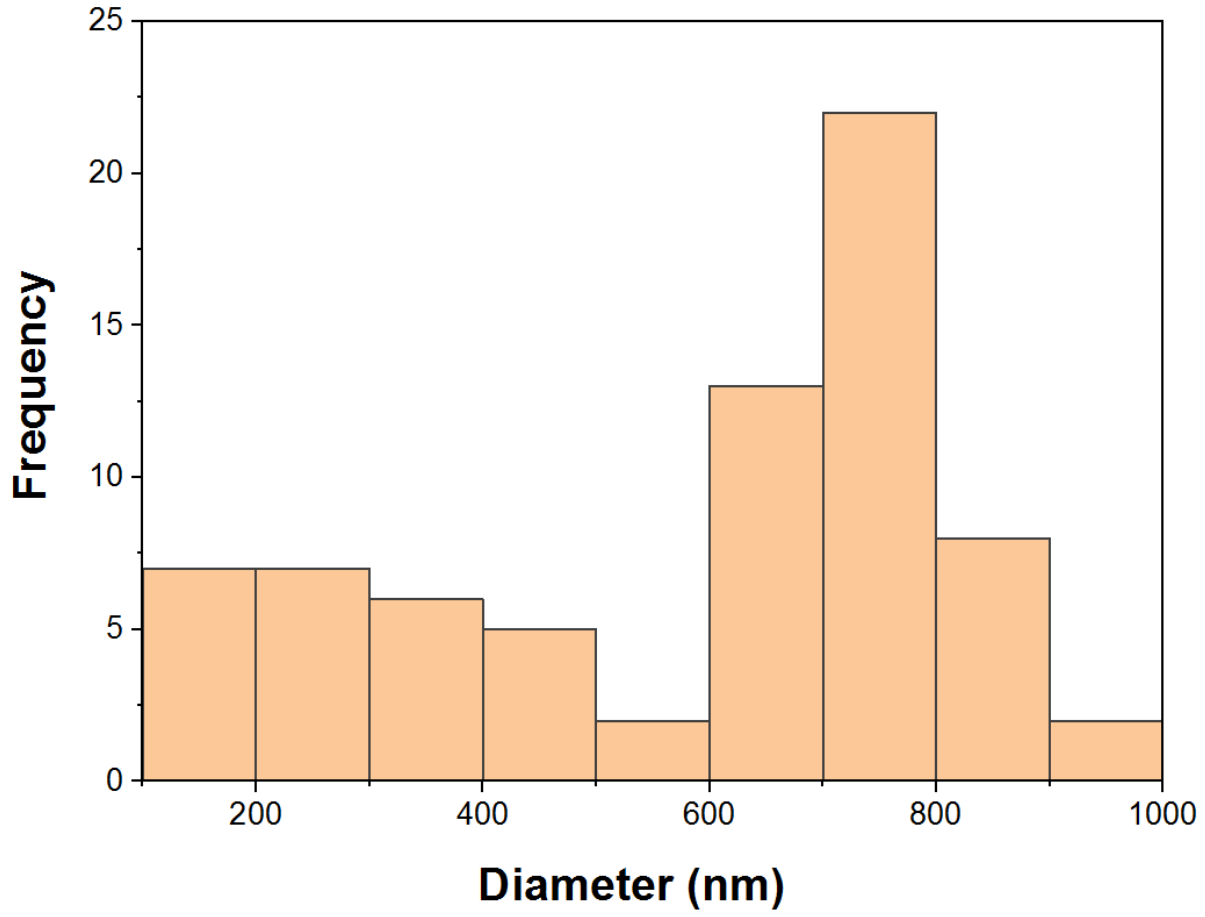

Figure D5 Size distribution histogram of VO_2 dispersed in PVP coatings on glass obtained using ImageJ software analysis for the SEM image of Figure 5.13 in the manuscript.

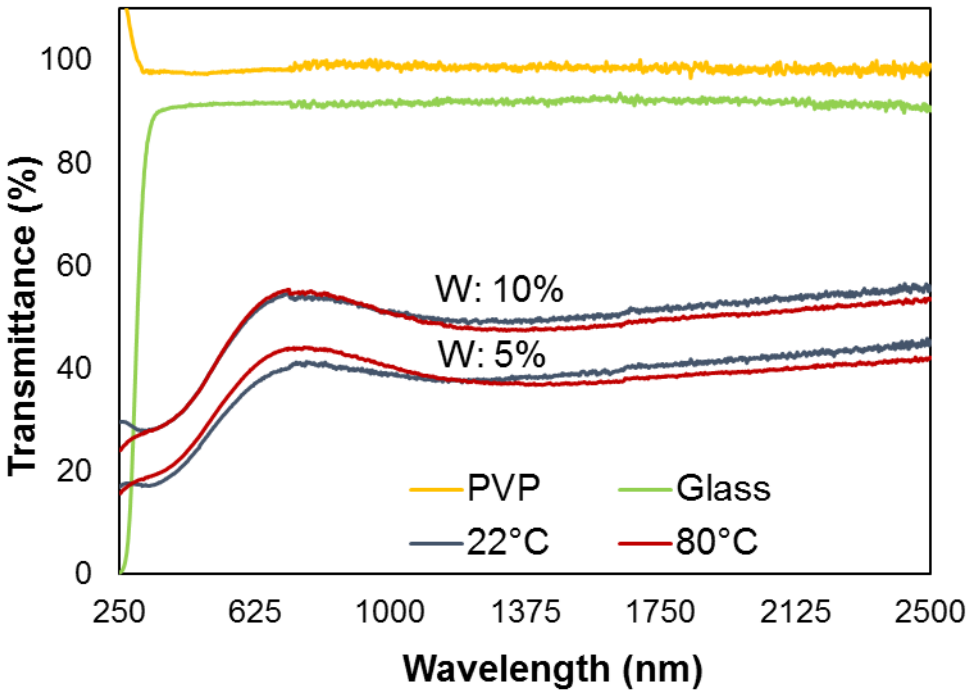

Figure D6 Optical transmittance spectra of glass microscope slide at RT (green), PVP coating on glass at RT, with no VO_2 (yellow), and 5at. % (blue/red) and 10 at. % (blue/red) W-doped-VO_2 coatings on glass. 22 °C: blue, 80 °C: red (Reference with respect to glass microscope slide at appropriate temperature).

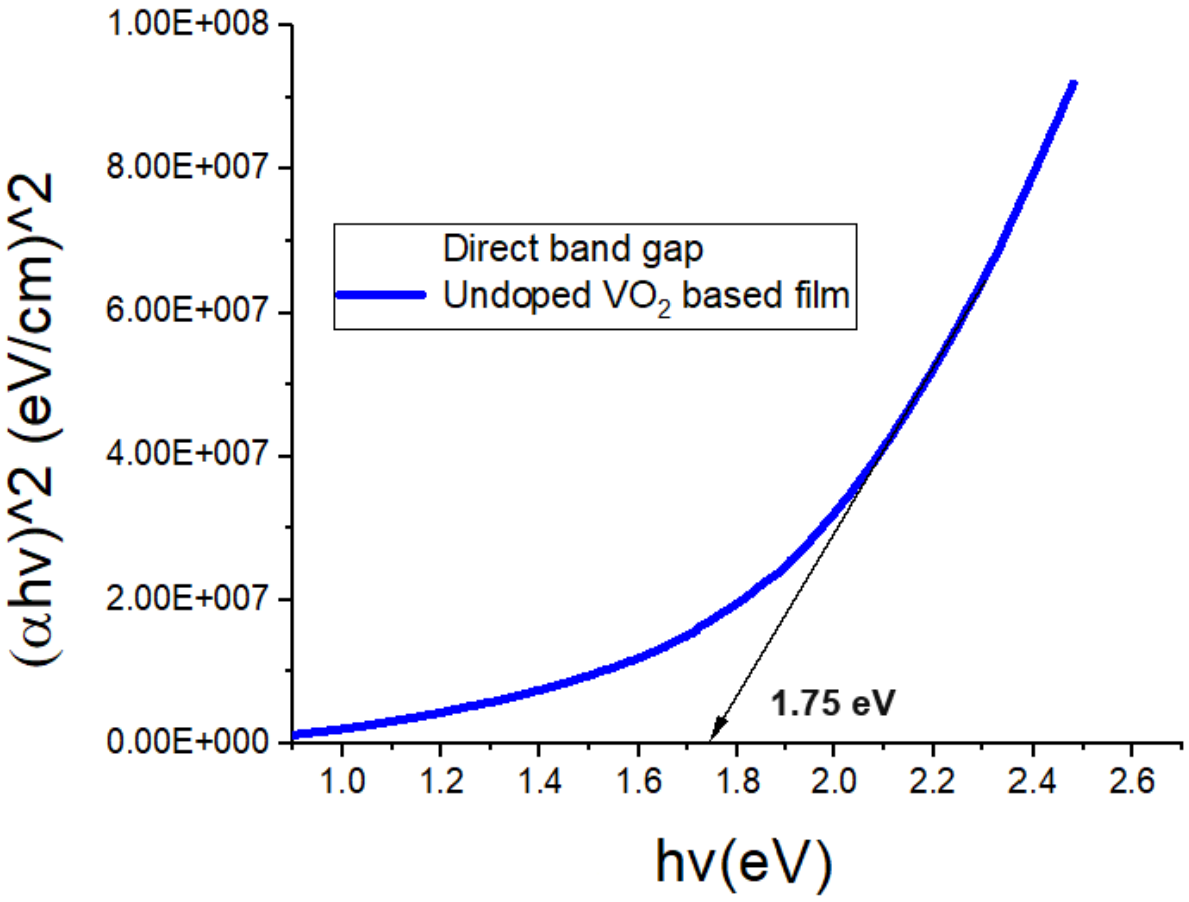

Figure D7 Tauc plot: optical absorption coefficient (αhv)^2 (eV/cm)^2 vs. phonon energy hv (eV) of the undoped semiconductor VO_2 (M) based film coated on the glass substrate.

APPENDIX E

Order Summary

Licensee:	uwo
Order Date:	Mar 30, 2018
Order Number:	4319090216341
Publication:	Journal of Materials Chemistry A
Title:	One-step hydrothermal synthesis of V1−xWxO2(M/R) nanorods with superior doping efficiency and thermochromic properties
Type of Use:	Thesis/Dissertation
Order Total:	0.00 USD

Order Summary

Licensee:	uwo
Order Date:	Mar 30, 2018
Order Number:	4319101336164
Publication:	CrystEngComm
Title:	Star-shaped VO2 (M) nanoparticle films with high thermochromic performance
Type of Use:	Thesis/Dissertation
Order Total:	0.00 USD

Order Summary

Licensee:	uwo
Order Date:	Mar 30, 2018
Order Number:	4319110315240
Publication:	Journal of Materials Chemistry A
Title:	Electrospun α-Fe2O3 nanostructures for supercapacitor applications
Type of Use:	Thesis/Dissertation
Order Total:	0.00 USD

Order Summary

Licensee:	uwo
Order Date:	Mar 30, 2018
Order Number:	4319110727996
Publication:	RSC Advances
Title:	Fabricating fiber, rice and leaf-shaped TiO2 by tuning the chemistry between TiO2 and the polymer during electrospinning
Type of Use:	Thesis/Dissertation
Order Total:	0.00 USD

Order Summary

Licensee:	uwo
Order Date:	Mar 29, 2018
Order Number:	4318440635410
Publication:	Physical Chemistry Chemical Physics
Title:	Orbital change manipulation metal–insulator transition temperature in W-doped VO2
Type of Use:	Thesis/Dissertation
Order Total:	0.0 USD

American Physical Society
Reuse and Permissions License

30-Mar-2018

This license agreement between the American Physical Society ("APS") and dicho zomaya ("You") consists of your license deta and the terms and conditions provided by the American Physical Society and SciPris.

Licensed Content Information

License Number:	**RNP/18/MAR/002826**
License date:	30-Mar-2018
DOI:	10.1103/PhysRevB.41.4993
Title:	Vacuum-ultraviolet reflectance and photoemission study of the metal-insulator phase transitions in ${\mathrm{VO}}_{2}$, ${\mathrm{V}}_{6}$${\mathrm{O}}_{13}$, and ${\mathrm{V}}_{2}$${\mathrm{O}}_{3}$
Author:	S. Shin et al.
Publication:	Physical Review B
Publisher:	American Physical Society
Cost:	USD $ 0.00

Request Details

Does your reuse require significant modifications: No

Specify intended distribution locations:	Worldwide
Reuse Category:	Reuse in a thesis/dissertation
Requestor Type:	Student
Items for Reuse:	Figures/Tables
Number of Figure/Tables:	1
Figure/Tables Details:	Figure: Band structure diagram of VO2
Format for Reuse:	Electronic

Information about New Publication:

University/Publisher:	uwo
Title of dissertation/thesis:	synthesis of chemically stable VO2 partilces using green solvents and their application as smart window
Author(s):	Dicho Zomaya
Expected completion date:	Sep. 2018

License Requestor Information

Name:	dicho zomaya
Affiliation:	Individual
Email Id:	
Country:	Canada

Brahlek, M., Zhang, L., Lapano, J., Zhang, H., Engel-Herbert, R., Shukla, N., Datta, S., Paik, H., Schlom, D. (2017). Opportunities in vanadium-based strongly correlated electron systems. *MRS Communications, 7*(1), 27-52 © Materials Research Society 2017, published by Cambridge University Press

Thank you for your request to reproduce the above material in your forthcoming PhD thesis, for non-commercial publication. Cambridge University Press are pleased to grant non-exclusive permission, free of charge, for this specific one time use, on the understanding you have checked that we do not acknowledge any other source for the material. This permission does not include the use of copyright material owned by any party other than the authors. Consent to use any such material must be sought by you from the copyright owner concerned.

CV: Dicho Zomaya

Profile

- PhD candidate in Chemical Engineering (expected to graduate in April 2019)
- Masters of Engineering; Chemical Engineering
- Bachelor of Science; Honours Specialization in Chemistry and Minor in Biology
- Experience working as a Graduate Teaching Assistant (GTA), R&D Chemical Engineer and Chemical Plant Process Operator

Skills Summary:

Research and Development

- Synthesized smart nanoparticles (NPs) in water using simple and novel methodologies
- Investigated the effect of different dopants on the phase transition and anti-oxidation property of smart NPs
- Modified the surface chemistry of NPs by blending with different polymers for application in smart coatings
- Improved the optical and thermochromic property of the smart coatings on glass due to excellent NPs dispersion
- Enhanced polyurethane foam products chemical & physical properties
- Designed different types of polyurethane foam product containers/bags/moulds
- Developed alternative formulations for polyurethane foam product

Laboratory Experimental Techniques

- Spectrometry analysis: Atomic Absorption, UV NIR VIS Spectrophotometry
- Physicochemical analysis: : SEM, AFM, NMR, FTIR, X-ray
- Thermal analysis: DSC, and TGA
- Particle size and size distribution analysis: DLS
- Equipment: Centrifuge, Spin Coater, Tube Furnace, Tensile Tester, Heat Sealer, QUV Machine, Viscometer, Carl Fischer Titrator

Computer and Technical Systems

- MS Office: Word, Excel, Power Point, Outlook, Project
- Modeling: ChemDraw, CorelDraw
- Processor: ImageJ, TA Universal Analysis, Origin

Conferences and Publications:

- Presented a poster in the International Conference on Quantum Dots (QD2018) held at Toronto University on the project titled ‘Aqueous Based Reflux Synthesis of W-doped VO_2 Delivering PVP-Coating with an Excellent Optical Property’.
- Manuscript: Dicho Zomaya, W-doped VO_2/PVP Coatings with Enhanced Thermochromic Performance, submitted to Solar Energy Materials and Solar Cells

Related Work Experience:

PhD/doctoral candidate, Western University., London, ON 2015-2019 (expected)
Thesis Title: "Synthesis of Chemically Stable VO_2 Particles Using Green Solvents and their Application as Smart Coatings"

- Synthesized smart materials (e.g. vanadium dioxide nanoparticles (VO_2-NPs)) in water using simple and novel methodologies
- Investigated the effect of different dopants on the phase transition and anti-oxidation property of smart NPs
- Modified the surface chemistry of nanoparticles by blending with different polymers for application in smart coatings
- Improved the optical and thermochromic property of the smart coatings on glass due to excellent NPs dispersion
- Teaching Assistant (Organic chemistry and Chemical engineering Lab courses)

Research and Development Chemical Engineer, Chemque Inc., Toronto, ON 2012-2013

- Improved polyurethane foam products physical and chemical properties
- Designed different types of polyurethane foam product containers, bags and moulds
- Alternative foam formulations
- Used tensile tester to evaluate the mechanical properties of materials using tension, compression, flexure, fatigue, impact, torsion, adhesion and hardness tests
- Conducted wide variety of testing and analysis by using AA, Gas and Liquid Chromatography, Heat Sealer, QUV machine, Viscometer, Carl Fischer Titrator, Hardness and impact Tester

Chemical Plant Process Operator, Neo Material Technologies Inc., Peterborough, ON 2012

- Performed laboratory techniques according to written procedures include: sample preparation, leaching, filtration, solvent extraction, disposal of samples and filing/logging of lab results/data
- Operated and maintained lab equipment and systems, including exposure to AA equipment
- Calibrated and set up equipment prior to use
- Conducted wide variety of testing and analysis on base and precious metal ores, industrial minerals and materials such as Indium and Galium
- Worked on batch process sampling & monitoring, material handling, solids filtration & management

Education and Training:
Chemical and Biochemical Engineering, PhD/doctoral candidate, University of Western Ontario (U.W.O.)

2015-2019(expected)
Chemical and Biochemical Engineering, Masters, University of Western Ontario (U.W.O.)
2010– 2011
Honours Specialization in Chemistry &Minor in Biology, **B. Sc.,** University of Western Ontario 2006–2010